

ABSTRACT

LEARY, JENNIFER DANA. Conductive Carbon-Based Nonwovens for Supercapacitor Electrodes and Related Electrochemical Technologies (Under the direction of Dr. Benoît Mazé and Dr. Behnam Pourdeyhimi).

Textiles offer two properties that are highly attractive for use in energy storage electrodes – flexibility and high specific surface area (SSA). Flexible electrodes are sought after for wearable applications, while high SSA electrodes promise enhanced energy density. For these two reasons, many authors have explored methods for converting fabrics into energy storage electrodes. Carbon-based conductors are particularly well-suited for the task due to their electrochemical stability. They can be integrated with textiles via two general routes: (1) high-temperature carbonization of fibers, or (2) coating of fibers with carbon nanoparticles. Conductive fabrics can then be activated and used as electric double-layer capacitor (EDLC) electrodes, or further treated with redox materials to perform as pseudocapacitor (PC) electrodes. A review of the literature revealed that a significant amount of research has been carried out into such treatments. However, their findings shed very little light on understanding how the underlying fabric properties play a role in the effectiveness of these treatments.

The first major goal of this research was to analyze carbon fiber nonwovens for use as supercapacitor electrodes. A tremendous variety of carbon fiber nonwovens are currently available in the market, and several of these materials were collected for use here. Many of these were found to be partially coated with a polymer binder for web cohesion, rendering them ill-suited for use as EDLC electrodes. Such electrodes rely on extremely high-SSA materials ($> 1000 \text{ m}^2 \text{ g}^{-1}$) which are prepared by converting carbon materials into activated materials at temperatures that would completely degrade the binder. A binder-free carbon fiber nonwoven was subjected to the activation treatment, but no microporosity was achieved. In order to understand what was preventing activation, carbon fiber nonwovens were fabricated in-house under known conditions. XRD, XPS and conductivity studies showed that the development of ordered sp^2 bonded carbon domains was a direct function of carbonization temperature. Nitrogen adsorption studies indicated that, as these ordered domains grew, activation became less possible. These findings suggest that the commercially available carbon fiber nonwoven was subjected to a high carbonization temperature, and that

its well-developed carbon microstructure prevented it from developing micropores. Although commercially available carbon fiber nonwovens were found to be unsuitable for activation, they were coated with polyaniline (PANI), a redox active species, and used as PC electrodes. In an initial study, specific capacitance was measured before and after deposition, and those which were binder-free showed a remarkable increase, from 0.02 F g^{-1} to over 14 F g^{-1} . PANI deposition was optimized by tuning deposition potential, aniline concentration and deposition duration. A potential of 0.744 V resulted in a symmetrical CV curve. When aniline concentration was increased to 0.5 M , the 20 minute deposition time resulted in a higher specific capacitance: 83 F g^{-1} based on total electrode mass, and 220 F g^{-1} in terms of PANI mass only.

The second major goal of this research was to determine how nonwoven properties affected the performance of carbon nanoparticle coatings. CNT and graphene dispersions were prepared, and many of the dispersion parameters were studied. Using ethanol instead of water eliminated the need for surfactants in CNT dispersions, and a method for obtaining highly concentrated graphene flake dispersions was found. These dispersions were applied onto nonwoven scaffolds and studied. The most influential structural parameter of the fabrics was found to be solid volume fraction (SVF). PANI was deposited onto the CNT and graphene coated nonwovens. Due to the higher conductivity of CNT, the deposition mass loading was double that obtained on the graphene coated scaffold. On the basis of electrode mass, specific capacitance was 49 F g^{-1} for CNT coated scaffolds, and 21 F g^{-1} for EGF coated scaffolds. However, capacitance was about equal on the basis of PANI mass (around 150 F g^{-1} of PANI). The relative similarity in performance indicated that graphene can be used as a safer and cheaper alternative to CNT in obtaining flexible, highly-conductive nonwoven supercapacitor scaffolds.

© Copyright 2016 Jennifer Dana Leary

All Rights Reserved

Conductive Carbon-Based Nonwovens for Supercapacitor Electrodes and Related
Electrochemical Technologies

by
Jennifer Dana Leary

A dissertation submitted to the Graduate Faculty of
North Carolina State University
in partial fulfillment of the
requirements for the degree of
Doctor of Philosophy

Fiber & Polymer Science *and* Textile Technology Management

Raleigh, North Carolina

2016

APPROVED BY:

Dr. Behnam Pourdeyhimi
Committee Co-Chair

Dr. Benoît Mazé
Committee Co-Chair

Dr. Xiangwu Zhang

Dr. Ericka Ford

Dr. Edmond Bowden

DEDICATION

This dissertation is dedicated to the element carbon, which has remarkable uses from charcoal / pencil drawing to conductive coatings.

BIOGRAPHY

Jennifer Dana Leary grew up in the foggy Sunset district of San Francisco. She studied painting as an undergrad at Cornell University, and discovered textiles towards the end of her time there. She moved to the UK to pursue a Masters in Design for Textile Futures at Central Saint Martins in London, where she carried out research into the possibility of magnetic textiles. This work was continued through a design collective called Puff & Flock, which was established to incubate such research projects. After moving back to the US (California) in 2011, she started to apply to PhD programs. Meanwhile, she founded a small business, Ferrofabric, where she continued to develop custom-made magnetic materials for designers. After being accepted to the NC State College of Textiles, she moved to Raleigh, NC. She will be obtaining a PhD in Fiber & Polymer Science and Textile Technology Management.

ACKNOWLEDGMENTS

I would like to express my deepest gratitude to my co-advisors, Dr. Behnam Pourdeyhimi and Dr. Benoît Mazé, for their guidance through the challenges of the past 3.5 years. Their advice has helped me in countless ways, from keeping my research focused to providing me with invaluable opportunities to gain leadership experience. I am extremely thankful for all the effort that they have dedicated to helping me grow.

Many thanks to my committee members, Dr. Ericka Ford, Dr. Xiangwu Zhang and Dr. Edmond Bowden, for their time and support. I would not be ready to defend if Dr. Ford had not sat me down in her office a little over a year ago and walked me through the structure of my prelim document. Dr. Bowden taught one of the best courses that I took at NC State, and I'm sure the notes will travel with me from bookshelf to bookshelf over the coming years. I also would like to acknowledge Dr. Zhang's support of graduate student activities as TECS Director of Graduate Programs.

I also owe appreciation to Farah Hamouda for all her hard work as an undergraduate researcher in this lab. Without her cheerful dedication, this dissertation would not exist (at least, not yet). Thanks to my many friends in the NWI Student Group for their insightful feedback and camaraderie. Additionally, to all my other friends (new and old, near and far) to whom I am immensely grateful for being so funny, interesting and supportive.

I am indebted to my whole family, especially my mother, for being endlessly understanding throughout my extensive journey of education. This includes the Rezaeis, for treating me like family over the past 3 years. Special thoughts go to the memories of my dad, Keisho VK Leary, whose wish for me to finish my PhD was a major motivation that kept me going.

Finally, a world of thanks to another PhD student whose support has never failed me – Farzad Rezaei. Anyone who knows him can attest that he is unbelievably generous with his time, knowledge, and his signature *joie de vivre*, of which I have been a very fortunate recipient as we passed through the College of Textiles side-by-side. *Merci*.

TABLE OF CONTENTS

LIST OF TABLES	vii
LIST OF FIGURES	ix
CHAPTER 1: Introduction Part I – Overview and Characterization of Electrodes for Electrochemical Technologies.....	1
1.1 Overview of Electrochemical Technologies	2
1.2 Supercapacitors	5
1.3 Characterization Methods and Metrics	16
CHAPTER 2: Introduction Part II – Overview of Nonwoven Technologies and Dissertation Outline.....	32
2.1 Overview of Nonwoven Technologies	33
2.2 Nonwoven Electrodes	38
2.3 Conductive Carbon Fiber Nonwovens.....	45
2.4 Conductive Carbon-Coated Nonwovens.....	61
2.5 Summary and Objectives	71
CHAPTER 3: Carbon Fiber Nonwovens as Double Layer Capacitor Precursor	75
3.1 Introduction.....	76
3.2 Experimental	78
3.3 Results and Discussion	80
3.4 Conclusions.....	94
CHAPTER 4: Carbon Fiber Nonwovens as Pseudocapacitor Scaffold.....	95
4.1 Introduction.....	96
4.2 Experimental	98
4.3 Results and Discussion	101
4.4 Conclusions.....	110

CHAPTER 5: Carbon Nanotube Coated Nonwovens as Flexible Supercapacitor Electrodes.....	112
5.1 Introduction.....	113
5.2 Experimental Procedures	115
5.3 Results and Discussion	118
5.4 Conclusions.....	133
CHAPTER 6: Graphene Coated Nonwovens as Flexible Supercapacitor Electrodes Part I - Comparison of Reduced Graphene Oxide with Exfoliated Graphite Flake.....	135
6.1 Introduction.....	136
6.2 Experimental.....	139
6.3 Results and Discussion	142
6.4 Conclusions.....	153
CHAPTER 7: Graphene Coated Nonwovens as Flexible Supercapacitor Electrodes Part II – Optimization of Exfoliated Graphite Flake Coating Method.....	154
7.1 Introduction.....	155
7.2 Experimental.....	157
7.3 Results and Discussion	161
7.4 Conclusions.....	180
CHAPTER 8: Conclusions and Recommendations.....	181
8.1 Overall Conclusions.....	182
8.2 Recommendations for Future Work.....	187
REFERENCES.....	188

LIST OF TABLES

CHAPTER 1 TABLES

Table 1: Examples of materials and corresponding SSA.	14
Table 2: Properties of a selection of gas diffusion layer materials. ⁴⁵	19

CHAPTER 2 TABLES

Table 3: Staple fiber based batch technologies and vertically integrated technologies used to fabricate nonwovens. ⁵³	34
Table 4: Comparison of properties and application scope for various ACF precursor. ¹¹³	60

CHAPTER 3 TABLES

Table 5: BET and DFT estimates of specific surface area for GDL materials activated under the conditions shown below.	81
Table 6: Carbonization and activation treatments for PAN fiber nonwovens.	83
Table 7: Elemental composition and mass loss for carbon fiber nonwoven samples.	84
Table 8: Interlayer spacing (d_{002}) and crystal dimensions (L_c and L_a) calculated from peak position and peak FWHM of XRD results.	87
Table 9: Activation treatment conditions for carbonized PAN nonwovens.	89
Table 10: Elemental composition and mass loss following activation for carbonized PAN nonwovens.	91
Table 11: BET and DFT specific surface area estimates, and DFT mode pore radius for activated PAN carbon fiber nonwovens.	94

CHAPTER 4 TABLES

Table 12: Specific capacitance of various carbon fiber nonwoven scaffolds, based on CP discharge at 0.5 mA, before and after deposition of PANI.....	102
Table 13: Specific capacitance values, shown both on the basis of total electrode mass as well as PANI mass only, for various aniline solution concentrations and deposition times.	109

CHAPTER 6 TABLES

Table 14: Circuit element values based on model circuit of resistor (R1) and constant phase element (Q1) in series, for PET 4DG samples coated with rGO and EGF.	148
Table 15: Specific capacitance based on total electrode mass and graphite mass only for rGO and EGF coated PET 4DG nonwovens, from galvanostatic charge-discharge tests.	152
Table 16: UV-vis absorbance values and derived graphene concentrations, based on three different absorption coefficient estimates.	163

CHAPTER 7 TABLES

Table 17: Average particle diameter for EGF dispersions sonicated by horn and by bath for various dispersions, based on DLS measurements and Zetasizer software.	166
Table 18: Specific double layer capacitance (EDLC) for samples with three different conductive coatings. Pseudocapacitance (PC) after PANI electrodeposition is also shown. Specific PC is calculated based on full electrode mass as well as PANI mass only.	179

LIST OF FIGURES

CHAPTER 1 FIGURES

Figure 1: Main categories of commercialized electrochemical (EC) technology, highlighting possible application areas for nonwoven electrodes.....	2
Figure 2: Essential functions of (a) a battery, (b) a fuel cell, and (c) a supercapacitor. ¹⁵	6
Figure 3: Power density range and energy density range for different types of devices. ¹⁸	6
Figure 4: (a) Illustration of original EDLC using lampblack. ¹⁹ (b) EDLC from Murata, typical of current devices. ²⁰	7
Figure 5: (a) Placement of an electrochemical capacitor in as a backup power source. ¹⁸ (b) Smoothing effect of supercapacitor on the discharge voltage from a Li battery to a load. ²³	8
Figure 6: Number of patents published each year relating to supercapacitor technology. ²¹	9
Figure 7: Representations of the (a) Helmholtz, (b) Gouy-Chapman and (c) Gouy-Chapman-Stern models of the electric double-layer, along with the distribution of potential. ⁸	10
Figure 8: (a) Space charge distribution from surface of electrode with graphite basal layer exposed to ionic solution. ³² (b) Schematic depiction and circuit element equivalent of capacitance layers extending within and beyond graphite surface. ³¹	11
Figure 9: Specifically adsorbed transition metal oxide clusters, which have multiple redox states and support fast intercalation of charged species. (a) Negatively charged electrode and (b) positively charged electrode.....	12
Figure 10: Cyclic voltammograms for (a) quasi-reversible Pb/PbCl ₂ battery reactions, (b) ideal capacitor, (c) ideal pseudocapacitor. ²⁶	12
Figure 11: Optimizing the pore size of activated carbon is more effective than simply increasing the pore volume. ²¹	16
Figure 12: Number of uses of different electrical metrics (R = resistivity, IPR = in-plane resistivity, TPR = through-plane resistivity, C = conductivity, SR = sheet resistivity, ESR = equivalent series resistance) along with the units used, among 78 instances.....	17
Figure 13: Plots of cyclic voltammetry showing (a) applied potential with fixed sweep rate (v), (b) typical resulting current showing development of double layer, and (c) current as a function of potential, which is known as the voltammogram. ¹	21

Figure 14: Features of a typical EDLC voltammogram, with modifications due to various physical properties shown. ³⁴	22
Figure 15: Specific power as a function of specific energy for a commercial 350 F supercapacitor from Maxwell Technologies. ⁴⁸	23
Figure 16: Relationship between AC current and AC voltage, showing typical phase shifts for capacitors, inductors and resistors.	24
Figure 17: (a) Nyquist plot of real component and imaginary component of the complex impedance, with each marker representing a different frequency. (b) Bode plot for the same circuit.	26
Figure 18: Nyquist plots for (a) a series RC circuit and (b) a parallel RC circuit with $R = 100\Omega$ and $C = 1\mu F$. ¹	26
Figure 19: (a) RC series circuit approximates the charge path of an EDLC electrode. R_s is solution resistance and C_{dl} is double layer capacitance. (b) PC electrode includes R_{ct} – charge transfer resistance – and C_{pc} – pseudocapacitance.	27
Figure 20: Surface functionalized activated carbon electrodes with (a) equivalent circuit and (b) EIS data. ³²	28
Figure 21: (a) Two-electrode setup with two identical electrodes. (b) Three-electrode setup with working electrode, reference, and counter electrode. Simplified equivalent circuits shown for each. ⁵⁰	29
Figure 22: Reported specific capacitance values for various active materials as taken from the literature. ⁵²	30
Figure 23: Various designs of fiber-based supercapacitor electrodes, divided into their “active” part and “non-active” part (A and B, respectively).	31

CHAPTER 2 FIGURES

Figure 24: (a) Two extruders aligned to spin a bicomponent fiber composed of two polymers. (b) Surface area for round, 4DG, and winged fibers as a function of diameter. ⁵⁷	36
Figure 25: Figure 3: Cross-sectional SEM of various microfibers: (a) Islands-in-the-Sea as-extruded, (b) washed winged fiber, (c) split segmented pie. ⁵⁸	36
Figure 26: Schematic of an open spunbond process with a belt collector. ⁵⁹	37
Figure 27: Carding machine for nonwoven web with single chute fed. ⁶⁰	38

Figure 28: Polymer fibers can be modified to be conductive via (a) metallic coating, (b) carbon particle coating, (c) intrinsically conductive polymer coating, (d) co-extrusion with conductive particles, (e) continuous carbon fiber, or (f) continuous metal fiber.	39
Figure 29: (a) Carbon fiber nonwoven used as wastewater treatment electrode, and (b) electrode with adsorbed reduced Cr ⁶⁺ . ⁷¹ (c + d) Nylon fiber coated with carbon nanotubes. ⁷²	41
Figure 30: (i) Variation in current with the mean linear flow rate for cells with (a) flat plate cathode, (b) 10 ppi RVC cathode, (c) 100 ppi RVC cathode, and (d) carbon felt cathode. (ii) Renocell cartridge. ⁸	42
Figure 31: (a) Placement of GDL in MEA; ⁷⁶ (b + c) Sigracet 10AA electrode: untreated carbon fiber spunlace; ⁷⁷ (d) Cross-section of the interface between catalyst, electrolyte, and GDL. ⁷⁸	43
Figure 32: Carbon-carbon bonds in a sheet of aromatic rings are responsible for the unique properties of carbon fiber. ⁵⁶	46
Figure 33: Cellulose molecule with two carbon rings. ⁵⁶	47
Figure 34: Cyclization of pendant nitrile groups during the PAN conversion process. ⁸²	47
Figure 35: Petroleum-based pitch molecules rich in aromatic rings. ⁵⁶	48
Figure 36: Simple overview of steps in the carbonization process.	49
Figure 37: (Top) In pre-carbonization, web is formed from carbon fiber. (Bottom) In post-carbonization, web is formed from polymer fiber and carbonized subsequently.	50
Figure 38: Illustration of a wet-laid carbon fiber / pulp blend sheet. ⁸⁹	51
Figure 39: Feeding layers of different types of fiber onto a wet-lay belt. ⁸⁹	51
Figure 40: Layers used in some needle-punched carbon fiber sheets: (a) High modulus unidirectional continuous carbon fiber held in place by disposable weft yarn. (b) Wet-laid staple carbon fiber sheet. ⁹¹	52
Figure 41: Groz-Beckert high performance Gebedur II needles compared to standard needles after heavy use with high strength fibers. ⁹³	52
Figure 42: Method for making PAN-ox preform from PAN-ox felt, and example of PAN preform. ⁹⁵	53
Figure 43: (a) Freudenberg continuous hydroentangling / carbonization line introduced in 2011. (b) An example of the highly flexible result. ⁴⁵	54
Figure 44: Meltblowing unit for mesophase pitch nonwoven. ⁹⁸	55
Figure 45: Electrospun PAN mat treated at increasingly intense carbonization temperatures, showing very little morphological change. ¹⁰⁰	56

Figure 46: The small overlap between carbon fibers and active carbons represents a minority of all manufactured carbon materials. ¹⁰⁵	58
Figure 47: (a) Schematic of branches pores in granular AC. (b) Straight pores in AC fiber. ¹¹⁰	58
Figure 48: de Levie’s transmission line model for porous electrodes was based on geometrically cylindrical, non-networked pores. ⁴⁹	59
Figure 49: model of three main CNT forms: (a) armchair, (b) zigzag and (c) chiral. ¹¹⁹	61
Figure 50: Schematic representation of CNT “skin” wrapped around cotton yarns. ¹²⁹	62
Figure 51: Anionic acid red dye molecule used to disperse CNTs for use in illustrated coating process. ¹³⁰	63
Figure 52: Photographic images of dipping procedure and cloth surface taken through multiple cycles. ¹³¹	64
Figure 53: Diagram showing exhaustion dyeing conditions used for (a) cotton fabric and (b) polyester fabric. ¹³³	65
Figure 54: Graphene – the “mother” of carbon nanomaterials, such as fullerenes, carbon nanotubes, and graphene sheets. ¹³⁴	66
Figure 55: (A) Schematic illustration of the sonicator-enabled graphite flake exfoliation process. Graphite flakes are combined with sodium cholate (SC) in aqueous solution and encapsulated by SC micelles. (B) Photograph of 90 µg mL ⁻¹ graphene dispersion in SC 6 weeks after it was prepared. ¹⁴²	67
Figure 56: Left: TEM image of graphene oxide monolayer (center). (A) Amorphous area with many defects. (B) Highlighted oxygen functionality in an ordered region, forming hydroxyl and epoxide groups. (C) Fully conjugated region showing pure graphene structure. ¹⁵¹ Right: Sequence of transformation of graphene to graphene oxide, then to reduced graphene oxide by hydrazine hydrate. ¹⁵²	68
Figure 57: (Left): GO coated cotton fibers prior to reduction. (Right): Closer view of same. ¹⁶⁶	70
Figure 58: Top: Illustration of polyester fibers coated with EGF, then deposited with MnO ₂ . Bottom: SEM of MnO ₂ and graphene coated fibers, at various scales.	71
Figure 59: Steps needed to form fiber-based supercapacitor electrodes, and possible methods.	72

CHAPTER 3 FIGURES

Figure 60: Nitrogen adsorption isotherms of carbon fiber nonwovens following activation treatment at three different activation temperatures.	81
--	----

Figure 61: XPS survey scans for commercial GDL carbon fiber nonwoven and PAN fiber nonwovens carbonized in the lab at different temperatures.	83
Figure 62: (a) Elemental composition of carbon fiber samples based on XPS survey scans. XPS scans focused on nitrogen peaks for samples carbonized at (b) 695°C, (c) 895°C, and (d) 1095°C.	85
Figure 63: IPR and TPR for carbonized samples.	86
Figure 64: (a) XRD counts per second (CPS) as a function of scattering angle for carbon fiber nonwovens, and (b) illustration of crystal dimension locations.	87
Figure 65: Crystal length (L_a) and width (L_c) for carbon fiber nonwovens carbonized at different temperatures, based on XRD measurements.	88
Figure 66: IPR and TPR for activated PAN nonwovens which had been carbonized at different temperatures.	92
Figure 67: Nitrogen adsorption isotherms for PAN nonwoven samples (a) after carbonization, and (b) after activation.	93
Figure 68: Pore size distribution for PAN nonwoven samples (a) after carbonization and (b) after activation.	93

CHAPTER 4 FIGURES

Figure 69: Deposition cell setup including working electrode, deposition substrate, reference electrode and Teflon frame.	99
Figure 70: The three primary forms of PANI in their undoped structures, in order of increasing oxidation: (a) leuco-emeraldine, (b) emeraldine, (c) pernigraniline.	103
Figure 71: Carbon fiber binder free material (BFCF-2) deposited with PANI at various deposition potentials: (a) 0.644 V, (b) 0.744 V, (c) 0.844 V, (d) 0.944 V, (e) 1.044 V and (f) 1.144 V, all vs. Ag/AgCl.	104
Figure 72: SEM images showing PANI deposited at (a) 0.644 V, (b) 0.744 V, (c) 0.844 V, (d) 0.944 V, (e) 1.044 V and (f) 1.144 V.	105
Figure 73: Specific capacitance as a function of the potential used during deposition, from 0.644 V to 1.144 V.	106
Figure 74: Cyclic voltammograms at a sweep rate of 10 mV / s for samples deposited at various potentials: (a) 0.644V, 0.744 V, 0.844 V. (b) 0.944 V, 1.044 V and 1.144 V (all vs. Ag/AgCl reference).	106

Figure 75: Specific capacitance as a function of deposition time used during deposition, from 1 minute to 20 minutes, at a deposition potential of 0.777 V (vs. Ag/AgCl).....	107
Figure 76: PANI deposited onto BFCF-2 for 20 minutes at 0.777V (vs. Ag/AgCl). (a) Front face of sample. (b) Back of sample.	108
Figure 77: Specific capacitance for samples treated with 0.01 M, 0.10 M and 0.50 M concentrations of aniline for various durations. (a) Values calculated on the basis of total electrode mass. (b) Values calculated based on PANI mass only.	108
Figure 78: Change in capacitance with cycle number for electrode formed from aniline concentrations of 0.1 M and 0.5 M at 0.777V vs Ag/AgCl for a duration of 20 minutes.	110

CHAPTER 5 FIGURES

Figure 79: CNT mass gain on PU sponge as a function of dip cycle number for water-based CNT dispersion (WBD) and ethanol-based CNT dispersion (EBD).....	119
Figure 80: Evolution of mass gain throughout one full dip cycle, including the washing step which causes the loss of surfactant mass in the water-based dispersion (WBD) coating.	119
Figure 81: CNT mass gain on PET winged fiber (WF) as a function of dip cycle number.	120
Figure 82: Electrical resistance as a function of dip cycle number for water-based CNT dispersion (WBD) and ethanol-based dispersion (EBD) on PU sponge.....	121
Figure 83: CNT mass gain as a function of dip cycle number for four types of PA6 fabrics coated with EBD.....	122
Figure 84: Comparison of SVF for various PA6 fabrics used in this study.	123
Figure 85: Comparison of SVF for substrates produced by various fabrication methods.....	124
Figure 86: Plots showing (a) CNT mass gain and (b) resistance for staple fiber nonwovens made from PET fibers of different diameters - 3, 6 and 15 denier.	124
Figure 87: SVF for 5 webs having the same basis weight and fiber composition – 3 den PET – but differing in compression level.	125
Figure 88: Four different nonwoven webs coated with CNT: (a) PA6 I/S NS, (b) PET WF, (c) PET 3 den 4x compressed, (d) PET 3den uncompressed.	126
Figure 89: Mass gain as a function of treatment cycle number for needlepunched staple fiber nonwovens made from various polymer types - cotton, PA6 or PET.	127
Figure 90: Cotton fiber (a) coated with CNT and (b) cut to show cross-sectional shape. PA6 fiber (c) coated with CNT and (d) cut to shown cross-sectional shape.	128

Figure 91: Double-layer capacitance for needlepunched staple fiber nonwovens coated with CNT. Specific capacitance shown (a) on the basis of total electrode mass and (b) on the basis of the CNT mass only.....	129
Figure 92: Electrical resistance of CNT-coated cotton fiber nonwovens. (a) Series resistance calculated from the galvanostatic discharge curve at three different current levels, as a function of CNT mass loading. (b) Nyquist plot showing impedance for coated (18%) and uncoated samples..	130
Figure 93: PET 4DG staple fiber nonwovens coated with (a + b) CNT and (c + d) subsequently deposited with MnO ₂	131
Figure 94: Binding energy of MnO ₂ -coated fiber surface elements as measured by XPS.....	132
Figure 95: Specific capacitance of MnO ₂ coated PET 4DG staple fiber nonwovens. Capacitance calculated on total electrode mass (grey markers) and MnO ₂ mass only (black markers).....	133

CHAPTER 6 FIGURES

Figure 96: Illustration of the 4DG TM fiber shape.....	140
Figure 97: Graphite mass as a percentage of initial fabric mass for PET 4DG staple fiber nonwovens coated with EGF and GO dispersions. Mass loading also shown for GO coated samples after reduction to rGO.....	143
Figure 98: UV-Vis absorption spectra for EGF dispersions sonicated for various durations.	144
Figure 99: IPR of PET 4DG nonwovens coated with GO and after reduction to rGO.	145
Figure 100: (a) IPR and (b) TPR of PET 4DG nonwovens coated with rGO and EGF.	146
Figure 101: Nyquist plots based on EIS tests of PET 4DG samples coated with (a) rGO and (b) EGF. Inset shows low impedance region.....	146
Figure 102: Laser confocal microscopy images of individual PET 4DG fibers coated with GO for (a) 10 cycles, (b) 20 cycles, (c) 40 cycles, and EGF for (d) 10 cycles, (e) 20 cycles and (f) 40 cycles...	149
Figure 103: Laser confocal microscopy images of (a) GO and (b) EGF coated onto glass slides and evaporated.	150
Figure 104: PET 4DG nonwoven coated with 20 cycles of (a) GO dispersion and (b) EGF dispersion. Inset of (a) shows webbing forming between adjacent fibers.	151
Figure 105: Charge relative to first discharge over the course of 11 charge-discharge cycles at 0.1 mA for EGF and rGO coated PET 4DG nonwovens.....	152

CHAPTER 7 FIGURES

Figure 106: Cross-sectional shapes of 4DG™ (left) and WF (right). ⁵⁷	158
Figure 107: UV-Vis absorbance spectra (range of 400 – 800 nm) for EGF dispersions sonicated by bath for various durations.	162
Figure 108: UV-Vis absorbance spectra (range of 400 - 800 nm) for EGF dispersions sonicated by horn for various durations and by bath for 100 hours.	162
Figure 109: EGF concentration as a result of sonication time, calculated based on absorbance coefficient of 1447 mL mg ⁻¹ m ⁻¹	164
Figure 110: Particle size distribution based on intensity for EGF dispersions sonicated by bath and by horn.	165
Figure 111: (a + b) PET 4DG coated with bath-sonicated EGF dispersion. Inset shows individual flakes on fiber surface.	166
Figure 112: Mass gain of graphite PET 4DG nonwoven samples coated with EGF sonicated by horn for 10 dip cycles, and by bath for 40 dip cycles.	167
Figure 113: IPR and TPR for PET 4DG coated with around 5% graphite mass from EGF dispersions prepared by different methods.	168
Figure 114: Specific capacitance based on galvanostatic charge-discharge tests for PET 4DG nonwovens coated with EGF prepared by different methods.	169
Figure 115: SEM images showing fiber shape and size of (a) 4DG and (b) WF fibers.	170
Figure 116: Mass gain of graphite compared to initial uncoated sample mass for PET 4DG and PET WF samples coated with horn-sonicated EGF dispersions.	171
Figure 117: EGF coated PET WF with (a) 5 coats and (b) 40 coats, and PET 4DG with (c) 5 coats and (d) 40 coats.	172
Figure 118: IPR for EGF-coated PET 4DG and PET WF nonwovens, shown as a function of (a) dip cycle number and (b) graphite mass loading.	173
Figure 119: TPR for EGF-coated PET 4DG and PET WF nonwovens, shown as a function of (a) dip cycle number and (b) graphite mass loading.	173
Figure 120: Specific capacitance based on galvanostatic charge-discharge tests for PET4DG and PETWF calculated based on (a) total electrode mass and (b) graphite mass only.	174
Figure 121: PET 4DG nonwovens coated with EGF and then electrodeposited with polyaniline. Number of EGF coatings is (a) 5, (b) 10, (c) 20, and (d) 40.	175

Figure 122: PET WF nonwovens coated with EGF and then electrodeposited with polyaniline. Number of EGF coatings is (a) 5, (b) 10, (c) 20, and (d) 40. 176

Figure 123: Electrical properties of PET 4DG coated with 16.5% CNT (A), 10.1% CNT (B) and 16.7% EGF. 177

Figure 124: PET 4DG fibers coated with 16.7% graphene (a) before and (d) after PANI electrodeposition; 10.1% CNT (b) before and (e) PANI electrodeposition; and 16.5% CNT (c) before and (f) after PANI electrodeposition. 178

Figure 125: After pseudocapacitive PANI layer is added to electrodes, specific capacitance shown normalized by (a) total electrode mass and (b) cost of unit cost of conductive carbon coating component. 179

CHAPTER 1: Introduction Part I – Overview and Characterization of Electrodes for Electrochemical Technologies

1.1 OVERVIEW OF ELECTROCHEMICAL TECHNOLOGIES

The controlled conversion of chemical to electrical energy, and vice-versa, factors into a range of processes as various as aluminum smelting and in-vivo neurochemical monitoring.¹ The vast array of electrochemical technologies can be broadly categorized according to the classification shown in Figure 1. Despite such diversity, a common set of fundamental rules underlies the transfer of energy in these technologies.

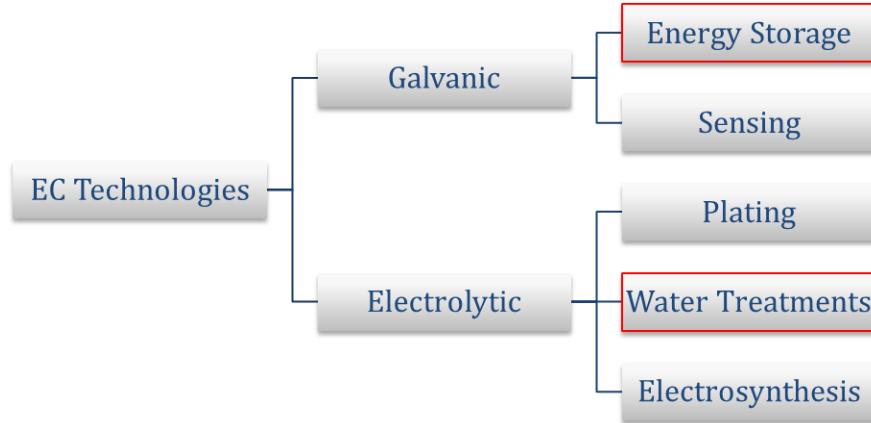


Figure 1: Main categories of commercialized electrochemical (EC) technology, highlighting possible application areas for nonwoven electrodes.

1.1.1 The Electrochemical Process

In an electrochemical cell, the redox reaction is a heterogeneous reaction occurring at two separate electrodes. At the anode, an oxidation reaction which separates the donor species (D) from n electrons takes place, while a reduction reaction between an acceptor species (A) and electrons occurs simultaneously at the cathode:



This leads to the overall cell reaction as shown below:



When viewing the electrochemical process through the lens of thermodynamics, the electrical potential of the cell (E) is related to the Gibbs free energy of reaction (ΔG) through:

$$\Delta G = -nFE \quad (4)$$

where n is the number of electrons transferred in a half-reaction and F is a constant - 96,485 C mol⁻¹ - that allows the potential (in volts, or J C⁻¹) to relate to free energy (J mol⁻¹). E is essentially the force of the reaction involved in reaching equilibrium. If E is positive, ΔG is negative, and thus the cell reaction is spontaneous. If E is negative, the cell reaction must be driven by an applied potential.²

Using the relationship in Eqn. 3, it is possible to find E based on the known potential in a standard state (E°) and the concentration of reacting species. This is based on the relationship between Gibbs free energy of reaction and Gibbs free energy of reaction in a standard state (ΔG°):

$$\Delta G = \Delta G^\circ + RT \ln Q \quad (5)$$

where Q is the reaction quotient. Substituting potential and standard-state potential for free energy and standard-state free energy:

$$-nFE = -nFE^\circ + RT \ln Q \quad (6)$$

This leads to the cornerstone relationship in electrochemistry, the Nernst equation for a half-cell:

$$E = E^{o'} + \frac{RT}{nF} \ln \frac{C_A}{C_{A^-}} \quad (7)$$

where C_A is the concentration of oxidized species and C_{A^-} is the concentration of reduced species in a half-cell. $E^{o'}$ is the *formal half-cell reduction potential*, and its use allows the remaining components of the reaction quotient to be held constant. $E^{o'}$ is measured against a standard reference electrode when the concentration of A is equal to A⁻. By knowing the formal potential of each half-cell reaction, as well as the concentration of the reduced and

oxidized species at both electrodes, the cell potential can be calculated from the two half-cell potentials - $E_{cathode}$ and E_{anode} – which are found according to the Nernst equation (Eqn. 8):

$$E_{cell} = E_{cathode} - E_{anode} \quad (8)$$

Basic familiarity with these governing principles enables efficient cell design.³ For example, two essential conclusions that can be drawn from a fundamental understanding of the electrochemical process are how much energy will be involved in the cell reaction, and whether the cell reaction will be spontaneous ($\Delta G < 0$) or non-spontaneous ($\Delta G > 0$). This distinction is necessary, as galvanic cells produce energy while electrolytic cells consume energy to drive their reactions.

In comparison to pure chemical reactions, electrochemically driven reactions are considered more environmentally benign, since the main reactant is usually the electron.⁴ Two particularly environmentally-friendly technologies are energy storage and water treatment.^{3,5} Batteries, supercapacitors and fuel cells are a necessary part of renewable energy systems, while water filtration helps to minimize environmental pollution.³⁻⁵ Water treatment innovation is driven by increasingly strict governmental regulations on permissible contaminant release levels in industries including the fine chemicals industry, textiles / tanning industry, pharmaceutical industry and more.⁶ Due to a global call for cleaner industrial practices and political interest in energy independence, research in both of these application areas is skyrocketing.

1.1.2 Applications for Nonwoven Electrodes

For both energy storage and water treatment, high specific surface area (SSA) electrodes are considered advantageous.^{7,8} The availability of active area on an electrode plays a direct role in determining the reaction rate, and in most cases, a high reaction rate – which manifests as the current – is desired. Effluents often present extremely dilute concentrations (~100 ppm)

of metal ions.⁹ According to Juttner (2000), two common limitations in water treatment cells are mass transport and electrode surface area, since the remediative action takes place at the cathode or anode surface.⁴ The use of 3D electrodes, in the form of foams, fabrics, granular columns and meshes, enables improved contact between contaminants and the anode/cathode.^{6,10}

The focus of this research will be three-dimensional electrodes applied in supercapacitors. High SSA electrodes are sought after for energy storage applications, and a wide range of materials has been considered. Foams may be metallized through electroplating, but the range of design possibilities such as pore size, polymer type and thickness is quite limited in comparison to textiles.¹¹ Among textiles, nonwoven structures are preferred to woven or knitted fabric structures because the absence of bundling between fibers, such as occurs in yarns, results in a more uniform flow of electrolyte around the porous electrode.^{7,12} Nonwoven webs can be engineered to have a wide range of structural and chemical characteristics. When made conductive via coating or pyrolysis, they can be used as electrodes in electrochemical cells.^{11,13,14} Nonwoven processing parameters and methods of obtaining conductivity will be outlined in the following chapter.

1.2 SUPERCAPACITORS

The family of devices that encompasses energy storage systems is made up of batteries, supercapacitors and fuel cells. Basic operating principles of these three types are shown below in Figure 2. In all cases, the external connection of both electrodes via a conductive pathway permits the cell to discharge, but each is characterized by unique functions. Batteries generate electricity due to oxidation reactions that cause cations (i.e. Li⁺) to be released from the anode. Fuel cells use channels to flow reactants into the cell from outside. Supercapacitors are characterized by quick electrode-electrolyte interface reactions that can either involve charge transfer with permanently adsorbed species (pseudocapacitance) or electrostatic charge separation (double layer capacitance).¹⁵⁻¹⁷

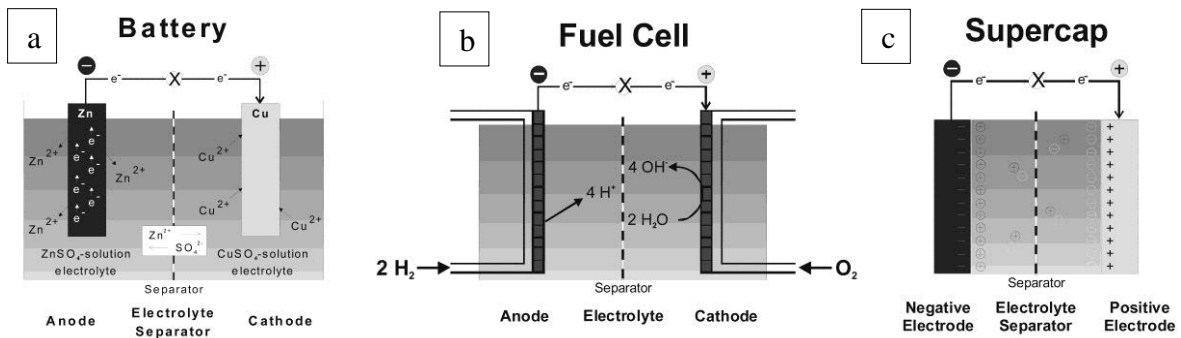


Figure 2: Essential functions of (a) a battery, (b) a fuel cell, and (c) a supercapacitor.¹⁵

Compared to batteries and fuel cells, supercapacitors provide an impressive specific power range, from around $10 - 10^6 \text{ Wh kg}^{-1}$, but the lowest specific energy range, from $0.1 - 10 \text{ Wh kg}^{-1}$.¹⁵ Figure 3 shows the unique ranges covered by each device type:

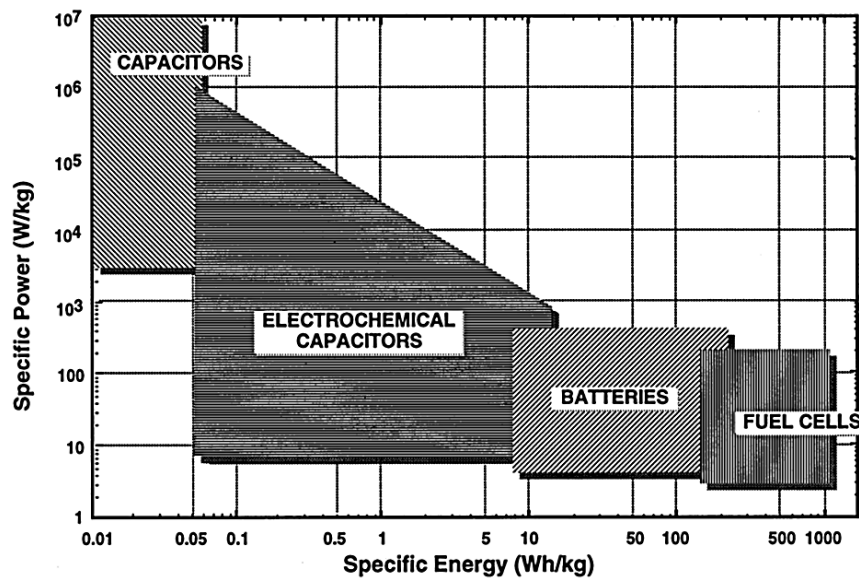


Figure 3: Power density range and energy density range for different types of devices.¹⁸

1.2.1 Supercapacitor History

The development of supercapacitors traces back to the mid-19th century experiments of Hermann von Helmholtz. Roughly a century after Helmholtz' work describing the molecular

structure of an “electric double layer”, this phenomenon was investigated as a means of energy storage. In a 1957 patent, assigned to General Electric, H. L. Becker recommends using “sticks of fired tar lampblack” as the electrode material since electrodes with rough or porous surfaces offer more surface area per unit mass for the charge to accumulate (Figure 4 a).¹⁹ At the time, tar lampblack was one of the highest SSA forms of carbon known.

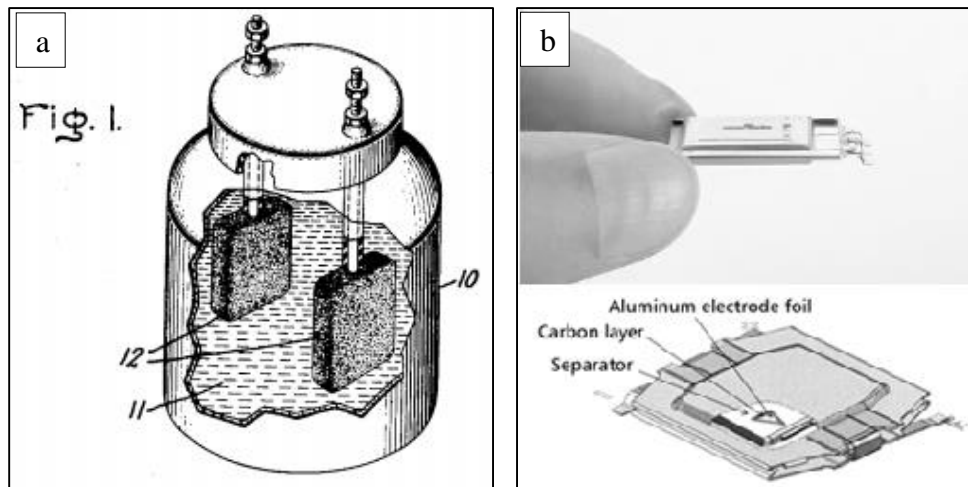


Figure 4: (a) Illustration of original EDLC using lampblack.¹⁹ (b) EDLC from Murata, typical of current devices.²⁰

Through the 1960's, several patents were filed by General Electric and Standard Oil of Ohio, but mass production was first carried out by Philips and Panasonic in the 1970's.²¹ Initially, commercial applications for supercapacitors were based on their high power density, and primarily focused on three areas:¹⁷

- Backup power sources in small consumer electronic devices, in case of short-term failure or voltage drop in primary power source (Figure 5, a + b).
- Main power source for toys and other low power rating devices, where they deliver short pulses of power and can be quickly recharged.
- Power storage for small solar devices such as watches and lanterns.

In 2002, Chu and Braatz studied the performance of a range of commercially available EDLCs as power-assist devices in hybrid vehicles.²² Tests were carried out in line with recommendations set by the Partnership for a New Generation of Vehicles (PNGV). The results showed improvement over earlier generation supercapacitors, with the Saft 3500 F supercapacitor (carbon electrodes, organic electrolyte) displaying the highest energy and power density. While performance was lower than that of Li-ion batteries, the authors noted the high stability, corrosion resistance and cost efficiency that could give supercapacitors an edge over batteries.²²

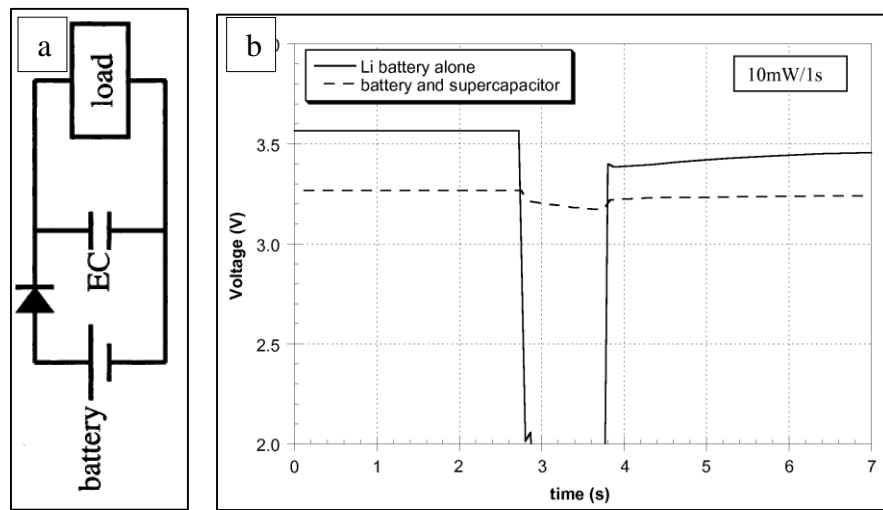


Figure 5: (a) Placement of an electrochemical capacitor in as a backup power source.¹⁸ (b) Smoothing effect of supercapacitor on the discharge voltage from a Li battery to a load.²³

The current size of the global supercapacitor market is around \$400 million, and is expected to reach \$520 million by 2018.²⁴ Although this figure is dwarfed in comparison to both the battery market (\$95 billion) and the dielectric capacitor market (\$17 billion), it has attracted almost 30 new manufacturers in the last decade. As a reflection of the growing interest in supercapacitors, the number of global patents granted annually is increasing exponentially (Figure 6).²¹ Leaders in the industry are Murata, Panasonic, Nippon Chem-Con, NEC-Tokin, and Maxwell Technologies. Demand for consumer electronics has continued to drive growth in traditional applications, while new uses have been found in the alternative energy realm.

Supercapacitors are being used in hybrid busses to store braking energy, in wind turbines to adjust the blades and for uninterruptible power supply (UPS) systems for solar power.^{24,25}

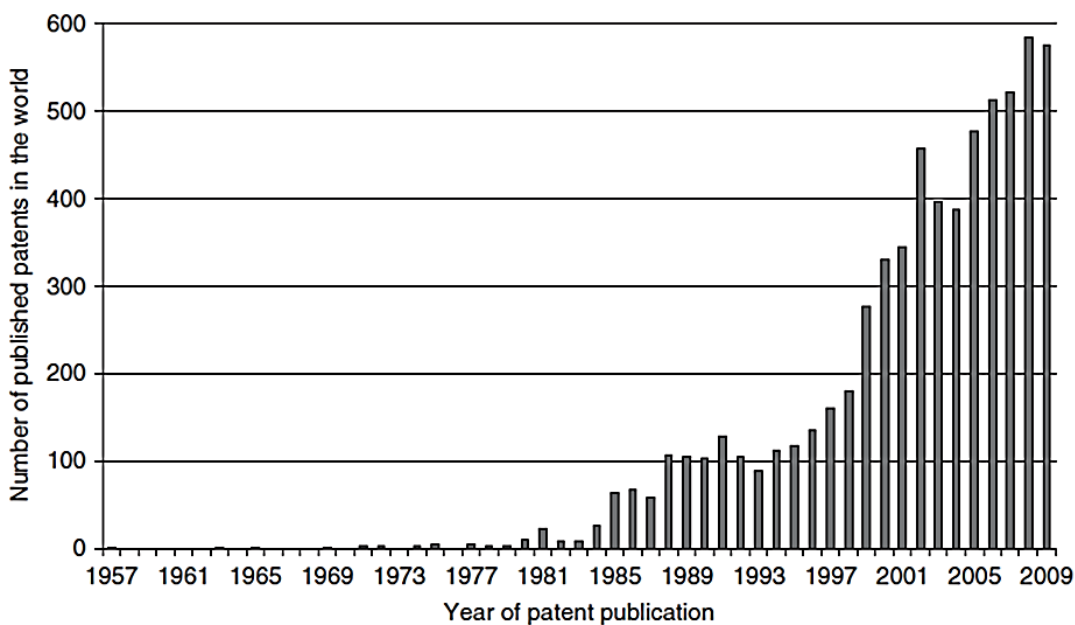


Figure 6: Number of patents published each year relating to supercapacitor technology.²¹

1.2.2 Basic Supercapacitor Mechanisms

Two types of mechanisms can be used to achieve supercapacitor charge storage behavior: electric double-layer capacitance (EDLC) and pseudo-capacitance (PC). These mechanisms are quite different. As outlined above, EDLC behavior was first described in the mid-19th century and commercialized in the mid-20th century, whereas the science and technology of PC behavior didn't gather momentum until the 1990s.^{16,26} Both types of supercapacitor electrodes are explored in this research; a brief introduction to each will be given in this section.

1.2.2.1 Electric Double-Layer Capacitance (EDLC)

Upon immersion in a liquid, an electrically charged surface will induce ordering of the ionically charged species in the region around the phase boundary. This phenomenon was first described by Helmholtz in 1853, who assigned the term “double layer” based on the presence of a closer, adsorbed plane composed of solvent molecules and ions (counter ions if

the surface is positively charged), and an adjacent plane of hydrated counter ions.⁸ These two planes have been designated the inner Helmholtz plane (IHP) and outer Helmholtz plane (OHP), respectively. This model was subjected to two major revisions – first to convert the IHP to a diffuse distribution of counter charges, and later to convert this diffuse distribution to a hybrid IHP-diffuse region (Figure 7).

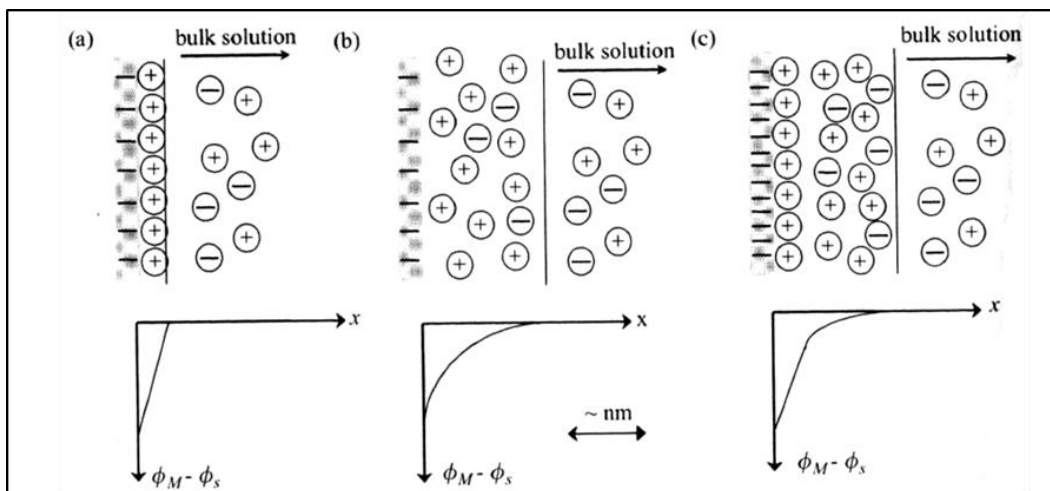


Figure 7: Representations of the (a) Helmholtz, (b) Gouy-Chapman and (c) Gouy-Chapman-Stern models of the electric double-layer, along with the distribution of potential.⁸

Typical double layer capacitance is in the range of $20 - 40 \mu\text{F cm}^{-2}$ for most electrodes, with the assumption that the electrode is metal.²⁷ Researchers have noted that a much lower double layer capacitance is obtained with activated carbon electrodes, which show an average maximum of around $5 \mu\text{F cm}^{-2}$.²⁸ This difference is typically attributed to electrolyte restriction, but another explanation is that the electrical properties of carbons and metals differ in important ways. Randin and Yeager carried out voltammetry studies on graphite electrodes in the 1970's which led to the conclusion that it can be considered semimetallic on its basal plane.^{29,30} Gerischer modified the Gouy-Chapman-Stern model of double layer capacitance to include a space charge capacity (C_{sc}) for semiconductor electrodes (Figure 8).³¹

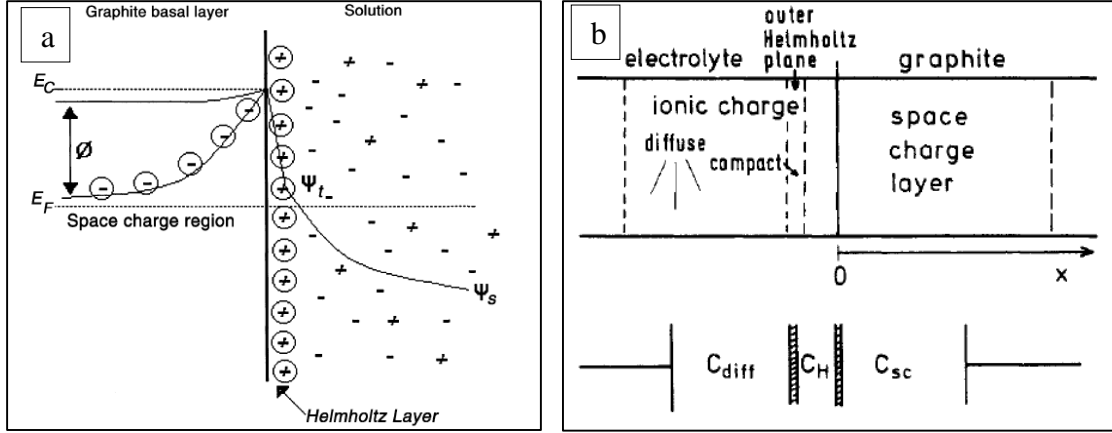


Figure 8: (a) Space charge distribution from surface of electrode with graphite basal layer exposed to ionic solution.³² (b) Schematic depiction and circuit element equivalent of capacitance layers extending within and beyond graphite surface.³¹

In most cases, the double-layer capacitance (C_{dl}) is limited by the space charge capacitance as it is typically lower than its parallel capacitances, the diffuse layer capacitance (C_{diff}) and the OHP capacitance (C_H):

$$\frac{1}{C_{dl}} = \frac{1}{C_{sc}} + \frac{1}{C_H} + \frac{1}{C_{diff}} \quad (9)$$

For graphite, with a charge carrier density of around 6×10^{18} carriers cm^{-3} and a dielectric constant around 3.0, specific capacitance can depreciate to $3.0 - 4.5 \mu\text{F cm}^{-2}$ (stress-annealed pyrolytic graphite, basal plane).³⁰ This low capacitance is direction-dependent: along the a -axis, electrons are conducted as if by a metal ($3.9 \times 10^{-5} \Omega\text{-cm}$); along the c -axis, they are transported as if in a semiconductor ($1.0 \times 10^{-2} \Omega\text{-cm}$).⁷ Because carbon surfaces are usually composed of a blend of these two types, a concrete value for surface-specific capacitance ($\mu\text{F cm}^{-2}$) cannot be given. Materials such as activated carbons present both basal- and edge-planes to the electrolyte, the ratio of which depends on production conditions.³²

1.2.2.2 Pseudocapacitance (PC)

Unlike EDLC, which is based on the simple principle of charge separation at the interface, PC involves faradaic redox reactions (Figure 9). Compared to EDLC electrodes, the aerial

specific capacitance of PC materials can be two to three orders of magnitude greater. For instance, Conway estimated the aerial specific capacitance of Pb to be $\sim 2000 \mu\text{F cm}^{-2}$, whereas carbon has been estimated to produce $2 - 20 \mu\text{F cm}^{-2}$.²⁶

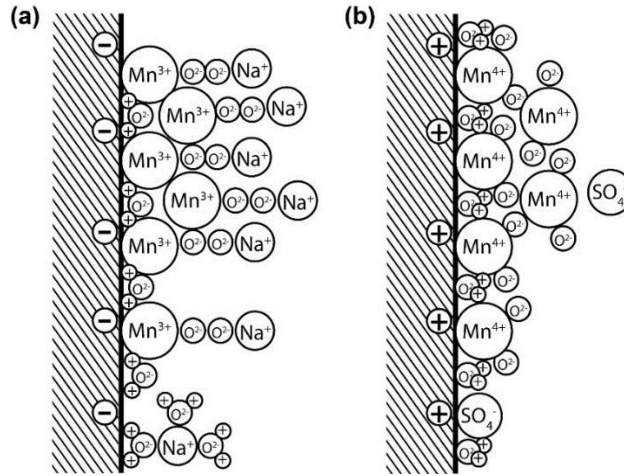


Figure 9: Specifically adsorbed transition metal oxide clusters, which have multiple redox states and support fast intercalation of charged species. (a) Negatively charged electrode and (b) positively charged electrode.

As is the case with batteries, charge transfer occurs when these species undergo reduction or oxidation. However, they are distinguished from batteries in that the active species are surface-adsorbed, causing the shape of the cyclic voltammogram to be closer to that of a capacitor (Figure 10).

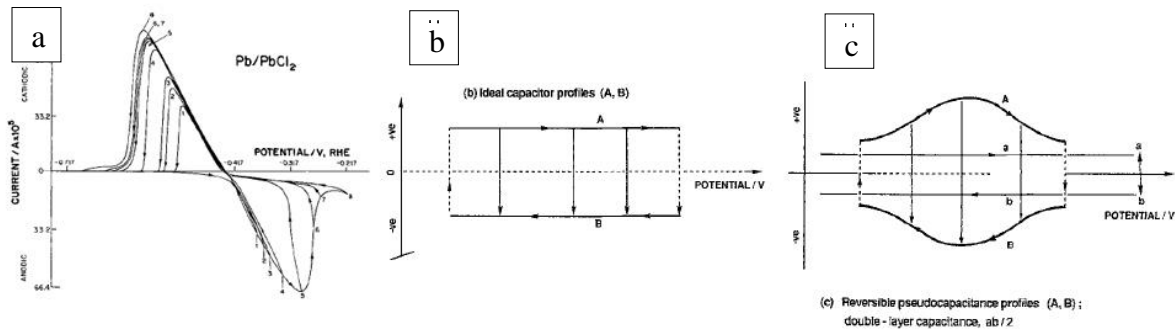


Figure 10: Cyclic voltammograms for (a) quasi-reversible Pb/PbCl₂ battery reactions, (b) ideal capacitor, (c) ideal pseudocapacitor.²⁶

Further distinctions between batteries and supercapacitors have been demarcated by Rudge et al.: (i) battery reactions involve a significant phase transformation, while pseudocapacitive reactions simply shuttle charge carriers (ions or electrons) without significant chemical reactions; (ii) the power density of battery reactions is significantly lower than pseudocapacitive reactions, due to the fast kinetics of the latter; (iii) the interfacial impedance of a pseudocapacitor approaches a phase angle of 90° as frequency decreases.¹⁶

Active materials for PC electrodes are selected on the basis of exhibiting capacitor-like behavior. Within the electrolyte voltage window, current should be relatively constant – this results when the oxidation process causes the redox potential to spread out over a sequence of events. Systems which show this behavior include selected polymeric and transition metal layers. RuO_2 , for example, undergoes a series of electron transfers at the redox center ($\text{Ru}^{2+} \rightarrow \text{Ru}^{3+}$, $\text{Ru}^{3+} \rightarrow \text{Ru}^{4+}$) which are compensated by transformation of OH^- to O^{2-} . The search for cheaper alternatives has led to much interest in MnO_2 , as well as conductive polymers such as polyaniline (PANI), polypyrrole (PPy) and polythiophene. When material cost is lowered, the amount used can be increased such as to balance out lower gravimetric-specific capacitances.

1.2.3 Role of Surface Area and Porosity

As with several other electrochemical technologies, supercapacitors stand to benefit from the higher reaction rate associated with three-dimensional electrodes. Porous electrodes have an internal surface area far exceeding their geometric surface, and are implemented to increase total current in such cases as wastewater remediation where the limiting current (I_L) is extremely low due to dilute reactant concentration in the bulk (C_i^*)⁹. Thus, electrode surface area (A) offers a direct route towards increasing the conversion rate when it is otherwise limited by the mass transfer coefficient (m_i).³³:

$$I_L(t) = nFAm_iC_i^* \quad (10)$$

By this relationship, it can be seen that increasing surface area theoretically results in increased capacitance.^{18,34} EDLC electrodes, having a much lower aerial specific capacitance than PC electrodes, require a great deal more surface area in order to form a viable supercapacitor. While PC electrodes can be constructed from macroporous (> 50 nm diameter) materials, EDLC electrodes call for microporous (< 2 nm diameter) materials.

Table 1: Examples of materials and corresponding SSA.

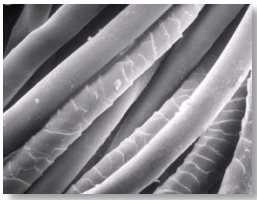
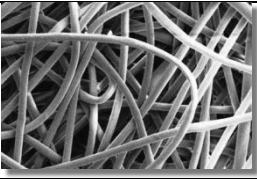
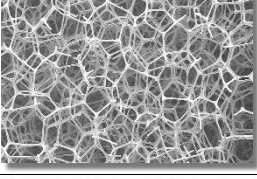
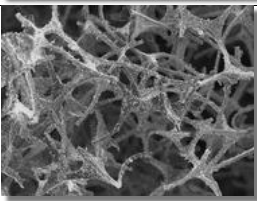
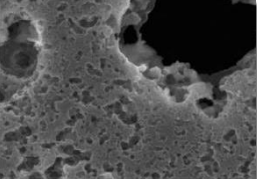
	Material	Typical SSA
	Standard round fiber (5 denier)	0.5 m ² g ⁻¹
	Low diameter round fiber (0.05 denier)	1 m ² g ⁻¹
	Carbonized polyurethane open cell foam	4 m ² g ⁻¹
	Multi-lobed winged fiber (1 denier) or electrospun round fiber (0.001 denier)	10 m ² g ⁻¹
	Activated carbonized polyurethane open cell foam	500 m ² g ⁻¹
	Activated carbonized particles	1000 – 2500 m ² g ⁻¹

Table 1 lists a range of high specific surface area (SSA) materials. EDLC specific capacitance is around $10 \mu\text{F cm}^{-2}$, so the resulting gravimetric-specific capacitance for a typical fibrous electrode with SSA of $1 \text{ m}^2 \text{ g}^{-1}$ would be just 0.1 F g^{-1} . Even if microfibers, with SSA up to $10 \text{ m}^2 \text{ g}^{-1}$ were used, specific EDLC capacitance would be a mere 1 F g^{-1} . PC materials, on the other hand, have aerial specific capacitance of around $2000 \mu\text{F cm}^{-2}$. Microfibers coated with PC material would thus yield gravimetric specific capacitance of 200 F g^{-1} , which already exceeds the standard performance expectation of 100 F g^{-1} . Activated carbons present a uniquely high SSA. As a result, EDLC electrodes are most commonly made from activated carbon in a granular form, compounded by polymer binder (i.e. PTFE). For an EDLC electrode with SSA of $1000 \text{ m}^2 \text{ g}^{-1}$, specific capacitance finally reaches a practically applicable value of 100 F g^{-1} .

Activated carbons are produced by extracting amorphous material between the ordered regions of carbon in carbon-based materials, resulting in extremely high SSA based on the micropore surfaces. Much attention has been devoted to determining the effect of pore size range and distribution on capacitance. Pores can be classified as micropores, mesopores or macropores based on diameters of $0.2 - 2 \text{ nm}$, $2 - 50 \text{ nm}$ and $50 - 1000 \text{ nm}$, respectively. Due to the relationship between debye length, solvated / unsolvated ions and pore radius, the electrolyte behaves differently in each of the three pore regimes.³⁵ Early on, the consensus was that pores smaller than the solvated ion size should be avoided. Activated carbons can be produced to have a SSA of up to $3000 \text{ m}^2 \text{ g}^{-1}$, but EDLC manufacturers recommended against exceeding $1500 \text{ m}^2 \text{ g}^{-1}$.²¹ Above this limit, it was thought that additional surface area would be obtained in the form of pores $< 1 \text{ nm}$ in diameter, which were considered less accessible by solvated ions and thus were thought to be under-utilized.^{28,34}

However, a recent review of the literature by Simon and Gogotski challenged this approach.¹⁷ Ion desolvation is evidenced by increased capacitance in pores $< 1 \text{ nm}$ (Raymundo-Pinero, 2006).³⁶ Targeting an optimal pore size and narrow pore size distribution is more effective than simply increasing pore volume and pore size (Figure 11). A wire-in-

cylinder model based on single de-solvated ion has been adopted. The ideal pore range size is now variously considered to be 0.7 – 0.8 nm,³⁷ or 1 – 2 nm.²⁸

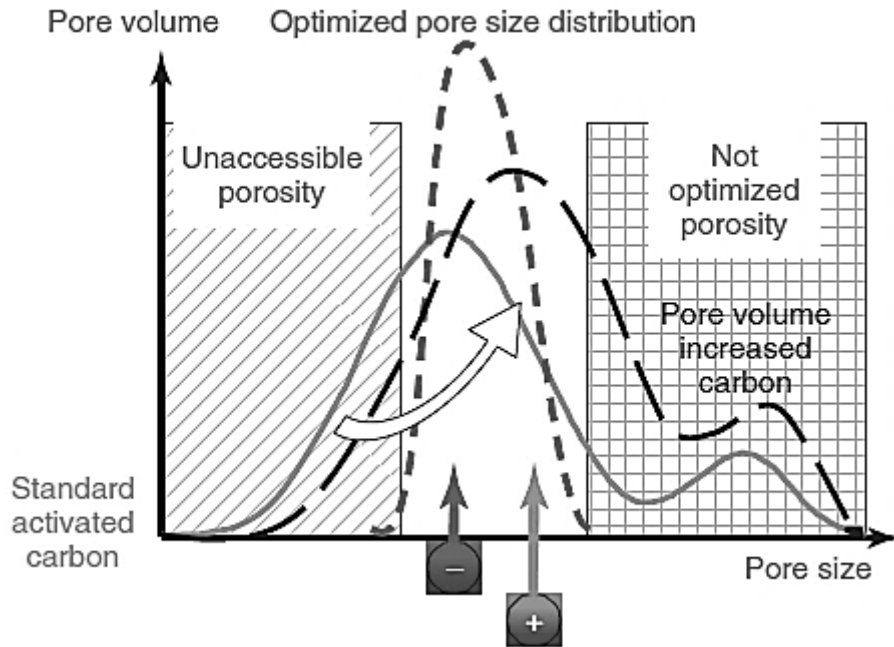


Figure 11: Optimizing the pore size of activated carbon is more effective than simply increasing the pore volume.²¹

1.3 CHARACTERIZATION METHODS AND METRICS

The following sections present a critical review of common methods that can be used to characterize the electrical and electrochemical performance of fibrous electrode materials for supercapacitors.

1.3.1 Characterization of Electrical Conductivity

Electrical resistivity (ρ) and its inverse, conductivity (σ) are related to material properties by the following:⁷

$$\rho = (Ne\mu)^{-1} = \sigma^{-1} \quad (11)$$

Where N is the density of charge carriers, e is the electronic charge, and μ is the mean mobility. While this theoretical approach may yield reasonable values for solid, homogenous materials, conductive fabrics offer a more complex situation. To begin with, they are composite materials, consisting of some combination of the following: dielectric polymer,

conductive polymer, graphitic carbon, amorphous carbon, metal, and air. Since they tend to be ductile, the contribution of this last component – air – is unpredictable due to the continuous changes in a fabric’s void structure. As a result, fabric structure is a key variable that affects the conductive network. Even two woven carbon textiles composed of the same type of carbon fiber will have disparate conductivities depending on the density of the weave structure. Due to this complexity, electrical properties of fabrics are difficult to model, and must be gathered experimentally.

Experimental values must also be considered carefully. Luo et al. note that conductivity data reported on the same type of reduced graphene oxide tends to vary by orders of magnitude between different groups.³⁸ The variation comes down to “area-selecting, measurement method, test equipment, and other random operations.”⁶² A survey of papers reporting electrical properties of conductive textiles is shown in Figure 12. Not only are at least six different metrics reported, but there is widespread disagreement in regards to the units of the different metrics.

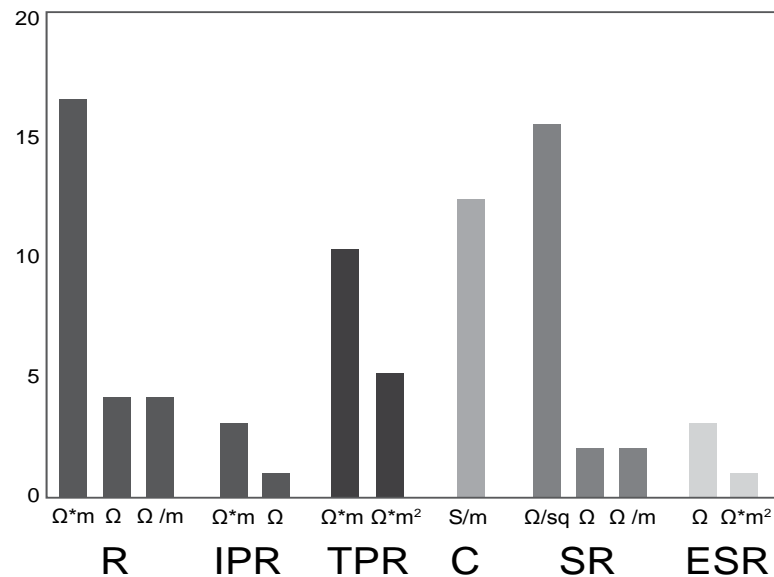


Figure 12: Number of uses of different electrical metrics (R = resistivity, IPR = in-plane resistivity, TPR = through-plane resistivity, C = conductivity, SR = sheet resistivity, ESR = equivalent series resistance) along with the units used, among 78 instances.

The common use of sheet resistivity (ρ_{sh}) in characterizing conductive textiles is based on the concept of a textile as planar material.³⁹ This concept is well-suited for a planar layer of conductive ink that sits atop the fabric, but is an over-simplification in the case of conformally coated fibers, where the conductive layer assumes the three-dimensional form of its fibrous scaffold. Owing to the presence of conductive junctions in the z-plane, a measurement of the resistance along one layer of the x-y plane does not sufficiently represent the ability of a conductive fabric to carry current.

Resistivity is another value commonly used in describing conductive textiles. Resistivity (ρ) and sheet resistivity are distinguished by the inclusion of the sample thickness in the former, and its exclusion in the latter. This is shown below, where R is the measured resistance ($\frac{\Delta V}{I}$), l is the distance between the two electrodes, w is the width of the electrodes and A is the cross-sectional area of the sample.^{40,41}

$$\rho = \frac{R * A}{l} = \Omega \cdot \text{m} \quad (12)$$

$$\rho_{sh} = \frac{R * w}{l} = \Omega/\square \quad (13)$$

Fibrous structures which are coated conformally with conductive materials present a three-dimensional morphology, consisting of intersecting branches and void spaces. Thus, resistivity is the preferred metric.

A further clarification should be made regarding the direction of current flow in relation to the sample orientation. Frequently, commercial specification sheets state whether resistivity values are *in-plane* (normal to the fabric sheet) or *through-plane* (perpendicular to the fabric sheet). An example is shown in Table 2, from Freudenberg Fuel Cell Component Technologies. This distinction is rarely made in academic literature, perhaps due to the absence of a standard test method for through-plane resistivity (TPR).⁴² In 2004, the US Fuel

Cell Council (USFCC) published a recommended procedure for testing TPR which appears to be based on a white paper from Keithley Instruments (Cleveland, OH).⁴³ Keithley had been commissioned from Quantum Composites, Inc. to develop a method for characterizing their bipolar plate materials.⁴⁴

Table 2: Properties of a selection of gas diffusion layer materials.⁴⁵

	H2315	H2315	H2315	H2315
	I6	C2	C4	I4 C9
HYDROPHOBIC TREATMENT	■			■
MICROPOROUS LAYER		■	■	■
Thickness@ 0.025 MPa (Internal) In μm	210	255	255	250
Thickness@ 1 MPa (Internal) In μm	175	215	215	210
Area weight (DIN EN ISO 29073-1) In g/m^2	115	135	135	135
Compression Set @ 1 MPa (Internal) In μm	3	8	8	8
TP electrical resistance @ 1 MPa (Internal) In $\text{m}\Omega \cdot \text{cm}^2$	7	10	8	8
IP electrical resistance (Internal) In Ω	0.8	0.8	0.8	0.7
TP air permeability* (DIN EN ISO 9237) In $\text{l}/\text{m}^2 \cdot \text{s}$	160	-	-	-
TP air permeability acc. to Gurley (ISO 5636-5) In s	-	70	50	30
IP air permeability@ 1 MPa (Internal) In μm^2	1.7	2.5	2.5	2.0
Tensile strength (DIN EN ISO 29073-3) In N/50 mm	80	80	60	70

* at 200 Pa pressure drop
 TP = through-plane, IP = in-plane
 (Rev. 04 – 13.02.2013)

All values represent averages which are subject to usual production tolerances. The values Any warranty and liability is subject to Freudenberg FCCT SE & Co. KG's General Terms of D

According to the USFCC, a circular sample of the test material should be placed between two gold-coated copper plates which are the same size as the sample. The plates are each connected to a sourcemeter and a voltmeter. A hydraulic lab press with a pressure display sandwiches the assembly with 1000 psi force, and voltage is read as a current (10 or 100 mA) is passed through. TPR is calculated from the resistance (R), electrode area (A) and sample thickness (l):

$$\rho_{TP} = \frac{R * A}{l} = \Omega \cdot \text{m} \quad (14)$$

Although this method was initially developed to characterize rigid bipolar plate material, TPR has been adapted to characterize thin, fibrous GDL materials as well. Rather than applying 1000 psi, a lighter load of around 150 psi is used.⁴⁶

In supercapacitors, the combined ohmic resistances of the cell can be measured using two different techniques: electrochemical impedance spectroscopy (EIS) and chrono-potentiometry (CP). As described in the following section, EIS matches cell resistance to a resistor element in a model equivalent circuit. In CP, a vertical region in the voltage plot can yield cell resistance through Ohm's Law. However, neither of these techniques can easily produce a value for the electrode resistance, since it is combined with electrolyte resistance and other ohmic resistances.

1.3.2 Characterization of Electrochemical Performance

1.3.2.1 Cyclic Voltammetry and Chrono-Potentiometry

Capacitive behavior follows Equation 15, where i is current (in amps, each equal to one coulomb per second), t is time (in seconds), q is charge (in coulombs, each equal to the charge of 6.241×10^{18} electrons), E is potential (in volts), and C is capacitance (in farads, each equal to one coulomb per volt):

$$C = \frac{\int i dt}{E} = \frac{q}{E} \quad (15)$$

An ideal capacitor is characterized by a single value of C , given in μF or F . When a constant voltage, E , is applied, current, i , will flow until the designated amount of charge has built up. However, current will continue flowing at a steady value if a voltage sweep is applied (voltage increases linearly according to a set sweep rate in $V s^{-1}$), in order to maintain a linearly increasing charge, q (Figure 13 a + b). Thus, C can be measured by applying a voltage sweep and integrating the current with respect to time. This concept utilized in *cyclic voltammetry*, where current is usually plotted as a function of voltage (Figure 13 c).

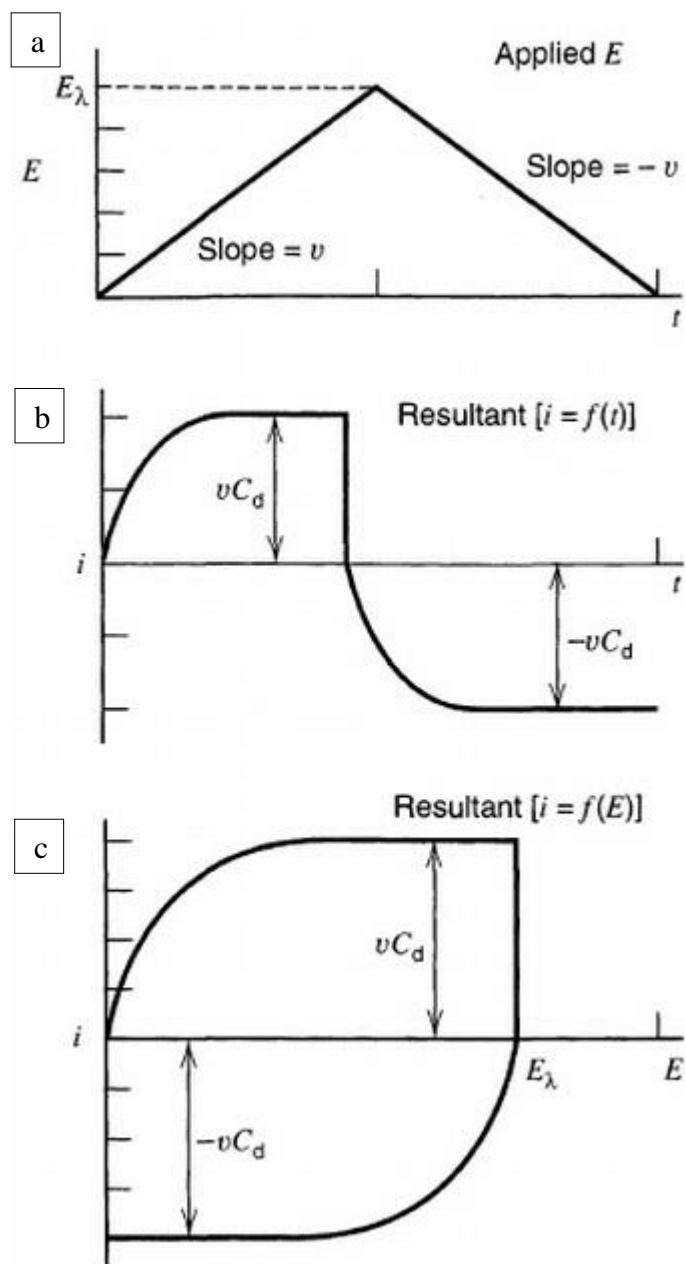


Figure 13: Plots of cyclic voltammetry showing (a) applied potential with fixed sweep rate (v), (b) typical resulting current showing development of double layer, and (c) current as a function of potential, which is known as the voltammogram.¹

Departures from ideal capacitor behavior are common, and affect the shape of the voltammogram. Figure 14 shows modifications that can be expected due to electrode resistance, microporosity and faradaic (i.e. redox) reactions.³⁴

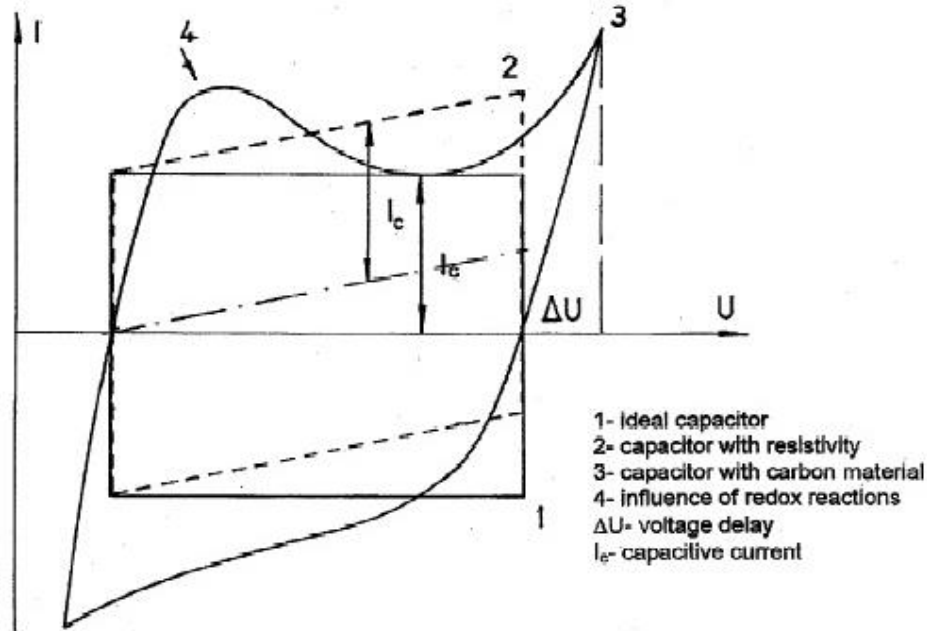


Figure 14: Features of a typical EDLC voltammogram, with modifications due to various physical properties shown.³⁴

Another technique used to obtain C is to apply a constant current and allow voltage to increase from zero. Once the voltage window maximum is reached, current is reversed in sign until voltage decays back to zero. This sequence is called galvanostatic charge-discharge, also known as current reversal *chrono-potentiometry*. Charge is calculated as the total current passed during the discharge cycle, which yields capacitance when divided by the voltage window.

Gravimetric energy density, or specific energy ($J g^{-1}$) can be derived from specific capacitance ($F g^{-1}$) via multiplying it by the square of the voltage window:^{18,47}

$$E_s = \frac{1}{2} C_s V^2 \quad (16)$$

However, specific energy is more typically reported in Wh kg⁻¹, which can be obtained by converting Joules to Watt-hours according to the following:

$$1 Wh = 3600 J \quad (17)$$

Specific power is easily found by dividing specific energy by the time of the discharge (t) given in hours:

$$P_s = \frac{E_s}{t} \quad (18)$$

P_s as a function of E_s may be plotted – this is known as a Ragone plot. Ragone plots are most often used to identify the power and energy ranges associated with a given device. Figure 15 shows a Ragone plot for a commercial supercapacitor (BCAP 350F Maxwell Technologies), along with associated time constants. Typical use is at 1.0 sec. The data for this plot was based on impedance testing, which will be covered in the following section.

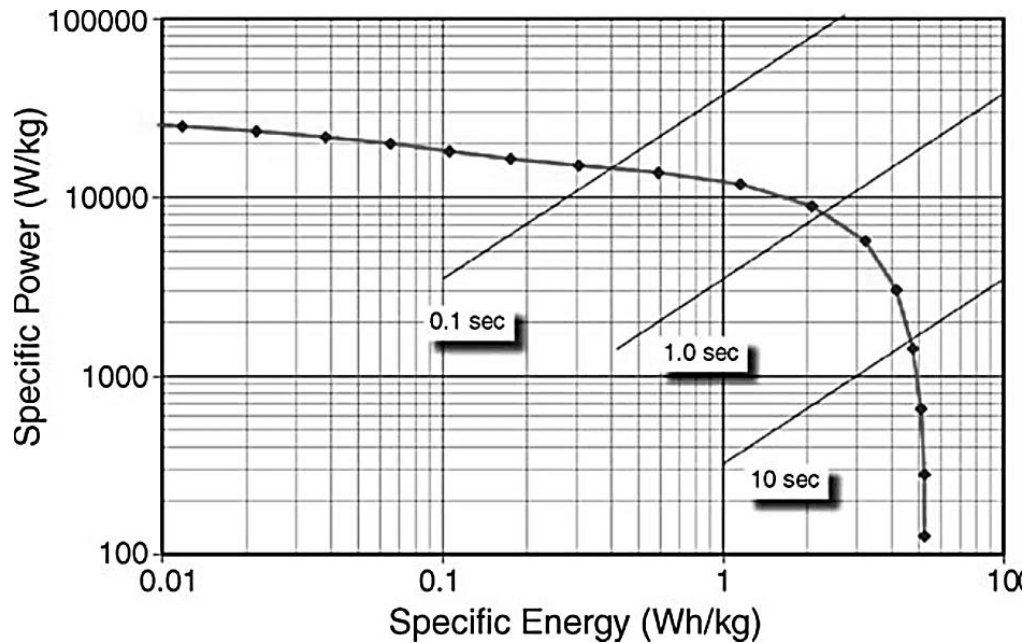


Figure 15: Specific power as a function of specific energy for a commercial 350 F supercapacitor from Maxwell Technologies.⁴⁸

1.3.2.2 Electrochemical Impedance Spectroscopy

Electrochemical impedance spectroscopy (EIS) has been used since the 1940's for electrode characterization.⁴⁹ EIS entails a sequence of low-amplitude sinusoidal voltage perturbations (~ 10 mV) applied to a three-electrode test cell (see following section regarding test cell setup). The sequence begins by alternating the voltage at a high-frequency signal, typically in the 10's to 100's of kHz, and measuring the current response. Subsequently, the signal frequency is lowered and the current is measured again, and so on until the frequency is in the low mHz range. At each point, the relationship between the voltage signal and the current signal is measured. The angle between E and I depends on whether the circuit is dominated by resistive, capacitive or inductive behavior (Figure 16). Across a capacitor, current leads voltage by a phase angle of 90° ; across an inductor, voltage leads current by 90° ; across a resistor, voltage and current are in phase.

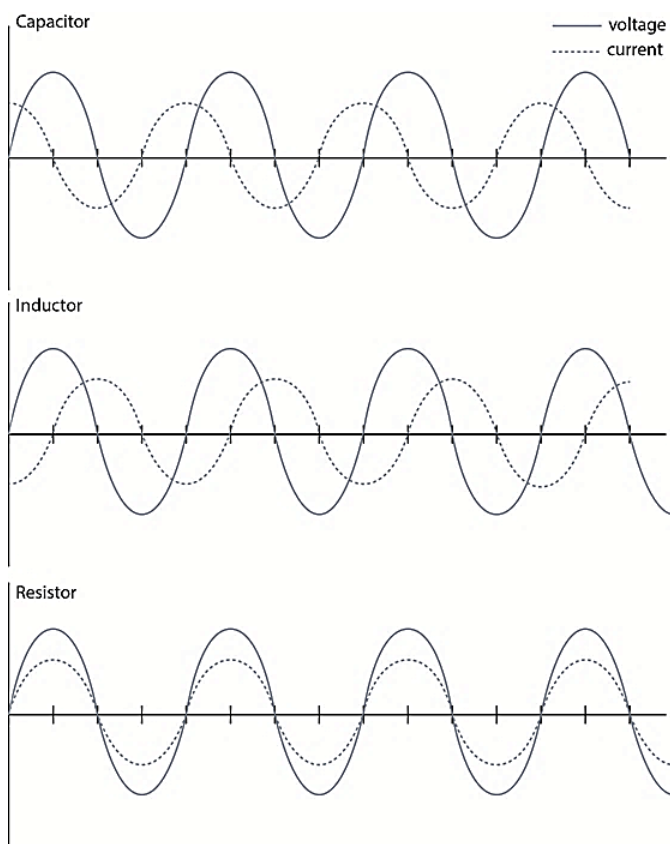


Figure 16: Relationship between AC current and AC voltage, showing typical phase shifts for capacitors, inductors and resistors.

The complex impedance, Z , is the vector sum of the real impedance (Z_{re} or Z') and the imaginary impedance (Z_{im} or Z''). At a given angular frequency (ω) complex impedance has a specific value and phase angle, but these components can change with frequency (f). For a single resistor with resistance R :

$$Z(f) = Z' = R \quad (19)$$

For a capacitor with capacitance C :

$$Z(f) = Z'' = -j \frac{1}{\omega C} \quad (20)$$

When a resistor and capacitor are in a series circuit, the complex impedance can be calculated as below:

$$Z(f) = Z' + Z'' = R + \left(-j \frac{1}{\omega C}\right) \quad (21)$$

While in parallel:

$$Z(f) = Z' + Z'' = \frac{R \left(\frac{1}{\omega C}\right)^2}{R^2 + \left(\frac{1}{\omega C}\right)^2} + \left(-j \frac{R^2 \left(\frac{1}{\omega C}\right)^2}{R^2 + \left(\frac{1}{\omega C}\right)^2}\right) \quad (22)$$

These examples demonstrate the central concept of EIS: the effect of signal frequency on complex impedance is highly dependent on circuit layout. This relationship can be plotted in two ways: a *Nyquist plot* shows the real part of the impedance on the x-axis and the imaginary part on the y-axis; a *Bode plot* shows frequency on the x-axis, total impedance on the y_1 -axis, and phase angle on the y_2 -axis (Figure 17, a + b).

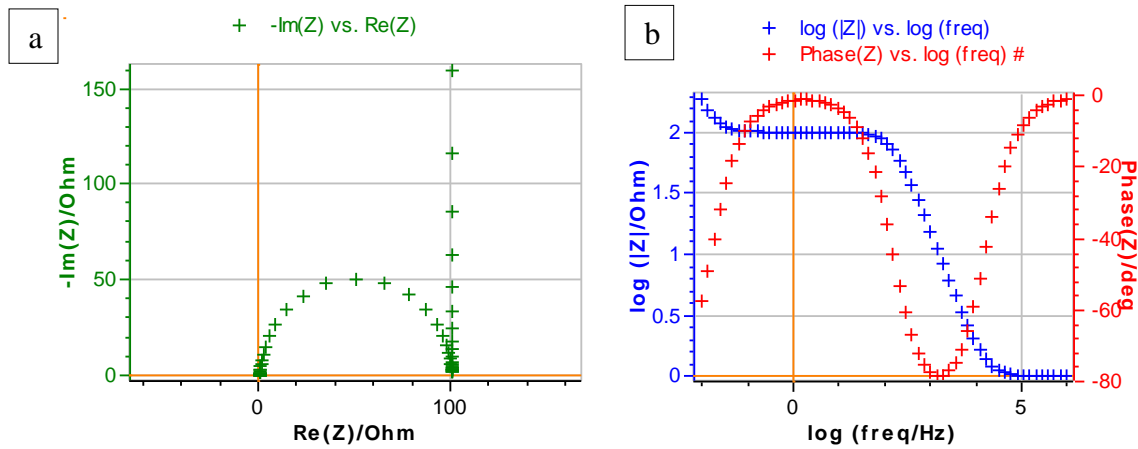


Figure 17: (a) Nyquist plot of real component and imaginary component of the complex impedance, with each marker representing a different frequency. (b) Bode plot for the same circuit.

In particular, the Nyquist plot is useful in that it displays characteristics that can be attributed to certain types of circuits. A simple example is an RC circuit, with one resistor and one capacitor. The plot will show a vertical line if the resistor and capacitor are arranged in series (Figure 18 a) but will show a semicircle if the resistor and capacitor are arranged in parallel (Figure 18 b).

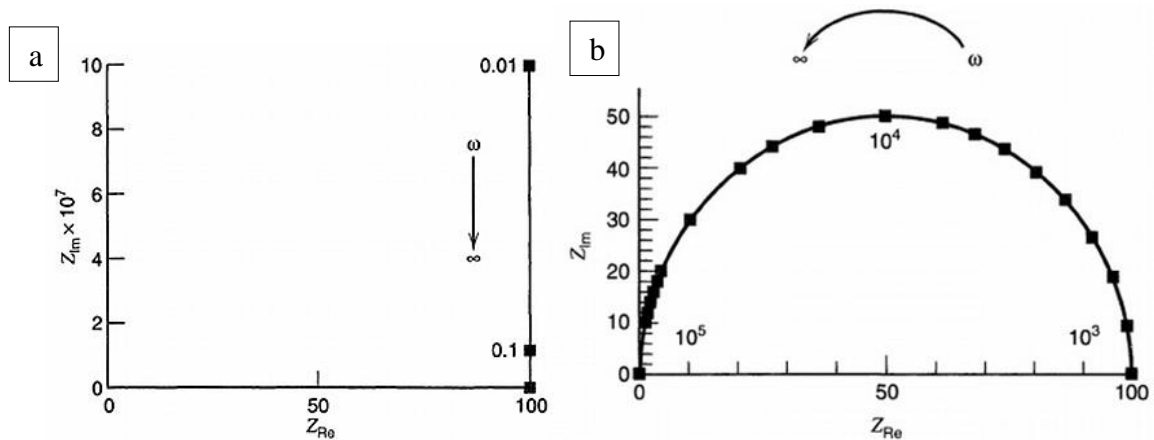


Figure 18: Nyquist plots for (a) a series RC circuit and (b) a parallel RC circuit with $R = 100\Omega$ and $C = 1\mu\text{F}$.¹

In supercapacitor electrodes, EDLC and PC electrodes produce different characteristic shapes. As the charge travels across an EDLC electrode, it must pass through the electrolyte

(a resistor) before it encounters the double layer (a capacitor). The ohmic resistances of the electrode and the current collector are next encountered – they join with the electrolyte resistance to form a single resistive element called the Equivalent Series Resistance (ESR). Thus, the basic equivalent circuit is R+C (Figure 19 a).

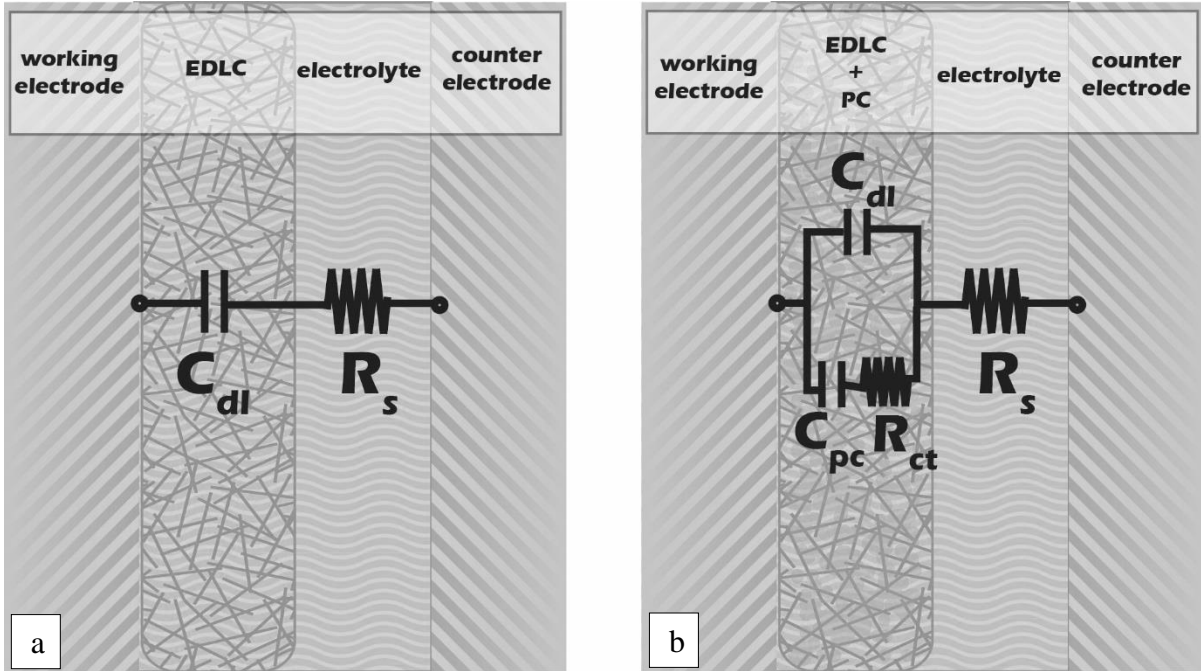


Figure 19: (a) RC series circuit approximates the charge path of an EDLC electrode. R_s is solution resistance and C_{dl} is double layer capacitance. (b) PC electrode includes R_{ct} – charge transfer resistance – and C_{pc} – pseudocapacitance.

On the other hand, charge passing through a PC electrode involves a charge-transfer resistance due to the redox reactions. The charge again encounters the ESR (a resistor), but then it has two options: it may pass through the PC material (a resistor in series with a capacitor) or it may pass through the double-layer (a capacitor). The basic equivalent circuit in this case is $R+C/(R+C)$ (Figure 19 b).

Once the circuit is identified, the values of the elements can be obtained via statistical matching between the measured circuit and the model circuit. A simulation software plugs values into the model until the differences minimize. The differences are expressed as a χ^2 value. Most of the supercapacitor characteristics that can be derived from the EIS technique

(equivalent series resistance, double-layer capacitance and pseudocapacitance) can also be measured by CV and CP. The advantage of EIS lies in identification of the equivalent circuit, which indicates whether any faradaic processes are involved. In many cases, EDLC electrodes exhibit pseudocapacitance due to residual oxygen-containing functionalities, and EIS is frequently employed to study this kind of mechanism. EIS is consequently considered one of the most useful analytical tools in supercapacitor characterization.⁴⁸

The example below is taken from a study of surface-functionalized activated carbon electrodes (Figure 20).⁵⁰ Experimental data taken at two DC voltages (-0.2 and -0.9 V) both exhibit a semicircular region associated with pseudocapacitance. The equivalent circuit used to fit the data includes a solution resistance (R_s), constant phase element for the double layer (CPE), faradaic resistance for the pseudocapacitance (R_F) and capacitor also for the pseudocapacitance (C_ϕ). The authors were able to calculate pseudocapacitance, double layer capacitance and charge transfer resistance for the electrodes.

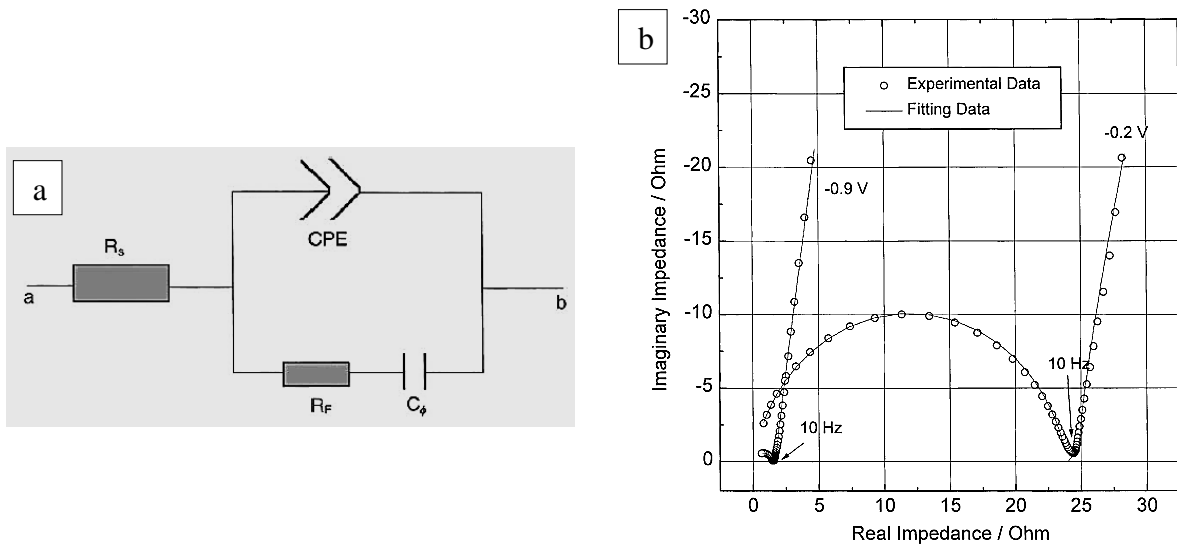


Figure 20: Surface functionalized activated carbon electrodes with (a) equivalent circuit and (b) EIS data.³²

1.3.2.3 Test Cell Design and Metrics

The comparison of various specific capacitance values reported throughout the literature is complicated by the fact that the choice of test setup affects the measured capacitance.⁵⁰ Setting up a fixture with which to test electrode performance can follow two different approaches: the *two-electrode test cell* or the *three-electrode test cell*.⁵¹ The two-electrode setup is essentially a model working cell in which both electrodes (working and counter) are often made from the same material (Figure 21 a). The three-electrode setup on the other hand only has one electrode – the working electrode - made from the material under examination. The counter electrode is typically a platinum wire or sheet, and the third electrode is a reference, placed near the surface of the working electrode (Figure 21 b).

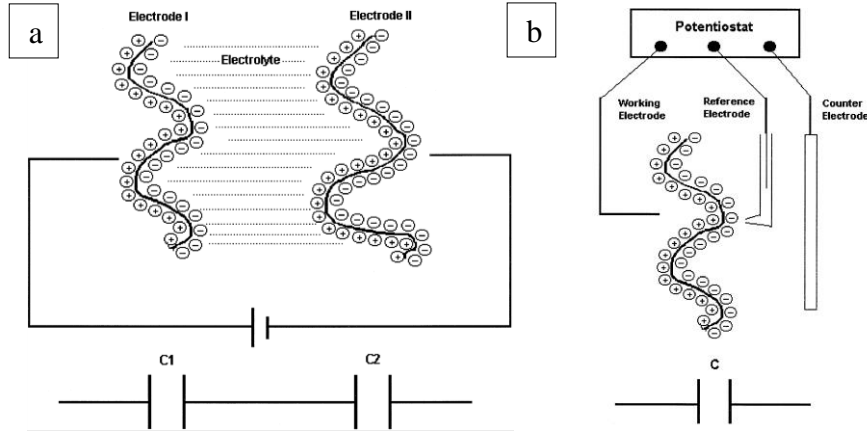


Figure 21: (a) Two-electrode setup with two identical electrodes. (b) Three-electrode setup with working electrode, reference, and counter electrode. Simplified equivalent circuits shown for each.⁵⁰

In the two-electrode setup, the two capacitor elements in series are identical in value, which results in a total capacitance (C_{2E}) of half that of each electrode. Total capacitance in the three-electrode setup (C_{3E}) is equal to the capacitance of one electrode (C) and is thus double the capacitance of the two-electrode setup (Eqn. 23).

$$C_{2E} = \frac{1}{2}C = \frac{1}{2}C_{3E} \quad (23)$$

Since total electrode mass for the two-electrode setup is double that of the three-electrode setup, specific capacitance ($C_{S,2E}$) is one quarter (Eqn. 24).

$$C_{S,2E} = \frac{C_{2E}}{2m} = \frac{1}{4} C_{S,3E} \quad (24)$$

Two electrode cells yield results which are closer to the expected device performance, while three-electrode cells more accurately provide material-specific electrochemical characterization. In the latter case, the reference electrode keeps track of the potential of reduction and oxidation events. Throughout this work, characterization using both two-electrode and three-electrode cells is undertaken, and is noted in experimental sections.

Another aspect of the inconsistency in reported values stems from determining which physical elements comprise the electrode mass (m , in Eqn. 24 above). For example, an electrode may contain granular activated carbon held together by PTFE binder, pasted onto an aluminum foil current collector. Will the binder component be included or excluded? The same question applies to the current collector. When m is restricted to only the active material (in this case, activated carbon) C_S will be greater than it would be if other parts of the electrode were included. This approach yields inflated values from a device design point of view, however it can be a useful way to compare new active materials (Figure 22).

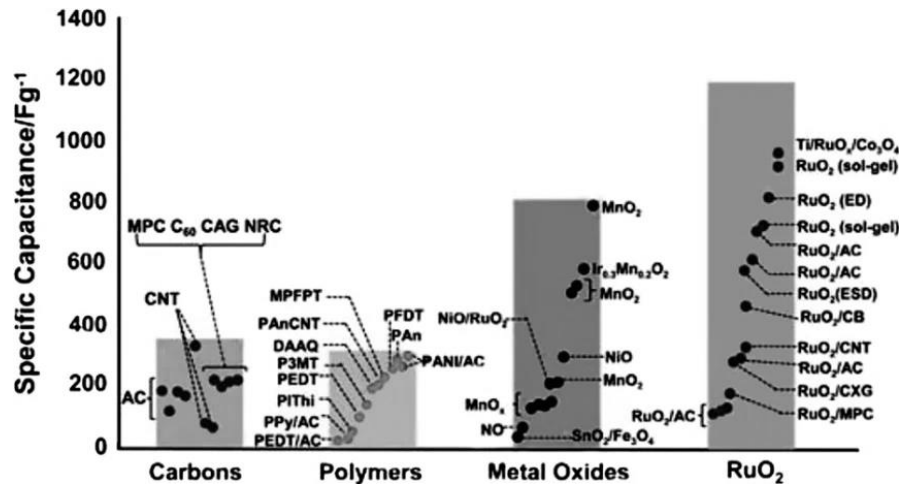


Figure 22: Reported specific capacitance values for various active materials as taken from the literature.⁵²

In fabricating electrodes, the materials shown in Figure 22 must be mixed with various additives. In addition to polymer binders used for stability, highly conductive materials are often needed to reduce ohmic resistances. Particularly regarding pseudocapacitive materials, such as conductive polymers and transition metal oxides, the electrode would not be sufficiently conductive based purely on the active material. An electrode consisting purely of RuO₂, for example, is not structurally or electrically robust. It must be decorated onto a scaffold. Many times, the active electrode component is so low in mass that accurate measurement is not possible without extensive error.⁵¹ Furthermore, in comparing various fiber-based electrodes, the core fiber cannot always be considered a non-active mass. Activated carbon fiber utilizes an unknown percentage of its overall depth (Figure 23). In order to maintain consistent, practical characterization of the various electrode materials to be considered in this research, the entire electrode mass will be used to calculate specific capacitance values.

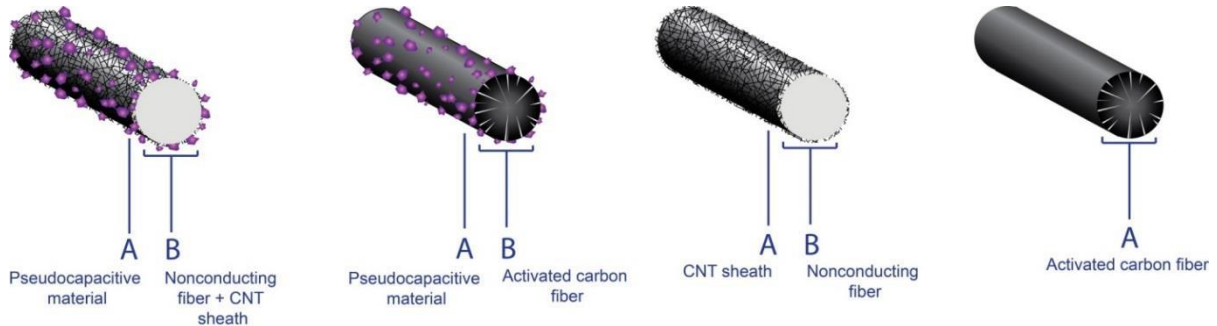


Figure 23: Various designs of fiber-based supercapacitor electrodes, divided into their “active” part and “non-active” part (A and B, respectively).

CHAPTER 2: Introduction Part II – Overview of Nonwoven Technologies and Dissertation Outline

2.1 OVERVIEW OF NONWOVEN TECHNOLOGIES

Nonwovens differ from traditional knit and woven textiles in that they may be formed from fibers directly by interlocking or bonding fibers. Owing to the vast array of available processing parameters, nonwovens are extremely varied in their structure.⁵³ This section aims to convey a simplified view of common materials and methods used to make nonwovens, along with their corresponding structural qualities, although it is by no means exhaustive. Additional attention will be given to the properties of interest for porous electrodes: specific surface area (SSA), porosity, web thickness, fiber geometry and fiber chemistry.

2.1.1 Nonwoven Processes

The basic technological systems used to form nonwovens must fulfill three functions: *preparation* of raw material to be shaped into a web, *formation* of the sheet or web from fibers or filaments, and giving the web integrity via *bonding*. A fourth function, *finishing*, is optional.

Depending on the raw material under consideration, these functions may be fulfilled by certain processes. Table 3 gives an overview of some basic material types and their associated technologies. Many innovative approaches fall outside of this basic technological framework, and in order to emphasize the importance of novel developments to the nonwoven industry, Batra and Pourdeyhimi offer a structural definition of nonwovens, which is not tethered to specific technologies or materials. Under this more flexible framework, nonwovens may be classified as *primary* (first order structures), *secondary* (second order structures) or *tertiary* (higher order structures).⁵³ Primary nonwovens encompass homogenous fiberweb structures and net-like web structures. Secondary nonwovens refer to heterogeneous fiberweb structures. Tertiary nonwovens include hybrid and multiplex structures.

Table 3: Staple fiber based batch technologies and vertically integrated technologies used to fabricate nonwovens.⁵³

	Raw Material Type	Preparation	Web Formation	Bonding	Finishing
Staple fiber based batch technologies	Staple fibers < 5mm	Defibrizing	Pulp airlay	Thermal bonding, Resin bonding	Mechanical, Chemical
	Staple fibers ≥ 10 mm	Opening, Blending	Carding, Conventional airlay	Needlepunching, Hydroentanglement, Thermal bonding, Resin bonding	Coloration, Printing, Mechanical, Thermal, Chemical
Integrated technologies	Staple fibers 10 – 25 mm	Stock preparation, Dilution, Wet end chemistry	Wetlay sheet formation, dewatering	Hydroentanglement, Thermal bonding, Resin bonding	Coloration, Mechanical, Chemical
	Polymer resin flakes	Crystallizing, Drying, Melt-extrusion, Quenching, Attenuation	Web lay-down	Needlepunching, Hydroentanglement, Thermal bonding, Resin bonding	Coloration, Printing, Mechanical, Thermal, Chemical
	PE resin	Flash spinning	Web lay-down	Hydroentanglement, Thermal bonding,	Mechanical, Chemical

2.1.2 Key Properties of Nonwovens

Nonwovens are highly engineered for specific applications, with their properties tailored as much as possible to attain the performance levels required for their given application. Properties can be thought of as relating to fiber, structure, or bonding. Examples of fiber-related properties are fiber orientation distribution, fiber diameter distribution, fiber SSA and fiber chemistry. Structure-related properties include pore size, porosity, and basis weight uniformity. Finally, bonding-related properties include adhesion, crossover, and web thickness. Among all of these, the key properties from an electrode point-of-view are fiber chemistry, SSA, porosity and web thickness:

Fiber Chemistry - A cornerstone property for any electrode is its electrical conductivity. Fiber-forming polymers are classified as dielectric materials, with relative permittivities (ϵ_r) ranging from 1.5 (polypropylene) to 4.0 (polyester).⁵⁴ Although dielectric materials are of use in conventional electrostatic capacitors, supercapacitors necessitate nonwovens which are semiconductors or conductors. Section 2.2 will detail the various processes which may be used to obtain electrical conductivity in nonwovens. One modification approach, coating, is likely to be impacted by the fiber chemistry due to the need for adhesion between the fiber and its conductive coating. Intermolecular bonding is governed by the types of functional groups present on the fiber surface and the coating particles.⁵⁵ Another modification approach to obtaining conductivity is carbonization, which is also impacted by fiber chemistry. Polyacrylonitrile (PAN), mesophase pitch, phenolic resin and cellulose are carbon-rich polymers known to be well-suited for obtaining electrically conductive carbon fibers.⁵⁶

Specific Surface Area - The shape of the fibers is also likely to have a bearing on electrode performance. SSA of fibers increases as their diameter (shown in denier and micron) decreases (Figure 24 b). The importance of fiber geometry can also be seen: for a given fiber diameter, round fibers have the lowest SSA while complex shapes such as multi-lobed “winged fiber” (WF) have a much higher SSA. Maximizing SSA can thus be accomplished with low-diameter fibers and/or complex cross-sectional shapes.

Multicomponent fiber spinning (Figure 24 a) is used to produce fibers made from more than one type of polymer, which are extruded in various conformations such as side-by-side, core/sheath, islands-in-the-sea (I/S), and others (Figure 25). Following extrusion, they may be kept in filament form or chopped into staple fiber lengths. Subsequently, the sections composed of different polymers may be split or washed so that one polymer dissolves and leaves behind a low diameter microfiber. For example, a fiber which is $\sim 20 \mu\text{m}$ in diameter as extruded can reduce to $0.3 \mu\text{m}$ after the sacrificial PLA sheath is dissolved (I/S fiber with 360 islands).

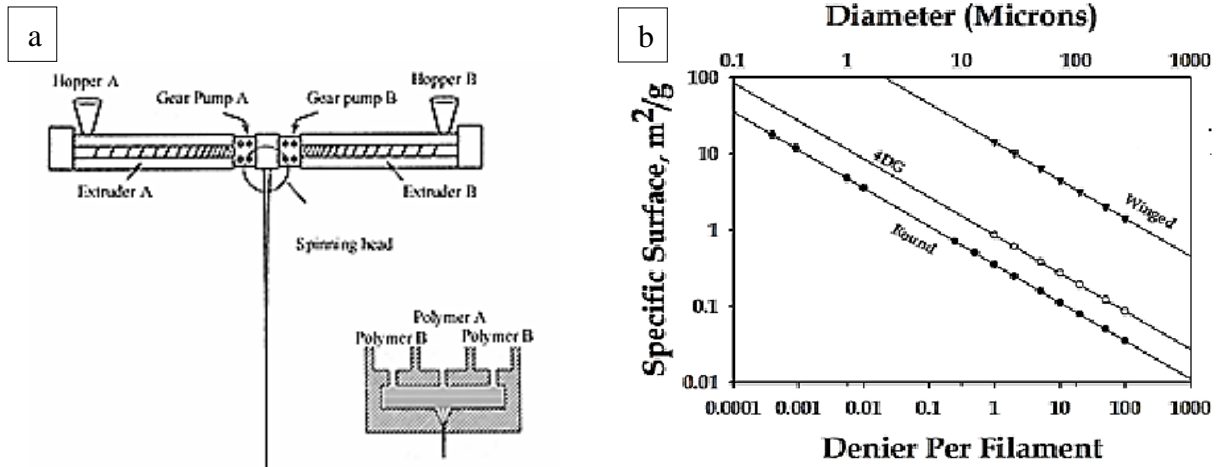


Figure 24: (a) Two extruders aligned to spin a bicomponent fiber composed of two polymers. (b) Surface area for round, 4DG, and winged fibers as a function of diameter.⁵⁷

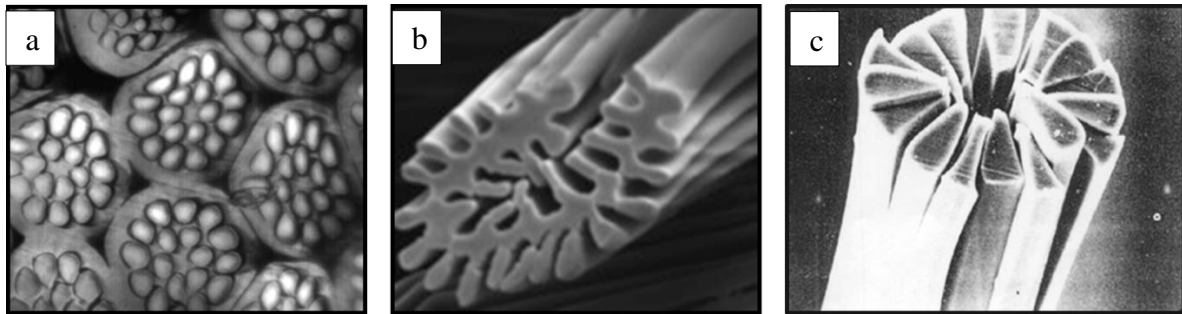


Figure 25: Figure 3: Cross-sectional SEM of various microfibers: (a) Islands-in-the-Sea as-extruded, (b) washed winged fiber, (c) split segmented pie.⁵⁸

Porosity – Three-dimensional electrodes are expected to facilitate the circulation of electrolyte throughout its pores. The porosity of a nonwoven structure is often characterized by its solid volume fraction (SVF), which is essentially the inverse of porosity. It indicates the fraction of the web volume which is occupied by solid (fiber) material, as opposed to void (air). For three-dimensional materials which contain any amount of void space, SVF (μ) is less than 1. It can be calculated according to Eqn. 25, where ρ_{web} is web density and ρ_{fiber} is fiber density.

$$\mu = \frac{\rho_{web}}{\rho_{fiber}} \leq 1 \quad (25)$$

Fiber-forming polymers have close density values, ranging from 94.6 g cm⁻³ for polypropylene to 1.45 g cm⁻³ for polyester. However, web density for different nonwovens varies greatly depending on web formation process and bonding conditions. Thus, SVF is primarily a factor of web processing technologies.

Web Thickness – Device design necessitates the consideration of electrode thickness. As with porosity, web thickness is a factor of processing technology and conditions. Commercial supercapacitors contain electrodes which range from 10’s to 100’s of microns thick, with the thinner electrodes favoring power density and the thicker materials favoring energy density.⁵¹ Typical spunbonded and meltblown webs measure in the 100’s of microns. At NC State University’s Nonwovens Institute (NWI), continuous bicomponent fibers can be extruded on a spunbond line and form the web structure in one step. Figure 26 shows a schematic of spunbond curtain spinning, in which the bicomponent fibers are extruded through the spin pack, quenched with cool air, drawn with the attenuating forced air, collected on the belt, and rolled up onto the winder.

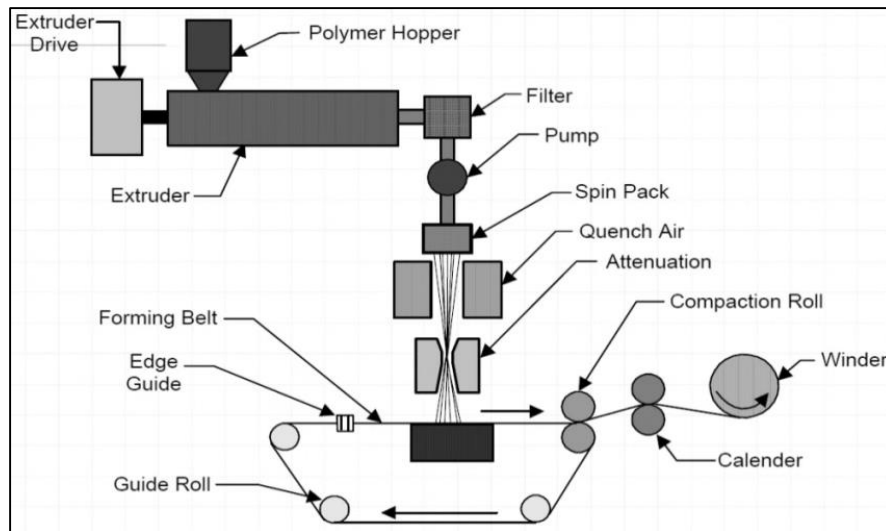


Figure 26: Schematic of an open spunbond process with a belt collector.⁵⁹

Staple fiber webs can be produced to be tissue-like, with wetlaid web thickness measuring in the 10's of microns. They can also be made to be more than 10^5 micron via carding and cross-lapping. Figure 27 shows the roller system of a Truetzschler carding machine, similar to the one in place at the NWI. The rollers are adorned with comb-like wires that break up fiber tufts, individualize and align them and optionally randomize the web. In order to tune the basis weight of the web and improve uniformity, carding can be followed by cross-lapping. As compared to the system shown in Figure 27, NWI uses a newer card (EWK) that has a series of smaller cylinders, workers and strippers and results in continuous opening, blending and carding during the process potentially leading to improved carding and better uniformity.

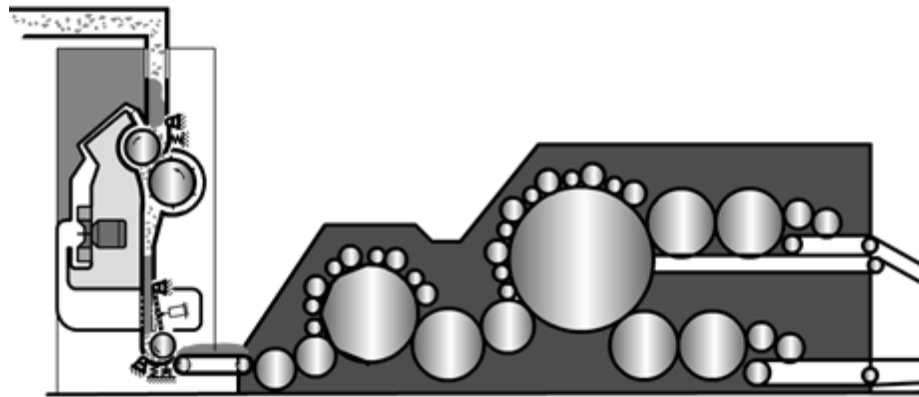


Figure 27: Carding machine for nonwoven web with single chute fed.⁶⁰

2.2 NONWOVEN ELECTRODES

While high SSA is an advantageous feature of energy storage electrodes, electrical conductivity is an indispensable necessity. The electrode passes current between the electrolyte and the current collector – an insulating electrode would block the flow of electrons. Furthermore, power (P), which is one of the key performance characteristics of electrochemical capacitors, decreases as device resistance (R) increases. This relationship is given according to Eqn. 26, where V_0 is the rated device voltage. As a result, most commercial supercapacitors are designed to have a very low device resistance from $0.2 - 4.0 \text{ m}\Omega$.⁶¹

$$P = \frac{V_o^2}{4R} \quad (26)$$

2.2.1 Obtaining Conductive Nonwovens

Converting dielectric polymer fibers to highly conductive fibers can be accomplished in a variety of ways. Screen printing has been extensively used, as detailed by Karaguzel.³⁹ However, for the construction of porous electrochemical electrodes, it is preferable to obtain a coating that does not require binder.^{62,63} In addition to being costly, binder impedes the flow of electricity. Significant binder-free processes to can be divided into three categories: *coatings, fillings* and *bulk conductive fibers* (Figure 28).

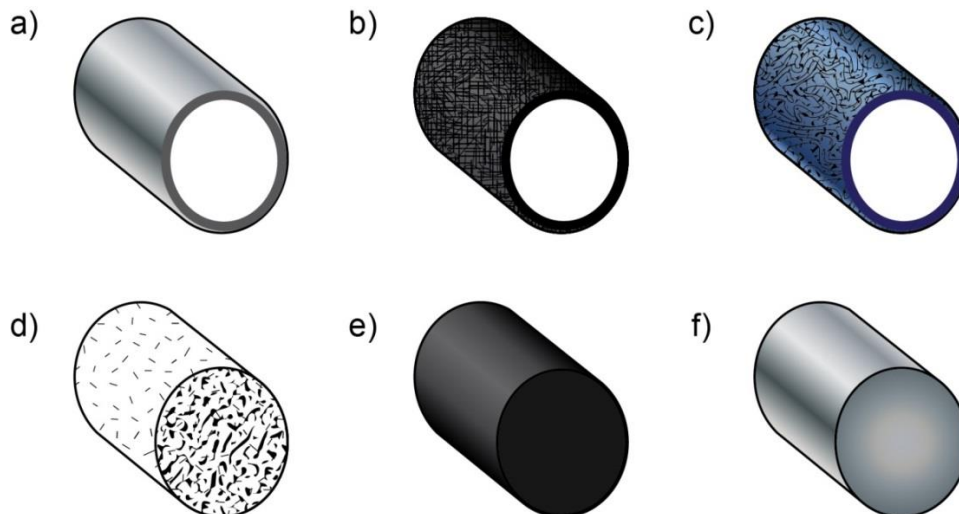


Figure 28: Polymer fibers can be modified to be conductive via (a) metallic coating, (b) carbon particle coating, (c) intrinsically conductive polymer coating, (d) co-extrusion with conductive particles, (e) continuous carbon fiber, or (f) continuous metal fiber.

Coatings, which ideally result in conductive sheaths wrapped conformally around individual fibers, are most commonly carried out using metallic, carbon or intrinsically conductive polymers (ICPs) (Figure 28, a – c). Binder-free metallic coatings can be achieved by seeding fibers with a catalyst and subsequently soaking them in a solution carrying metal ions (such as aurochloric acid or nickel sulfate).^{64,65} This method is known as electroless plating, since it

does not employ electricity.⁶⁶ A similar approach is used to obtain ICP coatings, although the deposition is usually an oxidative one. Polyaniline, polythiophene and polypyrrole can be polymerized on the surface of fibers via an in-situ chemical oxidative reaction.⁶⁷ Finally, conductive carbons coatings can be obtained through immersion of fibers and fabrics in well-dispersed nanoparticle suspensions. Carbon nanotubes and graphene have been shown to adhere to polymer surface without added binder.⁶⁸

The filler approach entails co-extruding blends of polymer and conductive particles (Figure 28, d). Metal particles, in the form of flake, wire or powder can be incorporated with thermoplastic chips, then formed into fibers.⁶⁹ Carbon particles, such as carbon black or carbon nanoparticles, may also be used according to the same procedure. Limitations to this approach include the high proportion of active material distributed away from the fiber surface, and the detrimental effect of high particle loading on the fiber extrusion process.⁵⁵

Bulk conductive fibers are composed entirely of conductive materials, and can be made from metals or from carbon (Figure 28 e + f). The process of forming metal fibers is known as bundle drawing. Bundle drawing begins with conventional metal wires which are grouped and clad in an iron tube. The whole group is drawn through a die which reduces the diameter by 10 – 20%. This step is repeated 20 – 40 times with increasingly narrow dies in order to reach fiber diameters as low as 4 μm .⁷⁰ Formation of carbon fibers, on the other hand, begins with polymeric precursors and involves slow pyrolysis to eliminate the non-carbon portion of the polymers. During the slow temperature ramp up to final heat treatment temperature (HTT), hydrogen, oxygen and nitrogen are expelled while carbon-carbon bonds are formed. An oxygen-free gas such as N_2 must occupy the furnace during carbonization to prevent the precursor from burning.⁵⁶

While all of these methods are feasible ways to form conductive nonwovens, not all are well-suited for the applications under consideration here. Although metal fibers and metal-coated fibers have been proposed as electrode materials, the fact remains that commercialized

supercapacitors are exclusively based on carbon electrodes.^{24,62} Carbon is chemically robust in a wide range of acidic and basic solutions.³⁴ Electrodes made of metals, on the other hand, can undergo undesirable redox reactions within the voltage window, or can erode and deposit onto the opposite electrode.¹⁹ Intrinsically conductive polymers can be applied as coatings onto textile fibers through in-situ chemical or electrochemical oxidative polymerization, yet these coatings suffer from poor durability under thermal and mechanical stress. Exposure to a temperature of 100°C for 20 hours can reduce polypyrrole conductivity below half its original value.⁶⁷ Furthermore, their electrical properties are a function of oxidation state, such that they would be unreliable scaffolds for pseudocapacitive materials. Among carbon-based conductive fibers, the coating and bulk conductive fiber types hold promise, while the filler type will not be considered due to the drawbacks previously mentioned. Figure 29 depicts the two approaches that will be the focus of this research: carbon fibers and carbon nanotube coated fibers.

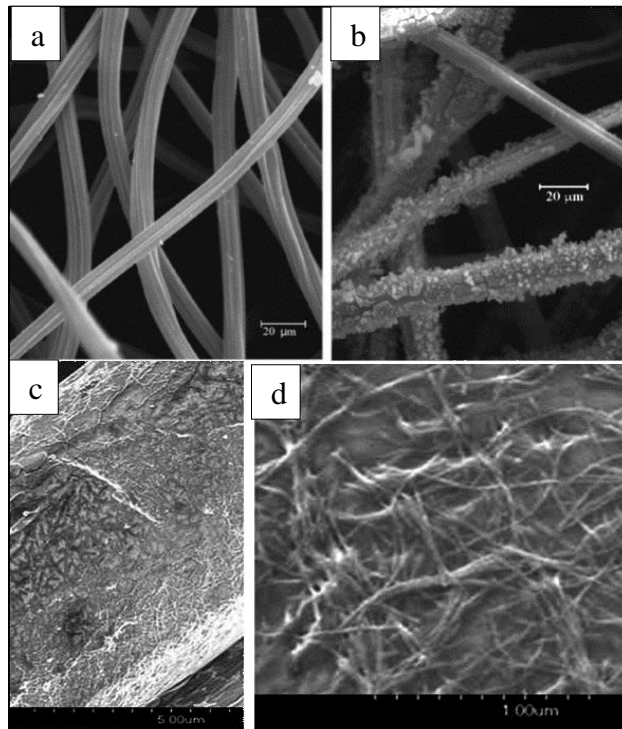


Figure 29: (a) Carbon fiber nonwoven used as wastewater treatment electrode, and (b) electrode with adsorbed reduced Cr^{6+} .⁷¹ (c + d) Nylon fiber coated with carbon nanotubes.⁷²

Electrical conductivity in carbons is expected to be incomparable to metals. Unlike metals, carbons have highly variable electrical properties.⁷ Depending on the preparation conditions, conductivity can be within the ranges of insulators, semi-conductors or metals.³⁴ This phenomenon can be attributed to the fact that the electrical properties of graphene crystallites show the highest anisotropy among all elements. Along the x-y plane, the dielectric constant, ϵ , is 2.61 while along the z-axis, $\epsilon = 3.28$.⁷³ As a consequence, conductivity is high ($1.61 \times 10^{15} \text{ sec}^{-1}$) in the x-y plane, while it is undetectable along the z-axis resulting in the highest ratio among all elemental materials.³² As was discussed in Chapter 1, this anisotropy affects the performance of double layer capacitors.

2.2.2 Current Types and Applications for Nonwoven Electrodes

Many academic studies have employed nonwovens as electrodes, and conductive nonwovens have already made their way into several commercial applications. Filter cartridges utilizing carbon “felt” as the cathode material have been developed to electrochemically remove trace metals from effluent.⁷⁴ Pletcher et al. compared the reaction rate of copper reduction ($1\text{mM Cu}^{2+} + 0.5\text{M Na}_2\text{SO}_4$) with various electrodes: planar, 10 pores per inch (ppi) reticulated vitreous carbon (RVC), 100 ppi RVC, and carbon felt. Figure 30 demonstrates the effectiveness of carbon fiber felt (d), and shows a treatment cell design based on this research.⁸

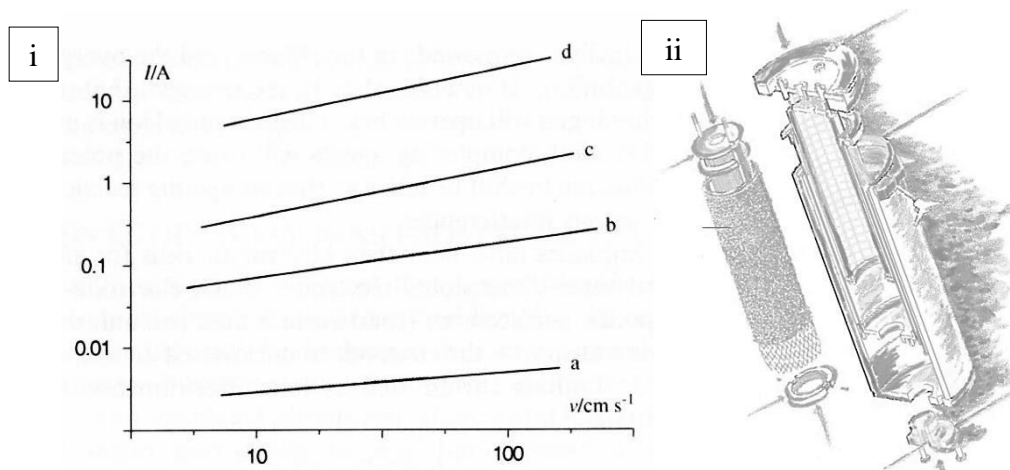


Figure 30: (i) Variation in current with the mean linear flow rate for cells with (a) flat plate cathode, (b) 10 ppi RVC cathode, (c) 100 ppi RVC cathode, and (d) carbon felt cathode. (ii) Renocell cartridge.⁸

Pb and PbO₂ can be electrolytically deposited on carbon fiber for use in lead-acid batteries.⁷ Sigracell, a division of the SGL Group, manufactures “battery felt” – a nonwoven made with either carbon or graphite fibers. The carbon fibers are lightweight and show excellent corrosion resistance within the voltage window of 1.4 V (in H₂SO₄). An especially prominent application for carbon fiber nonwovens is in fuel cells. The majority of fuel cells available today are polymer electrolyte membrane fuel cells (PEMFCs), which require porous, conductive electrodes to maintain contact between reactant gas and electrolyte (Figure 31).⁷⁵ Among these gas diffusion layers (GDLs), nonwoven carbon fiber substrates are the most common type, eclipsing the use of woven GDLs.⁷⁵

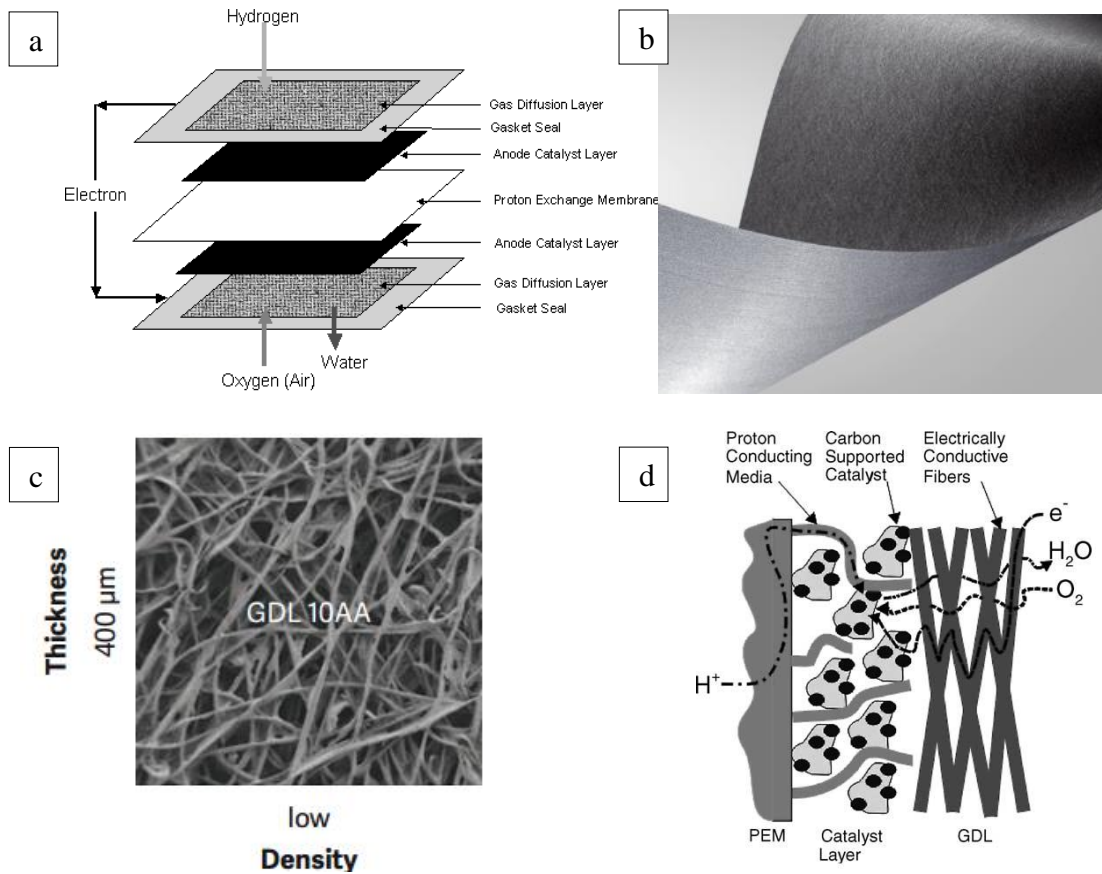


Figure 31: (a) Placement of GDL in MEA;⁷⁶ (b + c) Sigracet 10AA electrode: untreated carbon fiber spunlace;⁷⁷ (d) Cross-section of the interface between catalyst, electrolyte, and GDL.⁷⁸

The key producers of GDL technologies available on the market today are listed below, along with selected details of their product lines:

- Toray Industries International: Toray Industries, headquartered in Japan, has been a leader in the carbon fiber industry for many years. They produce a line of untreated wet-laid carbon fiber nonwovens designated for the fuel cell market. Their customers are fuel cell manufacturers such as Johnson Matthey who apply their own hydrophobic and catalyst layers.
- Zoltek: Zoltek was a carbon fiber technology start-up, based in St. Louis, that was recently (2013) purchased by Toray. They focus on woven carbon fiber fabrics.
- Freudenberg FCCT: Freudenberg Fuel Cell Component Technologies group is based in Germany. With related businesses in nonwoven filters and seals (NOK), Freudenberg is able to produce the following components: gas diffusion layer, fuel cell seal, fuel cell filter, fuel cell humidifier. They primarily produce nonwoven carbon fiber materials.
- SGL Carbon Corp.: The SGL group, also a German company, consists of several business units that relate to carbon products in a broad range of applications. Their gas diffusion layers are part of the SIGRACET Fuel Cell Components division.
- Ballard Power Systems: Ballard Power Systems is a major fuel cell provider, with a Material Products division that cells parts individually. They are based in Lowell, Mass.

Many of the leading automakers, including GM, Toyota, Honda, Hyundai and Daimler, have listed FCs as a major technological key to their zero-emissions vehicle programs.⁷⁵ The average automobile fuel cell stack is estimated to use 6.5 square meters of GDL material. This translates to an expense of \$325 in carbon electrode for every FC, based on the current cost estimated at \$50 / m². If the market for fuel cells grows by the estimated 25% per year, it could reach \$2.9 billion in 2015. Thus, sales of GDL materials can be expected to reach \$210 million by next year. However, there is pressure on fuel cell manufacturers to reduce costs in

order to make the FC technology more competitive with existing technologies. In the years from 2010 to 2014, the price was successfully decreased from \$42/Kw to \$30/Kw.⁷⁵ Carbon fiber nonwoven producers are likewise encouraged to continue finding ways to decrease cost while improving performance.

The engineering of nonwoven electrodes for fuel cells has developed in parallel to the growth of the fuel cell industry. Supercapacitors, which require many of the same electrode performance demands as fuel cells (high accessible surface area, high electrical conductivity, good stability, low cost) are likely to see a boom in demand as the electric vehicle and consumer electronics markets continue to expand. Currently, the vast majority of supercapacitor electrodes are constructed from activated carbon granules held together by PTFE binder. The aim of this research is to study the impact of nonwoven structural characteristics on their performance as supercapacitor electrodes.

2.3 CONDUCTIVE CARBON FIBER NONWOVENS

Early development of carbon fiber began in the late 19th century, starting with a patent by Thomas Edison for a lamp filament. The filament was made of cellulose-derived carbon fiber, and it would glow without degrading when electrical current was passed through it. Similar patents describe the carbonization of natural cellulosic fibers, such as jute and bamboo. Because of the poor strength retention of cellulose-derived carbon fiber, it wasn't recognized as a high modulus material until the 1960's, when Akiko Shindo of Japan's Government Industrial Research Institute (GIRI) began utilizing PAN as a carbon fiber precursor.⁷⁹ Shindo's work opened up new doors for carbon fiber applications. The Cold War arms race spurred high-strength carbon fiber research in the US and the UK in the 1970's, and as a result, much is now known about the effects of processing parameters on the properties of carbon fiber. In the 1980's, the discovery of high-modulus mesophase pitch carbon fibers ushered in a new generation of carbon fiber composite materials for high-performance aerospace needs.⁷⁹ During the course of research, many additional properties associated with carbon fibers, such as good electrical conductivity, thermal stability, and the potential to have high surface area, were discovered. Subsequently, carbon fibers were

cultivated for other applications and it is these other applications that have carved out the markets for carbon fiber nonwoven technologies. Examples of applications for carbon fiber nonwovens include high temperature thermal insulation for nuclear reactors, battery electrodes and filtration materials for chemical warfare protection.

2.3.1 Precursors and the Carbonization Process

Carbon fibers are derived from carbon-containing fiber precursors, and they obtain their unique properties from the predominance of C-C bonds in the organic polymer structure (Figure 32). C-C bonds are among the strongest known bonds, but process artifacts limit the actual strength to around 50% – 70% of the theoretical potential.^{56,79}

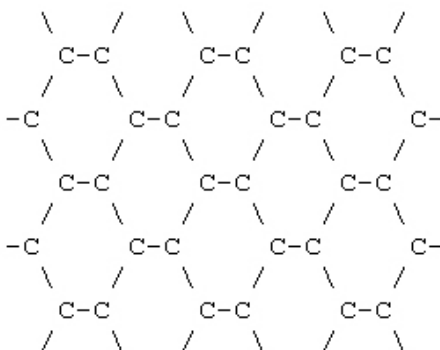


Figure 32: Carbon-carbon bonds in a sheet of aromatic rings are responsible for the unique properties of carbon fiber.⁵⁶

The first generation of commercially successful carbon fibers was derived from regenerated cellulose fibers. Natural cellulosic fibers such as cotton were deemed unusable due to their irregular and unpredictable fiber structure. Rayon was determined to provide the best results. The cellulose repeat unit (Figure 33), $C_6H_{10}O_5$ suggests a potential carbon fiber yield of 44%, but the actual yield is around 25% due to carbon losses.⁷⁹ The resulting fiber is relatively weak (400 – 700 MPa) due to mass loss and the graphite sheet alignment is poor. Modulus can be improved by applying tension during carbonization, but it is still lower than PAN-derived carbon fiber modulus.

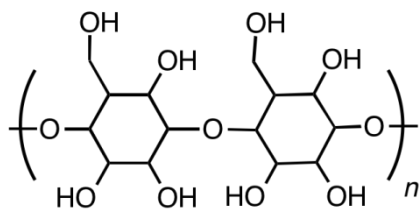


Figure 33: Cellulose molecule with two carbon rings.⁵⁶

PAN is currently the most widely used precursor fiber. It requires a stabilization process to reduce shrinking, during which the pendant nitrile groups are cyclized (Figure 34). Initiation of cyclization may be accomplished by anions, resulting in a lowered reaction temperature and slower, less damaging rate.⁸⁰ Thus, a small amount (usually ~ 1%) of co-monomer such as itaconic acid (IA) may be added to the acrylonitrile monomer.^{80,81} The PAN polymer is then spun to obtain fibers. The preferred method is wet spinning if the fiber is designed for carbonization; dry spinning results in a dogbone-shaped cross section with more voids in the microstructure.⁸² Following complete pyrolysis, the final carbon yield of PAN fibers is around 50% of the original mass.

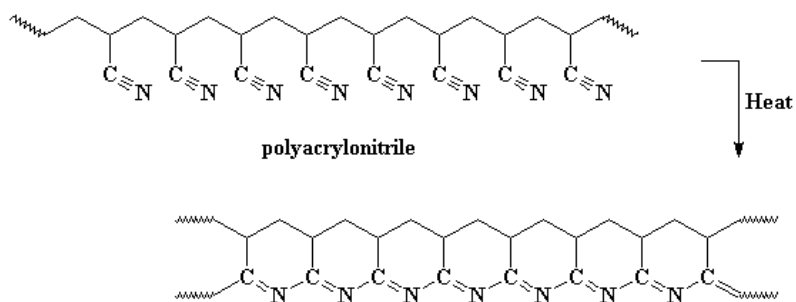


Figure 34: Cyclization of pendant nitrile groups during the PAN conversion process.⁸²

Mesophase pitch contains a high amount of carbon in its molecular backbone. It is mostly composed of semi-fused aromatic molecules (Figure 35). Pitch for carbon fiber is a byproduct of smelting and oil processing. The quality of pitch feedstock is an important parameter, and petroleum asphaltane is preferred because its contents are more well-known

and the viscosity is lower.^{56,83} The most important structural quality, however, relates to the crystallinity of the pitch. Mesophase pitch is a discotic liquid crystal obtained by the removal of low molecular weight particles and subsequent polymerization.⁸⁴ The resulting fiber morphology is determined by the parameters of the spinning system, especially the shape of the spinneret. Pitch is formed into fibers through extrusion: capillaries process pitch directly from melt, which gives it the advantage of being a solvent-free process.⁸³ Another advantage over PAN-based is that during graphitization, pitch-based carbon fibers do not need to be held under tension.⁵⁶ Yield of mesophase pitch fibers is around 90%.

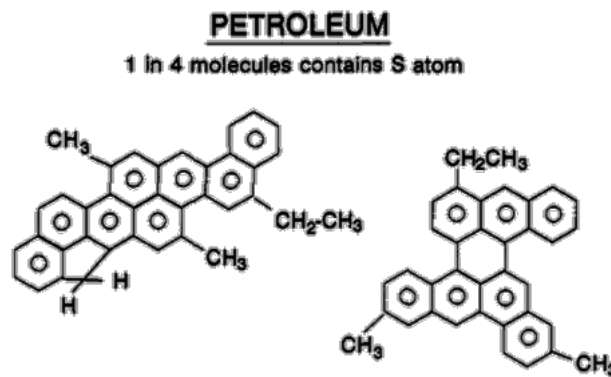


Figure 35: Petroleum-based pitch molecules rich in aromatic rings.⁵⁶

The precursor materials are converted to carbon through the process known as carbonization, which entails the controlled burn-off of all non-carbon elements. The choice of carbonization atmosphere, ramp rate, application of tension, temperature and duration play a role in the characteristics of the final product, and have been studied extensively.^{85,86} A simplified outline of the key steps for PAN carbonization is shown in Figure 36. First, the polymer molecules are stabilized in an oxygen-containing gas such as air. During this step, the molecules begin to dehydrogenate, oxidize, cyclize, decyanate and finally form cross-linked ladders between conjugated chains.⁸⁵⁻⁸⁷ This is a necessary and impactful step in the process of creating PAN-based carbon fiber, as it prevents undesired shrinking.⁸⁰

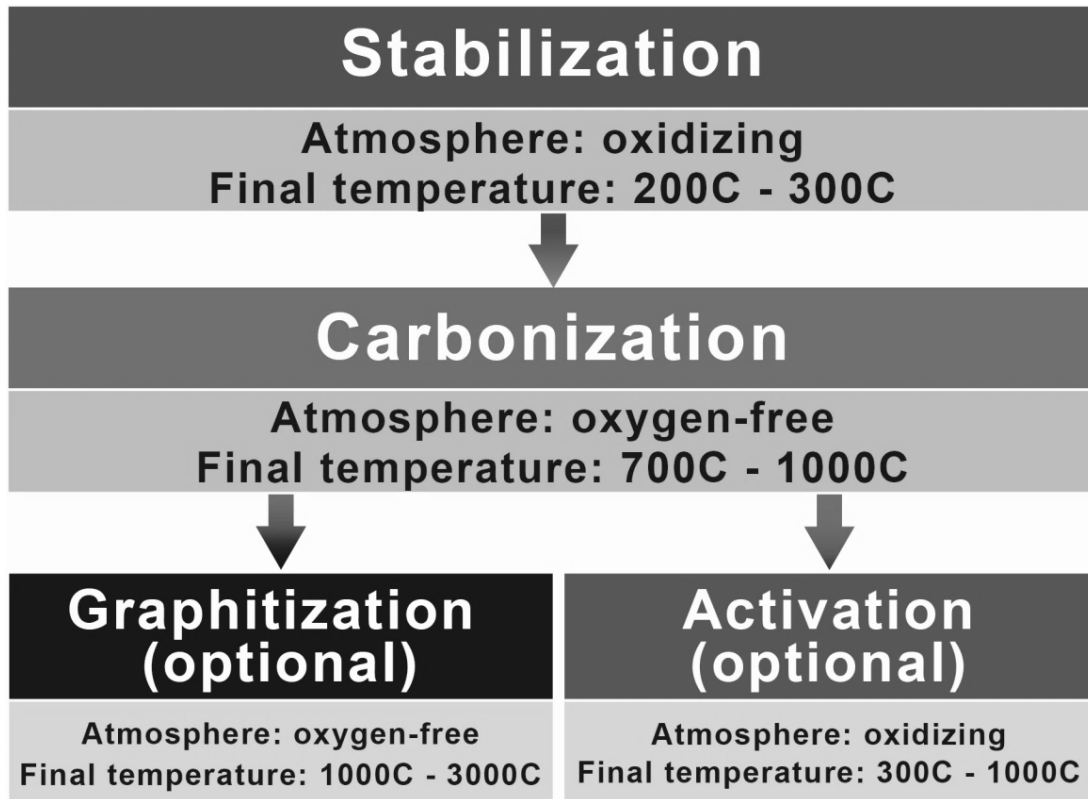


Figure 36: Simple overview of steps in the carbonization process.

After stabilization, the main carbonization step is carried out in an oxygen-free atmosphere, during which all non-carbon elements are expelled from the polymer. Carbonization can be halted at temperatures as low as 650°C, but can also continue up to around 2000°C. Ramp rate, holding time, final temperature, and atmosphere gas type all affect the yield. Graphitization is an optional step following carbonization, and it is distinguished by the resulting highly aligned graphite sheets that form. This process is the most energy-intensive, and is only undertaken if necessitated by the application. The strongest, stiffest, most electrically conductive carbon fibers result from graphitization. Activation is an optional step as well, but due to its importance in supercapacitor electrodes, activation will be covered in greater detail subsequently.

Pyrolysis can either be carried out prior to web formation (pre-carbonization) or following web formation (post-carbonization) (Figure 37). The precursor material may be in the form of a continuous fiber, a staple fiber, a yarn, a fabric, or even a fully formed product in its final shape, such as a brake disc.

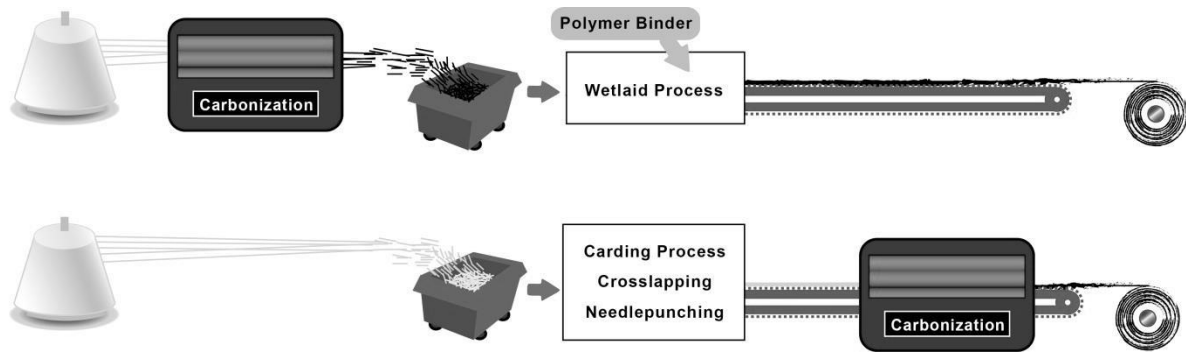


Figure 37: (Top) In pre-carbonization, web is formed from carbon fiber. (Bottom) In post-carbonization, web is formed from polymer fiber and carbonized subsequently.

In pre-carbonization, the primary nonwoven processing methods used to assemble carbon fibers are wet-lay and needlepunching. Battistelli and Giglia of American Cyanamide Corp. were the first to describe the use of carbon fiber in a wet-laid process, in 1985.⁸⁸ Their U.S. Patent, entitled *Non-Woven Activated Carbon Fabric* specifies short activated carbon fibers (1.5 cm maximum) to be blended with fibrillated acrylic fiber in water. “Flocculating and surface-active agents” could be added to prevent agglomerations of either component, resulting in a uniform dispersion of these materials with different surface energies. The acrylic fibrils are described as the binding element, entrapping the carbon fiber (Figure 38). In 2011, Nhan et al. of Kimberly-Clark were granted a patent for a paper-like conductive nonwoven which used a similar blend of short carbon fiber (here, derived from PAN) and thermoplastic or pulp fibers.⁸⁹ They introduce the idea of laying several layers of the paper-like material together, with only the core layer containing carbon fiber (Figure 38).

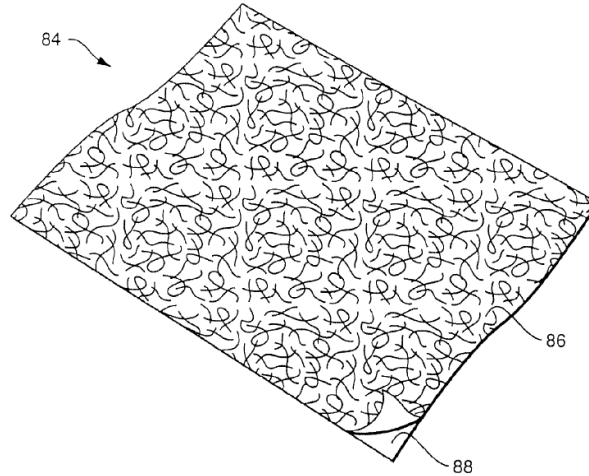


Figure 38: Illustration of a wet-laid carbon fiber / pulp blend sheet.⁸⁹

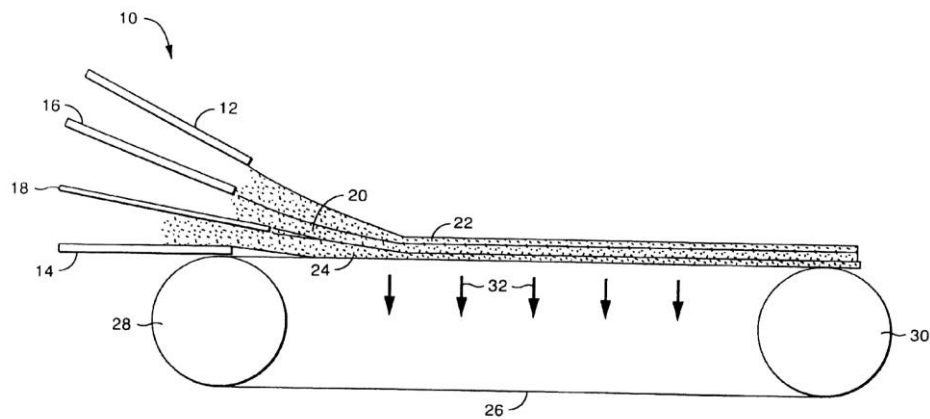


Figure 39: Feeding layers of different types of fiber onto a wet-lay belt.⁸⁹

The second pre-carbonization approach, needlepunching, can be used to bond together individual layers of fiber sheet materials which have been previously carbonized. These carbon fiber layers are typically bonded to form dense, thick (> 1000 gsm) carbon fiber nonwovens for use in high-friction / high-temperature applications such as aerospace brake discs. Due to the brittle nature of carbon fiber, special attention has been given to ensuring that the bonded layers are not excessively damaged as a consequence of the needling.⁹⁰⁻⁹² It has been determined that two different types of carbon fiber sheet must be sandwiched together in the layered structure – one to provide strength in the X-Y direction and one to provide fibers in the Z direction (Figure 40).

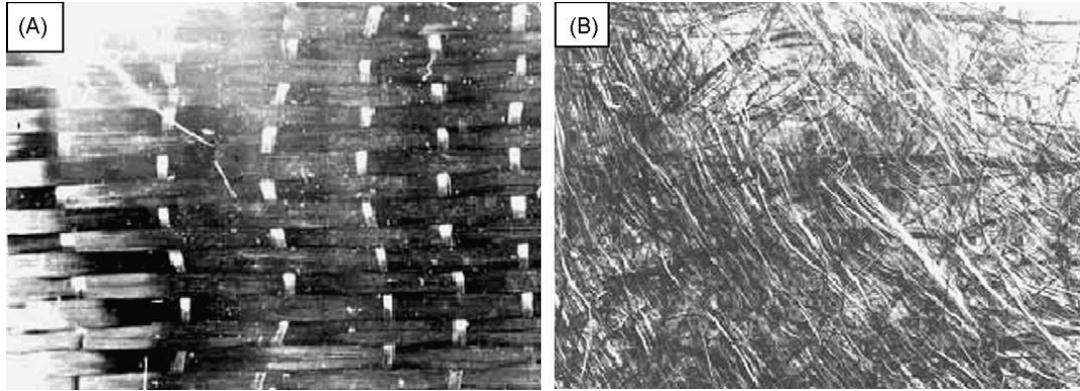


Figure 40: Layers used in some needle-punched carbon fiber sheets: (a) High modulus unidirectional continuous carbon fiber held in place by disposable weft yarn. (b) Wet-laid staple carbon fiber sheet.⁹¹

Needling carbon fiber has been found to cause heavy wear for standard needles, as barbs and tips wear down quickly due to high friction. To address this problem, Groz-Beckert has released two specialty needle types which are designed for high abrasive materials (Figure 41). The Gebedur I type has a titanium nitride coating, while the Gebedur II type is subjected to proprietary metallurgical treatment.⁹³ In addition to carbon fiber, these needles may also be used for needling glass fibers, ceramic fibers, and other high wear materials.

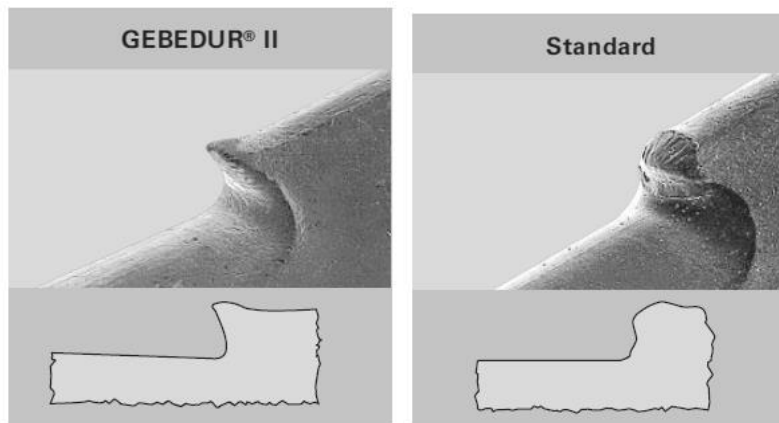


Figure 41: Groz-Beckert high performance Gebedur II needles compared to standard needles after heavy use with high strength fibers.⁹³

Turning to the post-carbonization approach, the variety of nonwoven processing methods used is much wider. Any method that can process PAN, oxidized PAN, pitch, or cellulose can be used prior to pyrolysis of the web. Pierson and Northrop studied the performance of different precursor fibers in post-carbonized needlepunched web.⁹⁴ This research was published at a time when rayon was still in wide use as a precursor material. Since axial tension can't be applied to fibers after they have been formed into felt, the authors found that rayon felt resulted in a very weak product. Oxidized PAN, however, is in a stabilized form which overcomes the need for tension during carbonization. One advantage of working with PAN fibers rather than pre-carbonized fibers is that PAN fibers are easier to mold, cut, and bond (Figure 42). After the final product shape is formed, the entire PAN preform can be carbonized.

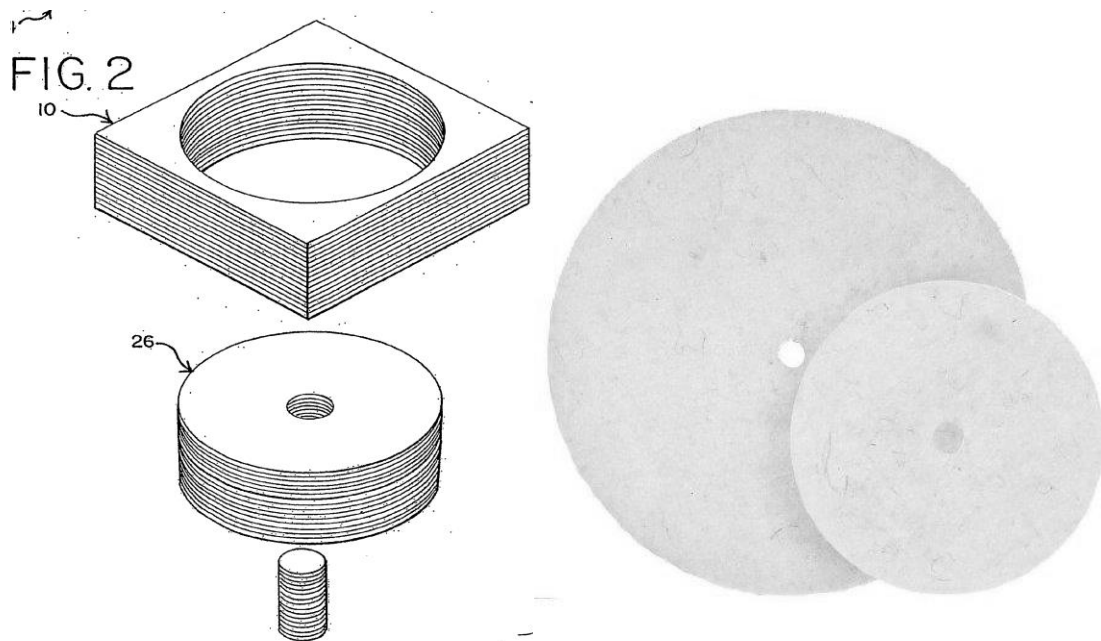


Figure 42: Method for making PAN-ox preform from PAN-ox felt, and example of PAN preform.⁹⁵

Recently, a patent filed by Schafer et al. of Freudenberg Nonwovens described the use of hydroentangling to bond carded PAN-ox staple fibers.⁹⁶ The patent claims that pre-forming

the fabric prior to carbonizing results in a flexible web which is easily rolled up for transportation. The Freudenberg patent also recommends including water soluble fibers that dissolve at two different temperatures. One type will dissolve in the hydroentangling step, leaving behind hollow channels in the path of the jet. Another will dissolve at a higher temperature, during a subsequent calendaring step. Again, the main advantage is that the result is highly flexible. The rigidity is reported to be below 8 taber. Figure 43 shows a Freudenberg hydroentangling / carbonizing line. While this method is promising, it is a relatively new development. Apart from the Freudenberg patent, no other literature on the subject could be found.

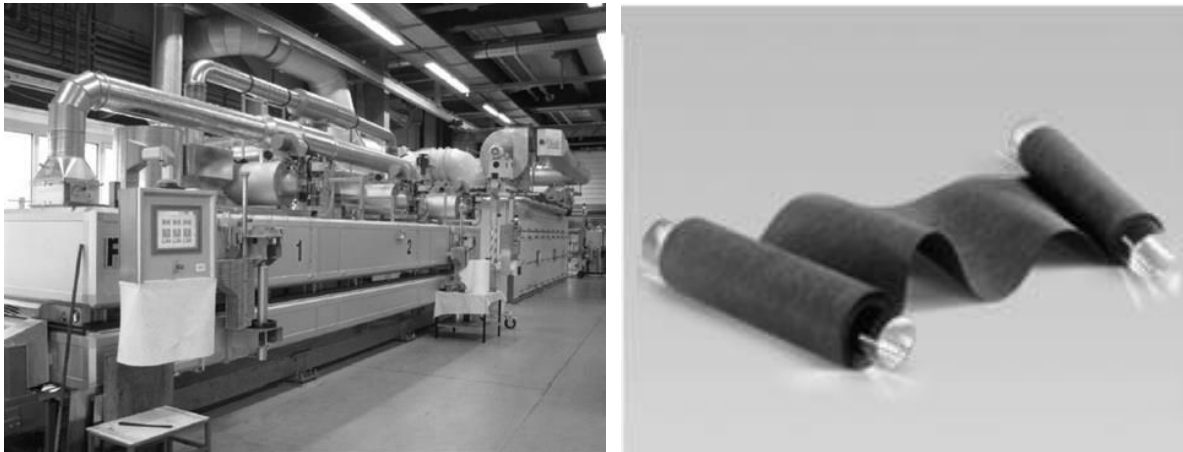


Figure 43: (a) Freudenberg continuous hydroentangling / carbonization line introduced in 2011. (b) An example of the highly flexible result.⁴⁵

Two processes have been used to successfully create pitch-derived carbon fiber nonwovens: centrifugal spinning and meltblowing.^{97,98} Centrifugal spinning is based on candy floss production, and is often used to obtain sub-micron scale fibers. However, since it is a melt spinning method, it has also been adapted for use with pitch. The pitch flows in from a heated feeder, then into a rotor enveloped by a thermocouple. From there, it spins out to the cone walls and is brought down to the conveyor belt by vacuum. Matthews et al. found that screening of the pitch when flowing through the feeder helped prevent it from clogging the

rotor.⁹⁷ The authors attached a lip onto the rotor which promoted extensional flow into fiber form.

Meltblowing can be used to make pitch nonwovens at a faster production rate (Figure 44). As in centrifugal spinning, the fiber diameter ends up being very low ($\sim 10 \mu\text{m}$). The resulting nonwoven is remarkable for its uniformity. However, during the carbonization step, the pitch typically shrinks from 5 – 50%. So, although the web has great uniformity following the meltblowing, the parts which are weaker tend to shrink more than the other parts, and this magnifies the slight inhomogeneities into larger disruptions in the uniformity. Nishimura et al. introduced the idea of cross-lapping meltblown sheets in order to avoid the problems caused by shrinking.⁹⁸ Rather than shrinking at the weak points, the web shrinks between the cross-lapped layers. Thus, the overall uniformity is not affected. This method has been used to create high basis weight materials up to 1000 gsm by cross-lapping thin meltblown webs.

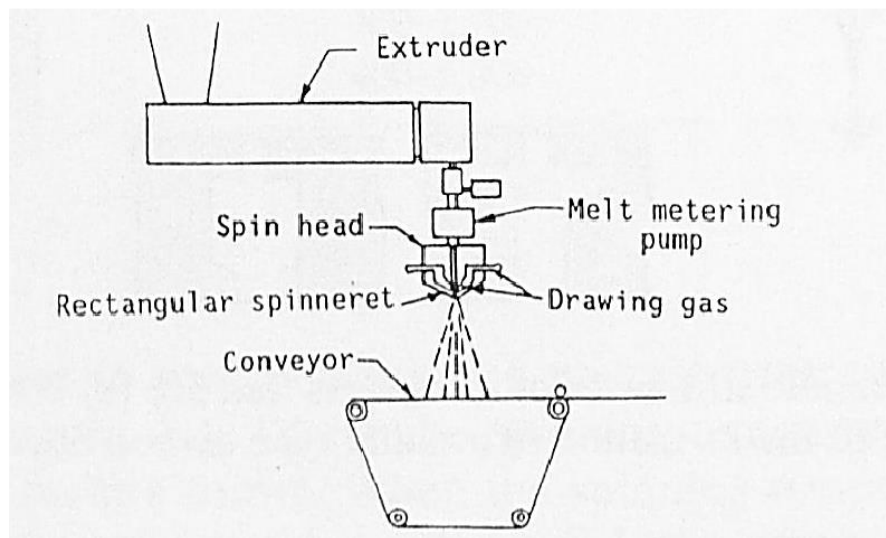


Figure 44: Meltblowing unit for mesophase pitch nonwoven.⁹⁸

Electrospinning and solution blowing are two popular lab-scale methods for spinning sub-micron scale fibers (Figure 45).⁹⁹ In electrospinning, a voltage drop is applied between a polymer solution-filled syringe and a metal collector plate. Solution blowing works on a similar scale, but uses a compressed air jet to attenuate the fiber stream rather than an electric

current. PAN may be used as the constituent polymer, and the resulting nanofiber PAN mat may be placed in a furnace for conversion to carbon fiber. The disadvantage of these methods is that they are limited in production scale, so the cost per unit area is relatively high. We may see electrospinning be adapted for high throughput production in the future, but for now, the applications are mostly limited to small scale electronic devices. On the other hand, the small scale brings some advantages. Many research labs are equipped with small furnaces and can easily carbonize electrospun mats. The small furnaces allow researchers to quickly change test parameters like polymer type, doping agents, heat treatment temperature, and activation method.¹⁰⁰ Electrospun mats have been studied extensively in the past few years, whereas with roll-to-roll processing methods, the furnaces are large, so studies require much time and energy costs to change any parameters.

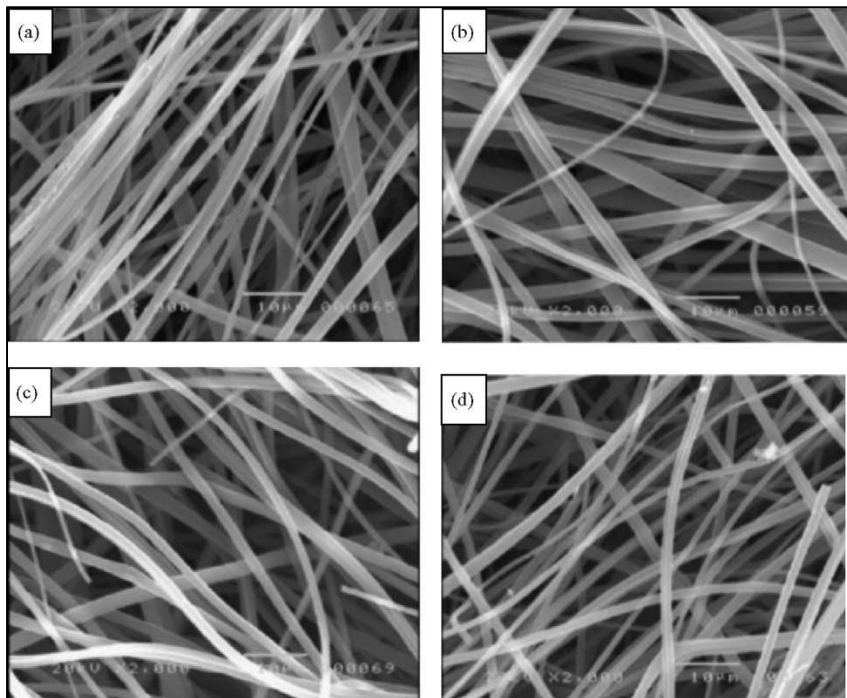


Figure 45: Electrospun PAN mat treated at increasingly intense carbonization temperatures, showing very little morphological change.¹⁰⁰

2.3.2 Activation

As mentioned previously, activated carbons (ACs) are among the highest known SSA materials, thus exhibiting uniquely high EDLC values. They may be derived from carbonized

natural or manmade precursors, and are subjected to a further step which causes closed nanoscale ducts to open up.¹⁰¹ These ducts are essentially the spaces between domains of highly ordered carbon. Prior to activation, the ducts may be filled with tenacious materials (amorphous carbon or hydrocarbons), or they may be hollow but obstructed. The activation process volatilizes these obstructions and ideally opens up the majority of such clogged ducts, converting them to pores and creating a predominantly microporous (< 2 nm diameter) material with remarkably high SSA (up to 3000 m² g⁻¹).⁶³ This process is achieved through the use of thermal elevation (> 300°C) in combination with gaseous (H₂O steam, CO₂, air, Cl₂ gas) or solid oxidizing chemicals (H₃PO₄, KOH, ZnCl₂).^{63,101} Examples of activation reactions are:



Applications for granular AC materials were first developed by the US Army's Chemical Warfare Services during World War I, who were exploring its use as a toxin adsorbent.¹⁰² The first mention of fibrous AC material (Figure 46) was of an activated carbon viscose rayon nonwoven in a 1964 patent filed by Union Carbide.^{103,104}

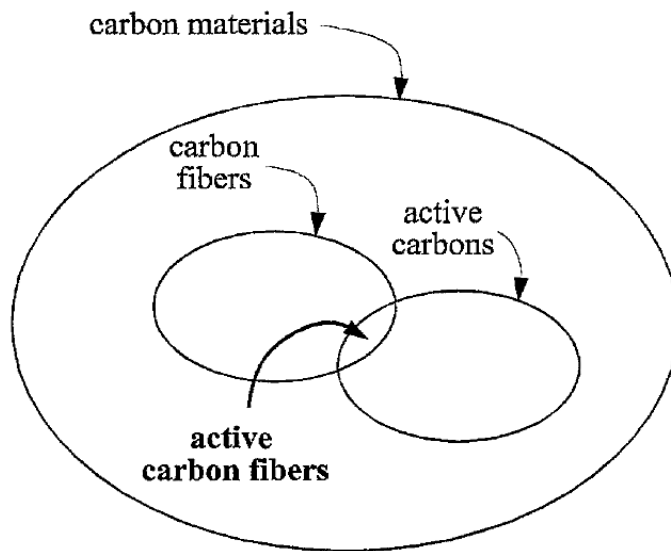


Figure 46: The small overlap between carbon fibers and active carbons represents a minority of all manufactured carbon materials.¹⁰⁵

Like granular AC, AC fiber (ACF) is well-suited for applications that require adsorption of small molecules, such as air purification, removal of impurities from oils, decolorizing and dye removal, and toxic gas filtration, to name a few.^{88,106,107} Matsuo et al. showed the excellent performance of corrugated nonwoven ACF derived from cellulose in a rotating absorption unit.¹⁰⁸ Unlike AC granules, the pore structure of AC fibers consists of straight, individuated channels (Figure 47), thought to result in faster adsorption kinetics as compared to the tortuous pores found in granules.^{108–110} For instance, the adsorption rate of methylene blue from solution was recorded to be ~100 times faster with ACF than with granular AC.¹⁰⁵

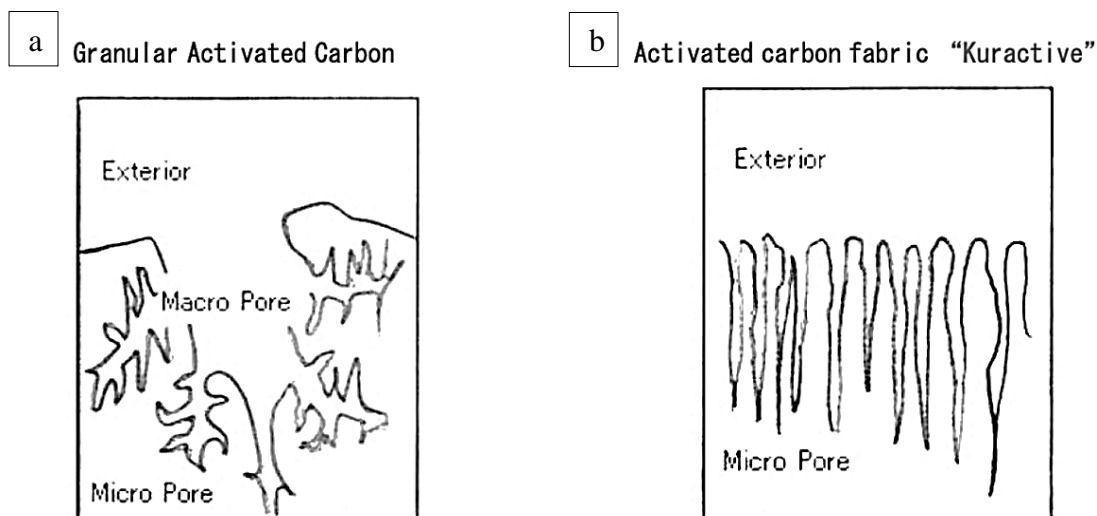


Figure 47: (a) Schematic of branches pores in granular AC. (b) Straight pores in AC fiber.¹¹⁰

Electric double layer capacitor (EDLC) electrodes are another application for which ACF may be suitable. Currently, the majority of supercapacitors are based on granular AC EDLC electrodes, typically formed with the aid of a polymeric binder (i.e. PTFE). However, the superior kinetics associated with ACF may result in improved power performance. Pore size and shape are closer to ideal. De Levie (1965) defined the “penetration depth” (λ) as a

function of pore radius (r_o), electrolyte resistance (ρ), angular frequency (ω) and double layer capacitance (κ)⁴⁹:

$$\lambda = \sqrt{\frac{r_o}{\omega\kappa\rho}} \quad (29)$$

This transmission line model is based on geometrically cylindrical, non-networked pores which are similar to the actual pore structure of ACF fibers (Figure 48)

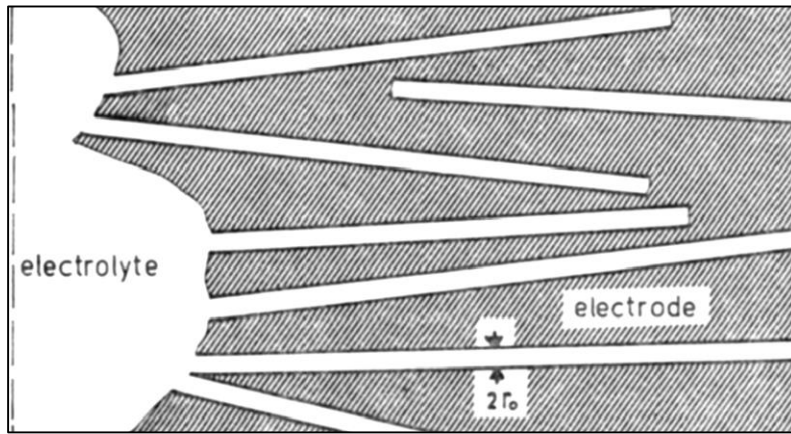


Figure 48: de Levie's transmission line model for porous electrodes was based on geometrically cylindrical, non-networked pores.⁴⁹

Nogami et al. (1982) were first to recognize the high double layer capacitance of ACF electrodes, and this work was followed by extensive research from Panasonic Corp. (Yoshida, Tanahashi and Nishino, IEEE Transactions 1987 – 1990).^{104,111–114} Extent of activation, controlled by activation times up to 60 minutes, was found to be directly correlated with specific capacitance.¹¹² The same group also examined the role of carbon fiber precursor. It was concluded that phenolic-resin was preferable for a number of reasons: it remained most flexible, retained the fewest surface acidic groups, and could reach the lowest resistance (Table 4).

Table 4: Comparison of properties and application scope for various ACF precursor.¹¹³

	Phenol	Rayon	Acryl	Pitch	Coconut granule charcoal
Surface area (m ² /g)	1500-2000	1400	900	700	800
Tensile strengths (Kg/mm ²)	50-70	5-10	200-250	60	—
Tensile modulus of elasticity (Kg/mm ²)	2000-3000	1000-2000	2000-3000	3000-3500	—
Specific electric resistance ($\times 10^{-5}\Omega\text{-cm}$)	1000-3000	2000-3000	800-1000	2000-3000	—
<u>Electrode types</u>					
Felt type,	Possible	Possible	Possible	Possible	Impossible
mat type					
Cloth type (plane, twilled)	Possible	Impossible	Impossible	Impossible	Impossible
Paper type	Possible	Possible	Impossible	Impossible	Possible
Principal properties of carbon fibers as polarizable electrode	Strong and flexible, most suitable as electrode	Hard and relatively fragile	Hard and relatively fragile, but in better than coconut granule charcoal	Hard and relatively fragile, but in better than coconut granule charcoal	To make a thin type electrode a collector is necessary and hence, capacitance performance is very small

Using phenolic-resin based ACF electrodes, specific capacitance of up to 113 F g⁻¹ was measured. Further research into aluminum-infused ACF electrodes, made of loose carbon fibers bonded with cellulose, was carried out by Maxwell Energy Products, Inc.^{115,116} Energy density of up to 8 Wh kg⁻¹ and power density above 500 W kg⁻¹ were reached.

Despite this promising performance, ACF is considered by some to be too costly as compared to granular AC.⁶³ On the other hand, ACF electrodes are known to be easier to handle, since they are compiled in a self-supporting sheet structure.^{34,105} Fibrous structures additionally promote better carbon-carbon contact, thus lowering internal resistance.¹¹⁵ The lack of polymer binder is also seen as a means to reduce electrode costs.¹¹⁷ A recent study by researchers at Donghua University examined the role of carbonization temperature in EDLC performance of PAN-derived ACF fabrics measured specific capacitance of over 200 F g⁻¹ despite a modest SSA of around 800 m² g⁻¹.¹¹⁸ The variety of methods available for activating carbonized nonwovens remains a rich area to explore. In terms of cost, nonwoven ACF is typically cheaper than woven ACF, which offers an advantage here.¹⁰⁹

2.4 CONDUCTIVE CARBON-COATED NONWOVENS

2.4.1 Carbon Nanotube Coatings

The potential application of carbon nanotubes (CNT) in supercapacitors was first suggested in 2002 by Baughman et al.¹¹⁹ The authors cite relevant physical properties - high SSA and porosity – coupled with potentially excellent ($4 \times 10^9 \text{ A cm}^{-2}$) electrical conductivity. The nanoscale structures are composed of rolled graphene sheets, and may be either single-walled (SWCNT) or multi-walled (MWCNT). The electrical properties are determined by the pattern of aromatic rings around the circumference (Figure 49). Three possible conformations – armchair, zigzag and chiral – are known.¹¹⁹ While zigzag and chiral CNTs are semiconductors, armchair CNTs are metallic. According to Baughman et al. (2002), “electron transport in metallic MWNTs and SWNTs occurs ballistically, over long nanotube lengths, enabling them to carry high currents with almost no heating.”

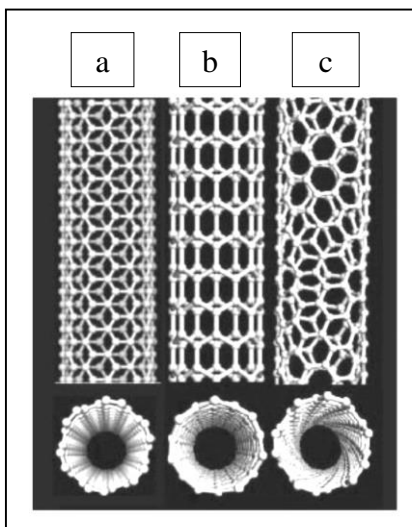


Figure 49: model of three main CNT forms: (a) armchair, (b) zigzag and (c) chiral.¹¹⁹

Buckysheets, or freestanding networks of pure CNT, were the first form of CNT double layer electrode material.¹²⁰ Capacitance values of between 15 and 200 F g^{-1} have been theorized, depending on how much of the nanotube array can be accessed by ions via electrolyte.

Recent attention has shifted to wrapping CNT networks onto high SSA scaffolds, such as foams and textiles, to promote electrolyte flow throughout a 3D architecture.¹²¹ Hecht et al.

first reported the binder-less coating of CNTs onto textiles.⁷² Since then, other methods for applying conductive carbon coatings to fabrics have included spraying, brushing, dipping, Mayer rod, and screenprinting.^{120–124} The characteristics of CNT coatings are influenced by the chemical and physical interactions between CNT and host substrate, but a consensus regarding the fundamental mechanism of fiber-CNT interaction has yet to emerge from the literature.

Hu et al. were the first to publish an extensive study on the use of CNT coated textiles for supercapacitor electrodes (Figure 50).¹²⁵ Two types of fabric were used, but details regarding these fabrics are largely left out of the report. One is described as ‘cotton sheet’ while the other as a ‘woven polyester fabric’. However, in the accompanying SEM images, a knit fabric is shown as the polyester fabric. Additionally, supplier information for the cotton fabric is provided, yet the supplier describes this product as a polyester nonwoven (Cloud 9 Dream Fleece).¹²⁶ Later publications from the same group contain similar ambiguities, which cloud the relationship between textile properties and the CNT coating.^{127,128}

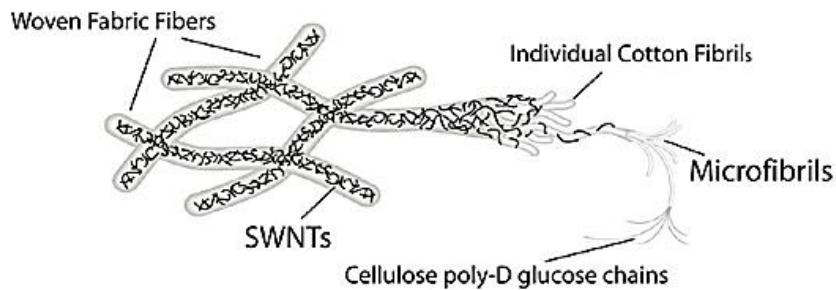


Figure 50: Schematic representation of CNT “skin” wrapped around cotton yarns.¹²⁹

CNTs exhibit attractive electrical properties, but also have properties that make them difficult to use in coatings. Their hydrophobic nature leads to bundling, or agglomeration, which causes them to drop out of aqueous solution unless modified.⁷² Zhang et al. functionalized SWCNTs using acid dye molecules which bonded easily to the CNTs through pi-pi stacking of the aromatic rings.¹³⁰ The CNTs dispersed well in solution, but the researchers anticipated

that the negatively charged hydroxyl and carboxyl groups on cellulose cotton would not favor bonding with the negatively charged CNTs. Thus, modifications were also applied to the cotton yarn prior to immersion (Figure 51).

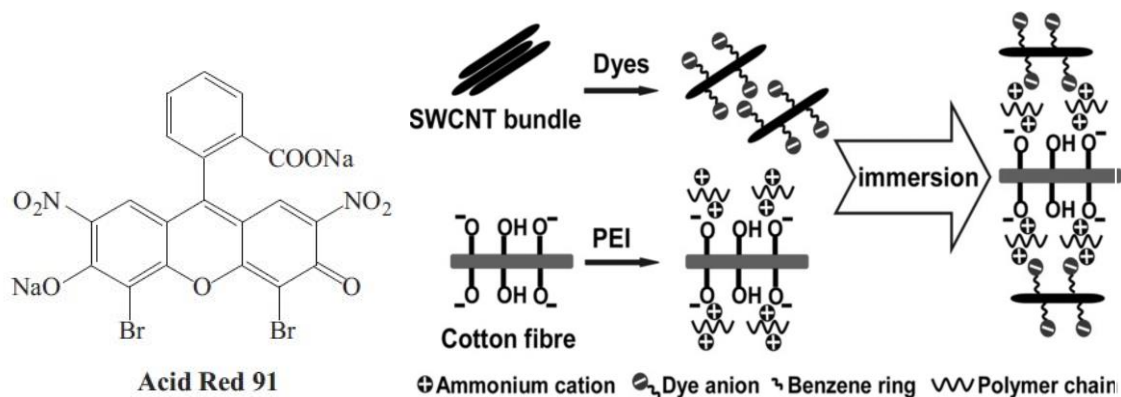


Figure 51: Anionic acid red dye molecule used to disperse CNTs for use in illustrated coating process.¹³⁰

In the original publication by Hecht et al., all processes employ suspensions ($0.2 - 0.5 \text{ mg mL}^{-1}$) in water stabilized by sodium dodecylbenzenesulfonate (SDBS) surfactant.⁷² The suspensions were reported to be stable for months, and the method that produced the most conductive coatings was incubating. These two findings formed the approach to CNT-coating which is most commonly used today. In a 2010 publication by the same group, a washing step was introduced to remove the surfactant molecules from the final coating.¹²⁵ Washing resulted in increased electrical conductivity, removing insulating surfactant particles that were impeding the flow of electrons between CNTs. The incubation process was replaced with a “simple dipping” process which was repeated a number of times to increase the CNT coating mass.

Wang et al. followed the same “simple dipping” procedure (Figure 52), using a surfactant-dispersed aqueous CNT solution, but found that a more thorough washing step was required between cycles.¹³¹ Three separate washes were needed to reduce resistance to an acceptable level. Furthermore, although resistivity continued to fall over the course of ten cycles,

specific capacitance based on the mass of CNTs began to decrease after five cycles (60 F g^{-1}).

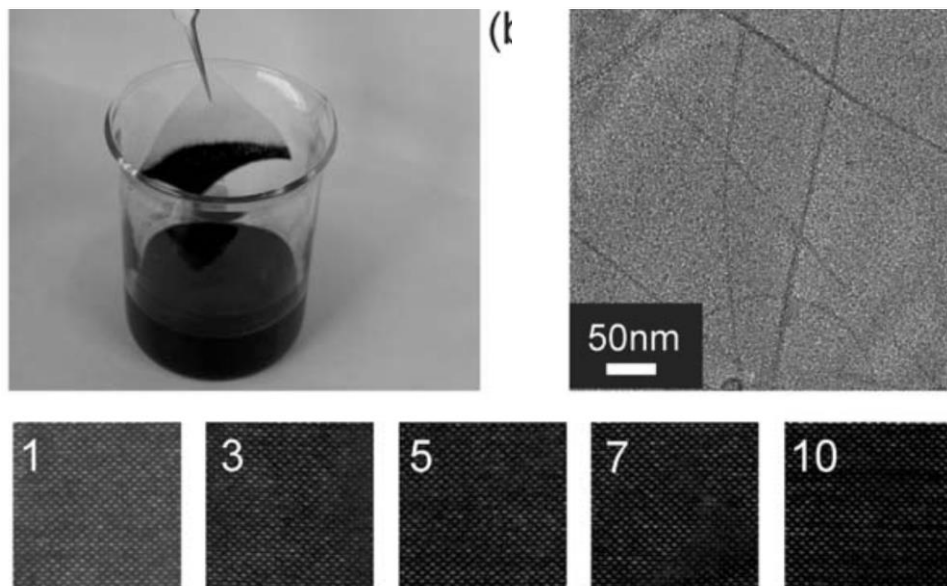


Figure 52: Photographic images of dipping procedure and cloth surface taken through multiple cycles.¹³¹

The dipping method has been adopted by many research groups because of its simplicity. However, these studies overlook the complexity of the interaction between fiber (its glass transition temperature T_g , for instance) and CNT dispersion. Panhuis et al. introduced the analogy of “textile dyeing” for the first time, thus suggesting the possibility of drawing on a more mature science for insight.¹³² Goncalves et al. also explored the possibility of treating CNTs exactly as dyestuffs (Figure 53).¹³³ The authors immersed cotton and polyester textiles in three types of CNT-water solutions and measured the “incorporation efficiency” by a standard whiteness test. A common exhaustion dyeing method was used, and various auxiliary additives, based on traditional dyeing of polyester and cotton, were introduced during the process.

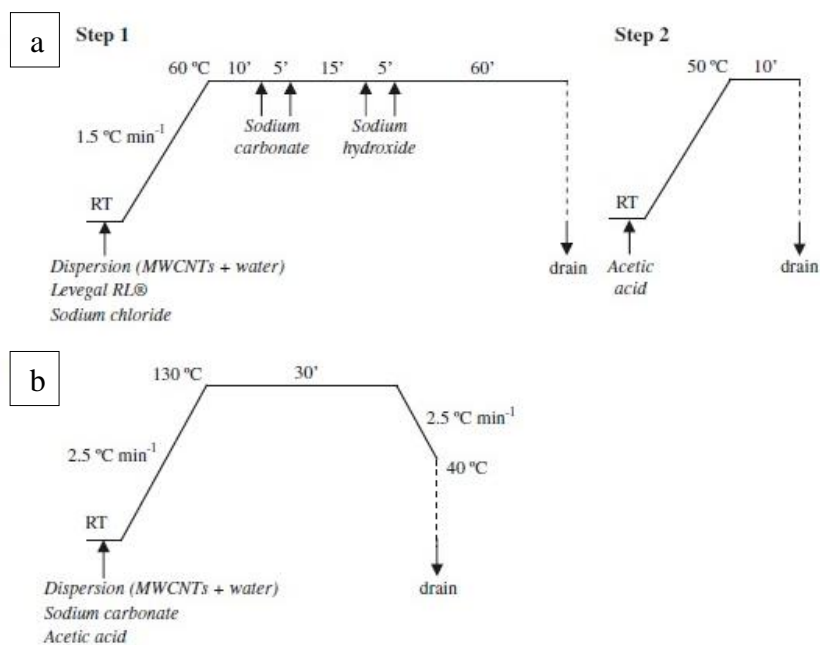


Figure 53: Diagram showing exhaustion dyeing conditions used for (a) cotton fabric and (b) polyester fabric.¹³³

For CNT-coated polyester, the authors observed that the CNTs seemed to be “growing from the fiber surface”, suggesting that they may be partially entrapped in the fiber surface. In this study, polyester had been taken above its T_g during the immersion process (to 130°C). It is postulated in this study that polyester partially absorbed the nanotubes into the free volume near the surface, whereas they are merely adsorbed or hydrogen bonded to the cotton surface. However, this is the first suggestion of *absorption* of nanotubes in the literature and requires deeper investigation. Throughout the literature, CNT dispersions of various formulas have been reported to be applied to cotton, polyester, rayon, nylon, and wool of various fabric structures – all with reasonable success.^{130–132} Low uptake has never been reported as a problem, and neither has adhesion, despite the variety of dispersants and substrate polymers. However, the studies from different groups use vastly different conditions and often obscure details about the textiles.¹²⁷ The literature is lacking a thorough, coordinated study into the behavior of CNTs on various types of polymer fiber surfaces.

2.4.2 Graphene Coatings

The unique electronic properties of single-layer aromatic sheets (Figure 54) were first understood in the mid-20th century by Wallace; consequently, the discovery of simple method for isolating highly ordered pyrolytic graphene (HOPG) by Geim and Novoselov in 2004 sparked enormous interest (a “gold rush”) within the scientific community.¹³⁴

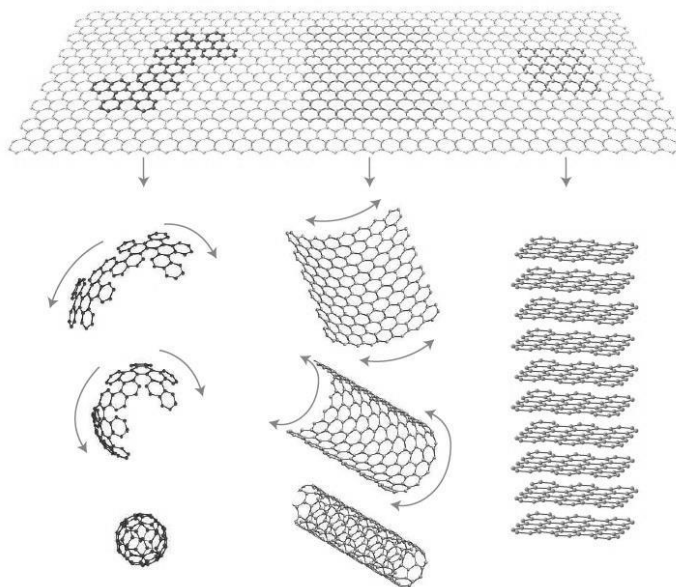


Figure 54: Graphene – the “mother” of carbon nanomaterials, such as fullerenes, carbon nanotubes, and graphene sheets.¹³⁴

Due to its high thermal conductivity ($5300 \text{ W m}^{-1} \text{ K}^{-1}$) and high carrier mobility ($200,000 \text{ cm}^2 \text{ V}^{-1} \text{ s}^{-1}$) at room temperature, applications in electronics, optics, and performance materials are being sought.¹³⁵ Graphene has been widely explored as a potential supercapacitor electrode material.^{124,128,136–141} Citing the high specific surface area of monolayer graphene sheets ($>2500 \text{ m}^2 \text{ g}^{-1}$) and its high conductivity, Stoller et al. formed EDLC electrodes from graphene and 3% (by weight) PTFE binder.¹³⁶ Specific capacitance of $85 - 135 \text{ F g}^{-1}$ was measured. Ye et al. prepared graphene electrodes by incorporating acetylene black (10% by weight) and PTFE (10% by weight), and spreading the mixture homogeneously onto nickel foam, and specific capacitance of 315 F g^{-1} was measured.¹³⁵

Two approaches to obtaining colloidal suspensions of individual graphene layers have been intensively explored during the last decade: exfoliation of graphite and reduction of graphene oxide. Exfoliation of graphite by mechanical processes is a simple approach based on two steps: extensive high-power shearing of graphite flakes in a chosen solvent, using sonication or high-shear mixing, followed by removal of the non-exfoliated sheets by centrifugal separation (Figure 55).¹⁴²

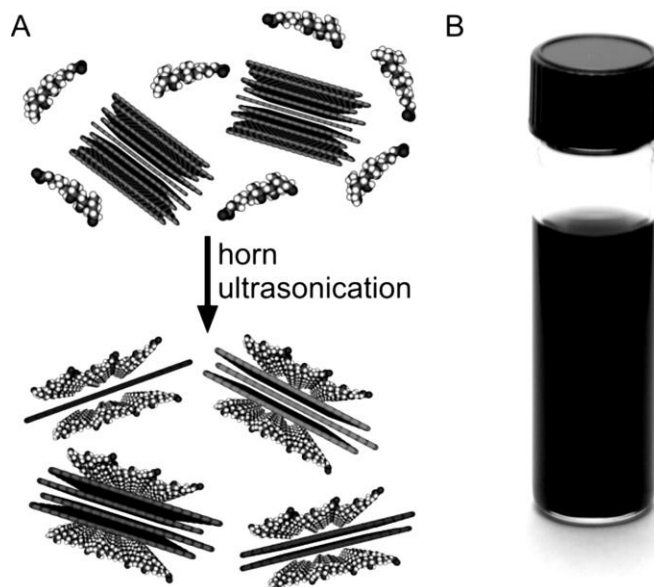


Figure 55: (A) Schematic illustration of the sonicator-enabled graphite flake exfoliation process. Graphite flakes are combined with sodium cholate (SC) in aqueous solution and encapsulated by SC micelles. (B) Photograph of $90 \mu\text{g mL}^{-1}$ graphene dispersion in SC 6 weeks after it was prepared.¹⁴²

Wang et al. (2014) attempted to increase concentration by matching solution surface energy to graphite surface energy via inclusion of alcohol.^{143,144} Other researchers have incorporated various surfactants to improve the shelf life of suspended hydrophilic nanoparticles in aqueous solutions by preventing reagglomeration.¹⁴⁵ Three major drawbacks which remain to be overcome are the low rate of exfoliation, which necessitates long hours of high-energy mixing, the damage incurred by nanoplatelets due to the mechanical force, which reduces the diameter of nanoplatelets, and the downstream need to remove surfactant from the solids.^{144,146} Researchers continue to investigate questions such as the most effective solvent

type, the effects of using various surfactants, and the impacts of processing parameters, like time and centrifugation frequency.¹⁴⁶

The most common alternative approach to graphite exfoliation involves the use of graphene oxide (GO) nanosheets.^{147,148} Chemically produced from graphite by one of three methods – Brodie, Hummers, or Staudenmeier – GO is hydrophilic and can easily be dispersed in water.¹⁴⁹ According to the Lerf-Klinowski model, GO sheets are thought to contain many covalently bonded epoxide and hydroxyl groups at sp^3 bonded sites along the basal plane, as well as a smaller amount of carboxyl and carbonyl groups at the edges (Lerf et al., 1997).¹⁵⁰ This model is supported by the TEM investigations of Erickson, et al (Figure 56).¹⁵¹

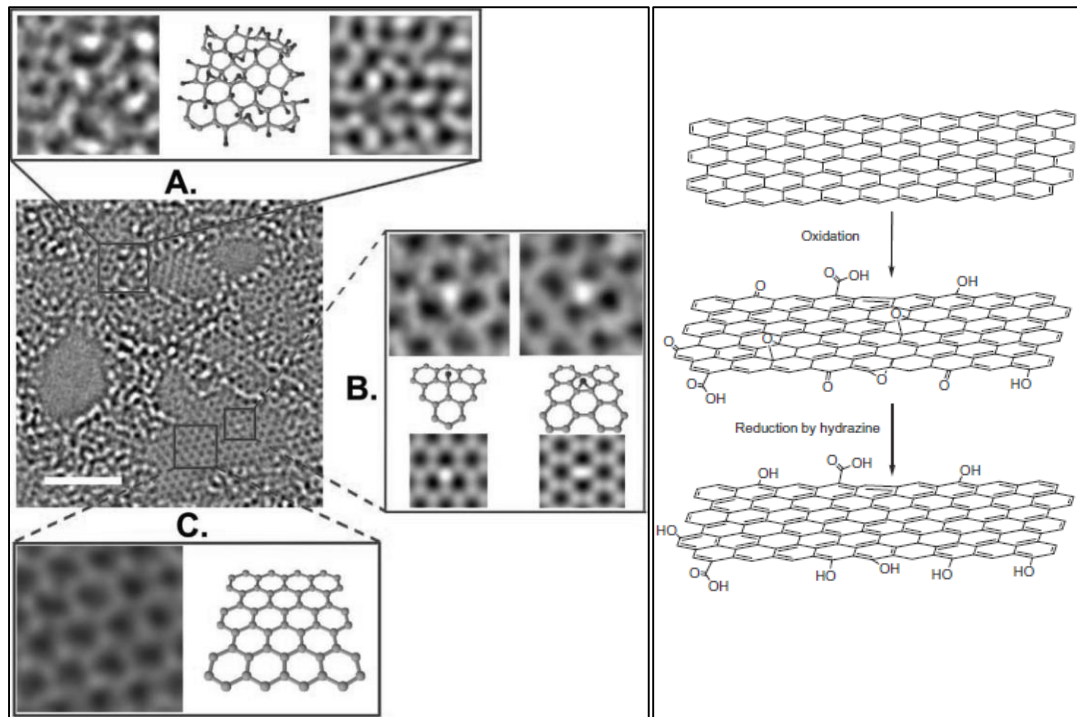


Figure 56: Left: TEM image of graphene oxide monolayer (center). (A) Amorphous area with many defects. (B) Highlighted oxygen functionality in an ordered region, forming hydroxyl and epoxide groups. (C) Fully conjugated region showing pure graphene structure.¹⁵¹ Right: Sequence of transformation of graphene to graphene oxide, then to reduced graphene oxide by hydrazine hydrate.¹⁵²

The C:O ratio of GO has been measured to be about 2:1.¹⁵³ Various reducing agents have been reported to increase the C:O ratio to 7:1 via NaBH₄, 12:1 via hydrohalic acid; 12.5:1 via vitamin C; 30:1 via BnOH.^{147,153–155} Chemical reduction rebuilds sp² carbon sites, thereby increasing electrical conductivity.¹⁴⁹ The reduction process provides more unsaturated carbon bonds, and a corresponding color change from brown to black is observed due to the regain of conjugation. However, GO does not become fully repaired during the process. Conductivity has been measured to be orders of magnitude lower than that of pristine graphene.¹⁵²

Binder-free coating of graphene onto polymeric fibers has been demonstrated in recent years, both by EGF and RGO. While great efforts have been dedicated to fine-tuning the preparation of both EGF and RGO, each still has its disadvantages and it remains unclear as to which is preferable for use as a coating for fibrous polymer scaffolds.¹⁵² In addition to differences in production costs, the two approaches cause various resulting material properties. Of note for application in energy storage is the possibility of residual pseudocapacitance deriving from the persistent oxygen functionalities on RGO.

Fugetsu, et al. were first to report the binder-free coating of polymer fibers with graphene.¹⁵⁶ In this study, the RGO approach was taken. GO was obtained by a modified Hummers method before being dispersed in water (0.1 mg mL⁻¹) and used to “dye” woven fabric (polyarylate fibers) via a vat exhaustion method. The coated fabric was then placed in a bath containing the reducing agent sodium dithionite (Na₂S₂O₄, also called sodium hydrosulfite) in order to convert the GO to RGO, resulting in resistivity as low as 10² Ω cm⁻¹. Around the same time, Zhou et al. also reported use of sodium dithionite to reduce GO/PVA composite, citing the historic use of sodium dithionite to reduce vat dyes in the textile industry.⁴¹ The exact reaction mechanism is not clear, as it seems to change partially through the reaction. For further reading on the subject, the reader may consult relevant articles.^{157–165} Analysis of the relationship between reaction rate and reaction products by Rinker (1959) indicated that

the reaction proceeded according to the following mechanism, affirmed by voltammetry studies by Mayhew (1977):



Shateri-Khalilabad and Yazdanshenas coated woven cotton in GO through up to 20 dip cycles (Figure 57) and compared reduction by NaOH, NaBH₄, N₂H₄, C₆H₈O₆ and Na₂S₂O₄.¹⁶⁶ The lowest resistance was measured following the reduction by Na₂S₂O₄, confirming its effectiveness at obtaining RGO coated fabrics. Despite these advances in RGO-coated fibers, supercapacitor electrodes from such materials have yet to be fabricated and / or tested.

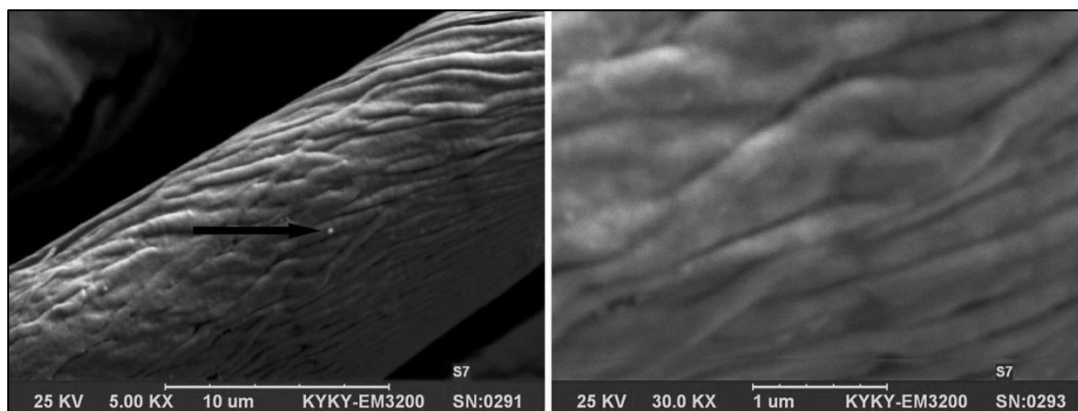


Figure 57: (Left): GO coated cotton fibers prior to reduction. (Right): Closer view of same.¹⁶⁶

EGF dispersions have also been used to coat fabrics. Yu et al. prepared EFG solution, which was then coated onto PET nonwoven over the course of 35 dip-dry cycles.^{138,145} A periodic HNO₃ soaking step was introduced to assist in surfactant removal. The samples were tested as electrodeposition scaffolds for MnO₂, proving able to support the growth of pseudocapacitive nanoparticles (Figure 58). The measured specific capacitance was reported to be 315 F g⁻¹, based on a low scan rate of 2 mV s⁻¹.

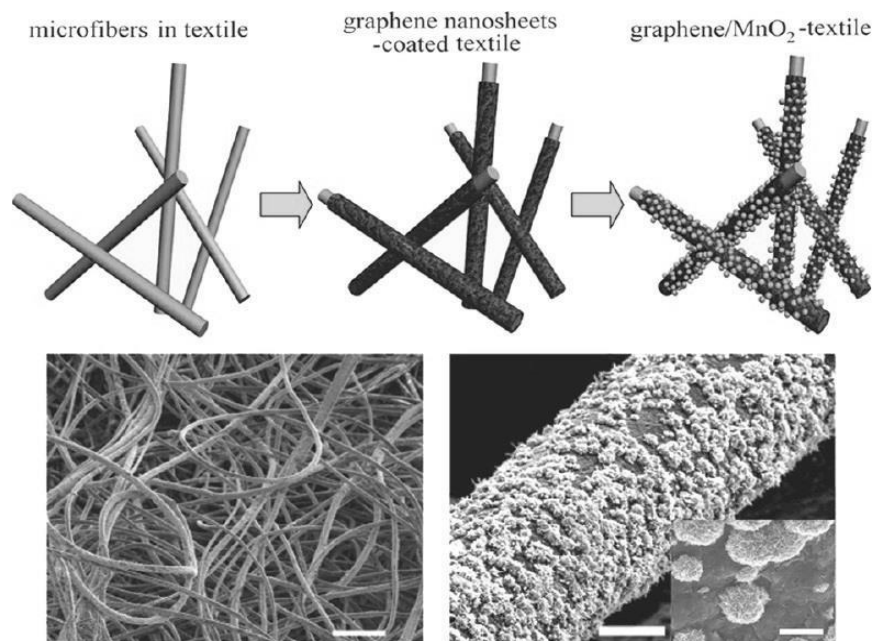


Figure 58: Top: Illustration of polyester fibers coated with EGF, then deposited with MnO₂. Bottom: SEM of MnO₂ and graphene coated fibers, at various scales.

2.5 SUMMARY AND OBJECTIVES

The starting point for this research was to develop CNT-coated nonwovens as wearable, flexible supercapacitors. By reviewing the literature, the need to understand the role of fabric structure has become clear. Nonwovens can be engineered to have a wide variety of structural and surface properties. To date, there has not been a comprehensive study aimed at optimizing nonwovens for use as nanoparticle coating substrates. Several widely cited reports contain unclear descriptions of fabric type and polymer type, further clouding the subject.^{125,127,128,167} In addition, process challenges, such as incomplete surfactant removal, are hampering the industrial adoption of CNT dispersions. After preliminary experiments, the focus broadened to encompass various types of conductive nonwovens, including carbon fiber nonwovens and graphene-coated nonwovens.

Nonwoven supercapacitor electrodes can be established via two routes: carbon fiber nonwovens and conformal nanoparticle coatings (Figure 59). The first broad goal of this

research is thus to evaluate commercially available carbon fiber nonwovens for use as EDLC and PC supercapacitor electrodes and understand how they may be improved. The second broad goal is related to conformal nanoparticle coatings. Although this approach has been explored, the literature is lacking an in-depth understanding of the role of the substrate.

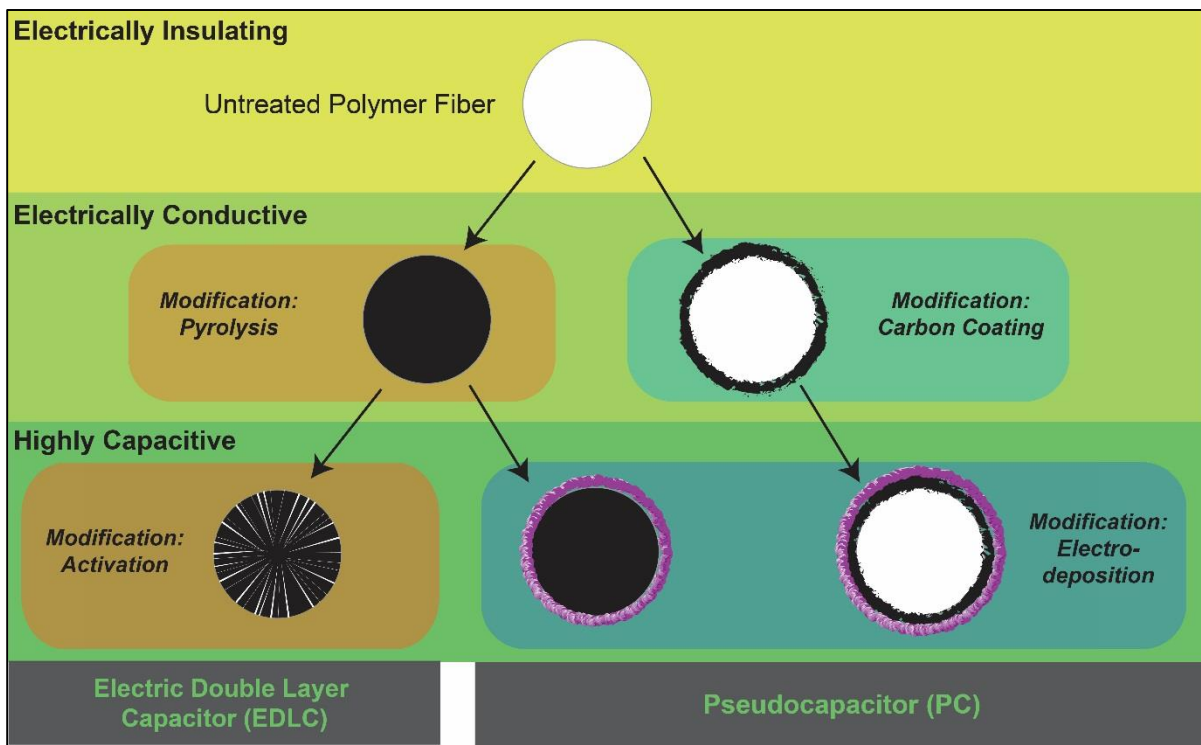


Figure 59: Steps needed to form fiber-based supercapacitor electrodes, and possible methods.

2.5.1 Research Objectives

Listed below are four research objectives intended to support these aims.

- **Objective 1: Carbon Fiber Nonwoven for EDLC**

The diversity of carbon fiber nonwovens available on the market is remarkable. Due to demands from various applications - electromagnetic shielding, high temperature thermal insulation, anti-static and anti-corrosion layers in composites, adsorbent materials and fuel cell components, to name a few - examples can be found with different precursors, packing densities, basis weights, consolidation methods, fiber

diameters, etc. In order to determine which materials are best suited for EDLC electrodes, a selection of commercial samples was collected. These varied in terms of basis weight (FibreGlast Carbon Veil was the lowest at 6.8 g m^{-2}). Different web production methods were also compared. The FibreGlast material is created from wet-laid staple carbon fibers bonded with a polymer resin, while Freudenberg H2315 is made of consolidated (hydroentangled) PAN fibers and carbonized as a web. Results of activation studies are presented in Chapter 3.

- **Objective 2: Pseudocapacitance from Carbon Fiber Nonwoven**

In addition to studying the potential application of commercially available nonwovens as double-layer capacitor electrodes, they were examined as scaffolds in PC electrodes. While the three-dimensional, porous nature of nonwovens is well suited for producing high surface area, high energy density electrodes, the relationship between their structural properties and their suitability as scaffolds for deposited materials is not well defined. Transition metal oxides (RuO_2 , IrO_2 , V_2O_5 , MnO_2 , Fe_3O_4 , etc.) and intrinsically conductive polymers (polyaniline, polythiophene, polypyrrole, polyacetylene, etc.) are two classes of materials which are used to create PC electrodes. They undergo multiple, kinetically fast faradaic reactions and are easily deposited onto electrode surfaces. Polyaniline (PANI) has been widely studied in the literature, and can be coated onto fibers through electrodeposition. Here, settings were optimized to maximize PC electrode performance, and the impact of structural characteristics of nonwoven scaffolds were determined. Results are presented in Chapter 4.

- **Objective 3: Evaluate the Role of Process Parameters in CNT Coatings**

In order to select a binder-free nanoparticle coating method, an understanding of the role of coating parameters must be developed. Aqueous dispersions of these functionalized CNT have been widely reported, but the poor dispersibility of the nanoparticles requires inclusion of surfactant. This leads to reduced conductivity in

the coated material, since a portion of surfactant remains embedded in the dried coating and physically interrupts contact between adjacent carbon nanoparticles. Critical variables that have been identified from the literature include nanoparticle type, solvent type, additives, dispersion method, and coating method. Alternative solvents which do not require surfactant were explored here, and dispersion methods and coating methods were also evaluated. In order to support the aim of optimizing nanoparticle coatings for supercapacitor electrodes, an array of nonwovens were engineered and coated. In order to study the effect of polymer type, nonwovens with comparable structural properties were fabricated from cellulose (cotton), polypropylene (PP), polyamide 6 (PA6) and polyethylene terephthalate (PET) fibers. The relationship between fabric properties and coating performance was determined by measuring mass gain, conductivity, double layer capacitance, and coating morphology. Chapter 5 discusses the results from these CNT studies.

- **Objective 4: Evaluate the Role of Process Parameters in Graphene Coatings**

Although CNT and graphene have both been explored as conductive coating material, the two have not been directly compared. Here, nanoparticle type was evaluated by optimizing and studying graphene coatings. Graphene is unstable in common solvents, so two precursor materials – dry graphite flakes and water-dispersed graphene-oxide nanoparticles – were purchased from Graphene Supermarket (Calverton, NY). Dry graphite flakes were dispersed in water according to the sonication method reported in the literature. The second approach, water-dispersed graphene oxide, required a post-processing treatment to reduce the graphene oxide. Reduction was carried out by sodium dithionite, and the effects of reduction conditions were evaluated. In order to understand the role of fiber geometry and web solidity in coating formation, various bicomponent fibers were compared. Electrodeposition of PANI was conducted to determine the performance of these substrates as PC electrodes, compared to similar CNT coated substrates. Chapters 6 and 7 present the results of this research objective.

CHAPTER 3: Carbon Fiber Nonwovens as Double Layer Capacitor Precursor

This chapter is a manuscript entitled “Activation of Carbon Fiber Nonwovens” by J. Leary, B. Maze and B. Pourdeyhimi which has been submitted for peer review to the Journal of Engineered Fibers and Fabrics.

3.1 INTRODUCTION

Electric double-layer capacitance (EDLC), named for the formation of the inner and outer Helmholtz planes (IHP and OHP), is an electrostatic charge separation which automatically arises at the electrode-electrolyte interface in an electrochemical cell.⁹ The resulting charge yields a low specific capacitance on the basis of electrode surface area (5 to 20 F cm⁻²).¹⁶⁸ When typical, planar electrodes are used, the EDLC effect is basically negligible. The key to exploiting the EDLC, found in the 1950's, was to employ extremely high specific surface-area (SSA) electrodes. One of the very first EDLC-based energy storage devices employed electrodes made from porous fired tar lampblack sticks.¹⁹ According to patent records, high-SSA activated carbon (initially termed "absorbent charcoal") was in use as early as the mid-19th century as a carrier for liquid nitro-compounds in explosive devices.¹⁶⁹ Other applications for micropore-ridden activated carbon grew to include the transportation of gasses or other volatile substances in the chemical industry, decolorizing and refining of oils, sugars and other substances, protective face masks and clothing in the defense industry, and consumer products such as filters for air and water.^{101,106 107 170,171} EDLC energy storage devices, called supercapacitors, began to use activated carbon in the mid-20th century, and granular activated carbon (GAC) is still the most commonly used active material in electrodes.

By using GAC in conjunction with conductive carbon black, polymer binder, and a current collector, gravimetric specific capacitance of 100 – 200 F g⁻¹ on the basis of activated carbon mass can be expected.⁶³ The carbon black serves the purpose of lowering electrical resistance while the current collector, usually a metal foil, efficiently transports electrons between electrodes and the external circuit. Polymer binder, usually PTFE serves the purpose of adhering electrode paste to foil. However, the presence of binder introduces several issues. It interrupts particle-particle contact, thereby increasing electrical resistance. Binder can also clog intergranular volumes, blocking the entrances to micropores, and it can reduce overall gravimetric specific capacitance by adding mass to the electrode without adding activity.²¹

Activated carbon fiber (ACF) cloth has been explored as a self-supporting electrode material which does not require a separate current collector.¹¹⁶ Inter-fiber cohesion holds the electrode together without any need for binder. ACF can be produced from isotropic pitch, phenolic resin, polyacrylonitrile (PAN) or cellulose fibers.^{108,109,172,173} The general production process is similar to that used in GAC, where a carbon-containing precursor is carbonized in a furnace under an oxygen-free atmosphere, then activated in an oxygen-containing atmosphere (typically CO₂ or a mix of steam and air). The resulting pore structure in GAC is networked and hierarchical, whereas in ACF, the pore structure consists of individual, slit-shaped pores.^{110,170,171} Adsorption kinetics studies have shown that ACF is more efficient as a result of this pore structure, since adsorbates can access micropores directly without needing to navigate through a network of pores with ever-decreasing diameters.^{171,174} Despite the potential for ACF to be used without binder and metal foil, as well as to improve electrode kinetics, one significant drawback is the lower bulk density of ACF cloth compared to GAC paste.¹⁷⁵

In a paste electrode, GAC particles are packed tightly with binder and carbon black, but in a cloth electrode the spaces between the ACF yarns represent underutilized volume. One report showed that although SSA was higher for ACF, GAC paste had a higher volume specific capacitance (18 F cm⁻³) compared to woven ACF (9 F cm⁻³).^{114,175} Here, it is important to consider the range of textile structures that ACF cloth could assume. Plainweave, constructed by regularly alternating yarns (bundles of staple fibers) is one of the oldest and most common textile structures. Spectracarb is a familiar example of plainwoven ACF cloth used in EDLC electrodes. The web solidity, or solid volume fraction (α), is the percentage of web volume occupied by solid fiber. It is calculated as:

$$\alpha = \frac{\rho_{web}}{\rho_{fiber}} = \frac{W}{L * \rho_{fiber}} \quad (32)$$

Where ρ_{web} is the density of the web, W is the basis weight of the web, ρ_{fiber} is the density of the polymer, and L is the web thickness. According to the Spectracarb specifications, solidity is only around 15%, meaning that 85% of the fabric volume consists of unoccupied space.¹⁷⁶

Nonwoven textile structures are made by compiling individual fibers into mat-like sheets, without first bundling the fibers into yarns. This type of fabric structure includes felt, one of the oldest textiles known to man, as well as high-tech textiles used today in filtration and composites.⁵³ Compared to the woven carbon fiber fabric cited above, nonwoven gas diffusion layer (GDL) material was measured in this lab to have solidity of 25% and higher. As a result of their higher bulk density, this study focuses on carbon fiber nonwovens for use as ACF electrodes. Carbon fiber nonwovens can vary widely in their basic properties, depending on the application they are designed for, which ranges from anti-static sheets to high temperature furnace insulation.⁷⁹ Most carbon fiber nonwovens use polymeric resin adhesive to compile carbonized fibers, while few are mechanically compiled. This study focuses on the activation of a binder-free carbon fiber nonwoven GDL, since any adhesive resin would be vaporized during the activation process, leaving behind disassembled fibers. Mass loss, electrical resistance, x-ray diffraction (XRD) studies, x-ray photoelectron spectroscopy (XPS) studies and nitrogen adsorption studies are employed to understand the various responses to the activation process. The challenges to activation are identified and examined by comparing the GDL material to carbon fiber nonwovens prepared under controlled thermal conditions in the lab.

3.2 EXPERIMENTAL

3.2.1 Materials

Carbon fiber GDL material with a thickness of 0.2 mm and basis weight of 95 g m⁻² was obtained from Freudenberg Fuel Cell Technologies (Germany). According to the manufacturer, the GDL material is formed by first air-laying long PAN fibers, calendaring them to obtain uniform thickness, hydroentangling to improve fabric strength, and finally

carbonizing at a high temperature. Carbon fiber nonwovens were also prepared in the lab. The precursor fibers were made from continuous PAN filament (2 denier) obtained from Oak Ridge National Laboratories (Oak Ridge, TN).

3.2.2 Methods

GDL material was activated in an OTF-1200X-UL quartz tube furnace from MTI Corp. (Richmond, CA) under bone-dry CO₂. Although a steam-containing mixture can be used for activation, CO₂ has been shown to produce a narrower pore size distribution.¹⁷⁷ For the carbon fiber nonwovens prepared in house, PAN filament was first cut to a staple fiber length of 2 inches, crimped, and coated with an anti-static finish in the Staple Fiber Laboratory in the Nonwovens Institute (Raleigh, NC). A model carding machine from Davis & Furber Machine Co. (Andover, MA) was used to form 200 g m⁻² sheets, which were then permanently bonded with a mini needlepunch loom from Dilo, Inc. (Eberbach, Germany). PAN fiber nonwovens were stabilized under air, carbonized under argon and activated under bone-dry CO₂ in the quartz tube furnace. All gas was supplied by Airgas, Inc. (Radnor, PA).

3.2.3 Characterization

Sample mass was measured using a MS Semi-Microbalance from Mettler Toledo (Columbus, OH). Surface area and pore size distribution were studied using an automated gas sorption analyzer (AutoSorb iQ from Quantachrome Instruments, Boynton Beach, FL). Samples weighting 0.1 – 0.2 g were cut and loaded into 12 mm sample holders, degassed using the built-in degas ports, and LN₂ was used for the physisorption process. Results were analyzed using AsiQWin software. XPS and XRD studies of powdered samples (prepared by glass mortar and pestle) were carried out at the Analytical Instrumentation Facility (Raleigh, NC) using a PHOIBOS 150 analyzer and Rigaku Smartlab, respectively. Electrical resistance in the x-y fabric direction is termed in-plane resistance (IPR), while electrical resistivity in the z-direction is termed through-plane resistivity (TPR). IPR was found by measuring the current while applying a 1V potential using a VMP3 potentiostat/galvanostat from Bio-Logic USA, Inc. (Knoxville, TN). TPR was found by measuring potential while applying an alternating current of 1 mA from one face of the fabric to the other via copper electrodes,

using an in-house setup with a 2182A Nanovoltmeter and 6220 DC Precision Current Source from Keithley Instruments, Inc. (Cleveland, OH).

3.3 RESULTS AND DISCUSSION

3.3.1 Activation of Carbon Fiber Nonwovens

The initial precursor for activated carbon fiber nonwovens was a binder-free commercially available carbon fiber nonwoven designed for use as a GDL for polymer electrolyte membrane fuel cells (PEMFCs). Here, the GDL material was subjected to activation treatments at three different temperatures: 500°C, 700°C and 900°C. The activation gas used was CO₂, which is a common atmosphere used to remove carbon through the following reaction:



This reaction targets the more volatile amorphous carbon sheets which are located between ordered carbon regions. With the removal of these sheets, narrow crevices between neighboring ordered domains are opened up, thus forming the well-known micropore structure.

Following the activation procedure, the three samples were examined by gas adsorption. Nitrogen adsorption isotherms are commonly used to reveal the ultra-high SSA afforded by the prevalent micropores. The resulting isotherms, shown in Figure 60, differed from the Type I isotherms that would be expected from a high-SSA material. As defined by Brunauer et al., Type I isotherms show a sharp rise in specific volume at lower relative pressures due to extensive microporosity.¹⁷⁸ Instead, these materials exhibit Type III isotherms, which are characteristic of poor interaction between a material and an adsorbate due to the virtual absence of microporosity.

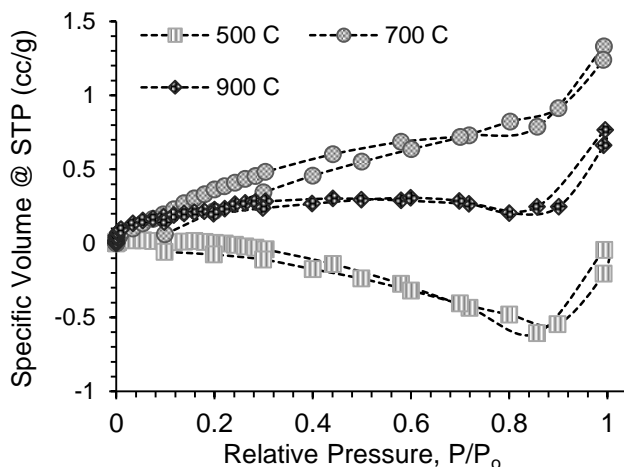


Figure 60: Nitrogen adsorption isotherms of carbon fiber nonwovens following activation treatment at three different activation temperatures.

Specific surface area (SSA) was estimated from the adsorption isotherm by the Branauer-Emmett-Teller (BET) model as well as by density functional theory (DFT). According to estimates by Chappas and Pourdeyhimi, round fibers such as those used in this material with a diameter in the range of 10 – 20 μm should have an initial SSA in the range of 0.1 – 1 $\text{m}^2 \text{g}^{-1}$ prior to activation.⁵⁷ The 500°C treatment resulted in SSA of 0.165 $\text{m}^2 \text{g}^{-1}$, 700°C yielded 1.337 $\text{m}^2 \text{g}^{-1}$, and 900°C only resulted in 1.298 $\text{m}^2 \text{g}^{-1}$, showing no appreciable improvement in SSA following the activation treatments (Table 5).

Table 5: BET and DFT estimates of specific surface area for GDL materials activated under the conditions shown below.

Starting Material	Activation Temperature	Activation Gas	Dwell Time	SSA	
				Estimated by BET Method	Estimated by DFT Method
Carbonized GDL Material	500°C	CO ₂	30 min	0.165 $\text{m}^2 \text{g}^{-1}$	0.079 $\text{m}^2 \text{g}^{-1}$
	700°C		30 min	1.337 $\text{m}^2 \text{g}^{-1}$	0.466 $\text{m}^2 \text{g}^{-1}$
	900°C		60 min	1.298 $\text{m}^2 \text{g}^{-1}$	0.590 $\text{m}^2 \text{g}^{-1}$

Resistance to activation could be attributed to the processing conditions (time, temperature, activation gas). However, previous studies by other groups have demonstrated successful activation of carbonized PAN at temperatures ranging from 600°C to 1000°C.^{173,179} Dwell

times have ranged from 5 minutes to 60 minutes.^{180,181} For example, Yang et al. obtained an activated carbon fiber with SSA of $>190 \text{ m}^2 \text{ g}^{-1}$ by heating carbonized PAN fibers under CO_2 at 600°C for 40 minutes.¹⁷⁹

An alternative explanation for the activation failure could be the physical properties of the carbon fiber material used here. Since it is a proprietary material, specific details about the material and fabrication methods are unclear. Several studies have implied that PAN-derived carbon fiber can be too graphitic and resist activation if carbonized under certain conditions.^{180,182,183} Additionally, while carbon fiber derived from PAN have the potential to be activated under the conditions listed in Table 5, those derived from pitch require much longer dwell times.¹⁸⁴

In order to determine whether resistance to activation is due to the carbonization treatment or the carbon fiber precursor, nonwoven PAN samples were prepared in the lab, carbonized to various extents, and subjected to a fixed activation treatment. The results were analyzed and compared to the GDL material.

3.3.2 Carbonization of PAN Fiber Nonwovens

Continuous PAN fiber was cut and crimped to form staple fiber, then carded and needlepunched to form a nonwoven web. In a quartz tube oven, the webs were stabilized, carbonized and activated according to the program laid out in Table 6. All samples were stabilized under the same conditions, but three different carbonization temperatures were used. The groups of samples, designated Sample A, Sample B and Sample C, were carbonized at 695°C , 895°C and 1095°C , respectively. After carbonization at these different temperatures, all sample groups were activated under the same conditions. The treatments were designed to examine the impact of carbonizing PAN below, at or above the subsequent activation temperature.

Table 6: Carbonization and activation treatments for PAN fiber nonwovens.

Designation	Pre-cursor	Stabilization				Carbonization			
		Temp	Rate	Gas	Dwell Time	Temp	Rate	Gas	Dwell Time
Sample A	PAN	215°C + 250°C	2°C / min	Air	2 hr + 2 hr	695°C	5°C / min	Argon	30 min
Sample B						895°C			
Sample C						1095°C			

Following the carbonization step, XPS was used to probe the elemental composition at the sample surface. Figure 61 shows the survey scan results for the three carbonized PAN fabrics – Sample A, Sample B and Sample C – as well as the survey scan of the commercial GDL material. The similar shape of the curves is evidence of similar material composition among all samples. Xie and Sherwood carried out XPS studies comparing PAN-based carbon to pitch-based carbon.^{185,186} The presence of nitrogen and oxygen functionalities in the commercial sample confirms that it is in fact derived from PAN rather than pitch.

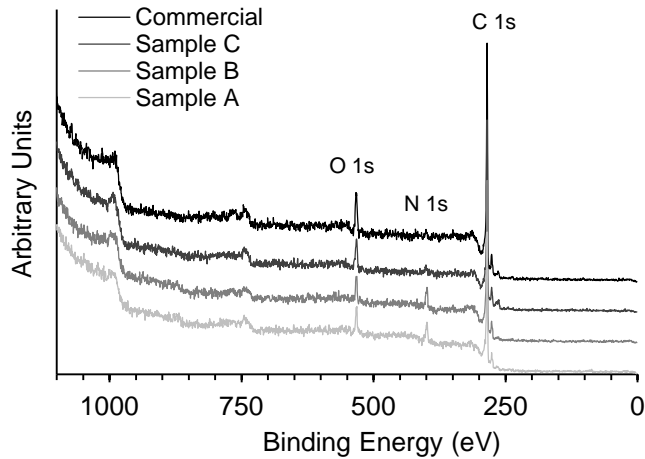


Figure 61: XPS survey scans for commercial GDL carbon fiber nonwoven and PAN fiber nonwovens carbonized in the lab at different temperatures.

The elemental composition was determined based on the survey scans, with results listed in Table 7. For the samples carbonized in the lab, the atomic concentration of carbon becomes higher as carbonization temperature increases. This is to be expected, since temperature increase drives the reactions that remove non-carbon elements from the fiber. The effect of temperature is also reflected in the mass loss, with Sample A showing the lowest mass loss

(28.2%) and Sample C showing the highest (54.7%). Increased mass loss at higher temperatures can be attributed to burn-off of nitrogen. Nitrogen concentration showed a dramatic decrease with temperature, especially between Sample B and Sample C. Compared to the samples carbonized in the lab, the commercial GDL material had a lower concentration of nitrogen than Sample C. This implies that it was likely carbonized at or above a temperature of 1095°C.

Table 7: Elemental composition and mass loss for carbon fiber nonwoven samples.

	Sample A	Sample B	Sample C	Commercial Material
	Carbonized at 695°C	Carbonized at 895°C	Carbonized at 1095°C	Carbonized
Atomic % C	80.8	83.6	87.6	87.6
Atomic % N	10.4	9.4	2.7	1.7
Atomic % O	8.8	7.1	9.7	10.8
N/C Ratio	0.129	0.112	0.031	0.019
O/C Ratio	0.109	0.084	0.111	0.123
Mass loss after carbonization	28.2%	34.2%	54.7%	Unknown

Nitrogen mass loss is often associated with the replacement of carbon-nitrogen bonds with carbon-carbon bonds. Taking a closer look at the nitrogen 1S peaks of the XPS scans, these peaks not only become smaller as the carbonization temperature increases (to the point of being negligible for the commercial GDL material) but the peak shape changes. The shape of the nitrogen peaks for Samples A – C are shown in Figure 62. While both P1 and P2 decline with temperature, the ratio of P1/P2 increases. P1, in the vicinity of 401 eV, is associated with sp^2 bonding such as N substituted in a graphite sheet. P2, in the vicinity of 399 eV, is associated with sp^3 bonding.¹⁸⁷ Perfect hexagonal graphite sheets contain sp^2 bonded carbon atoms, which confer many of the properties associated with carbon fiber applications (high strength, good electrical conductivity). The XPS results imply that as temperature increases, the prevalence of sp^2 bonded carbon increases as well.

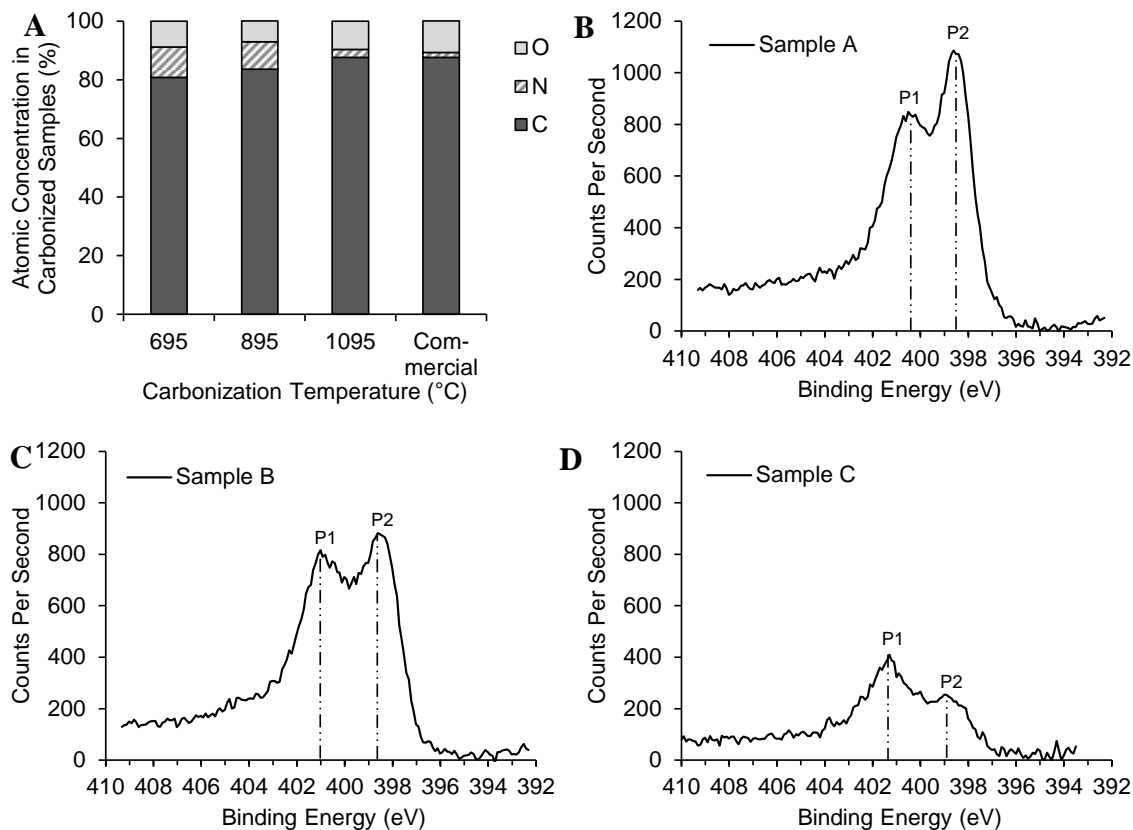


Figure 62: (a) Elemental composition of carbon fiber samples based on XPS survey scans. XPS scans focused on nitrogen peaks for samples carbonized at (b) 695°C, (c) 895°C, and (d) 1095°C.

The loss of nitrogen and the increase in sp^2 bonded carbon should be accompanied by an increase in electrical conductivity. Figure 63 shows the results of through-plane resistivity (TPR) and in-plane resistance (IPR) tests. The two tests – IPR and TPR - are carried out using instrumentation designed to show conductivity in the x-y direction and the z-direction, respectively. They show that resistance according to both measures drops as a function of carbonization temperature, confirming the formation of carbon-carbon bonds throughout the structure as carbonization temperature increases.¹⁸⁸

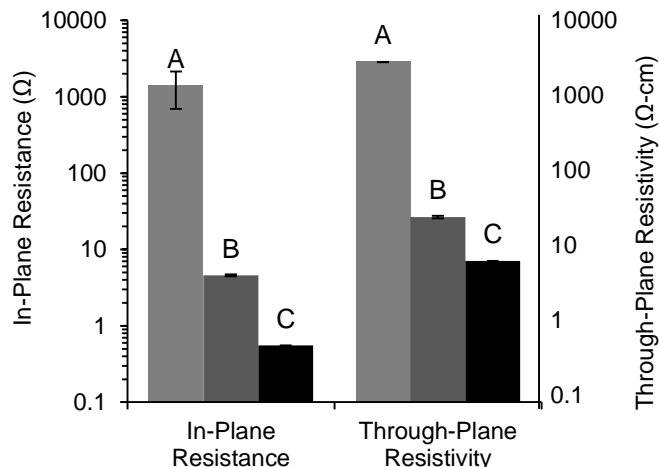


Figure 63: IPR and TPR for carbonized samples.

3.3.3 Structural Comparison of Carbonized PAN Fiber Nonwovens

X-ray diffraction was used to gain information about the packing structure of the carbon sheets in the sample fibers. Because the activation process proceeds by attacking amorphous carbon between tightly-packed regions, it should become more difficult as tightly-packed regions grow to occupy more of the fiber structure.¹⁷¹ Samples were ground into fine powder and the reflected signal as a function of 2θ scattering angle was recorded (Figure 64 a). Earlier studies have shown that peak height increases as carbonization temperature increases, and this was also observed here.¹⁸⁸ The peak locations were similar among all samples, corresponding to the well-known locations of graphite peaks: around 25° for the 002 peak and around 44° for the 100 peak. In a region of packed carbon sheets, the former corresponds to the cumulative sheet width (L_c) and the latter corresponds to the transverse sheet length (L_a) (Figure 64 b).¹⁸⁸ These dimensions are based on the widely-accepted model of microfibrils composed of carbon sheets, with needle-like voids between them.¹⁷⁴

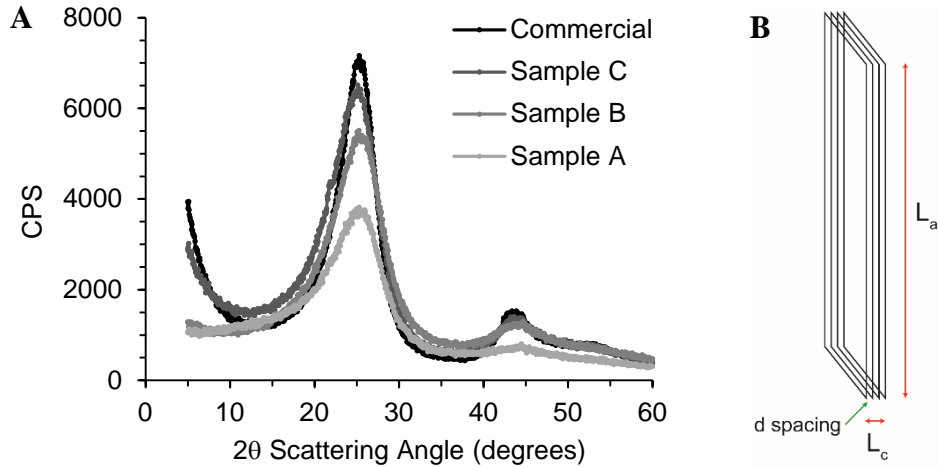


Figure 64: (a) XRD counts per second (CPS) as a function of scattering angle for carbon fiber nonwovens, and (b) illustration of crystal dimension locations.

Values for the interlayer spacing (d_{002}) can be approximated by using the Bragg equation (Eqn 34), where λ is the K-alpha wavelength for Cu radiation (1.54 Å).

$$d_{hkl} = \frac{\lambda}{2 \sin \theta} \quad (34)$$

Table 8 shows the interlayer spacing as calculated for Samples A – C and the commercial GDL material. Apparently, there is no clear temperature-dependent trend. However, all values fall between the spacing associated with high modulus and low-modulus PAN-derived carbon fiber, which are 0.340 nm and 0.355 nm, respectively.

Table 8: Interlayer spacing (d_{002}) and crystal dimensions (L_c and L_a) calculated from peak position and peak FWHM of XRD results.

Sample	Peak Position ₀₀₂ (2 Θ°)	d ₀₀₂ (nm)	FWHM ₀₀₂ (2 Θ°)	L _c Size ₀₀₂ (nm)	Peak Position ₁₀₀ (2 Θ°)	FWHM ₁₀₀ (2 Θ°)	L _a Size ₁₀₀ (nm)
Sample A	25.53	0.347	7.67	1.06	44.37	8.07	2.18
Sample B	25.43	0.350	7.28	1.12	43.91	5.92	2.96
Sample C	25.27	0.352	6.88	1.18	43.54	5.43	3.22
Commercial Sample	25.44	0.350	5.13	1.59	43.44	4.33	4.04

The “crystallite size” (sheet length and width) can be found using Scherrer’s formula (Eqn. 35), where B is the full width half maximum (FWHM) of the peak in $2^\circ\Theta$ and K is a correction factor of 0.9.

$$\text{crystallite size} = \frac{K\lambda}{B \cos \theta} \quad (35)$$

Results for L_a and L_c are shown in Figure 65. Crystal width (L_c) increases with carbonization temperature. Keeping in mind that width is composed of a number of graphite sheets, L_c can be divided by the thickness of the interlayer spacing (d_{002}) to approximate the average number of sheets in each crystallite region. This gives 4 for Sample A, 4.2 for Sample B, 4.4 for Sample C and 5.5 for the GDL material. Length (L_a) also increases steadily with carbonization temperature, demonstrating that graphite sheets grow as a function of heat. There is a big jump from Sample C to the commercial GDL sample. On the basis of the L_a and L_c values, the GDL shows better developed carbon structure as compared to all samples prepared in the lab. For the lab samples, carbon structure development is a function of temperature, so it is probable that the GDL material was carbonized at a higher temperature than all these.

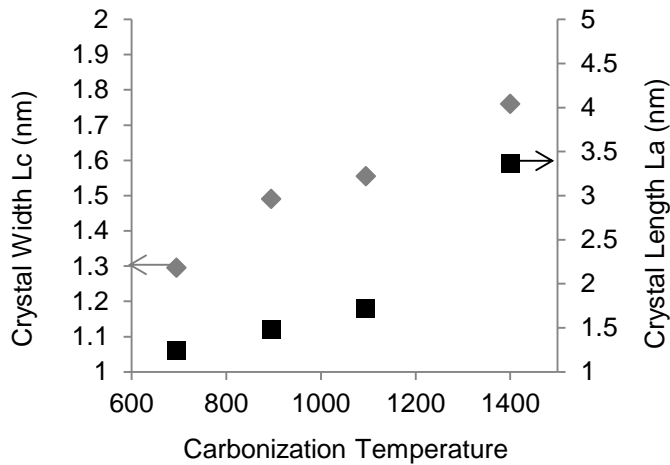


Figure 65: Crystal length (L_a) and width (L_c) for carbon fiber nonwovens carbonized at different temperatures, based on XRD measurements.

3.3.4 Activation of Carbonized PAN Fiber Nonwovens

Following the carbonization step, all sample groups were activated under CO₂ at 895°C, with the same ramp rate, gas and dwell time (Table 9). This activation process had failed to affect the GDL material, and the aim was to determine which of the controlled samples, if any, could successfully be activated.

Table 9: Activation treatment conditions for carbonized PAN nonwovens.

Precursor		Activation			
		Temp	Rate	Gas	Dwell Time
Sample A	PAN Carbonized at 695°C	895°C	10°C / min	CO ₂	60 min
Sample B	PAN Carbonized at 895°C				
Sample C	PAN Carbonized at 1095°C				

XPS was again carried out to investigate whether the activation step had caused any further changes to the elemental composition of the samples. The carbon, nitrogen and oxygen concentrations for Samples A and B had undergone similar changes (

Table 10). Both experienced an increase in the prevalence of carbon during activation, along with corresponding decreases in nitrogen and oxygen. The activation process also impacted mass loss. Mass loss increased from 28% to 54% for Sample A, and from 34% to 57% for Sample B. For Sample C, however, mass loss (around 55%) hardly changed. In general, Samples A – C showed striking differences in elemental composition and mass loss when they were carbonized, but the activation process minimized these differences and brought Samples A and B much closer to Sample C on these measures.

Table 10: Elemental composition and mass loss following activation for carbonized PAN nonwovens.

	Sample A	Sample B	Sample C
	Carbonized at 695°C	Carbonized at 895°C	Carbonized at 1095°C
	Activated at 895°C	Activated at 895°C	Activated at 895°C
Atomic % C	85.6	85.3	86.4
Atomic % N	8.0	8.6	5.3
Atomic % O	6.4	6.1	8.3
N/C Ratio	0.093	0.091	0.061
O/C Ratio	0.074	0.076	0.096
Mass loss after activation	54.0%	57.2%	55.3%

Electrical properties were also greatly levelled by the activation process. Sample A had shown the highest IPR and TPR following the carbonization process, since it had been treated at the lowest carbonization temperature (695°C). Following activation, IPR and TPR of Sample A matched those of Sample B, and both had dropped significantly during this step (Figure 66). As discussed earlier, the presence of nitrogen in carbon sheets indicates sp³ bonded carbons, which do not participate in electron flow. Therefore, the loss of nitrogen as indicated by the XPS results would be expected to cause a drop in electrical resistance. Sample C (carbonized at 1095°C) had the lowest IPR and TPR prior to activation and maintained the lowest resistance following activation. Nitrogen levels were also lowest in this sample both before and after activation.

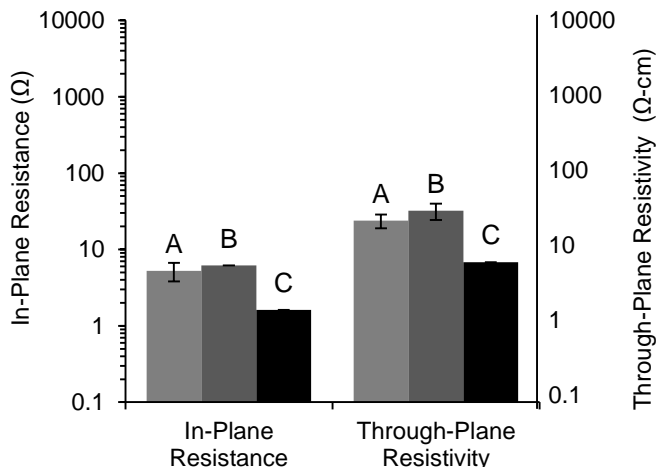


Figure 66: IPR and TPR for activated PAN nonwovens which had been carbonized at different temperatures.

3.3.5 Surface Area and Pore Structure of Carbonized PAN Fiber Nonwovens after Activation

All three sample groups showed similar mass loss, elemental composition and electrical properties following activation. However, Sample A and B were much more affected by the activation process on these measures. In order to determine which, if any, of the samples had been successfully activated, nitrogen adsorption was used to probe SSA. Prior to the activation process, the shape of the isotherm (Figure 67a) was a slightly concave line, similar to those of the GDL material samples shown earlier and typical of a Type III isotherm. Surface area for the non-activated sample was estimated by BET to be $6.1 \text{ m}^2 \text{ g}^{-1}$, and $2.5 \text{ m}^2 \text{ g}^{-1}$ by DFT. Figure 67b shows the isotherms for all activated samples. The isotherm shape was distinctly altered by activation for all samples. Among these, Sample A and Sample B exhibited Type I isotherms which result from a predominantly microporous structure.¹⁷⁸ SSA calculated by the BET method was $205 \text{ m}^2 \text{ g}^{-1}$ for Sample A and $192 \text{ m}^2 \text{ g}^{-1}$ for Sample B. Sample C, with a significantly lower specific volume adsorbed, exhibited a Type II isotherm, indicative of combined micro- and mesoporosity. The BET SSA for Sample C was only $11 \text{ m}^2 \text{ g}^{-1}$. This indicates that the extent of activation was much lower for Sample C than for Samples A and B. It has been observed that initial crystallinity of PAN affects final activated SSA. Higher initial MW leads to better developed carbon structure, and less well-developed

activated pore structure.¹⁷⁹ Here, a connection between crystallinity of the carbonized fibers, which were derived from the same PAN precursor, and the development of pore structure is shown.

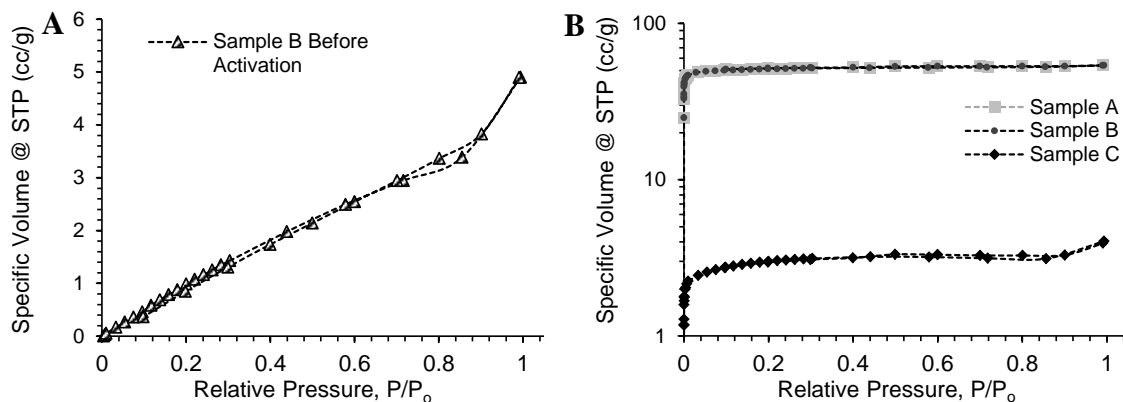


Figure 67: Nitrogen adsorption isotherms for PAN nonwoven samples (a) after carbonization, and (b) after activation.

Based on DFT calculations, a pore size curve can be obtained. Figure 68a shows pore size before activation, which indicates that the material can be classified as mesoporous (pore radius of 10Å - 250Å). Figure 68b shows pore size for all samples after activation. Micropores are defined as having pore radius below 10Å. It appears that the activation process has resulted in microporous materials for all samples.

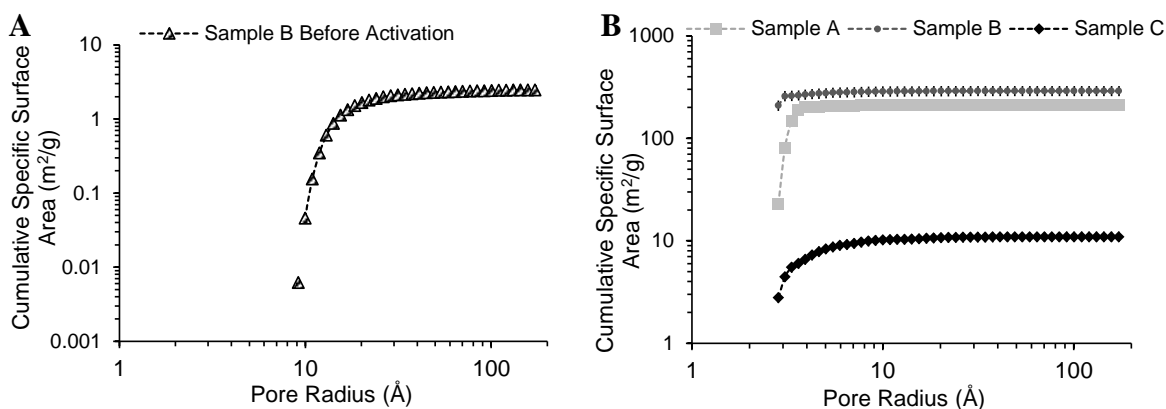


Figure 68: Pore size distribution for PAN nonwoven samples (a) after carbonization and (b) after activation.

Mode pore radius, listed in Table 11, is similar for all materials (around 3Å). However, the pore curve highlights the fact that Sample C has a significantly lower SSA as compared to Samples A and B, as was noted above. Although Sample C has been activated, it is to a very minor extent.

Table 11: BET and DFT specific surface area estimates, and DFT mode pore radius for activated PAN carbon fiber nonwovens.

Activation Precursor		SSA after Activation		Mode Pore Radius
		Estimated by BET Method	Estimated by DFT Method	Estimated by DFT Method
Sample A	Carbonized at 695°C	205.38 m ² g ⁻¹	224.58 m ² g ⁻¹	3.330 Å
Sample B	Carbonized at 895°C	192.36 m ² g ⁻¹	240.47 m ² g ⁻¹	2.840 Å
Sample C	Carbonized at 1095°C	10.88 m ² g ⁻¹	10.77 m ² g ⁻¹	2.835 Å

3.4 CONCLUSIONS

This study focused on the effect of carbonization temperature on subsequent activation. Initially, a commercially carbonized GDL material was used since industrially produced carbon fiber materials have superior uniformity compared to those produced in the lab. BET analysis showed that the material could not be activated by CO₂ under reasonable conditions (900°C for 60 min). XPS results showed that the GDL was derived from PAN. Virgin PAN fibers were then formed into nonwovens and carbonized at three different temperatures – 695°C, 895°C and 1095°C. The sample carbonized at the highest temperature (Sample C) showed the most highly developed graphitic sheet structure. After subjecting all samples to the same activation procedure (895°C for 60 min), BET analysis showed that Sample C was mostly resistant to activation. Both samples carbonized at or below the activation temperature, however, showed significant microporosity. In conclusion, it is clear that poor initial carbon sheet formation leads to a higher potential for subsequent activation. Carbon fiber nonwovens such as GDL materials are developed to have excellent conductivity, thus their highly developed carbon structure renders them unamenable to activation.

CHAPTER 4: Carbon Fiber Nonwovens as Pseudocapacitor Scaffold

This chapter is a manuscript entitled “Preparation of Pseudocapacitor Electrodes via Electrodeposition of Polyaniline on Nonwoven Carbon Fiber Fabrics” by J. Leary, F. Hamouda, B. Maze and B. Pourdeyhimi published in the Journal of Applied Polymer Science (2015) DOI:10.1002/APP.43315

4.1 INTRODUCTION

Since the synthesis of polyacetylene in 1974, intrinsically conductive polymers (ICPs) have been widely explored for various applications^{189,190} thanks to their tunable conductivity and low material cost.¹⁹¹ Polypyrrole (PPy), polythiophene (PT), polyethylenedioxythiophene (PEDOT) and polyaniline (PANI) are a few of the more commonly studied ICPs. With differences in their conductivity, stability and processability, each is suitable for its own range of applications. Here, we focus on PANI for use as a redox material in pseudocapacitive supercapacitors, a class of energy storage devices which present superior power density compared to the majority of batteries and fuel cells. They are typically either constructed with porous activated carbon electrodes backed by current collectors, forming electric double-layer capacitors (EDLC), or with redox active materials coated onto current collectors, forming pseudocapacitors.

PANI is preferred to other ICPs for use as a pseudocapacitive material due to its stability, low cost and high theoretical specific capacitance (i.e. 750 F g^{-1} vs. 210 F g^{-1} for PEDOT).^{16,191–194} The electrochemical charge storage mechanism of PANI in a symmetrical supercapacitor involves simultaneous oxidation and reduction reactions at two adjacent electrodes. A fully charged state is achieved when one electrode has reached maximum electron doping and the other electrode is completely de-doped. A discharged state is seen when there is an equal partial de-doping on the two electrodes.¹⁶ Thus the true maximum specific capacitance that can be expected from a PANI supercapacitor is half of its full theoretical value, or 325 F g^{-1} , although experimental values have been reported to range from 160 F g^{-1} to over 1000 F g^{-1} .^{90,167}

Control over PANI reaction steps, rates and products can be achieved through variation of the monomer type,¹⁹⁵ deposition duration,¹⁹⁶ deposition potential,¹⁹⁷ and aniline concentration.^{189,198,199} For instance, Genies et al. observed a change in current density during the potentiostatic electrodeposition of PANI depending on the deposition potential used.¹⁹⁷ In an aqueous sulfuric acid medium, a potential of 1.0 V (vs. SCE) resulted in the highest

current density, while the lowest current density occurred at 1.4 V. A later study by Kanamura et al. found that current density during deposition impacted the morphology and discharge characteristics of the deposited species, implying that discharge behavior could also be impacted by tuning the deposition potential.²⁰⁰ In addition to its morphology, the conductivity of PANI is crucial to its performance in an electrochemical capacitor. ICPs derive their electrical conductivity from their conjugated structure. While in a conductive state, they can be considered to be either positively charged ('p-doped') or negatively charged ('n-doped'). Over-oxidation or reduction can establish an insulating 'undoped' state.^{197,201} In the case of PANI, interest is focused upon the emeraldine salt form, as this is considered its most electrically conducting state.^{191,202–205} Control of oxidation state can be imparted during the synthesis process, which is achieved by chemical or electrochemical means. Although chemical polymerization exhibits increased bulk yields over electrochemical methods, the latter provides superior control over the resulting charge state of the polymer.^{193,206} Electrochemical synthesis further provides the advantage of coating the polymerized material directly onto a conductive scaffold such as a three-dimensional carbon substrate, yielding a ready-made supercapacitor electrode with low equivalent series resistance (ESR).¹⁸⁹

Carbon fiber fabric (CFF), also termed carbon cloth (CC) in the literature, is an ideal scaffold for PANI deposition due to its low electrical resistance and flow-through structure. Without being subjected to a micropore-developing activation procedure, CFF has a low specific surface area ($\sim 1 - 10 \text{ m}^2 \text{ g}^{-1}$) and thus exhibits very little capacitance. Following deposition, the PANI-coated CFF can be directly used as a pseudocapacitive-type supercapacitor electrode. A significant increase in capacitance between a PANI deposited CFF electrode and a bare CFF electrode has already been reported.⁹⁰ However, the particular fabric structure of the CFF is important to consider. Prior research has generally explored polyaniline deposition onto woven fabrics.¹⁶⁷ Through visual analysis of PANI coating on an electrode, a positive correlation between uniform distribution of active material and capacitance levels has been noted.²⁰⁷ Typical woven fabrics are composed of yarns, in which fibers are tightly

twisted together, whereas in typical nonwoven fabrics, the fibers are individualized and uniformly distributed in a web. Thus, nonwovens can potentially provide ideal fiber arrangements upon which to deposit PANI. In this report, a variety of nonwoven CFF materials were compared as substrates for polyaniline electrodeposition. Through varying monomer concentration, deposition potential and deposition time, the effects of processing conditions were also examined.

4.2 EXPERIMENTAL

4.2.1 Materials

Four commercially available nonwoven CFFs were collected: thick binder-free carbon fiber fabric sample 1 (BFCFF-1) and thin binder-free carbon fiber fabric sample 2 (BFCFF-2) are both made from polyacrylonitrile webs prepared by carding and hydroentangling, and subsequently carbonized; nickel-plated carbon fiber fabric (NPCFF) is wet-laid carbon staple fiber bonded by polymer resin binder and plated with nickel; carbon fiber veil fabric (VCFF) is tissue-like wet-laid carbon staple fiber bonded by a polymer resin binder. Aniline (certified ACS grade 99%), sulfuric acid (4N solution, certified pH 4.4), and sodium sulfate anhydrous (granular 10 – 60 mesh, certified ACS grade) were purchased from Fisher Scientific. Whatman grade 413 filter paper (VWR) was used as the separator material in the test cells.

4.2.2 Deposition of PANI onto Carbon Fiber Fabric

Samples of each of the four CFF types were coated with PANI under the same conditions. The CFF samples, measuring 4 cm x 4 cm were pressed against a stainless steel electrode in a custom made deposition cell (Figure 69) fitted with an Ag/AgCl (saturated NaCl) reference electrode (+0.196 V vs. NHE, -0.044 V vs. SCE). The cell was then immersed in an aqueous solution containing 0.1 M aniline and 0.5 M Na₂SO₄. A stainless steel counter electrode was employed. A potential of 0.894 V vs. Ag/AgCl (0.850 V vs. SCE) was applied for 10 minutes, causing the oxidative polymerization of aniline on the nonwoven CFF surface. Following deposition, each sample was rinsed under running DI H₂O for 20 seconds on each side and dried at 70°C under air.

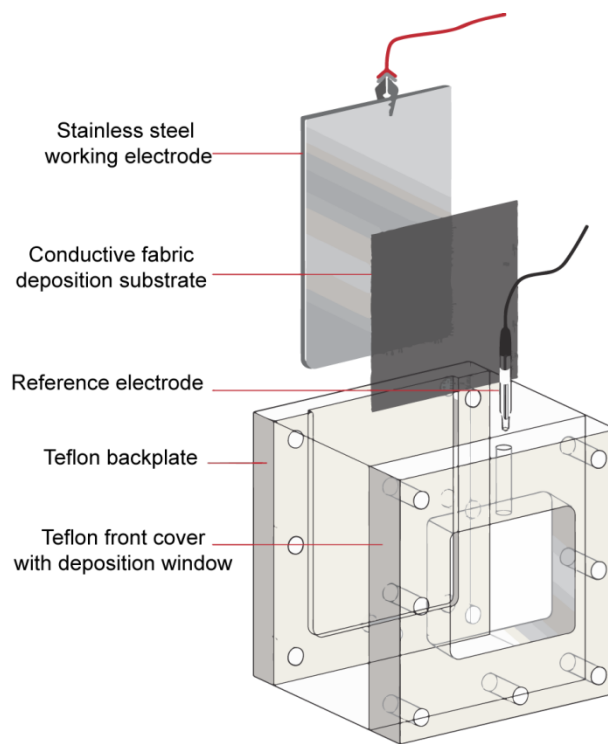


Figure 69: Deposition cell setup including working electrode, deposition substrate, reference electrode and Teflon frame.

The coated CFF samples were then tested for specific capacitance, and among the four types, one which exhibited a large capacitance increase was subjected to further experimentation with deposition settings. For the subsequent deposition studies, the applied voltage was set to between 0.644 V and 1.144 V (vs. Ag/AgCl) in 0.1 V increments (0.644 V, 0.744 V, 0.844 V, 0.944 V, 1.044 V, 1.144 V). Within a limited range of 0.744 V – 0.944 V, the potential was varied in 0.033 V increments (0.744 V, 0.777 V, 0.811 V, 0.844 V, 0.877 V, 0.911 V, 0.944 V). Next, in order to study the effect of deposition time, the duration was set to 1, 5, 10 and 20 minutes, under a fixed potential. The effect of aniline concentration was also studied by preparing aniline solutions with concentrations of 10 mM, 100 mM and 500 mM, and carrying out deposition under set potential. All experimentation was carried out using a VMP-3 potentiostat / galvanostat (Bio-Logic Science Instruments, Claix, France).

4.2.3 Characterization

Electrochemical testing was carried out using a symmetrical two-electrode cell, with both electrodes taken from the same sample. Aqueous 0.5 M Na₂SO₄ was used as the electrolyte, and standard cellulose filter paper was used as the separator. Cyclic voltammetry (CV) was conducted at sweep rates of 10, 50 and 100 mV s⁻¹ to track the redox reactions of the deposited PANI, and chrono-potentiometry (CP) was carried out at 0.5, 1 and 2 mA to measure the capacitance of the deposited PANI.

CP was repeated for 10 cycles to ensure stability, and the charge value used in calculations was taken from the last cycle, using a current of 0.5 mA. Equation 36, based on the series capacitor circuit model of a two-electrode cell,³⁶ was then used to obtain the gravimetric specific capacitance C_s (in units of F g⁻¹, where F = Coulomb/V). Q is charge (in Coulombs), calculated as the product of the discharge current and the discharge time. ΔV is the voltage window. Throughout this study, the voltage window was fixed at 0.8 V (starting at 0.0 V and ending at 0.8 V vs. Ag/AgCl). The two electrode masses, represented by m_1 and m_2 (in grams) were measured using a Mettler-Toledo model MS105 balance (readability = 0.01 mg).

$$C_s = \frac{Q}{\Delta V} \left(\frac{m_1 + m_2}{m_1 * m_2} \right) \quad (36)$$

Unless designated otherwise, electrode mass includes CFF + PANI mass. It is worth noting that this approach differs from the more common practice of considering solely PANI mass and excluding contributions from CFF mass, which yields values that appear much higher.⁹ Including all electrode materials (CFF + PANI) results in a lower value but a more relevant measure in terms of application standpoint. It is also a more reliable determination, since obtaining a measurement of PANI mass on the electrode is complicated by the fact that the initial mass of each bare carbon electrode (m_{carbon} in grams) can only be estimated based on

the average areal density of the carbon fiber fabric (ρ_c in units of g cm^{-2}) and the area of the electrode ($A_{electrode}$ in units of cm^2):

$$m_{carbon} = A_{electrode} * \rho_c \quad (37)$$

Following deposition, the total electrode mass (m_t in grams) is obtained by weighing, and the PANI mass on the electrode (m_{pani} in grams) is then assumed to be:

$$m_{pani} = m_t - m_{carbon} \quad (38)$$

Cycle life was tested by measuring capacitance change over the course of 4000 charge-discharge cycles. The morphology of PANI depositions was examined using SEM (Phenom Pro, Eindhoven NL), and color changes were documented by digital camera (Olympus STYLUS SZ-16).

4.3 RESULTS AND DISCUSSION

For the initial screening, various nonwoven CFF materials were deposited with PANI from a solution of 0.1 M aniline monomer in dilute H_2SO_4 for 10 minutes. Capacitance of the samples was tested before and after deposition (Table 12). Before deposition, all four samples – BFCFF-1, BFCFF-2, NPCFF and VCFF – showed small capacitance values well below 1 F g^{-1} , arising due the electric double layer, which produces an electrostatic charge separation on the electrode surface and is surface area dependent. The highest double layer capacitance was measured for VCFF, which was the veil-like material. This may be attributed to higher specific surface area due to lower fiber diameter. The typically low specific surface area (SSA) of CFF dictates that they are poor double layer capacitors unless the fiber surface is treated by physical or chemical activation to open up scores of micropores along the surface and increase SSA up to $2000 \text{ m}^2 \text{ g}^{-1}$. Activation treatment is not the focus of the current study, rather the focus is on improving capacitance by adding a pseudocapacitive

layer. Thus, while the capacitance values of the untreated samples indicated that they are poor electric double layer capacitors, they are useful as a starting material for a study which is focused on the impact of deposited PANI.

Table 12: Specific capacitance of various carbon fiber nonwoven scaffolds, based on CP discharge at 0.5 mA, before and after deposition of PANI.

Substrate	Initial Specific Capacitance (F g ⁻¹)	Specific Capacitance after PANI Deposition (F g ⁻¹)
VCFE	0.22 F g ⁻¹	4.47 F g ⁻¹
NPCFF	0.06 F g ⁻¹	3.29 F g ⁻¹
BFCFF-1	0.02 F g ⁻¹	14.81 F g ⁻¹
BFCFF-2	0.02 F g ⁻¹	14.44 F g ⁻¹

Specific capacitance values following deposition reflect the contribution of pseudocapacitive PANI. Although untreated VCFE had the highest initial specific capacitance, it only showed an increase of one order of magnitude, while NPCFF increased by two orders of magnitude upon PANI treatment. The two binder-free materials – BFCFF-1 and BFCFF-2 – which had the lowest specific capacitance initially, showed the highest final specific capacitance values. These represented increases of three orders of magnitude.

Compared to BFCFF-1, BFCFF-2 is thinner, which allows for better penetration of PANI. Therefore, BFCFF-2 was selected for further experiments with deposition conditions on the basis of the increase in capacitance that was exhibited in the initial screening. Six deposition potentials, between 0.644 V and 1.144 V vs. Ag/AgCl, were applied. This range was chosen to coincide with the range of potentials typically used in potentiostatic polymerization of aniline.¹⁸⁹ PANI is a polymorph, with its particular form depending on oxidation state. Since the PANI produced here was synthesized across a range of potentials, it is possible that a variety of the well-known forms would be exhibited among the different samples. Figure 70 illustrates the chemical structures of three of the primary forms: leucoemeraldine, emeraldine and pernigraniline.¹⁹¹

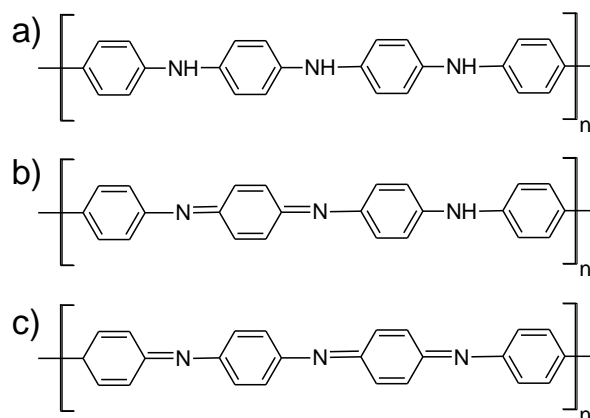


Figure 70: The three primary forms of PANI in their undoped structures, in order of increasing oxidation: (a) leuco-emeraldine, (b) emeraldine, (c) pernigraniline.

Digital images and corresponding SEM results of the PANI-coated carbon fiber show various colors associated with each potential (Figure 71 and Figure 72). At 0.644 V, digital images indicate that the surface is free of PANI (Figure 71a). At 0.744 V and beyond, PANI is deposited on the carbon fiber nonwoven. A distinct color shift from 0.744 V (teal) to 0.944 V (navy blue) can be seen, beyond which the color is stable (Figure 71d – f). This phenomenon, known as electrochromism, is in agreement with the reported observations.¹⁹⁷ PANI is well known for its visible response to changes in pH - a feature which is utilized in applications such as gas sensors.²⁰⁷

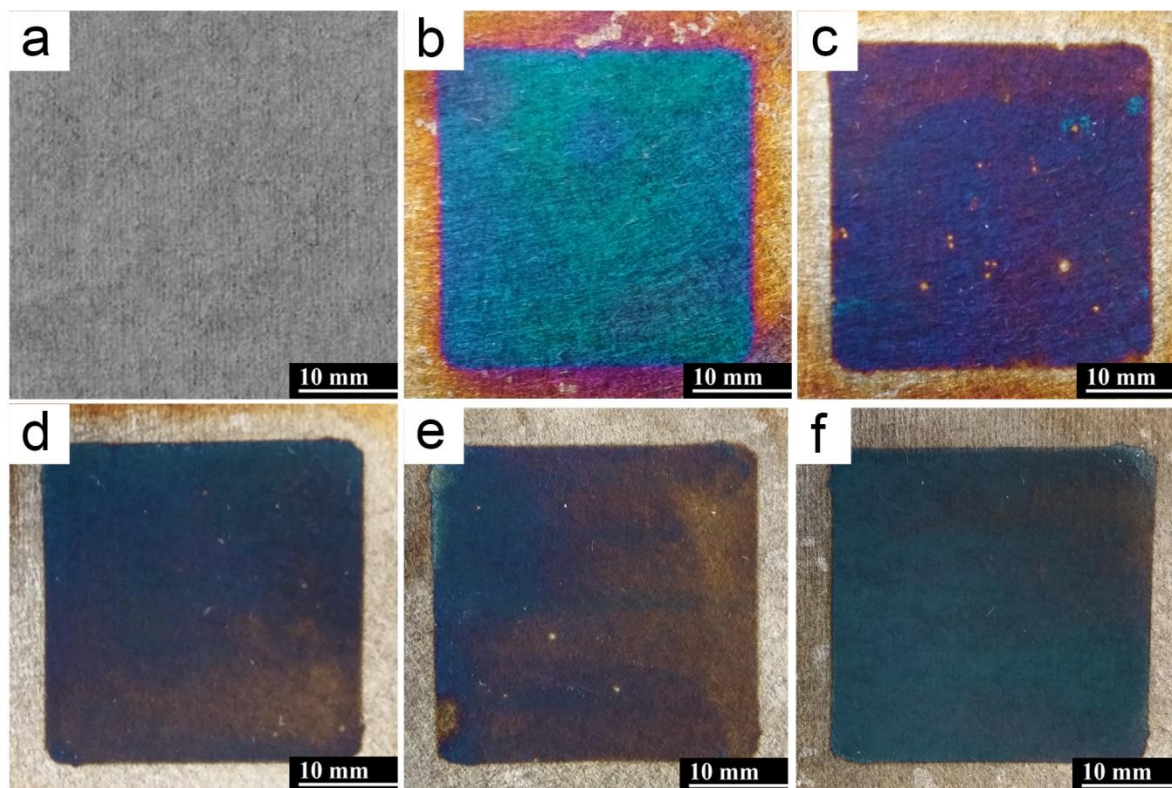


Figure 71: Carbon fiber binder free material (BFCF-2) deposited with PANI at various deposition potentials: (a) 0.644 V, (b) 0.744 V, (c) 0.844 V, (d) 0.944 V, (e) 1.044 V and (f) 1.144 V, all vs. Ag/AgCl.

In terms of the morphology, SEM of the 0.744 V sample (Figure 72b) shows a slightly cracked film-like coating on the fibers, along with randomly dispersed particle-like clusters. Carlin et al. employed ellipsometry to track changes in coating thickness through the duration of deposition and found that in early stages, PANI formed as a film, as the aniline monomer initially came into contact with the electrode surface.¹⁹⁶ After a buildup of film ~150 nm thick, they found that the morphology changed to form fiber-like structures. Similarly, distinct morphologies are observed on the samples under SEM in the present study. It should also be noted that unusually dense growth is seen at 0.944 V (Figure 71d), which can be explained by the non-homogeneity seen in the digital image – some regions have dense clusters, while others are sparse.

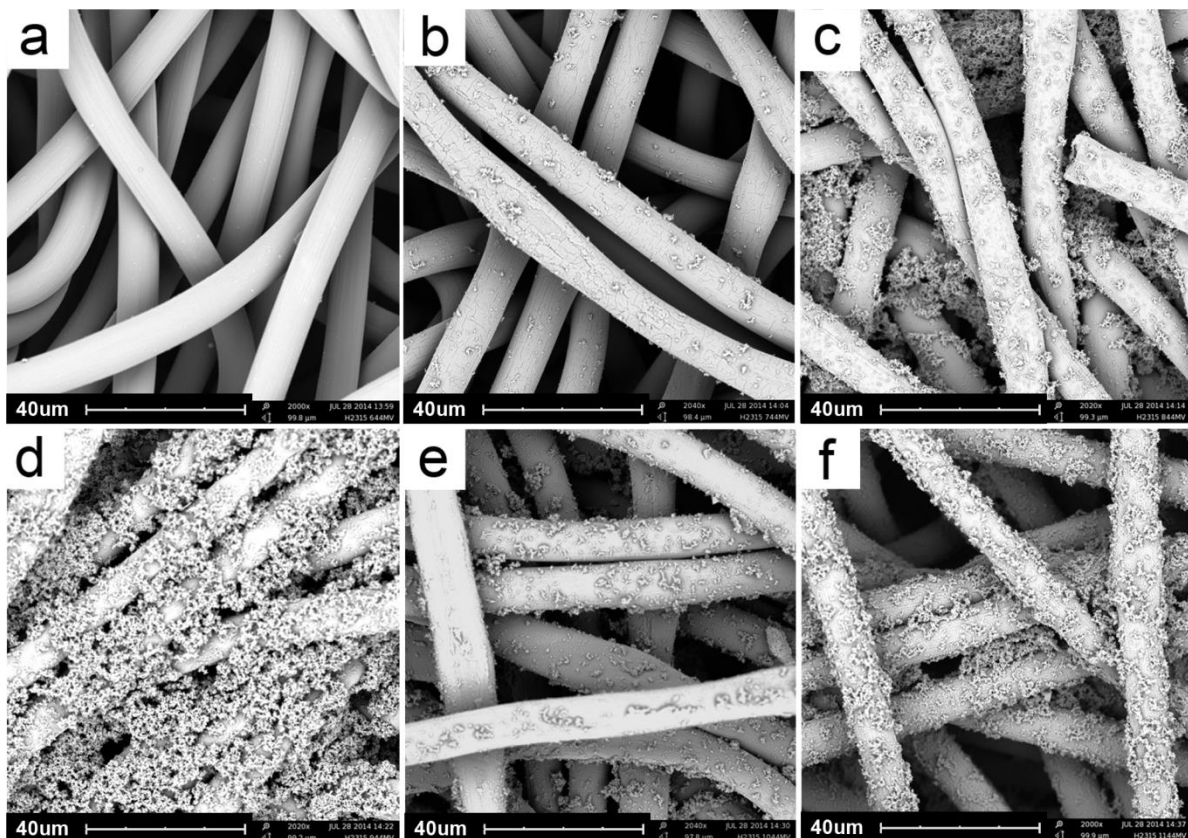


Figure 72: SEM images showing PANI deposited at (a) 0.644 V, (b) 0.744 V, (c) 0.844 V, (d) 0.944 V, (e) 1.044 V and (f) 1.144 V.

Following CP tests, specific capacitance was calculated on the basis of total electrode mass (CFF + PANI). As was indicated with SEM and digital imaging, the sample with PANI deposited at 0.644 V showed no redox behavior. Onset of capacitance appeared at 0.711 V and continued to rise until 0.744 V, after which it hovered around a value of $\sim 18 \text{ F g}^{-1}$ for the remainder of samples (Figure 73). A correlation between the color of the polymer and specific capacitance was not evident from the CP results.

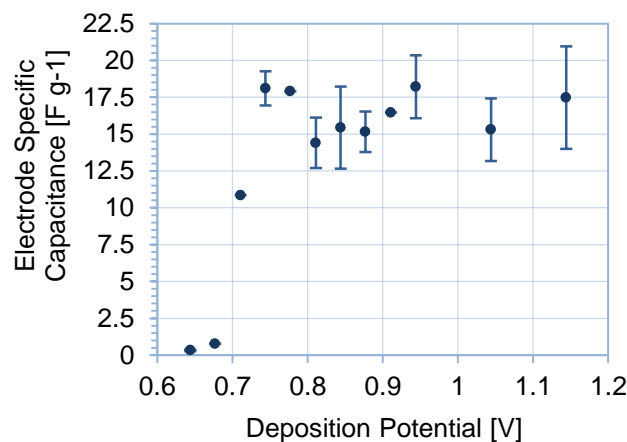


Figure 73: Specific capacitance as a function of the potential used during deposition, from 0.644 V to 1.144 V.

CV curves (Figure 74) showed more of a correlation with the color shift trend. The most symmetrical reduction and oxidation curves are seen for the samples treated at 0.744 V and 0.777 V (Figure 74a), following which the curve became highly asymmetrical (Figure 74b). Although the reactions appear to be reversible (no change was observed over the course of ten cycles) the ideal CV shape for a supercapacitor is rectangular – thus, deposition potentials at 0.844 V and above should be avoided. Furthermore, it was observed that PANI only deposited on the face of the fabric for these samples prepared, whereas at 0.777 V and below, PANI could be seen on both the face and back of the sample.

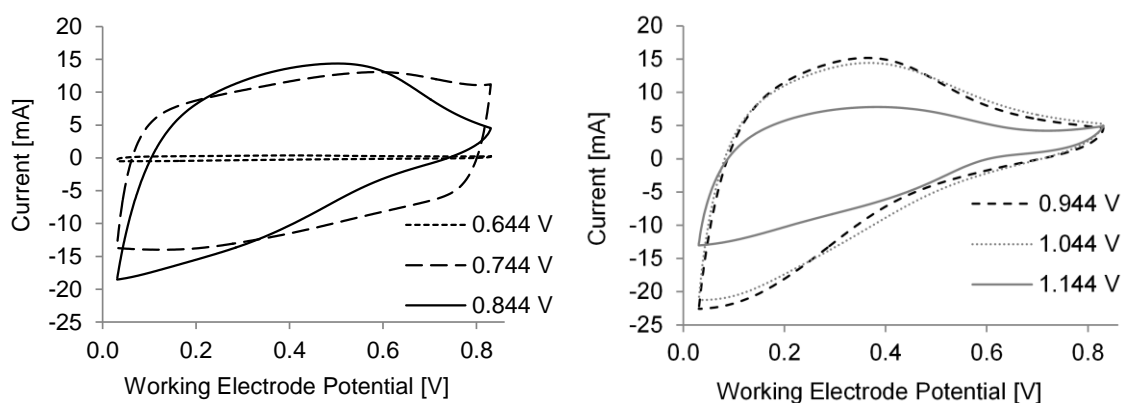


Figure 74: Cyclic voltammograms at a sweep rate of 10 mV / s for samples deposited at various potentials: (a) 0.644V, 0.744 V, 0.844 V. (b) 0.944 V, 1.044 V and 1.144 V (all vs. Ag/AgCl reference).

Following the deposition of PANI at various potentials, 0.777 V was chosen for further experiments and deposition time was examined (Figure 75). Specific capacitance reached a maximum of around 17.5 F g⁻¹ at 10 minutes of deposition.

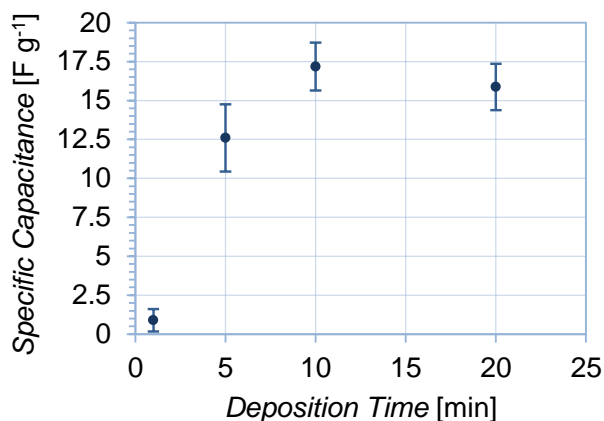


Figure 75: Specific capacitance as a function of deposition time used during deposition, from 1 minute to 20 minutes, at a deposition potential of 0.777 V (vs. Ag/AgCl).

Aniline concentration was varied between 0.01 M and 0.5 M, and deposition time was also varied from 5 – 20 minutes. Surprisingly, the color resulting from the highly concentrated (0.50 M) solution was distinctly different from the bright light green that had been seen at lower concentrations. Figure 76 shows the deep black color of the PANI on these samples – more similar to the color seen on samples deposited at high potentials. However, unlike the high potential samples, PANI was coated throughout the thickness of the material, appearing on both the face (Figure 76a) and the back (Figure 76b) of the samples. The color change between 0.10 M and 0.50 M remains unexplained.

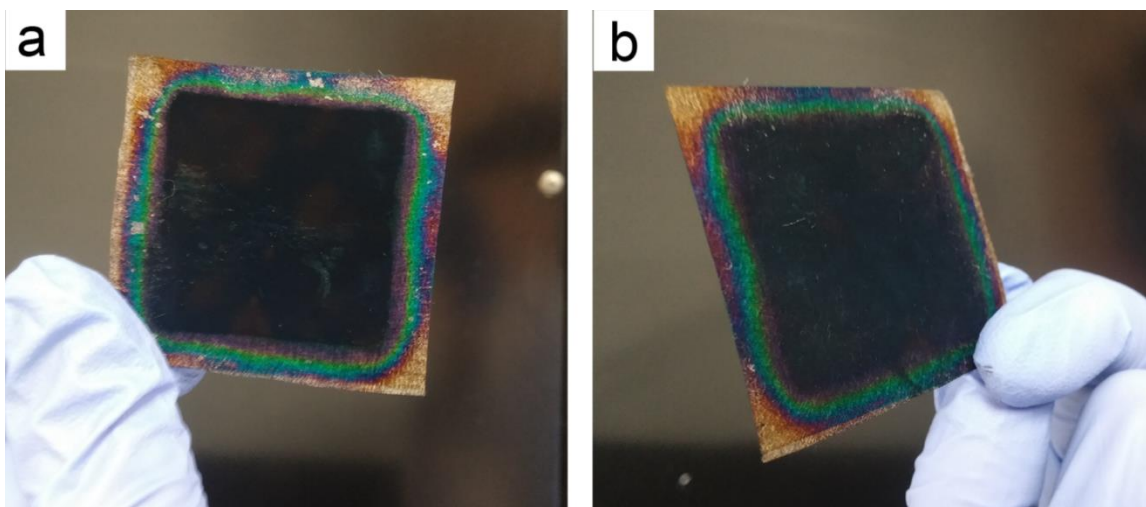


Figure 76: PANI deposited onto BFCF-2 for 20 minutes at 0.777V (vs. Ag/AgCl). (a) Front face of sample. (b) Back of sample.

Even at low deposition times, the 0.5 M solution produced dramatically higher specific capacitance than previous results (Figure 77a). While the highest specific capacitance obtained from 0.10 M solution had been $\sim 18 \text{ F g}^{-1}$ (10 minutes), the 0.50 M solution resulted in $\sim 42 \text{ F g}^{-1}$ after just 5 minutes. At 10 minutes, it was nearly 60 F g^{-1} . While a threshold appeared after 10 minutes for lower concentrations, specific capacitance continued to increase and reached over 80 F g^{-1} at 20 minutes for 0.5 M concentration.

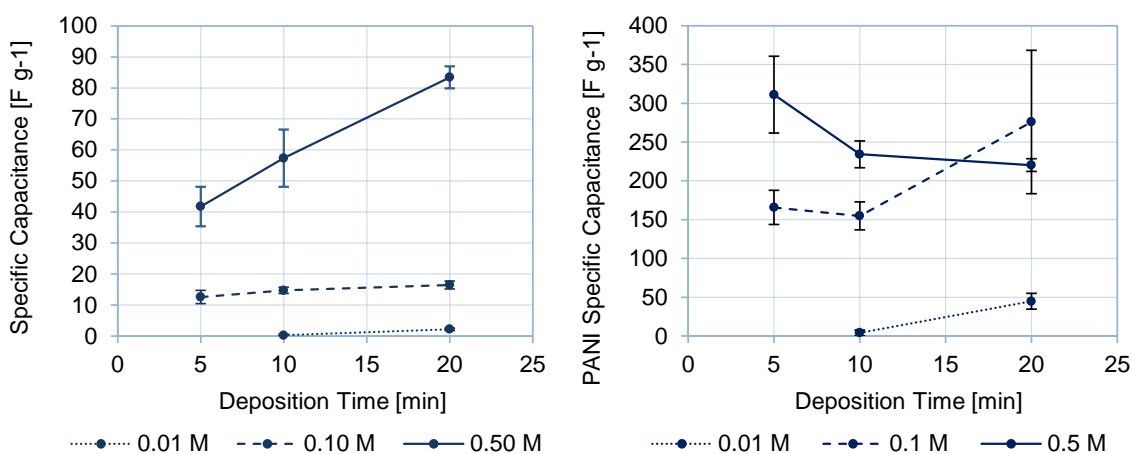


Figure 77: Specific capacitance for samples treated with 0.01 M, 0.10 M and 0.50 M concentrations of aniline for various durations. (a) Values calculated on the basis of total electrode mass. (b) Values calculated based on PANI mass only.

For the sake of comparison with results from the literature, the specific capacitance is also calculated solely on the basis of PANI mass and is presented in Figure 77b. Considering that the theoretical maximum specific capacitance of PANI is 325 F g^{-1} , the values shown here are very promising. For the lower concentrations, 0.01 and 0.1 M, PANI specific capacitance rises with deposition time, reaching $\sim 275 \text{ F g}^{-1}$ (Table 13). This trend reverses somewhat for the 0.5 M concentration, where increased deposition time leads to lower PANI specific capacitance. This can be explained by the higher PANI loading seen at 20 minutes (33 wt %) as compared to five minutes (12 wt %). All else being equal, if a given total capacitance is attributed to a higher mass, specific capacitance will be lower. Another example of this effect is observed at 20 minute deposition times for the 0.1 M and 0.5 M aniline solutions. The former results in an average PANI specific capacitance of 275 F g^{-1} , while the latter is around 220 F g^{-1} despite having a higher average total specific capacitance ($\sim 83 \text{ F g}^{-1}$ compared to $\sim 16 \text{ F g}^{-1}$). Again, the elevated PANI specific capacitance is due to a relatively low PANI mass loading (4 wt%).

Table 13: Specific capacitance values, shown both on the basis of total electrode mass as well as PANI mass only, for various aniline solution concentrations and deposition times.

Aniline Concentration	Deposition Time (minutes)	Average Specific Capacitance (F g^{-1})	
		Based on measured total electrode mass	Based on estimated PANI mass only
0.01 M	10	0.3	4.2
	20	2.2	44.6
0.10 M	1	0.9	19.8
	5	12.6	165.6
	10	17.2	154.8
	20	15.9	275.8
0.50 M	5	41.8	311.1
	10	57.4	234.2
	20	83.4	220.3

Observed flaking of the PANI deposited from 0.5 M solutions hinted that gains in specific capacitance could be accompanied by loss of cycle life. Electrodes prepared by 20 minute depositions from 0.1 M and 0.5 M aniline solutions were charged and discharged galvanostatically at 2.0 mA and 2.4 mA, respectively, for 4000 cycles between 0.0 V and 0.8 V (Figure 78). During the first 500 cycles, the 0.5 M sample showed a much steeper capacitance loss, but the 0.1 M sample performance continued to decline steadily for the remainder of the tests so that by 4000 cycles, the percentage loss was comparable. Still, the final specific capacitance was around 24 F g^{-1} for the 0.5 M sample, as opposed to around 6 F g^{-1} for the 0.1 M sample, leading to the conclusion that high concentration is preferred despite early degradation.

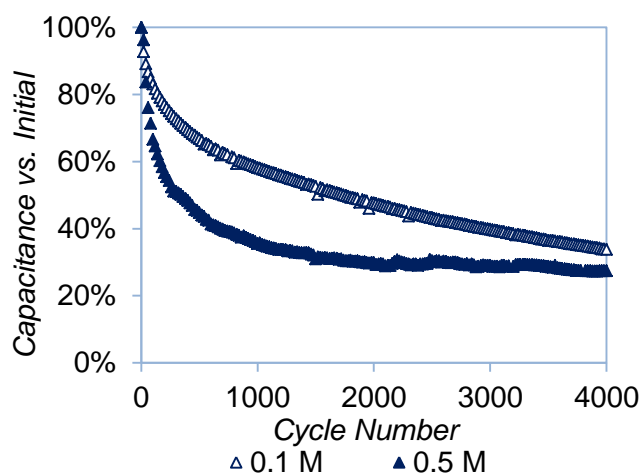


Figure 78: Change in capacitance with cycle number for electrode formed from aniline concentrations of 0.1 M and 0.5 M at 0.777V vs Ag/AgCl for a duration of 20 minutes.

4.4 CONCLUSIONS

Among nonwoven carbon fiber fabrics tested, the binder free materials (BFCF-1 and BFCF-2) showed the largest increase in capacitance following PANI deposition. Below 0.710 V vs. Ag/AgCl, PANI polymerization did not occur at significant rates. Between 0.744 V and 1.144 V, specific capacitance as a function of deposition potential was relatively stable.

However, only samples below 0.777 showed reversible reactions based on analysis of the cyclic voltammograms. Additionally, the mass of deposited PANI was concentrated at the face of the carbon fiber nonwoven for depositions carried out above 0.777 V which may have led to caking at higher aniline concentrations or deposition times. Therefore, deposition from 0.744 V – 0.777 V is recommended for the potentiostatic method.

The biggest impact on performance was caused by varying the aniline concentration. The highest total specific capacitance in this study (80 F g^{-1}) was obtained from a solution of 0.5 M aniline at a 20 minute deposition time. High PANI specific capacitance values (350 F g^{-1}) were also recorded. It is yet to be determined whether further improvement could be seen at higher concentrations and longer deposition times. Increasing deposition time had a positive effect on capacitor performance, but reached a threshold for the 0.1 M samples beyond which very limited improvement, or even decrease, could be seen. This was likely due to inaccessible PANI following maximum coverage of the substrate fibers. Future work will focus on determining the threshold deposition time for 0.5 M aniline solutions.

CHAPTER 5: Carbon Nanotube Coated Nonwovens as Flexible Supercapacitor Electrodes

This chapter is a manuscript entitled “Preparation of Carbon Nanotube Coated Nonwovens as Flexible Supercapacitor Electrodes”, by J. Leary, E. Fox, B. Maze and B. Pourdeyhimi, and will be submitted to the Journal of the Textile Institute.

5.1 INTRODUCTION

Flexible electronic devices have the potential to introduce a new level of convenience and connectivity into our everyday lives via integration into soft or pliable articles, such as clothing, bedding, vehicle interiors, draperies, headwear, footwear, watches and other accessories.^{208,209} Metal-polymer composites are widely regarded as promising materials for these products, yet applications such as energy storage systems require more stable conductors.³⁴ Carbon nanotubes (CNT), having the potential to transport electrons with negligible resistive heating, are expected to be useful as an alternative to metals in this regard.¹¹⁹ The co-extrusion of CNT/polymer blends has been extensively studied.^{210–212} However, a major limitation in creating conductive co-extruded CNT/polymer composites is the maximum CNT concentration that can be achieved. A volume fraction of 0.025 CNT in polypropylene matrix causes melt viscosity to increase by a factor of more than 100, resulting in challenges to melt processability, especially in the form of fibers.²¹³

A common method for making polymer-CNT composite electrodes, analogous to that used for granular activated carbon, is to form a paste out of CNT and polymer binder. The pastes, in which polyvinylidene fluoride typically serves as the binder material, are formed through compression rather than extrusion and thus can reach CNT concentrations of up to 90%.^{192,214–217} Yet for applications in electrochemistry, where electron-transfer occurs at the interface between electrode and electrolyte, encapsulating CNT within polymer binder renders them unable to perform their desired function. Consequently, different methods for concentrating CNT at the electrode surface are under development. Several studies have focused on simply omitting the binder. These binder-free networks form sheets known as buckypaper and are typically obtained by filtering surfactant-enabled aqueous CNT dispersions.^{215,218} Such freestanding, bendable and electrically conductive sheets may be used alone as electrodes, or even enhanced via electrodeposition of pseudocapacitive materials such as polypyrrole (PPy) or MnO₂.^{219,220}

In the effort to increase electrode surface area, thereby enhancing the limiting current of an electrochemical cell, several groups have explored the possibility of wrapping buckypaper onto 3D substrates. Hecht et al. were first to report binder-free CNT coatings applied onto porous scaffolds.⁷² CNT networks were coated onto woven military camouflage fabric of undisclosed polymer type via application of a surfactant-enabled aqueous dispersion.^{218,221} Subsequent studies have concluded that applying multiple CNT dispersion dip cycles progressively reduce resistivity, as increasing density of CNT intersections raises the probability of electron conduction.^{128,130} Other key parameters highlighted in subsequent studies is the concentration of CNT in the dispersion, a factor of the type of dispersion agent, preparation method, and nanotube type used.^{72,123,125,132,222–224} However, very little attention is given to the role of the substrate itself.

Binder-free CNT networks been wrapped onto cotton yarn,^{130,222} woven cotton fabric,^{133,225} woven polyester fabric,¹³³ silicone film,²²⁶ knit wool/lycra fabric,¹³² multi-filament polyester yarn,²²⁷ cellulose paper,²²⁴ nylon braiding,²²⁸ and nylon parachute fabric.²²⁸ Despite the breadth of scaffold types employed, the adsorption mechanism has rarely been discussed. Although a group of highly cited publications advance hydroxyl-carboxyl interactions as the bonding mechanism between CNT and nonwoven fabric or sponge, the polymer types are poorly identified in these reports.^{125,127–129} Elsewhere in the literature, contradictions can be seen. While Zhang et al. suggest that nylon fabric surface energy is too low to bond with CNTs, others employ nylon successfully.^{228,229} Similarly, while Goncalves et al. assume that polyester and cotton substrates require auxiliary chemicals in order to bond with CNTs, several studies demonstrate otherwise.^{133,225,227} In order to gain valuable insight into CNT-wrapped fibers and foams, it was recently pointed out in a review article by Cao et al. that there is a need to determine the influence of scaffold properties such as polymer type, fiber diameter and fabric construction.²³⁰

In this study, CNT dispersions were formulated using carboxyl-functionalized SWNTs in either water or ethanol. Based on the concept that high specific surface area materials lead to

better energy density, low-diameter fibers were initially examined. These were made of either polyethylene terephthalate (PET) or polyamide 6 (PA6), and were formed by bicomponent fiber spinning in the shape of winged fiber (WF) or island-in-the-sea fiber (I/S). Woven and nonwoven fabric structures were compared, and the effect of web solidity was studied. To isolate the effect of polymer type from fabric geometries, PA6, PET, and cotton nonwovens with similar structures were then created. By focusing on a range of fibrous scaffolds, several key relationships between fabric properties and coating performance were identified.

5.2 EXPERIMENTAL PROCEDURES

5.2.1 Preparation of CNT Dispersions

Single-walled carbon nanotubes (P3-SWNTs), produced by the electric arc discharge method and purified in nitric acid, were purchased from Carbon Solutions, Inc. (Riverside, CA). P3-SWNTs are functionalized with carboxylic acid groups as a result of the nitric acid treatment.²³¹ The average CNT bundle diameter is 2 – 4 nm, the average bundle length is 1.0 μm , and the ratio of semiconducting to metallic nanotubes is 2:1. Reagent-grade ethanol and sodium dodecylbenzene sulfonate (SDBS) were purchased from Sigma-Aldrich Corporation (St. Louis, MO). Deionized water was used throughout the study. Two types of CNT dispersion were prepared: pure reagent-grade ethanol was sonicated with 1 mg mL⁻¹ CNT, and pure deionized water was sonicated with 10 mg mL⁻¹ SDBS and 1 mg mL⁻¹ CNT. In both cases, the dispersion was first placed in an ultrasonic bath for 5 minutes (Branson 2800) then subjected to sonic horn for 60 minutes at frequency of 20 kHz and 500 W (QSonica Q500).

5.2.2 Preparation of Fabric Substrates

Polyurethane foam sponges (Scotch-Brite Dobbie Cleaning Pads) were purchased and cut into 1 mm thick sheets. Woven nylon (PA6) fabric was obtained from the NC State Textile Engineering Chemistry and Science department. The following nonwoven substrates were fabricated at the Nonwovens Institute (NWI) at NC State: polyester winged fiber (PET WF), nylon winged fiber (PA6 WF) and nylon island-sea (PA6 I/S) microfiber nonwovens were formed through spunbonding and hydroentangling; PA6 I/S microfiber nonwovens with

different web densities were formed by adjusting the hydroentangling jet spacing to a narrow spacing of 0.6 mm (PA6 I/S NS) or a wide spacing of 4.8 mm (PA6 I/S WS); cotton staple fiber (cotton NP), nylon staple fiber (PA6 3 den, PA6 15 den) and polyester staple fiber (PET 3 den, PET 6 den) nonwovens were formed through carding, crosslapping and needlepunching; polyester multi-lobed staple fiber (PET NP 4DGTM) nonwovens were formed through carding, crosslapping, pre-needling and hydroentangling.

5.2.3 Coating of Fabrics with CNT

Each fabric sample was rinsed in ethanol to remove any residual surface finishes. Following rinsing, the fabric was cut to samples size (6.5 cm diameter circle) and immersed in 40 mL of fully concentrated ethanol-based CNT dispersion. The flask was placed in a shaker-incubator (Amerex SteadyShake 757) set to 250 rpm, and processed at 70°C for 25 minutes. The sample was then removed from its flask and dried at 80°C for 25 minutes. Samples treated with aqueous dispersions were rinsed thoroughly in deionized water to remove surfactant, then dried again. After finding that rinsing was unnecessary with the ethanol-based dispersions, the washing step was left out. This dip-dry cycle was repeated as many times as needed to obtain the desired uptake.

5.2.4 Electrodeposition of MnO₂

MnO₂ was deposited potentiostatically from a solution containing 67 mM MnSO₄ and 330 mM Na₂SO₄ onto a 3.5 cm x 3.5 cm square of the CNT-coated nonwoven using a potentiostat / galvanostat (BioLogic VMP-3). The applied potential was 1 V vs. Ag/AgCl (3 M NaCl), and the deposition time varied from 30 to 300 seconds. To obtain an even distribution of MnO₂, modification of the reported preparation method was required.¹²⁸ The major improvement in the new configuration is that the stainless steel backing piece is in contact with the entire nonwoven sample. The use of 316 stainless steel precludes the corrosion that was observed on the electrode leads when using the dip coating technique. The steel has a resistance that is effectively zero relative to the resistance of the CNT/nonwoven material, thus, MnO₂ is equally likely to deposit evenly over the entire exposed surface. There will,

however, be a gradient in MnO₂ through the thickness of the material, but a gradient in this direction will not result in MnO₂ loading variances for each electrode.

5.2.5 Characterization of Electrical Properties

Electrical resistance was tested by a two-probe method, by applying a 1.0 V potential across an edge of the treated specimen with a constant spacing and measuring the resulting current. This method provides values that can be used to reliably compare the different samples that are prepared in this lab. Although surface resistivity has been reported in units of Ω / sq . by other groups, these measurements vary extensively even among similar materials.^{72,128}

5.2.6 Characterization of Capacitance

CNT-coated samples were tested for specific double layer capacitance, while samples coated with MnO₂ were tested to obtain pseudocapacitance values. Two-electrode test cells were constructed using two 1.3 cm circular pieces of the treated samples as the electrodes, and Whatman filter paper as separator. All three components were sandwiched between two stainless steel current collectors inserted into Teflon plates, and held together by steel screws. The cell was connected to a potentiostat / galvanostat (BioLogic VMP-3) and immersed in 0.5 M Na₂SO₄ aqueous electrolyte. The voltage window was set to 0.8 V, and chrono-potentiometry (CP) was carried out at 0.5, 1 and 2 mA to measure the electric double-layer capacitance (EDLC) of the CNT-coated fabrics. CP was repeated for 10 cycles to ensure stability, and the charge value used in calculations was taken from the last cycle, using a current of 0.5 mA. Equation 39, based on the series capacitor circuit model of a two-electrode cell,³⁶ was then used to obtain the gravimetric specific capacitance C_s (in units of F g^{-1} , where $\text{F} = \text{Coulomb/V}$). Q is charge (in Coulombs), calculated as the product of the discharge current and the discharge time. ΔV is the voltage window. The two electrode masses, represented by m_1 and m_2 (in grams) were measured using a Mettler-Toledo balance (readability = 0.01 mg).

$$C_s = \frac{Q}{\Delta V} \left(\frac{m_1 + m_2}{m_1 * m_2} \right) \quad (39)$$

5.2.7 Characterization of Coating Structure

Surface morphology of the coated fibers was investigated with a Field Emission Scanning Electron Microscope (FEI Verios 460L, Analytical Instrumentation Facility, NC State University). X-ray photoelectron spectroscopy (SPECS System with PHOIBOS 150 Analyzer, Analytical Instrumentation Facility, NC State University) was used to analyze the surface composition of samples.

5.3 RESULTS AND DISCUSSION

5.3.1 Formulation of CNT dispersion

In order to compare the effectiveness of the two different solvents – water and ethanol – two different CNT dispersions were prepared. One was made by dispersing CNT and the surfactant SDBS in water, as reported in previous publications.²³² The second was made by dispersing CNT in ethanol, without surfactant or any other dispersing aid. Sheets of sponge material were dipped into the two different dispersions, then dried. After drying, the sponges were then washed to remove any residue. In the case of the water-based dispersion (WBD), this residue included the surfactant. Following the wash, the sponges were dried. This “dip cycle” process was repeated four times. The sponges were weighed after each full dip cycle, and the increase in mass as compared to the original mass of uncoated sponge was recorded. Figure 79 shows these results. It is immediately apparent that, in the case of the WBD-coated sponge, mass gain per dip cycle is highly irregular.

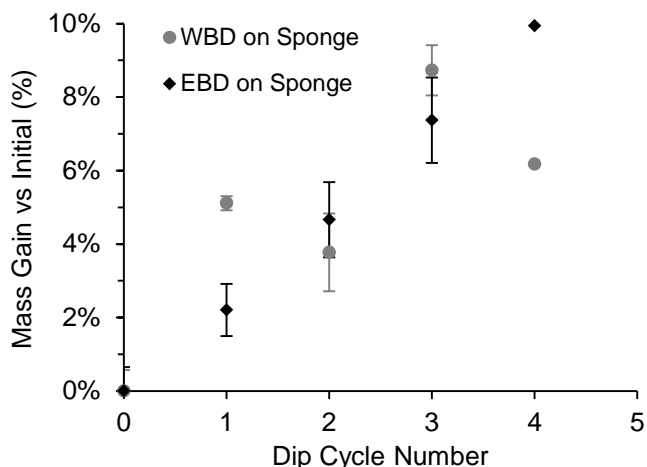


Figure 79: CNT mass gain on PU sponge as a function of dip cycle number for water-based CNT dispersion (WBD) and ethanol-based CNT dispersion (EBD).

The washing step is intended to remove most of the surfactant (Figure 80), but an unknown amount may still remain after this step. The fluctuation of mass gain is an effect of incomplete surfactant removal. In stark contrast, the ethanol-based dispersion (EBD) coated sponges showed a very regular pattern of mass gain with each dip cycle. This difference can be attributed to the surfactant, which is present in the WBD but absent in the EBD. Ultimately, EBD leads to a higher overall uptake of CNT mass following several dip cycles.

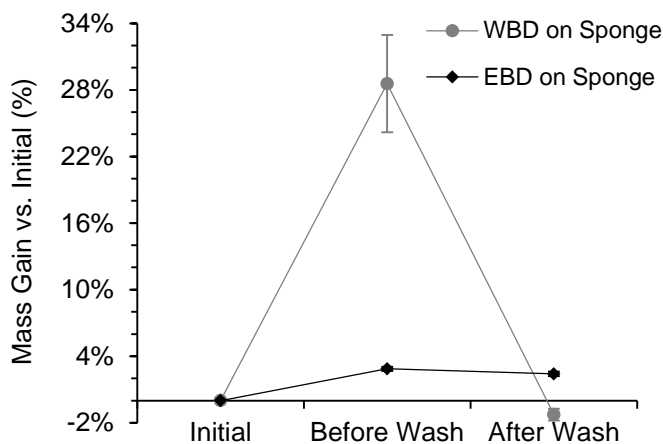


Figure 80: Evolution of mass gain throughout one full dip cycle, including the washing step which causes the loss of surfactant mass in the water-based dispersion (WBD) coating.

The experiment was repeated using PET WF nonwoven rather than sponge, confirming that the EBD results in higher CNT mass gain in the case of fabric substrates as well as sponge substrates. Cumulative mass gain was around 6% after three cycles with the EBD, much higher than the 1% attained with the WBD (Figure 81).

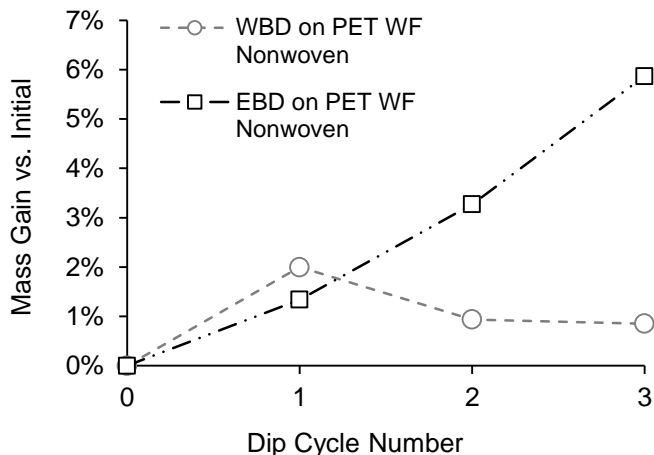


Figure 81: CNT mass gain on PET winged fiber (WF) as a function of dip cycle number.

Figure 82 shows that electrical properties were also improved more efficiently using the EBD. Resistance of CNT-coated sponge was measured after each full dip cycle. After each step, resistance was lower for the EBD-coated sponge than the WBD-coated sponge. By the end of the fourth cycle, the EBD-coated sponge had an average resistance of 82 Ω while the WBD-coated sponge had an average resistance of 687 Ω .

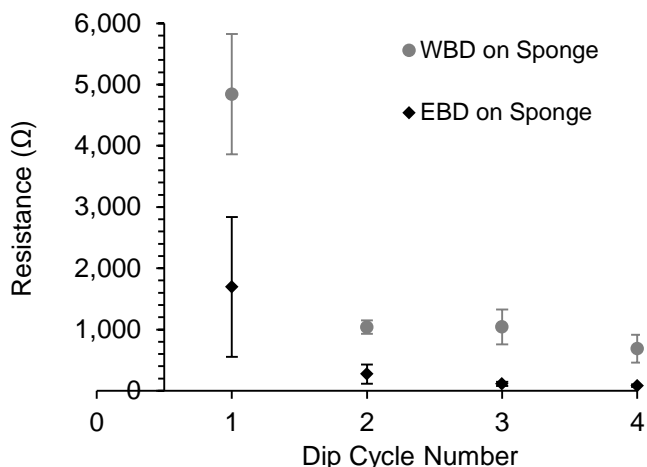


Figure 82: Electrical resistance as a function of dip cycle number for water-based CNT dispersion (WBD) and ethanol-based dispersion (EBD) on PU sponge.

In conclusion, the EBD dispersions resulted in a more effective conductive network of CNT on both substrates (sponge and PET WF nonwoven). Ethanol has the advantage of a lower surface tension than water, avoiding the need for surfactants or other dispersing agents which cause obstructions in the CNT network and are difficult to remove.

5.3.2 CNT Coating of High Surface Area Textiles

A variety of PA6 fabrics were coated with CNT using the EBD. Figure 83 shows that mass gain as a function of dip cycle number is highly dependent on the type of fabric used. By the end of the third cycle, the woven fabric had an average mass gain of 2.95% while the PA6 I/S WS fabric had an average mass gain of 14.19%.

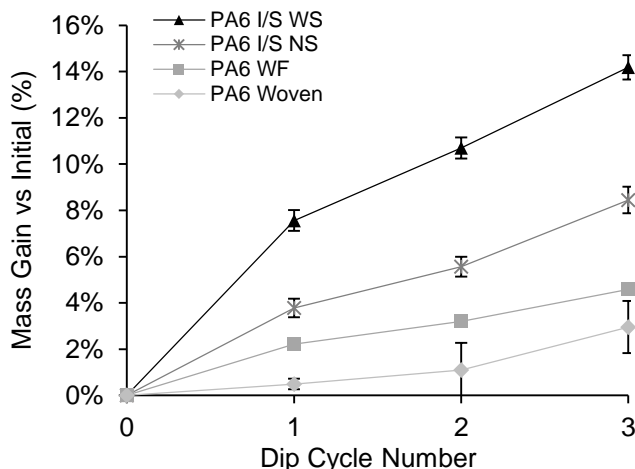


Figure 83: CNT mass gain as a function of dip cycle number for four types of PA6 fabrics coated with EBD.

This discrepancy is not linked to polymer type, since all fabrics in this group are made of PA6 fibers. However, it could be due to differences in the specific surface area (SSA) or the solid volume fraction (SVF) of the webs. The diameter of the fibers used in the yarns of the woven fabric is around 20 μm , while the fiber diameter for the PA6 I/S fabrics is around 2 μm , giving the latter a SSA of around ten times the former. In other words, there is about ten times more surface area for CNT to encounter in the PA6 I/S fabrics. This could certainly lead to higher mass gain per cycle. However, the PA6 I/S WS fabric and the PA6 I/S NS fabric have the same fiber diameter (same SSA), yet still show a large discrepancy in CNT mass gain.

Web solidity, or SVF, is a term used for the amount of fabric volume occupied by solid fiber (as opposed to open void spaces between the fibers). SVF of the PA6 fabrics is shown in Figure 84. Within this group of fabrics, the woven fabric has the lowest amount of void space (highest SVF) while the PA6 I/S WS has the highest amount of void space (lowest SVF). As SVF increases, fabric structure is more closed, and mass gain decreases. It appears that a fabric structure with more void space allows better circulation of the CNT during the coating process, enabling a higher uptake of CNT.

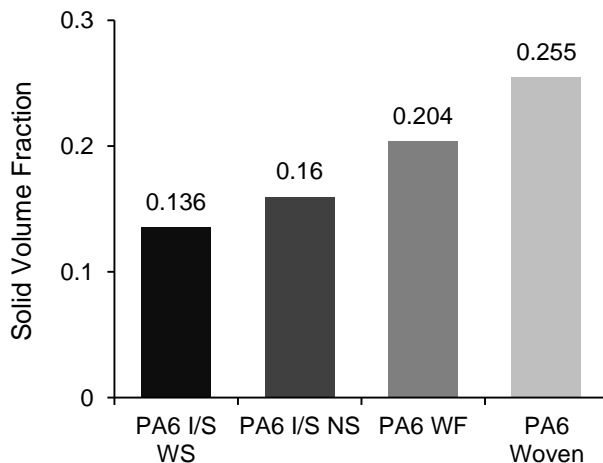


Figure 84: Comparison of SVF for various PA6 fabrics used in this study.

5.3.3 CNT Coating of Carded and Needleponched Staple Fiber Nonwovens

The SVF of a nonwoven is highly dependent on the methods used to form fibers and bond the webs. In the spunbond process, molten polymer is extruded onto a moving conveyer belt, directly forming a web. The web typically has low cohesive strength because the polymer is cooled by the time it hits the belt, so an additional bonding step is required. High-pressure water jets can entangle the fibers together, mechanically bonding them, in the process known as hydroentangling. The result of spunbonding and hydroentangling is highly compacted webs. Figure 85 shows that such webs used in this study were in the 10% – 20% SVF range. In contrast, processing of staple fiber through carding and needlepunching leads to loftier webs. Staple fibers are formed by processing molten polymer through spinnerets, collecting the cooled fibers, and chopping the continuous fibers into short “staple” lengths. Carding forms a soft, high-loft web composed of individualized staple fibers, but it lacks any cohesive strength. Typically, carded webs are bonded mechanically through needlepunching. Such webs used in this study were in the range of 1% - 3% SVF. This range is much closer to the SVF of the PU sponge used earlier in this and other studies, which is 1.5%.

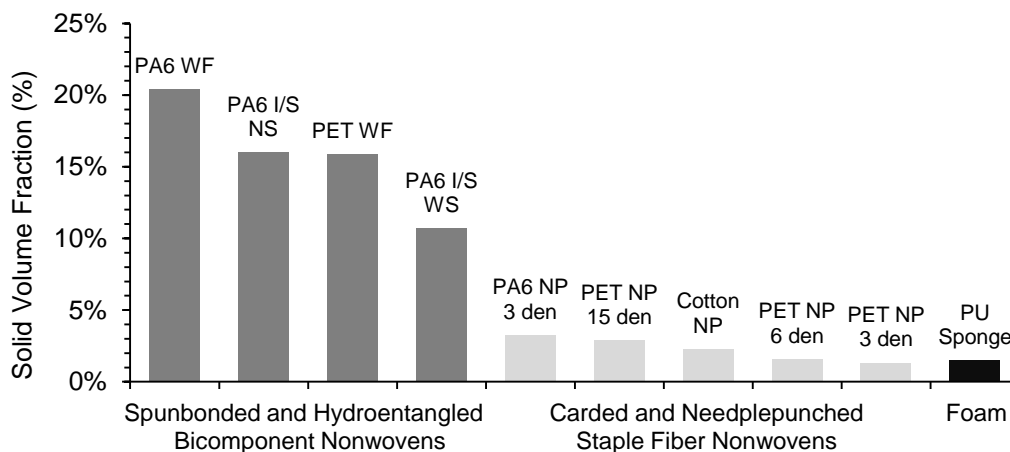


Figure 85: Comparison of SVF for substrates produced by various fabrication methods.

After determining the need for low SVF substrates, several staple fiber nonwovens were prepared. Webs using PET fibers with various diameters were formed through carding, cross-lapping and needlepunching. Lower fiber denier indicates lower fiber diameter. Figure 86a shows that lower fiber diameter webs resulted in higher CNT mass gain per dip cycle. This is consistent with the observation that higher SSA, associated with lower fiber diameter, should result in higher CNT mass gain for webs which otherwise share the same structure. The results also support the conclusion that lower SVF results in higher CNT mass gain, since the 3 denier web had the lowest SVF among this group. Figure 86b illustrates that electrical resistance drops with each dip cycle number, consistent with earlier findings of the CNT-coated sponge.

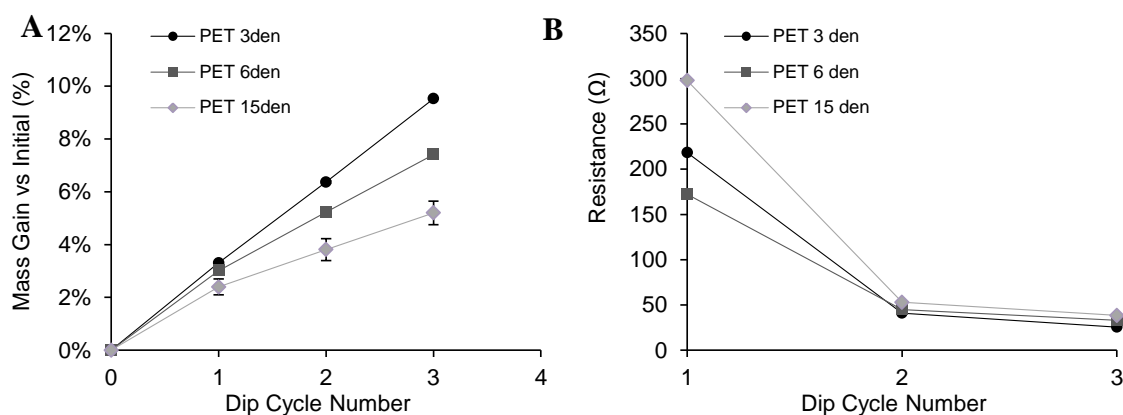


Figure 86: Plots showing (a) CNT mass gain and (b) resistance for staple fiber nonwovens made from PET fibers of different diameters - 3, 6 and 15 denier.

In order to isolate the effect of web solidity from fiber diameter and SSA, webs having the same fibers and basis weights were prepared with different SVFs. This was achieved by blending 90% PET 3 denier staple fibers with 10% binder fibers, which melt at a lower temperature than the PET. The web can be compressed to a fixed thickness by melting the binder fibers while holding it in the desired thickness. Five different thicknesses were obtained – one with no compression and four with incrementally increasing levels of compression. This resulted in five different degrees of solidity (Figure 87).

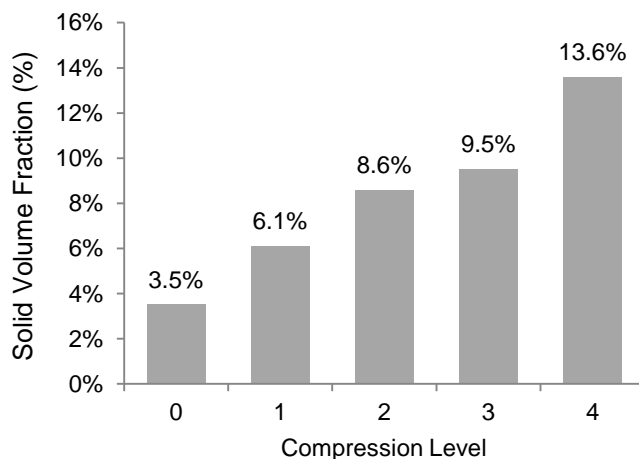


Figure 87: SVF for 5 webs having the same basis weight and fiber composition – 3 den PET – but differing in compression level.

The effect of decreasing SVF on the coating morphology can be seen using SEM (Figure 88). Figure 88a and Figure 88b show two spunbond hydroentangled materials – PA6 I/S NS and PET WF – coated with CNT EBD. The CNT coating forms a sheet-like layer that sits atop the web. Due to the high SVF, access to the interior of the web is restricted. With each dip coating cycle, the voids between fibers become clogged with sheets of CNT. This is in keeping with the observation that increased SVF leads to lower CNT mass gain. Figure 88c and Figure 88d show two carded and needlepunched PET 3 den staple fiber webs coated with CNT EBD. The one with a compression level of 4 exhibits the same caked coating morphology seen with the spunbond webs. The SVF of this web is 13.6%, approaching the SVF of the spunbond webs shown (15%). On the other hand, the SVF of the uncompressed web (Figure 88d) is much lower, at 3.5%. Interestingly, no webbing of CNT within the void

spaces of this uncompressed web can be seen. Within this group, it is the only substrate that results in the fibers being conformally coated with CNT.

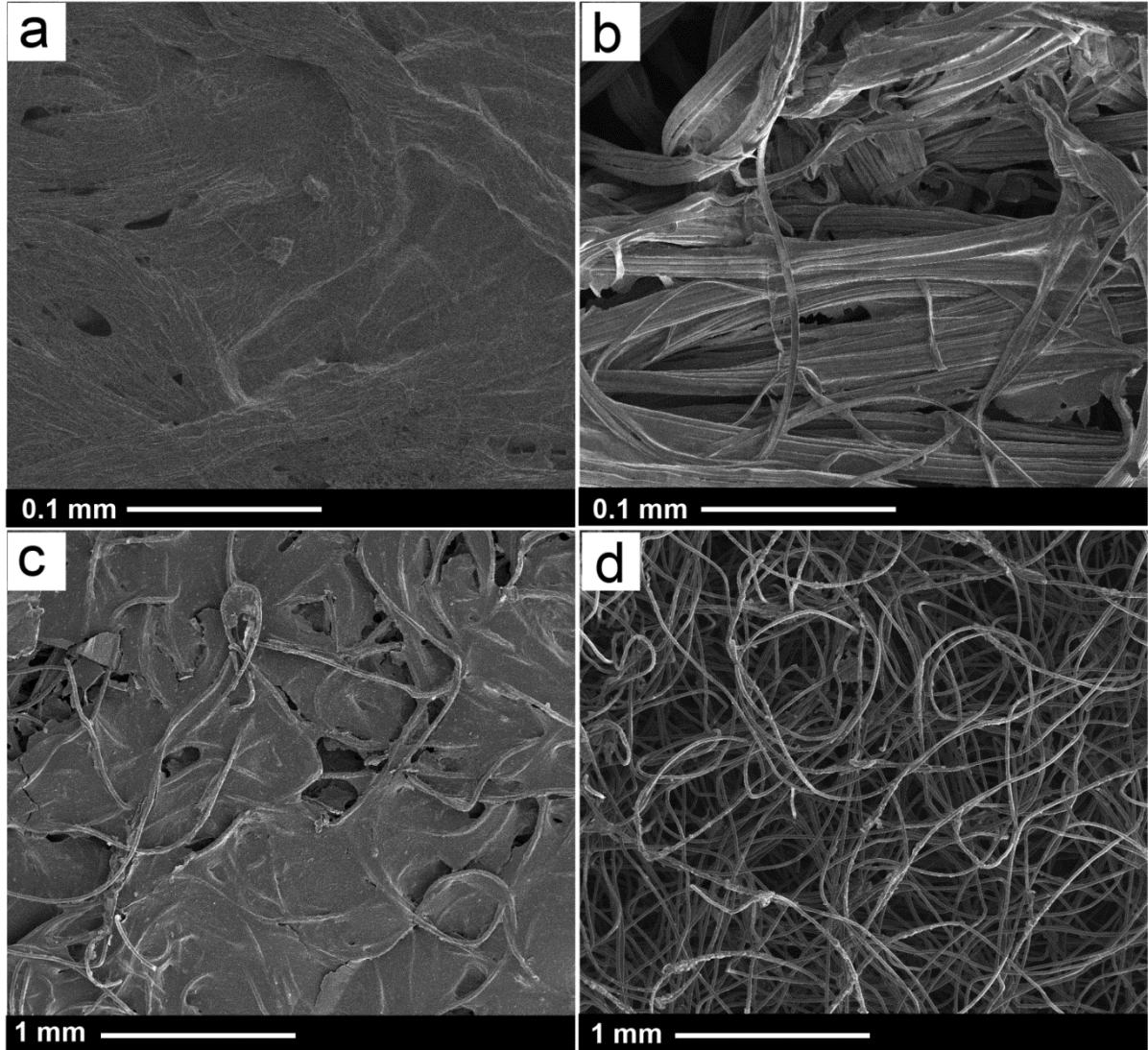


Figure 88: Four different nonwoven webs coated with CNT: (a) PA6 I/S NS, (b) PET WF, (c) PET 3 den 4x compressed, (d) PET 3den uncompressed.

5.3.4 CNT Coating onto Various Polymers

In order to determine whether the polymer type of the fiber would have a significant impact on CNT mass gain, three substrates were prepared with the same structure but made from different polymers. Meltspun PET staple fibers, meltspun PA6 staple fibers, and bleached

cotton staple fibers were each carded and needlepunched to form webs with the same basis weight (mass of 50 grams per square meter) and with a low SVF (at or below 3.5%). Over the course of 5 cycles of immersion in EBD on a shaker plate, the cotton web showed a higher uptake as compared to the other polymer types (Figure 89). The CNT, functionalized with carboxyl groups, may have stronger van der Waals interactions with certain polymers. Cotton is composed primarily of the polysaccharide cellulose, which is rich in highly polar hydroxyl groups (6 per repeat unit). PA6 is a type of polyamide which also contains a highly polar functional group – amides – but at a much lower concentration (1 per repeat unit), and PET has weakly polar ester groups (2 per unit). If van der Waals interactions are responsible for CNT mass gain, as suggested by Hu et al., it would follow that cotton would have the highest uptake, followed by PA6 and then PET.¹²⁵

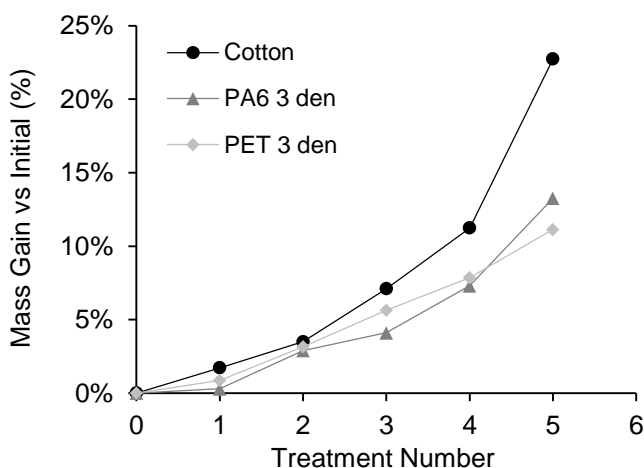


Figure 89: Mass gain as a function of treatment cycle number for needlepunched staple fiber nonwovens made from various polymer types - cotton, PA6 or PET.

Another possible explanation for the superior CNT uptake of cotton is its higher SSA. Figure 90b shows that the kidney-shaped cross-sectional shape of the cotton fibers has internal curvatures, whereas Figure 90d shows that the PA6 and PET fibers extruded through spinnerets have a round cross section. Cotton’s kidney shape results in more surface area per given mass, allowing crevices and other irregularities for the CNT to bond to (Figure 90a and Figure 90c).

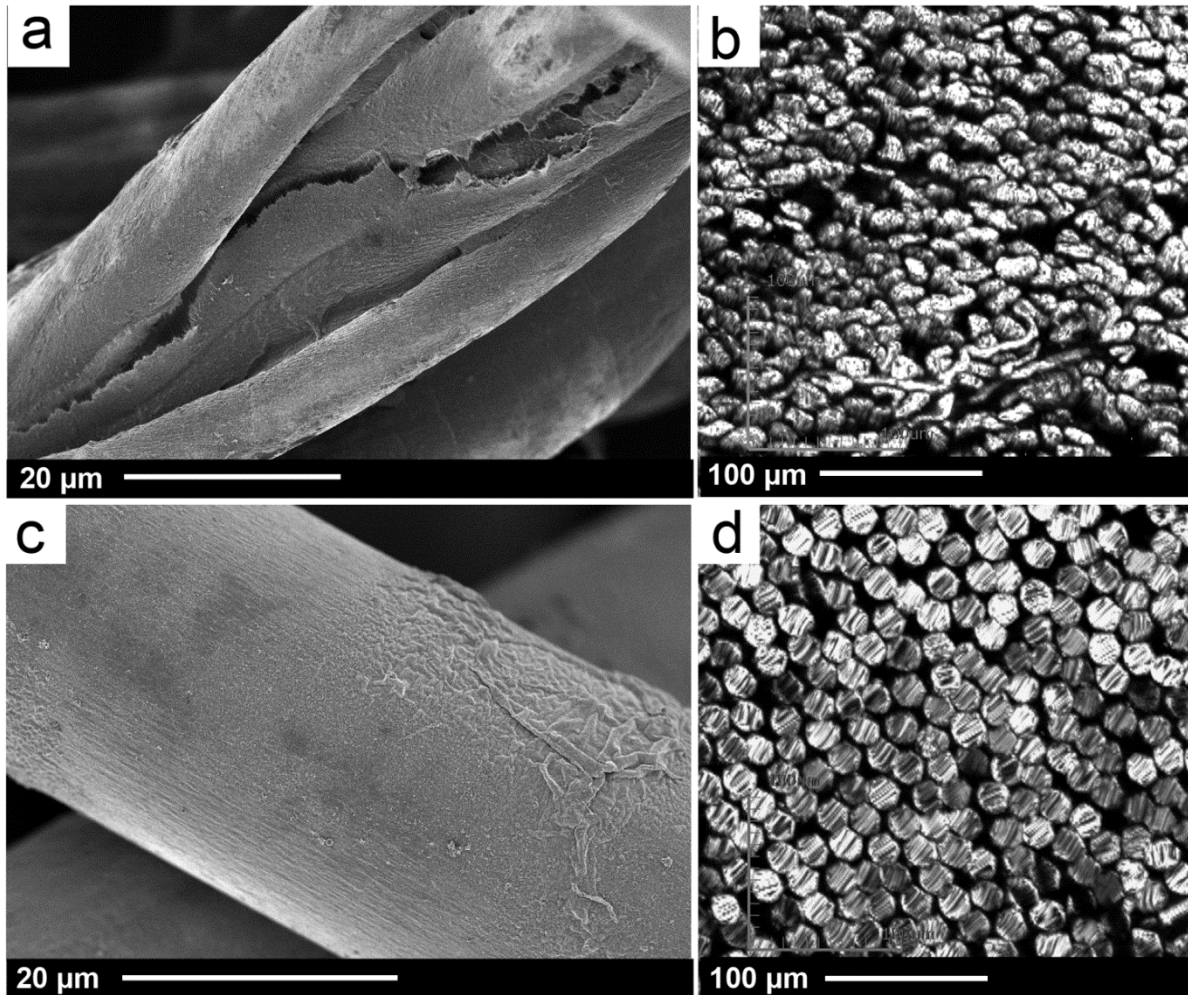


Figure 90: Cotton fiber (a) coated with CNT and (b) cut to show cross-sectional shape. PA6 fiber (c) coated with CNT and (d) cut to shown cross-sectional shape.

5.3.5 Supercapacitors from CNT-Coated Nonwovens

In terms of applications, these materials can be used in supercapacitors. Double layer capacitors are a type of supercapacitor based on ultra-high SSA conductive materials. Typically, they are manufactured using activated carbon granules, with $SSA > 1000 \text{ m}^2 \text{ g}^{-1}$ thanks to the presence of micropores throughout the granule surface. Although SSA of the CNT-coated nonwovens was not measured, it is unlikely that they could have such a high surface area due to the absence of micropores. Double layer capacitance of the CNT-coated nonwovens was measured using galvanostatic charge-discharge measurements, showing low specific capacitance values: $< 11 \text{ F g}^{-1}$ based on total electrode mass (Figure 91a) and $< 60 \text{ F}$

g^{-1} based on CNT mass only (Figure 91b). Notably, the polymer type does not seem to affect the capacitive behavior of the CNT. Regardless of polymer type, a CNT mass gain of 1% leads to a specific capacitance increase of around 0.5 F g^{-1} based on the slope of the line-of-best-fit for the data in Figure 91a.

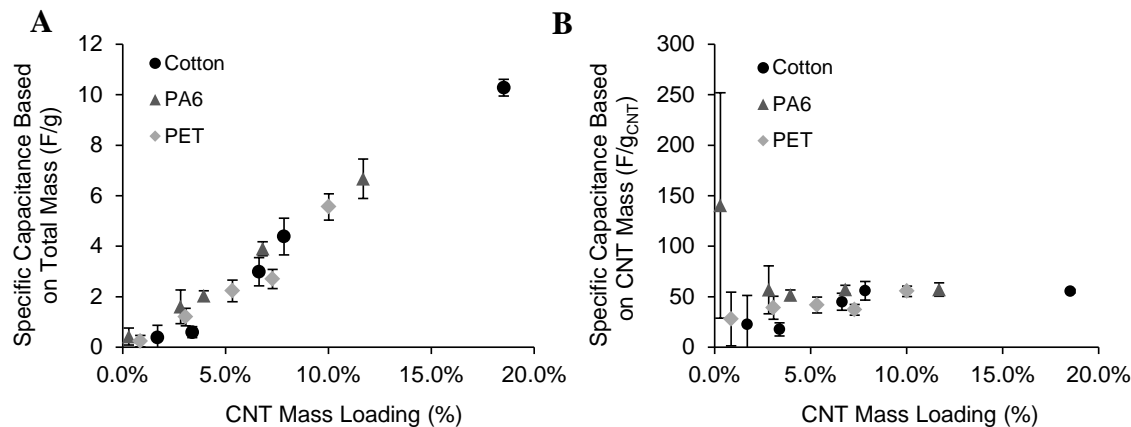


Figure 91: Double-layer capacitance for needlepunched staple fiber nonwovens coated with CNT. Specific capacitance shown (a) on the basis of total electrode mass and (b) on the basis of the CNT mass only.

Although the CNT-coated fabrics would make inferior double-layer capacitors, they can be utilized in another type of supercapacitor - pseudocapacitors. Pseudocapacitors employ redox materials adsorbed onto conductive scaffold electrodes. Others have demonstrated that fibrous conductive electrodes can be coated with redox materials to obtain high-performance pseudocapacitors.^{167,230} The key requirement for this application is low electrical resistance. Based on the galvanostatic charge-discharge curves, series resistance could be calculated. Figure 92a shows resistance drop as a function of CNT mass loading, falling below 8Ω for the cotton nonwovens with the heaviest coating. Electrochemical impedance spectroscopy was also used to assess the electrical properties of CNT-coated cotton (Figure 92b). The CNT coating causes impedance to drop by two orders of magnitude. This improved electrical conductivity indicates that the CNT-coated substrates can be used as scaffolds for the electrodeposition of redox materials.

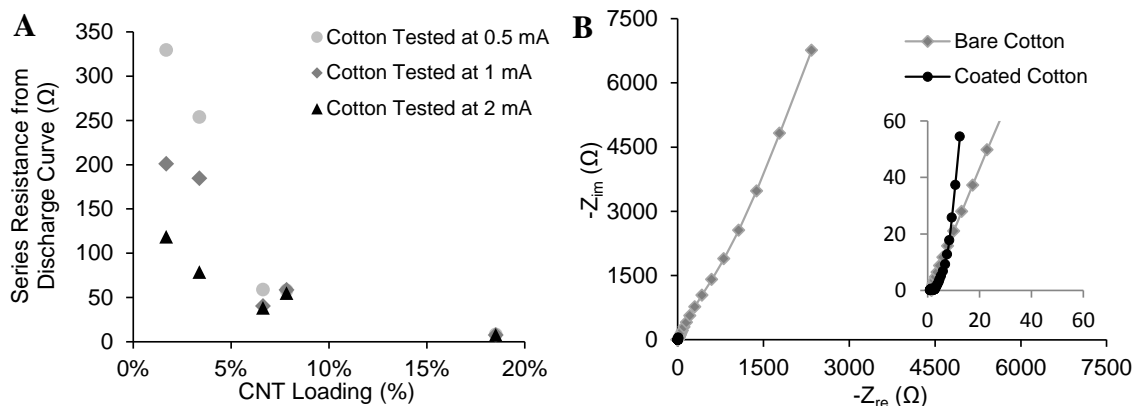


Figure 92: Electrical resistance of CNT-coated cotton fiber nonwovens. (a) Series resistance calculated from the galvanostatic discharge curve at three different current levels, as a function of CNT mass loading. (b) Nyquist plot showing impedance for coated (18%) and uncoated samples.

5.3.6 Pseudocapacitive MnO₂ on CNT-Coated PET 4DG Staple Fiber Nonwovens

The high SSA and low SVF structure of the needlepunched cotton resulted in high CNT mass uptake, but the natural fiber has many irregularities in terms of cross-section and length. In order to ensure better uniformity, meltspun PET staple fibers with a 4DGTM cross-sectional shape were used. 4DGTM fibers are engineered to have a regular multilobal cross-section, similar to cotton. Low SVF webs with excellent uniformity and high SSA were formed by carding, cross-lapping, light needling, and hydroentangling PET 4DGTM fibers. These fibers were carried through 3 CNT coating cycles (Figure 93 a + b), then deposited with pseudocapacitive MnO₂ (Figure 93 c + d) for durations ranging from 30 seconds to 5 minutes. Mass loading ranged from 0.5% to almost 5% depending on deposition time.

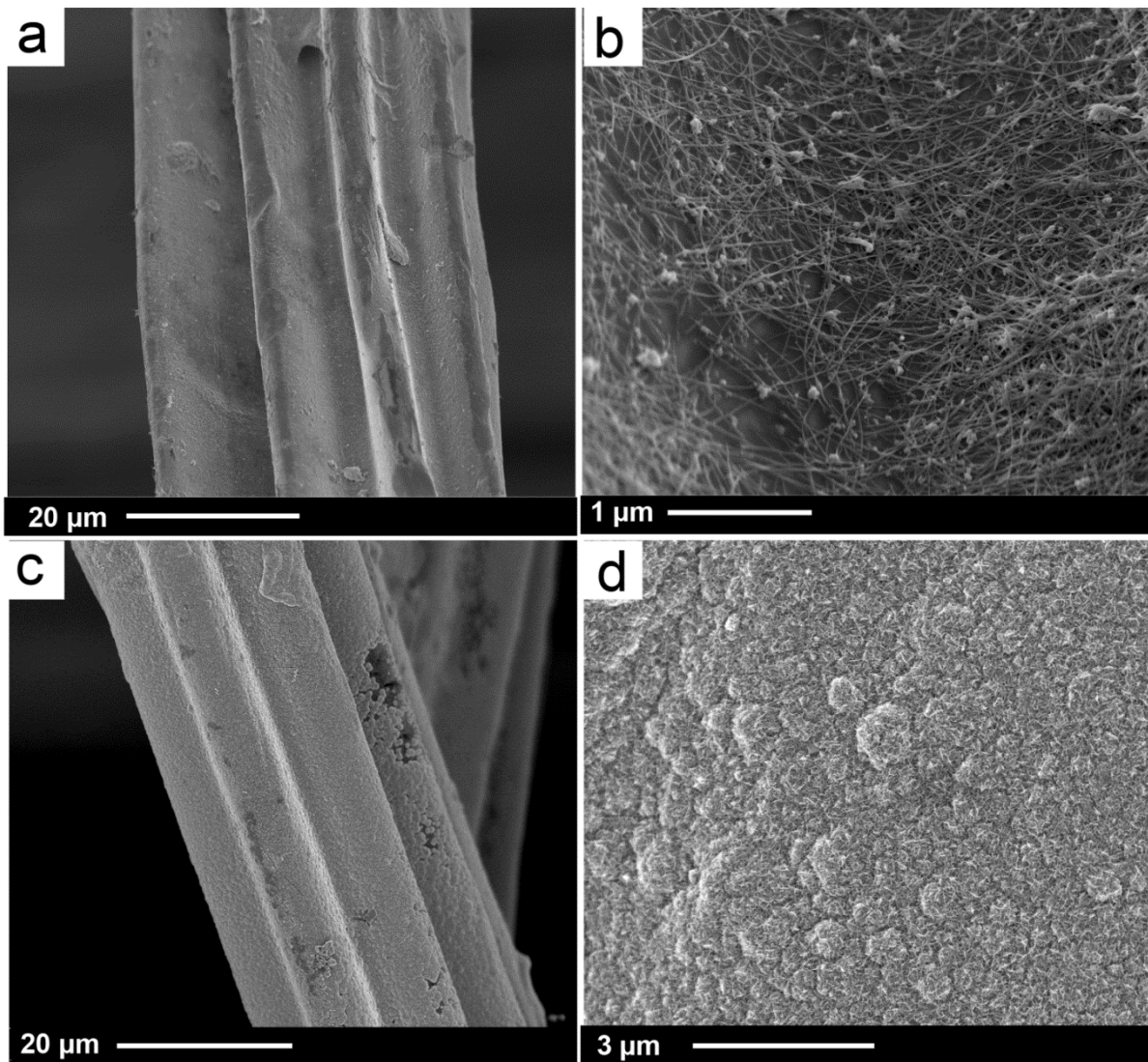


Figure 93: PET 4DG staple fiber nonwovens coated with (a + b) CNT and (c + d) subsequently deposited with MnO₂.

Nanoclusters grew on the CNT-covered fibers, consistent with the observations of other groups.¹²⁹ To confirm the identity of the Mn oxides, XPS studies of the fiber surface were carried out. Figure 94 shows the high-resolution XPS scan of the Mn 2p core level. Compared to spectra of other oxidation states such as Mn²⁺ and Mn³⁺, which show major peaks around 641 eV, the Mn⁴⁺ 2p_{3/2} spectrum is expected to show a peak shifted to the high

energy side, at 642 eV or higher.²³³ The appearance of a major peak at 642.3 eV indicates the formation of MnO₂.

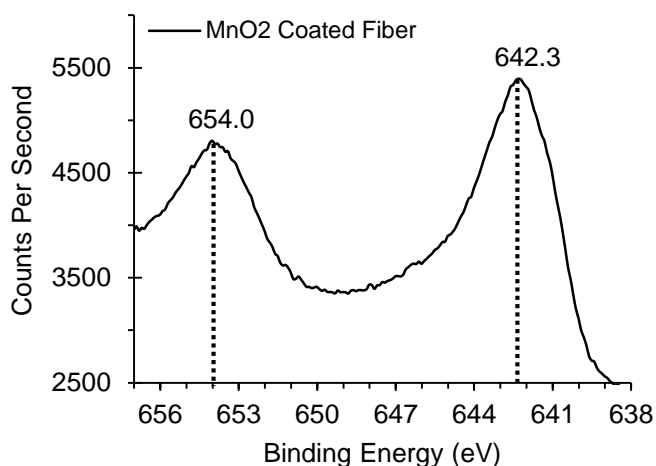


Figure 94: Binding energy of MnO₂-coated fiber surface elements as measured by XPS.

To test the performance of MnO₂-coated CNT fiber nonwovens as pseudocapacitor electrodes, test cells were assembled. Charge-discharge cycles were carried out at 0.5 mA, and capacitance was measured based on the final discharge value. EDLC, calculated from charge-discharge tests of fibers prior to electrodeposition, was subtracted in order to focus on the capacitance contributed by MnO₂. Figure 95 shows the specific capacitance of the electrodes. Specific capacitance is shown here based on two measures – capacitance per gram of MnO₂ mass, and capacitance per gram of total electrode mass. Clearly, since the mass of MnO₂ is only a small fraction of the overall electrode mass, these values will be much higher. Indeed, values for MnO₂-specific capacitance range from over 400 F g⁻¹ for the light coatings to around 200 F g⁻¹ for the heavier coatings, whereas values range from around 6 F g⁻¹ to 14 F g⁻¹ for total specific capacitance.

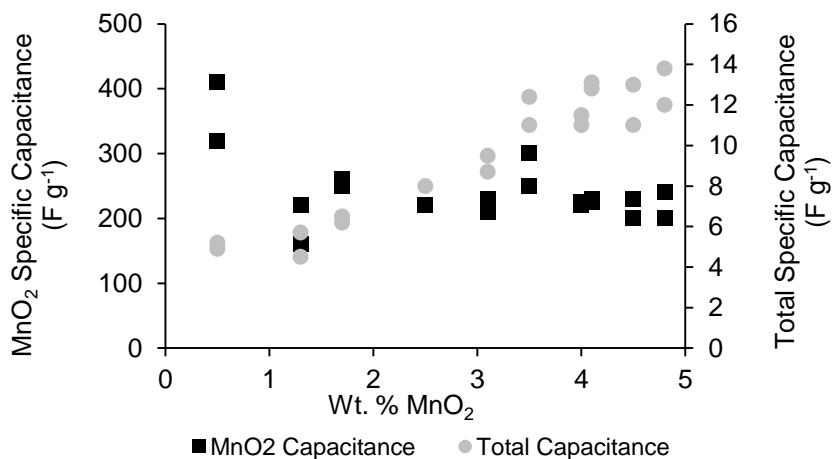


Figure 95: Specific capacitance of MnO₂ coated PET 4DG staple fiber nonwovens. Capacitance calculated on total electrode mass (grey markers) and MnO₂ mass only (black markers).

Both calculation methods are worth considering. While reports from academic laboratories tend to focus on reporting specific capacitance in terms of active material (i.e. MnO₂) only,¹²⁸ according to a review by Obreja, industry incorporates entire cell mass into calculations of specific capacitance, energy and power.²³⁴ Thus, specific capacitance as reported by academic sources may be 1000's of F g⁻¹, while industrial reports report specific capacitance of state-of-the-art supercapacitors to be around 5 – 20 F g⁻¹. In many ways, although less thrilling, the latter category represents a more practically relevant measure.

5.4 CONCLUSIONS

The aim of this study was to understand the relationship between fabric structure and CNT coating performance. Initially, high-surface area spunbonded and hydroentangled nonwovens were studied. Among these, it was seen that CNT mass gain showed a correlation with web solidity, or SVF. As a result, webs with lower SVF were produced through a different web formation process – carding. SEM images revealed that active materials were unable to penetrate into the interior fibers of high-SVF nonwovens, but were evenly distributed throughout the fibers of the low-SVF nonwovens. The impact of fiber polymer type was also investigated. A comparison of low-SVF PA6, PET and cotton nonwovens was carried out.

CNT mass loading and electrical resistance drop were most efficient for the cotton substrates, like due to greater surface functionality and higher surface area of cotton fibers. Although PA6 and PET fibers lagged behind cotton, they still showed excellent mass gain and resistance drop. Finally, a multi-lobed PET fiber was formed into a low-SVF web and coated with CNT to be used as a pseudocapacitor scaffold. Due to the low electrical resistance of the CNT-coated materials ($\sim 8 \Omega$), electrodeposition of MnO_2 was successfully carried out. Specific capacitance reached 14 F g^{-1} when calculated based on entire electrode mass, and $> 400 \text{ F g}^{-1}$ when calculated based on MnO_2 mass only. These findings clarify some of the ambiguity surrounding supercapacitor electrodes based on nonwoven substrates.

**CHAPTER 6: Graphene Coated Nonwovens as Flexible
Supercapacitor Electrodes Part I - Comparison of
Reduced Graphene Oxide with Exfoliated Graphite Flake**

6.1 INTRODUCTION

The past several years have seen a spike of research into conductive coatings on macroporous polymer scaffolds for energy storage applications. Carbon-based conductors are the preferred coating materials thanks to their superior chemical^{19,34} and mechanical¹⁶⁶ stability as compared to metals. Although solution-deposited carbon nanotube (CNT) coatings have received the vast majority of attention,^{167,230,235} the cost of purified CNT (\$300 - \$1000 per gram)²³¹ prohibits its adoption on an industrial scale. Several studies have alternatively examined conformal graphene coatings on macroporous polymer scaffolds.^{124,138,236} Graphene is the monolayer, 2D allotrope of sp² bonded carbon and has received considerable attention since Geim and Novoselov first isolated it for study.¹³⁴ In addition to possessing excellent electrical conductivity,²³⁷ the cost of natural graphite (\$0.02 per gram) is attractive from a commercial standpoint.¹⁴² However, processing challenges for obtaining highly concentrated graphene dispersions are greater¹⁵² and conductivity of the resulting graphene coatings remains several orders of magnitude lower than CNT-wrapped samples.²³⁶

Although pure graphene is difficult to disperse in a range of common solvents,^{149,238} aqueous dispersions of graphene oxide (GO) can form concentrations up to 7 mg mL⁻¹.^{144,147} GO is most commonly formed from natural graphite flake according to the process described by Hummers, which introduces oxide groups onto the basal plane (primarily tertiary alcohols and epoxides) and the sheet edges (primarily carboxyl and carbonyl groups)¹⁵³ at a C:O ratio of 2.1 to 2.9.²³⁹ Although the widespread disruption of graphene's sp² bonded structure by oxide groups renders GO nonconductive, several routes to achieving reduced graphene oxide (rGO) are well known in the literature. Among the chemical, electrochemical, plasma-induced and thermal reduction methods, the chemical approach is best suited to high-throughput industrial-scale GO coatings since polymer substrates are easily degradable, especially by thermal exposure.¹⁵⁴ Stankovich et al. demonstrated the successful conversion of GO to rGO via hydrazine (N₂H₄), which proceeds by epoxy ring-opening reactions.^{149,152} Other chemical routes, ranging from sodium borohydride (NaBH₄) to Vitamin C (L-ascorbic acid), have been explored as a consequence of the high toxicity and embrittling effect of

hydrazine.^{154,240,241} Nonetheless, as revealed by TEM imaging¹⁵¹ and measurement of electrical properties,¹⁴² the sp^2 -bonded network in rGO is incomplete and disordered. Shin et al. reduced GO by various methods and found that the highest C:O ratio for rGO was only 6.2.¹⁵⁴ As a result of its incomplete repair, rGO has conductivity similar to that of graphite (2500 S m^{-1})¹⁵³ rather than pristine graphene (10^6 S m^{-1}).^{151,156}

A different pathway to dispersing graphene is sonication-assisted exfoliated graphite flake (EGF) with surfactants typically utilized as dispersing aids. The three steps involved in this process can be simplified as: dispersion of graphite in the solvent, exfoliation of graphite into individual or few layers, and purification by sedimentation and centrifugation.²⁴² Khan et al. obtained concentrations of up to 1 mg mL^{-1} by using the solvent NMP.¹⁴⁴ NMP has a surface tension ($\gamma = 40.8 \text{ mN m}^{-1}$) close to that of graphene ($\gamma = 54.8 \text{ mN m}^{-1}$),²⁴³ but from an environmental and economic point of view, water is the preferred solvent.¹⁵² Concentrations of graphene dispersed in water tend to be no higher than around 0.1 mg mL^{-1} ,¹⁴² although Wang et al. were able to reach an ultimate graphene concentration of 0.46 mg mL^{-1} by adding 10 wt% ethanol to water, lowering surface tension to 48 mN mL^{-1} .¹⁴³ Prolonging the duration of the sonication step is another way to increase concentration. Lotya et al. obtained concentrations of 0.3 mg mL^{-1} after extending the sonication time to nearly 18 days (430 hours).¹⁴⁵ Despite these various approaches, the concentration range of EGF dispersions remains much lower than that of GO dispersions. Additionally, the use of extensive sonication can result in smaller flake dimensions ($0.25 - 0.75 \mu\text{m}$ for EGF compared to several μm for rGO) which can negatively impact electrical properties.^{144,156,242}

In 2011, Yu et al. applied the sonication-assisted EGF method to create graphene-coated textiles.²⁴⁴ Following the technique reported by other groups, graphite flake (3 mg mL^{-1}) and sodium cholate surfactant (0.5 mg mL^{-1}) were dispersed in water via 5 hours of bath sonication. Purification was achieved by 12 hours of sedimentation and one hour of centrifugation (1500 rpm). Once this EGF dispersion was prepared, a nonwoven textile made of polyester (PET) staple fiber ($20 \mu\text{m}$ diameter) was coated via 35 sequences of dip-dry

cycles. Compared to earlier work by the same group, resistance of their EGF coatings ($10^3 \Omega/\text{sq.}$) was much higher than that of their CNT coatings ($10 \Omega/\text{sq.}$).¹²⁹ However, it was found that soaking the fabrics in 6M HNO_3 every 5 cycles lowered the electrical resistance, and the resulting samples were conductive enough to be used successfully as electrodeposition substrates for MnO_2 . Two different studies, on the other hand, have presented methods of coating textiles with GO and subsequently converting to rGO.^{156,166} Sodium dithionite ($\text{Na}_2\text{S}_2\text{O}_4$) is widely known in the textile industry as a reducing agent used in vat dyeing, and it has been shown to be the most effective chemical to convert GO-coated textiles to rGO-coated textiles.²⁴⁵ Shateri-Khalilabad and Yazdanshenas found that GO-coated cotton had a resistivity of $34,600 \text{ k}\Omega \text{ cm}^{-1}$ when reduced by sodium borohydrate and $19 \text{ k}\Omega \text{ cm}^{-1}$ when reduced by sodium dithionite.¹⁶⁶

Due to the small number of studies examining graphene-coated textiles, and the various advantages and disadvantages associated with each of the two main dispersion approaches - GO and EGF – it is not yet clear which is better suited for application in textile supercapacitors. This research is focused on comparing the performance of GO and EGF dispersions when coated onto a PET staple fiber nonwoven. The fiber has a multi-lobed cross section which yields a high specific surface area, and a lofty fabric structure was chosen to support facile flow of the coating material around the individual fibers. Coatings are compared on the basis of mass gain per dip-dry cycle, electrical resistance in the through-plane and in-plane directions, and the morphology of the final coatings. Since the materials are developed for use as supercapacitor electrodes, electrochemical performance is also analyzed. Electrochemical impedance spectroscopy (EIS) reveals types of reactions occurring at the electrode surface and the impedance values associated with these processes. Specific capacitance gives a measure of the electric double-layer capacitance (EDLC) that can be expected from the electrodes as well.

6.2 EXPERIMENTAL

6.2.1 Materials

Aqueous single-layer GO dispersions (0.5 mg mL^{-1}) with a flake size of $0.3 - 0.7 \text{ }\mu\text{m}$ were purchased from Graphene Laboratories, Inc. (Calverton, NY). Dry graphite flakes with lateral dimensions of $150 \text{ }\mu\text{m}$ and greater were also purchased from Graphene Laboratories, Inc. HNO_3 (70 wt%) from Sigma-Aldrich Co. (St. Louis, MO) was diluted to 3.0 M in water. Cholaic acid sodium salt (SC) was purchased from Thermo Fisher Scientific (Waltham, MA) to be used as a surfactant. Na_2SO_4 , used in the electrolyte, and $\text{Na}_2\text{S}_2\text{O}_4$, used for the GO reduction, were also purchased from Thermo Fisher Scientific. Deionized water was used throughout the study.

6.2.2 Preparation of Exfoliated Graphite Flake Dispersion

Dry graphite flakes and SC were added to deionized water at concentrations of 3 mg mL^{-1} and 0.5 mg mL^{-1} , respectively, under 250 rpm magnetic stirring. The mixture was transferred to a bath sonicator (Branson 2800) and sonicated for various durations, ranging from 25 – 200 hours. Bath water temperature was kept below 50°C . Following sonication, the mixture was allowed to settle overnight, during which time the heaviest particles formed a sediment. The non-sedimented mixture was transferred to 50 mL centrifuge tubes, centrifuged at 1500 rpm for 60 minutes (Hermle Z300 Universal). Following centrifugation, the top 75% of supernatant was separated out and used as the purified exfoliated graphite flake (EGF) dispersion.

6.2.3 Fabrication of Nonwoven Substrates

PET staple fibers with a multi-lobed 4DGTM cross-sectional shape (Figure 96) and length of 2 inches were formed into a web at the Nonwovens Institute (NWI) at NC State University. First, fibers were mechanically opened, then processed through a feeding system and formed into a card (Trützschler High-Speed Nonwoven Card EWK 413). The card was folded via a crosslapper (Asseline Profile 415-FD) to obtain a final basis weight of 100 g m^{-2} , then lightly bonded with a pre-needler (Trützschler Single Board Needle Loom ENL). The web was fully

bonded using hydroentangling (Fleissner Aquajet 2000). The final web volume was occupied by 3% fiber and 97% air.



Figure 96: Illustration of the 4DG™ fiber shape.

6.2.4 Coating Process

PET 4DG substrates, prepared according to the process above, were cut into circular sample sized pieces (3 inch diameter). Prior to coating, the samples were first rinsed in water and ethanol to remove dirt and residues, and dried under air at 80°C for one hour. Next, they were coated with a graphene dispersion (either GO or EGF) by a series of dipping/drying cycles. The number of cycles ranged from 10 – 40. In the case of the EGF coating, after each 5 cycles, the samples were soaked in 3 M HNO₃ and then rinsed in deionized water to remove surfactant. In the case of the GO coating, the samples were carried through a chemical reduction step at the end of the coating process.

6.2.5 Reduction of Graphene Oxide Coatings

PET 4DG substrates were coated with GO as described above. An aqueous solution of the reducing agent sodium dithionite (Na₂S₂O₄) was carefully prepared to avoid oxygen exposure. Dissolved oxygen was removed from the water according to the freeze-thaw-pump process described by Pashley et al.²⁴⁶ Na₂S₂O₄ was added to the degassed water (13 mg mL⁻¹) in a nitrogen-filled glovebox. GO-coated samples were placed in the solution beakers and stirred gently for 15 minutes, undergoing a reduction reaction. The exact reaction mechanisms remain unclear, but it has been proposed that carbonyl, epoxide and hydroxyl can be reduced through several steps.²⁴⁷ As reported by Camacho et al., the following steps occur.¹⁶² First, sodium dithionite dissociates into sodium cations and dithionite anions:



Dithionite anions react with oxide and hydroxide groups, producing sulfate and sulfite ions:



Sulfite further reacts with oxygen to form sulfate:



After the reduction process, the samples were briefly rinsed in degassed water, removed from the glovebox, rinsed in deionized water and finally dried under air at 80°C for one hour.

6.2.6 Characterization of Dispersions and Coatings

A UV-Visible spectrophotometer from Thermo Scientific was used to carry out light absorption studies of the EGF dispersions, with results recorded by VISIONpro software. Mass changes due to the coating and reduction processes were recorded using a Mettler-Toledo model MS105 balance (readability = 0.01 mg). Coating surface characteristics were investigated using the Olympus FV1200 Laser Scanning Confocal Microscope.

6.2.7 Electrical Properties of Coatings

Electrical resistance in the x-y fabric direction, in-plane resistance (IPR), was found by measuring the current while applying a 1V potential using a VMP3 potentiostat/galvanostat from Bio-Logic USA, Inc. (Knoxville, TN). *IPR*, in Ω , was calculated by the following equation:

$$IPR = \frac{\Delta V}{I} \quad (43)$$

Electrical resistivity in the z-direction, through-plane resistivity (TPR), was found by measuring resistance while applying an alternating current of 1 mA from one face of the fabric to the other via copper electrodes, using an in-house setup with a nanovoltmeter and current source from Keithley Instruments, Inc. (Cleveland, OH). The TPR testing apparatus was set up in accordance with the US Fuel Cell Council's electrical conductivity testing protocol.⁴³ *TPR*, in Ω -cm, was calculated by Equation 44, where *R* is resistance in Ω , *A* is sample area in cm^2 , and *l* is sample thickness in cm:

$$TPR = \frac{R \cdot A}{l} \quad (44)$$

6.2.8 Electrochemical Properties of Coatings

Electrochemical impedance spectroscopy (EIS) was carried out to investigate the electrical and electrochemical performance of the graphene-coated samples. A three-electrode setup was constructed using a Pt current collector, an Ag/AgCl reference electrode, and a Pt counter electrode (fixed distance). The test cell was immersed in 1.0 M Na₂SO₄ electrolyte and an alternative potential of 0.5 mV was applied across a range of frequencies by the BioLogic VMP-3. The ZFit function of EC-Lab software was used to determine the best fitting model circuit and circuit element values. To measure the electric double-layer capacitance (EDLC), test cells were constructed using two 1.3 cm circular pieces of the treated samples as the electrodes, and Whatman filter paper as separator. These were sandwiched between two stainless steel current collectors and Teflon plates. The cell was connected to the BioLogic VMP-3 and immersed in 0.5 M Na₂SO₄ electrolyte. The voltage window was set to 0.8 V, and chrono-potentiometry (CP) was carried out to measure the electric double-layer capacitance (EDLC) of the CNT-coated fabrics. CP was repeated for 10 cycles to ensure stability, and the charge value used in calculations was taken from the last cycle, using a current of 0.1 mA. Equation 45, based on the series capacitor circuit model of a two-electrode cell,³⁶ was then used to obtain the gravimetric specific capacitance C_s (in units of F g⁻¹, where F = Coulomb/V). Q is charge (in Coulombs), calculated as the product of the discharge current and the discharge time. ΔV is the voltage window. The two electrode masses are represented by m_1 and m_2 (in grams).

$$C_s = \frac{Q}{\Delta V} \left(\frac{m_1 + m_2}{m_1 * m_2} \right) \quad (45)$$

6.3 RESULTS AND DISCUSSION

6.3.1 Coating of Nonwovens with Graphite Dispersions

The carded and hydroentangled PET 4DG staple fiber nonwovens were carried through multiple dip coating cycles using either GO or EGF dispersions. The average graphite loading per dip cycle was higher for the nonwovens coated with GO than those coated with

EGF. Figure 97 shows that each GO coating cycle resulted in a mass gain of 0.53%, while each EGF coating cycle resulted in a mass gain of 0.13%. As a result, the average mass gain was over 20% after 40 cycles of GO coating. Following the reduction process which transforms GO to rGO using sodium dithionite, some graphite is lost and the total mass loading drops by 3% to 17%. For EGF coating, the total mass gain after 40 dip cycles was just 5.6%.

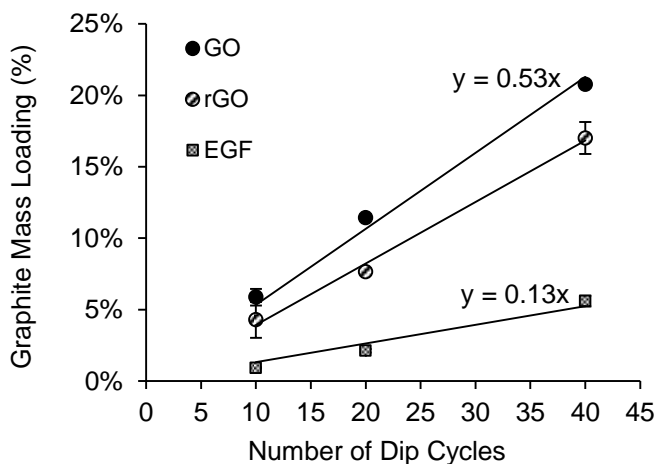


Figure 97: Graphite mass as a percentage of initial fabric mass for PET 4DG staple fiber nonwovens coated with EGF and GO dispersions. Mass loading also shown for GO coated samples after reduction to rGO.

Clearly, use of the GO dispersion results in a more efficient coating process. Compared to EGF, GO requires around 1/5 of the number of coating cycles to reach a given mass gain. This discrepancy can be attributed to differences in dispersion concentration. The GO dispersions were used as-purchased, at a concentration of 0.5 mg mL^{-1} . The EGF dispersions were obtained by bath sonication of graphite flake in water with the dispersing aid sodium cholate. Although ethanol was considered as a possible additive to lower surface tension, the absorbance of this formulation didn't show significant improvement. Previous studies have shown that extensive sonication duration is needed to obtain desirable concentrations of EGF dispersion. Sonication time of 50 hours was used since it yielded the highest concentration, as indicated by the UV-Vis absorbance spectra (Figure 98).

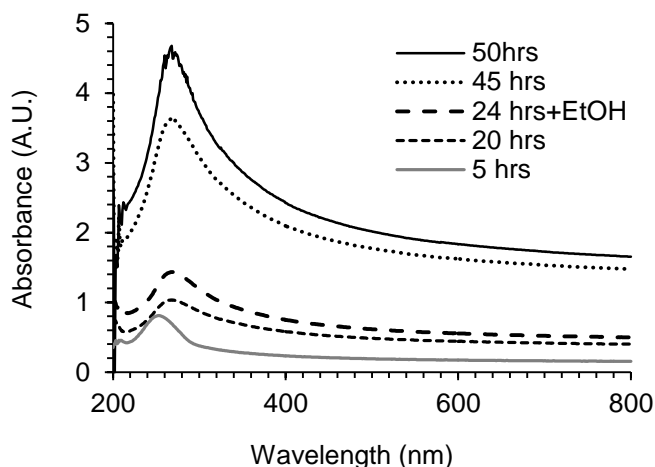


Figure 98: UV-Vis absorption spectra for EGF dispersions sonicated for various durations.

Concentration can be estimated according to the method described by Khan et al.¹⁴⁴ Based on their estimate of the extinction coefficient ($\epsilon = 3620$) and the absorbance of 660 nm wavelength light measured by UV-Vis here (1.766 for 50 hrs sonication time), concentration of the EGF dispersion would be 0.12 mg mL^{-1} . This is around 1/5 of the GO dispersion concentration, thus we would expect each EGF coating to be lighter than each GO coating.

6.3.2 Electrical Properties of EGF and GO Coated Nonwovens

GO is able to form stable aqueous dispersions thanks to the proliferation of oxide groups on the surface and edges of the graphene sheets. After the GO sheets are coated onto the fibers, it is necessary to carry out a reduction treatment in order to improve the electrical conductivity. In the oxidized form, graphene's hexagonal array of sp^2 -bonded carbons is broken by many sp^3 bonds, interrupting the flow of electricity along the molecular plane. The double bonds can be restored by removing the oxide groups through a chemical reducing agent, sodium dithionite. The in-plane resistance (IPR) was measured before and after the conversion of GO to rGO (Figure 99). The rGO-coated nonwovens display a resistance around three orders of magnitude lower than the GO-coated nonwovens. This dramatic improvement in electrical conductivity is evidence of the effective repair of a significant amount of the carbon-carbon double bonds.

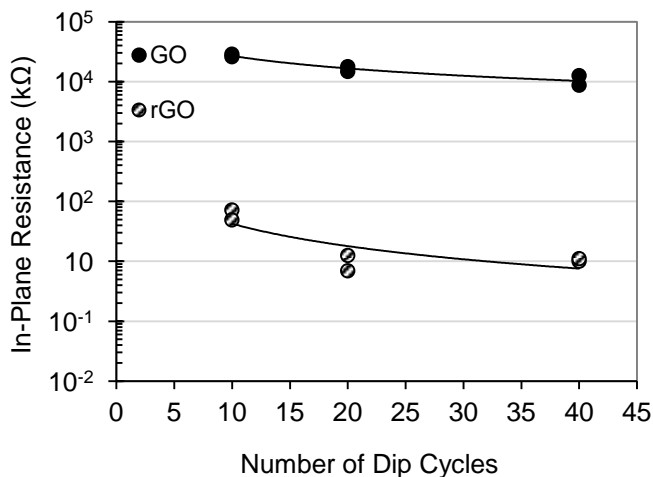


Figure 99: IPR of PET 4DG nonwovens coated with GO and after reduction to rGO.

Figure 100 compares the electrical properties of rGO and EGF coated nonwovens. The electrical resistance of the in-plane direction was measured by applying a potential of 1V along one edge of the sample and measuring the current passed through the same path. Electrical resistance of the through-plane direction was measured by sending a fixed current from the front side of the sample to the back, measuring the resulting potential through the fabric. It is important to measure the flow of electricity in both directions, since the coated fabric is a 3-dimensional object which may have anisotropic electrical properties. Figure 100a shows that the IPR of rGO-coated nonwovens is much higher than for EGF-coated nonwovens for all mass loadings in this study. EGF leads to a resistance of under 0.7 kΩ at 5.5% graphite loading, while the average resistance of rGO samples with a similar loading is around 50 kΩ. Figure 100b shows that TPR of EGF is also lower than TPR of rGO, supporting the conclusion that EGF leads to better electrical conductivity even with its lower graphite mass loadings. Although the mass loading of EGF is 80% less than GO after 40 dip cycles, electrical conductivity in the in-plane and through-plane directions are both higher.

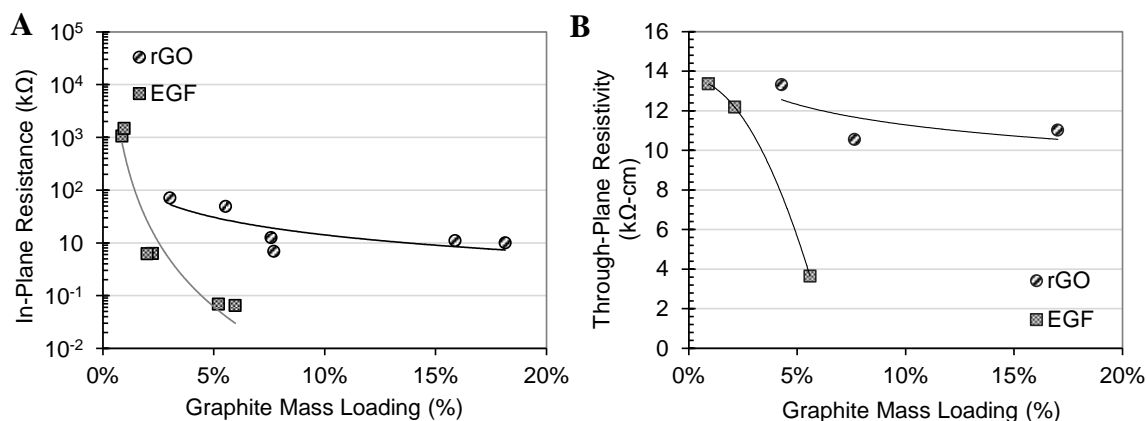


Figure 100: (a) IPR and (b) TPR of PET 4DG nonwovens coated with rGO and EGF.

Another method that can be used to measure electrical properties is electrical impedance spectroscopy (EIS). EIS is carried out by placing the sample in a three-electrode cell and immersing it in electrolyte, then measuring the impedance at a range of AC signal frequencies. The frequency-dependent response is shown in a Nyquist plot, which tracks how the relationship between real and imaginary impedance changes as frequency decreases. The high frequency response is close to the origin, and vice-versa. If the electrode provides less resistance, the overall impedance will be closer to the origin. As seen in Figure 101, increasing the number of coatings results in lower impedance for both the rGO and EGF samples. This is consistent with the IPR and TPR measurements above, and follows what we would expect.

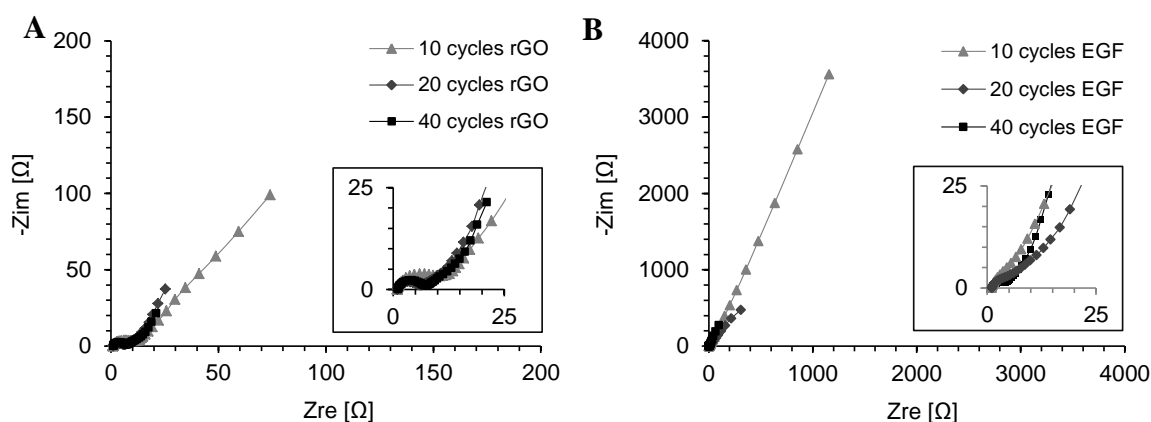


Figure 101: Nyquist plots based on EIS tests of PET 4DG samples coated with (a) rGO and (b) EGF. Inset shows low impedance region.

Since RC circuits also show frequency-dependent impedance behavior, the measured response is usually examined to determine what circuit layout is analogous to the path that an electron takes through the electrode. For example, a simple series RC circuit (analogous to double layer capacitance) would produce a straight line on the Nyquist plot, whereas a simple parallel RC circuit (analogous to pseudocapacitance) would result in a semicircle. Looking at the shapes of the curves in Figure 101a and Figure 101b, the EGF samples depict the series RC behavior associated with a double-layer capacitor, while the rGO samples form arcs, showing pseudocapacitor-like behavior. Since neither are coated with additional redox material, both would be expected to behave as double layer capacitors. The appearance of pseudocapacitive behavior in the rGO samples may be indicative that oxide groups remain bonded to the graphene sheets.

Both sets of EIS results were fitted to the same model circuit in order to compare the values of different circuit elements. Many types of circuits were tested, but the best fit came from restricting the match to the results obtained at signals between 1 Hz and 10^4 Hz. The model circuit was based on a double layer capacitor, consisting of a resistor, R1, in series with a constant phase element, Q1. The divergence from ideal capacitor behavior is given by a1, which reduces below 1 to compensate for non-ideal behavior. The Z-Fit program of EC-Lab was used to determine values of circuit elements that would give the closest match possible to the experimental curves, indicated by a low χ^2 value (Table 14). The value of the R1 for rGO increased from 0.932 to 1.402 Ω , and Q1 also increases slightly from 10 to 40 dips. For EGF, R1 decreased as expected from 0.829 Ω to 0.272 Ω . Q1 increased by more than an order of magnitude, and was two orders of magnitude higher than that of rGO. For application as an energy storage electrode, lower resistance and higher double-layer capacitance is desired, again indicating that EGF is a more suitable coating material than rGO.

Table 14: Circuit element values based on model circuit of resistor (R1) and constant phase element (Q1) in series, for PET 4DG samples coated with rGO and EGF.

	Reduced Graphene Oxide (rGO)			Exfoliated Graphite Flake (EGF)		
	10 dips	20 dips	40 dips	10 dips	20 dips	40 dips
R1 (Ω)	0.932	1.017	1.402	0.829	0.478	0.272
Q1 ($F s^{a1}$)	6.45x 10 ⁻⁴	7.06x1 0 ⁻⁴	9.13x 10 ⁻⁴	3.19x 10 ⁻³	1.91x1 0 ⁻²	6.04x1 0 ⁻²
a1	0.815	0.805	0.785	0.644	0.411	0.278
χ^2	0.026	0.043	0.047	0.189	0.399	0.418

6.3.3 Coating Morphology

Although none of the graphene coatings show potential as standalone double layer capacitors, they may perform as scaffolds for the electrodeposition of pseudocapacitive materials. This has already been demonstrated by Yu et al.²⁴⁴ Since conductivity is an essential requirement for such scaffolds, the focus of this study has been on how to obtain the highest conductivity possible by comparing two different coating approaches. In addition to having sufficient electrical conductivity, the scaffold morphology is important. Chapter 3 demonstrated the effect of inter-fiber voids being clogged with carbon nanotubes. Due to the use of highly compacted fabric scaffolds, carbon nanotube sheets formed on the surface of the fabric, shutting off access to the interior of the fabric by subsequent electrodeposition of MnO₂. In order take advantage of the surface area provided by a fibrous scaffold, pseudocapacitive material must be deposited onto the entire 3D architecture of the fabric. The interior fibers, as well as the surface fibers, should be coated uniformly.

Figure 102 shows the 4DG fiber coated with the two different forms of graphene dispersion – EGF and GO. After 20 dip coating cycles (Figure 102b), the GO sheets appear to form the coating by wrapping around the fiber and closing off the channels of the 4DG grooves. After 40 dip coating cycles (Figure 102c) the GO sheets can also wrap around more than one fiber,

binding them together. The EGF instead appears to coat the fibers in a fish-scale manner (Figure 102d), forming a conformal layer on the fiber surface rather than resting on the ridges of the grooves. After 40 dip coating cycles (Figure 102f), the EGF begins to fill in the channels. In conclusion, it appears that the EGF builds up on the fiber surface and then packs into the fiber grooves, whereas the GO sheets drape around the fibers without filling the channels and may bind neighboring fibers together.

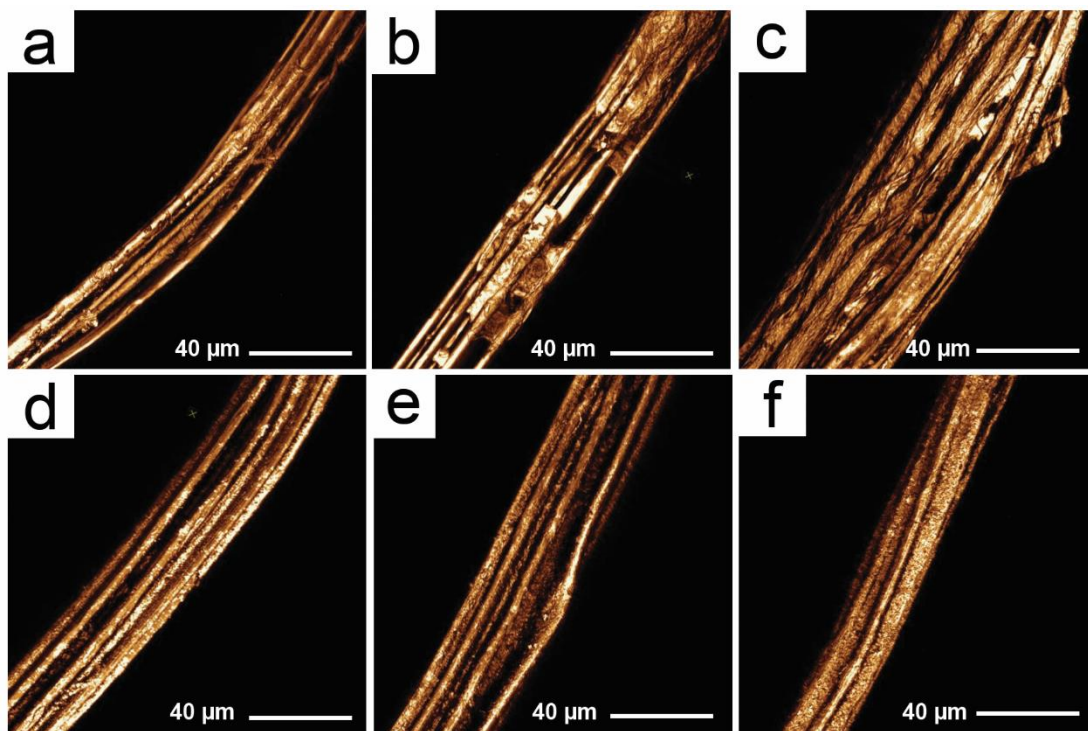


Figure 102: Laser confocal microscopy images of individual PET 4DG fibers coated with GO for (a) 10 cycles, (b) 20 cycles, (c) 40 cycles, and EGF for (d) 10 cycles, (e) 20 cycles and (f) 40 cycles.

The ability of the EGF to cover the 4DG fiber surface in “scales” of graphite can be attributed to the size of the flakes. Figure 103 was obtained by coating a glass slide with GO (Figure 103a) and another one with EGF (Figure 103b). The single GO sheet shown in Figure 103a extends beyond the frame of the microscope image, and is clearly much larger than the 4DG fiber, whose diameter is approximately 20 μm. The size of a GO sheet dwarfs that of the EGF flake – thousands of which can be seen creating a glitter-like texture in Figure 103b. The smaller size of the EGF particles allows them to coat the 4DG surface as individual

pieces. Like the tiny scales on a lizard, the small particles are able to coat all of the intricate shapes on the surface. The GO is more like pages of newspaper used to wrap a fish – the shape of the original object is lost under these large sheets.

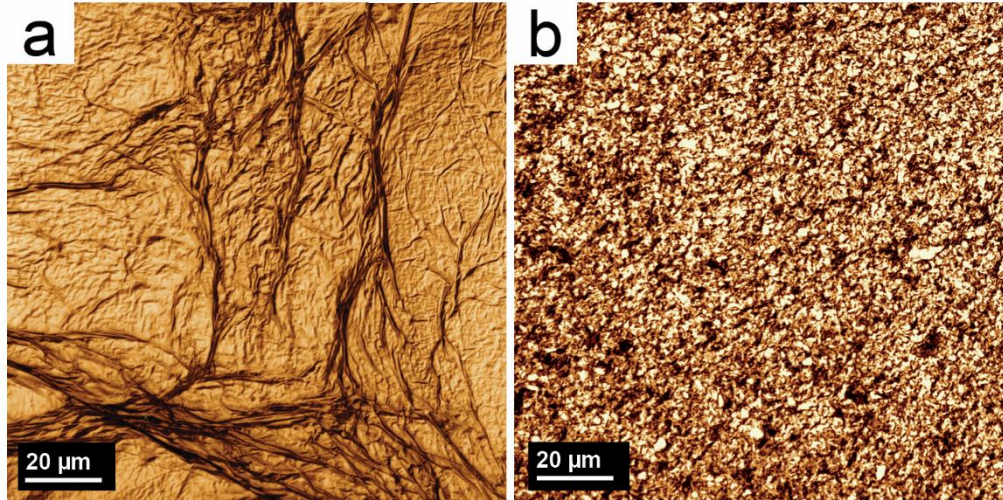


Figure 103: Laser confocal microscopy images of (a) GO and (b) EGF coated onto glass slides and evaporated.

The large size of the GO sheets can cause problems at the fabric-level as well as the fiber-level. Figure 104a shows the fabric coated with GO, and the inset image displays GO sheets forming bridges between the different fibers. When such bridges form, they introduce obstructions into the fabric structure. Materials from future coating processes will encounter these obstructions, and will get trapped rather than moving further into the interior of the fabric. Figure 104b shows the fabric coated with EGF. Even after 40 dip cycles, no bridging is observed. Considering the small scale of the EGF particles, they are not large enough to be attached to two distantly neighboring fibers.

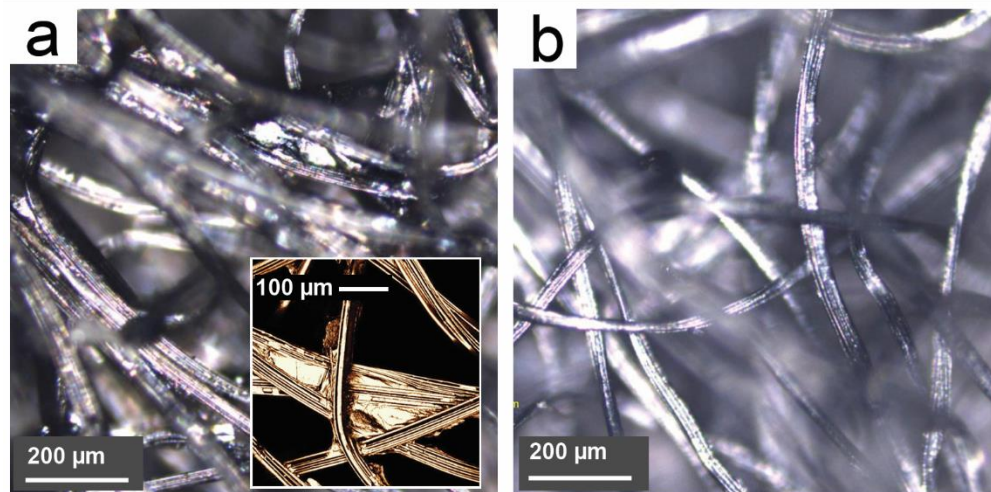


Figure 104: PET 4DG nonwoven coated with 20 cycles of (a) GO dispersion and (b) EGF dispersion. Inset of (a) shows webbing forming between adjacent fibers.

6.3.4 Double Layer Capacitance of EGF and rGO Coated Nonwovens

Double layer capacitors obtain their charge storage ability from the high surface area of the electrode material. The most common electrode material used is activated carbon ($SSA > 1000 \text{ m}^2 \text{ g}^{-1}$), and it is typically blended with carbon black and polymer binder in order to improve conductivity and strength, respectively. Galvanostatic charge-discharge cycles were carried out using symmetrical two-electrode cells of rGO and EGF coated nonwovens. Capacitance values were calculated by dividing the total charge of the last discharge cycle by the potential window. It is important to avoid using values from the first few charge-discharge cycles, as electrodes tend to undergo irreversible reactions early on. Figure 105 shows how the charge value changes over the course of the 11 cycles carried out in this study.

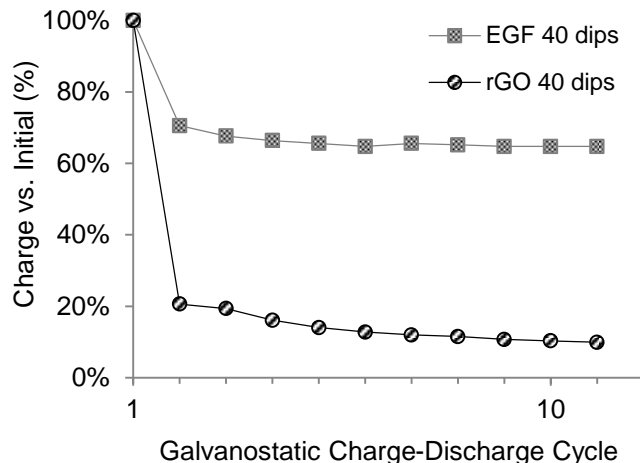


Figure 105: Charge relative to first discharge over the course of 11 charge-discharge cycles at 0.1 mA for EGF and rGO coated PET 4DG nonwovens.

After a stable charge is obtained and capacitance is calculated, specific capacitance is then found by dividing capacitance by electrode mass. Researchers are divided on whether to consider the mass of inactive materials (such as the nonconductive polymer fiber in this case) in electrode mass. Table 15 shows specific capacitance values based on total electrode mass (graphite + polymer), as well as specific capacitance based on active electrode mass only (graphite only). When entire electrode mass is considered, the rGO electrodes never rise above 0.01 F g^{-1} , and only reach 0.09 F g^{-1} when graphite mass alone is considered. EGF also shows low specific capacitance values, reaching a high of only 2.12 F g^{-1} . Specific capacitance of activated carbon is around 2 orders of magnitude higher.

Table 15: Specific capacitance based on total electrode mass and graphite mass only for rGO and EGF coated PET 4DG nonwovens, from galvanostatic charge-discharge tests.

	Reduced Graphene Oxide (rGO)			Exfoliated Graphite Flake (EGF)		
	10 dips	20 dips	40 dips	10 dips	20 dips	40 dips
Graphite mass (%)	4.3±1.3	7.7±0.1	17.0±1.1	0.9±0.1	2.1±0.1	5.6±0.4
C_s based on total electrode mass (F g⁻¹)	0.01±0.0	0.01±0.01	0.01±0.01	0.01±0.0	0.05±0.03	0.24±0.09
C_s based on graphite mass (F g⁻¹)	0.08±0.02	0.09±0.07	0.03±0.02	0.76±0.12	1.06±1.04	2.12±0.74

6.4 CONCLUSIONS

This study compared two distinct approaches to obtaining graphene-coated fabrics. GO can easily form aqueous dispersions. The absence of surfactant or other dispersing agent results in a simple one-step coating process. However, in order to remove the oxide groups and repair the graphene hexagonal structure, an additional chemical reduction step must be carried out. The EGF dispersion here was prepared by extensive (50 hours) bath sonication, and surfactant was required as a dispersing agent. Compared to the GO dispersion, which has a concentration of 0.50 mg mL^{-1} , the EGF dispersion is very dilute. Even after 50 hours of sonication, the concentration was estimated to be 0.12 mg mL^{-1} . As a consequence, it is faster to obtain a given coating weight using GO than using EGF. Following 10 dip coating cycles using GO, mass gain was around 5%. To reach this same level using EGF, 40 dip coating cycles were required. On the other hand, the EGF coatings presented many important advantages. On all measures of electrical properties, EGF coatings exhibit better conductivity. EGF samples reached IPR of $0.6 \text{ k}\Omega$, TPR of $\text{k}\Omega\text{-cm}$ and ESR of $272 \text{ m}\Omega$ despite having a lower coating mass than rGO samples. Electrochemical impedance spectroscopy and galvanostatic charge-discharge results indicated that the rGO coatings exhibited unstable pseudocapacitive behavior. This is likely due to residual oxide groups which were not completely removed during the sodium dithionite reduction process. Many researchers have observed that GO typically retains some oxide groups when converted to rGO by a wide range of methods. Complete reduction of GO presents a significant processing challenge. Another advantage associated with the EGF coatings is the morphology of the coating. The small EGF particles form a scale-like conformal coating of the 4DG surface, while the large sheets of GO become entangled between neighboring fibers and block access to the grooves in the 4DG fiber surface. As an approach to obtaining conductive nonwoven fabrics for electrodeposition scaffolds, EGF promises chemical stability and high electrical conductivity. Future studies will focus on improving the dispersion concentration and the electrodeposition process.

**CHAPTER 7: Graphene Coated Nonwovens as Flexible
Supercapacitor Electrodes Part II – Optimization of
Exfoliated Graphite Flake Coating Method**

7.1 INTRODUCTION

As consumers grow to expect their electronic devices to assume ever-more diverse shapes and textures, conductive textiles continues to gain attention.²⁰⁹ Conductive textiles may be composed of fine metal filaments, metal-coated fibers or fibers that integrate conductive polymers.²⁰⁸ For applications requiring chemical stability and mechanical robustness, such as flexible batteries or other energy storage devices, carbon is preferred as the conductor over metals.³⁴ One specific example is the development of fiber-based supercapacitor electrodes. Supercapacitors are renowned for their high power density as compared to batteries, yet their sub-par energy density has led to interest in using high-surface area electrodes.¹²¹ Electric-double layer capacitance (EDLC) devices rely on non-faradaic charge storage at the electrode-electrolyte interface, but even fibrous electrodes don't offer enough surface area to make them viable supercapacitors. Activated carbons having specific surface area (SSA) upwards of $2500 \text{ m}^2 \text{ g}^{-1}$ are typically used for EDLC electrodes.²¹ Conductive fibers can, however, be coated with redox-active materials such as transition metal oxides or conductive polymers, resulting in high performance supercapacitors of the type classified as pseudocapacitors.¹⁶⁷ The fiber scaffolds offer a 3D architecture to support the flow of electrolyte throughout the pseudocapacitive network.²³⁰

The most widely documented type of conductive coating material for this application is carbon nanotubes (CNT).^{125,167,227,229,235} In a typical process, COOH-functionalized CNT are dispersed in a surfactant-water solvent mixture via horn or bath sonication. The polymer scaffold is then dipped repeatedly into the CNT dispersion until electrical resistance is adequately lowered. Hu et al. measured a sheet resistance of $10 \text{ } \Omega/\text{sq.}$ after just three dip-dry cycles.¹²⁹ A major impediment to the adoption of CNT-coated textiles is their prohibitive cost (\$300 - \$1000 per gram).²³¹ Graphene, by contrast, is derived from low-cost natural graphite (\$0.02 per gram).¹⁴² Several researchers have consequently investigated graphite-derived graphene as an alternative dispersant in conductive coatings.^{144,146,248} Some have focused on high-concentration graphene oxide (GO) dispersions, which can be coated onto the substrate and then subjected to a chemical treatment – typically sodium dithionite ($\text{Na}_2\text{S}_2\text{O}_4$) –

converting GO to reduced graphene oxide (rGO) by removing a portion of the oxide groups.^{156,166,245} The biggest downfall to this approach is that the sp^2 -bonded network of rGO remains partially disordered, never quite approaching the excellent electrical properties promised by pristine graphene.¹⁵³ Our group has observed that the residual oxide groups from GO-coated supercapacitor electrodes undergo irreversible and undesirable redox reactions during cycling and are ultimately poor conductors.

Natural graphite can also be exfoliated in water via ultrasonication with the aid of amphiphilic surfactant.¹⁴² Although this exfoliated graphite flake (EGF) method produces coatings having better electrical properties than rGO, EGF dispersions suffer from low concentration.¹⁴⁶ According to the standard EGF dispersion preparation method, concentrations between 0.01 - 0.1 mg mL⁻¹ can be expected.^{142,249} Different tactics have been explored to overcome this challenge. Lotya et al. prolonged sonication time to 430 hours (nearly 18 days), and were able to increase concentration up to 0.3 mg mL⁻¹.¹⁴⁵ Meanwhile, other studies have shown that modifying the solvent surface tension or optimizing surfactant component can lead to concentrations from 0.5 – 1.0 mg mL⁻¹.^{143,144,250} However, these techniques also rely on extensive sonication times. In attempting to reduce the time needed for experiments, Guardia et al. started with a much higher graphite concentration (100 mg mL⁻¹) compared to most studies (3 mg mL⁻¹), thereby reducing the sonication time required for a 0.1 mg mL⁻¹ dispersion from 200 hours to 2 hours.^{145,250} Green and Hersam were able to achieve the same results in just 1 hour by using a more powerful form of sonication (horn sonication).¹⁴²

This study focuses on increasing EGF dispersion concentration by using horn sonication and elevating the initial concentration of natural graphite. The dispersion concentrations are compared to bath-sonicated EGF dispersions on the basis of UV-vis absorption measurements. Quality of the graphene flakes is examined using dynamic light scattering (DLS) particle size measurements. Textile samples are coated with the various EGF dispersions and compared in terms of mass gain, electrical conductivity and EDLC

performance. The substrate properties represent another set of variables that may affect the performance of graphene-coated textiles. To date, the few reports of graphene coatings have used various substrates: woven vectran,¹⁵⁶ woven cotton,¹⁶⁶ and nonwoven polyester²⁴⁴. The potential impact of substrate properties has not been reported previously, and the vast discrepancies between the coating methods masks any effects that could be extrapolated. In this study, the impact of specific surface area (SSA) is considered by comparing the mass gain, electrical properties and electrochemical performance of textiles with two different SSA coated with the same EGF dispersion. The study concludes with a comparison of CNT and graphene coated textiles, using both as scaffolds for the electrodeposition of pseudocapacitive polyaniline (PANI).

7.2 EXPERIMENTAL

7.2.1 Preparation and Characterization of Aqueous Graphite Dispersions

Dry graphite flake was added to deionized water at various concentrations (3 - 30 mg mL⁻¹) and SC was added at 0.5 mg mL⁻¹. Graphite flakes with lateral dimensions of $\geq 150 \mu\text{m}$ were purchased from Graphene Laboratories, Inc. (Calverton, NY), while the dispersing agent cholaic acid sodium salt (SC) was purchased from Thermo Fisher Scientific (Waltham, MA). Dispersion was accomplished either through bath sonication (Branson 2800 Ultrasonicator) or horn sonication (QSonica Ultrasonic Processor Q500 with ½” titanium alloy horn tip). When the bath sonicator was used, sonication time ranged from 50 – 200 hours and water temperature was kept below 50°C. When the horn sonicator was used, amplitude was set to 50%, sonication time ranged from 2 – 10 hours, and the process was carried out in an ice bath. Following sonication, the mixtures were allowed to settle overnight, and the heaviest particles formed a sediment at the bottom of the container. The non-sedimented mixture was transferred to 50 mL centrifuge tubes, centrifuged at 1500 rpm for 60 minutes (Hermle Z300 Universal). After centrifugation, the top 75% of supernatant was separated out and used as the purified exfoliated graphite flake (EGF) dispersion. A UV-Visible spectrophotometer (Thermo Scientific Evolution500) was used to carry out light absorption studies of the EGF and GO dispersions, with results recorded by VISIONpro software. Dynamic light scattering

(DLS) using a Zetasizer Nano ZS (fitted with red 633 nm laser) was carried out to examine the flake size distribution in the dispersions. DLS results were analyzed by number and intensity using the on-board Zetasizer software.

7.2.2 Formation of PET Nonwovens

Two polyester nonwovens were used: polyester 4DGTM carded web (PET 4DG) and polyester winged fiber spunbonded web (PET WF). Cross-sectional shapes of the two fiber types are shown below (Figure 106).

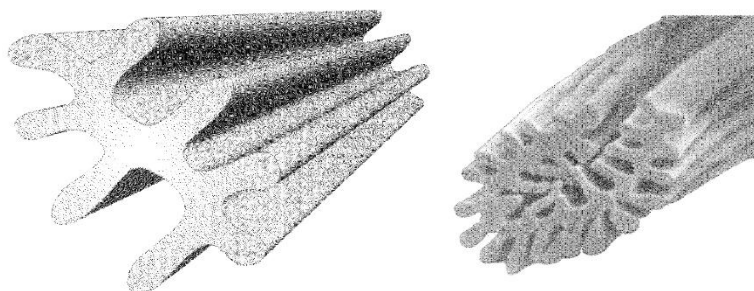


Figure 106: Cross-sectional shapes of 4DGTM (left) and WF (right).⁵⁷

The PET WF was obtained from Allasso Industries, Inc. (Raleigh, NC). The web was formed out of continuous bicomponent PLA/PET fibers in a spunbond process. Hydroentangling was used to bond the web and wash away the sacrificial PLA, leaving behind a strong fabric made of high surface area PET fibers. The final PET WF web volume was occupied by 20% fiber and 80% air.

The PET 4DG was formed at the Nonwovens Institute (NWI) at NC State University. Staple fibers with multi-lobed 4DGTM cross-sectional shape and length of 2 inches were mechanically separated, then processed through a feeding system and formed into a card (Trützschler High-Speed Nonwoven Card EWK 413). The card was folded via a crosslapper (Asseline Profile 415-FD) to obtain a final basis weight of 100 g m⁻², then lightly bonded with a pre-needler (Trützschler Single Board Needle Loom ENL). The web was fully bonded

using hydroentangling (Fleissner Aquajet 2000). The final PET 4DG web volume was occupied by 6% fiber and 94% air.

7.2.3 Graphene Coating Process

PET 4DG and PET WF substrates, prepared according to the process above, were cut into circular sample sized pieces (3 inch diameter). Prior to coating, the samples were first rinsed in water and ethanol to remove dirt and residues, and dried under air at 80°C for one hour. Next, they were coated with the EGF graphene dispersion in a sequence of between 5 and 40 dip/dry cycles. In order to eliminate surfactant from accumulating in the dried coating, the dip/dry process was interrupted after every 1% in mass gain, and samples were soaked in 3 M HNO₃ for one hour. Next, they were removed, rinsed in abundant DI water, dried under air, and the dip/dry process was resumed. HNO₃ (70 wt%) was purchased from Sigma-Aldrich Co. (St. Louis, MO) and diluted to 3.0 M in deionized water. Mass changes due to the coating and reduction processes were recording using a Mettler-Toledo model MS105 balance (readability = 0.01 mg). Coating surface characteristics were investigated with a field-emission scanning electron microscope at the Analytical Instrumentation Facility (Raleigh, NC) as well as a laser scanning confocal microscope (Olympus FV1200).

7.2.4 Characterization of Electrical Properties

Electrical resistance in the x-y fabric direction, in-plane resistance (IPR), was found by measuring the current while applying a 1V potential using a VMP3 potentiostat/galvanostat from Bio-Logic USA, Inc. (Knoxville, TN). *IPR*, in Ω , was calculated by the following equation:

$$IPR = \frac{\Delta V}{I} \quad (46)$$

Electrical resistivity in the z-direction, through-plane resistivity (TPR), was found by measuring resistance while applying an alternating current of 1 mA from one face of the fabric to the other via copper electrodes, using an in-house setup with a nanovoltmeter and current source from Keithley Instruments, Inc. (Cleveland, OH). The TPR testing apparatus was set up in accordance with the US Fuel Cell Council's electrical conductivity testing

protocol.⁴³ TPR , in $\Omega\text{-cm}$, was calculated by Equation 47, where R is resistance in Ω , A is sample area in cm^2 , and l is sample thickness in cm :

$$TPR = \frac{R \cdot A}{l} \quad (47)$$

Electrochemical impedance spectroscopy (EIS) was carried out to investigate the electrical and electrochemical performance of the graphene-coated samples. A three-electrode setup was constructed using a Pt current collector, an Ag/AgCl reference electrode, and a Pt counter electrode (fixed distance). The test cell was immersed in 1.0 M Na_2SO_4 electrolyte and an alternative potential of 0.5 mV was applied across a range of frequencies by the BioLogic VMP-3. Na_2SO_4 , used in the electrolyte, was purchased from Thermo Fisher Scientific. The ZFit function of EC-Lab software was used to determine the best fitting model circuit and circuit element values.

7.2.5 Electric Double Layer Capacitance

To measure the electric double-layer capacitance (EDLC), test cells were constructed using two 1.3 cm circular pieces of the treated samples as the electrodes, and Whatman filter paper as separator. These were sandwiched between two stainless steel current collectors and Teflon plates. The cell was connected to the BioLogic VMP-3 and immersed in 0.5 M Na_2SO_4 electrolyte. The voltage window was set to 0.8 V, and chrono-potentiometry (CP) was carried out to measure the electric double-layer capacitance (EDLC) of the CNT-coated fabrics. CP was repeated for 10 cycles to ensure stability, and the charge value used in calculations was taken from the last cycle, using a current of 0.1 mA. Equation 48, based on the series capacitor circuit model of a two-electrode cell,³⁶ was then used to obtain the gravimetric specific capacitance C_s (in units of F g^{-1} , where $\text{F} = \text{Coulomb/V}$). Q is charge (in Coulombs), calculated as the product of the discharge current and the discharge time. ΔV is the voltage window. The two electrode masses are represented by m_1 and m_2 (in grams).

$$C_s = \frac{Q}{\Delta V} \left(\frac{m_1 + m_2}{m_1 \cdot m_2} \right) \quad (48)$$

7.2.5 Electrodeposition and Characterization of Pseudocapacitor Performance

Polyaniline (PANI) was electropolymerized on the surface of the EGF-coated fibers. The electrodeposition procedure followed the methods outlined in our earlier study.²⁵¹ Briefly, graphene-coated samples, measuring 4 cm x 4 cm were immersed in an aqueous solution containing 0.25 M aniline and 0.5 M H₂SO₄. Aniline and sulfuric acid were both purchased from Thermo Fisher Scientific. A stainless steel counter electrode was employed. Using the BioLogic VMP3 potentiostat/galvanostat, a potential of 0.777 V vs. Ag/AgCl (0.733 V vs. SCE) was applied for 20 minutes, causing the oxidative polymerization of aniline on the graphene-coated nonwoven surface. Following deposition, each sample was rinsed under running DI H₂O for 20 seconds on each side and dried at 70°C under air for one hour. Pseudocapacitance was tested in the same manner as EDLC, described in the preceding section.

7.3 RESULTS AND DISCUSSION

7.3.1 Highly Concentrated Graphite Dispersions

EGF dispersions were first prepared according to the method commonly reported by others.^{145,244} Lotya et al. found that bath sonication time was the limiting factor in increasing the ultimate flake concentration in the dispersions. From around 50 to 200 hours of sonication time, concentration seemed to plateau at around 0.15 mg mL⁻¹, gradually increasing to around 0.3 mg mL⁻¹ after 430 hours of sonication time. These results were partially reproduced here by using the same concentrations of graphite flake and surfactant in water (Figure 107). Four batches were prepared with different sonication times up to 200 hours, and UV-vis absorption spectra showed a marked increase in concentration from 25 to 50 hours. Between 50 and 100 hours, a less significant increase was obtained and absorbance did not increase at all between 100 and 200 hours. Sonication time was not extended beyond 200 hours, since prolonging sonication past one week makes the process increasingly less relevant from the perspective of industrial applications.

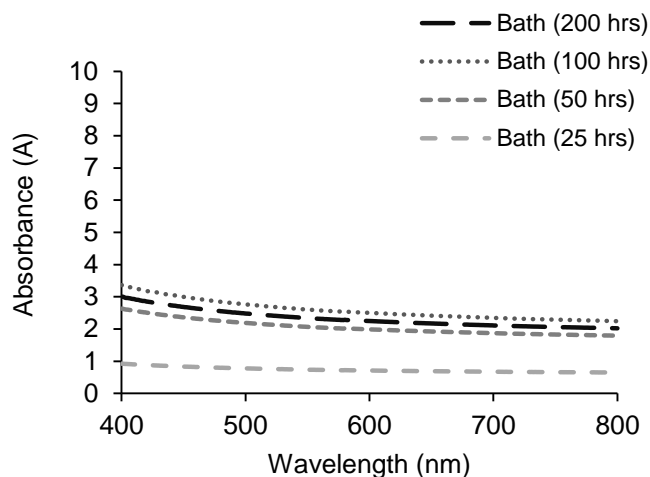


Figure 107: UV-Vis absorbance spectra (range of 400 – 800 nm) for EGF dispersions sonicated by bath for various durations.

100 hours of bath sonication requires two weeks of lab time, which limits the practicality of this method. In an effort to shorten the preparation duration, a more powerful horn sonicator was employed. Although bath sonication has been assumed to minimize damage to flakes, a report by Green and Hersam utilized horn sonication in their experiments.¹⁴² In addition, the initial graphite concentration was increased tenfold to 30 mg mL^{-1} , still lower than that used by Guardia et al. in their study on the effect of surfactant type.²⁵⁰ Here, horn sonication was carried out for various durations, from 2 – 10 hours. Using the new method, the absorbance after just 4 hours of horn sonication surpassed 100 hours with bath sonication (Figure 108).

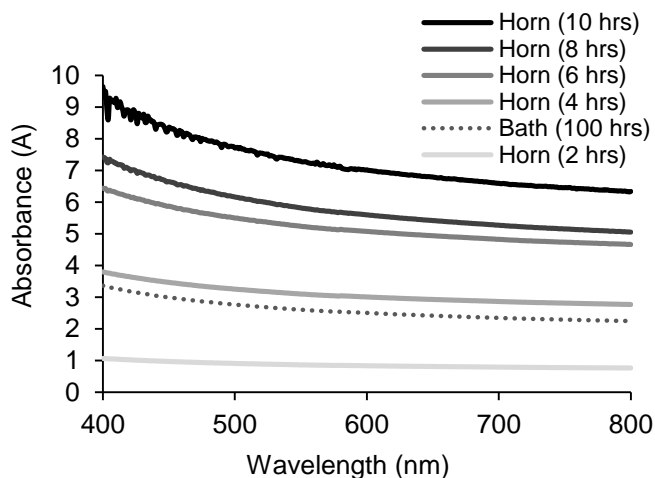


Figure 108: UV-Vis absorbance spectra (range of 400 - 800 nm) for EGF dispersions sonicated by horn for various durations and by bath for 100 hours.

Several groups have previously employed Beer's Law to determine dispersion concentration from the absorbance value (A) at 660 nm.^{142,144,145} The following expression is used to calculate graphene concentration (C_g):

$$C_g = \frac{A}{\alpha * l} \quad (49)$$

The path length (l) is based on the cuvette size, and the absorption coefficient (α) is a constant that is determined experimentally. It was found that dispersion concentration was linearly related to A/l , exhibiting Lambert-Beer behavior, and the slope gave an absorbance coefficient of $\alpha = 1447 \text{ mL mg}^{-1} \text{ m}^{-1}$, slightly higher than that measured by Lotya et al. ($1400 \text{ mL mg}^{-1} \text{ m}^{-1}$).²⁴⁹ Table 16 displays the various results of concentration calculations using these three different coefficient values.

Table 16: UV-vis absorbance values and derived graphene concentrations, based on three different absorption coefficient estimates.

Sonication Method	Sonication Time (hrs)	Absorbance at 660 nm	Graphene Concentration (mg mL⁻¹)
Horn	2	0.808	0.140
	4	2.914	0.503
	6	4.916	0.849
	8	5.388	0.931
	10	6.738	1.164
Bath	50	1.912	0.330
	100	2.400	0.415
	200	2.159	0.373

Figure 109 displays concentration as a result of sonication time, showing values obtained with different sonication methods. It can be seen that a few hours (anything more than two hours) of horn sonication results in higher EGF concentrations than hundreds of hours of bath sonication. For horn-sonicated dispersions, concentration ranges from 0.14 mg mL^{-1} to 1.16

mg mL⁻¹ depending on sonication time. This latter value meets the high concentrations achieved by using NMP and other harmful solvents, and is nearly an order of magnitude greater than what is achievable using the bath sonication method.

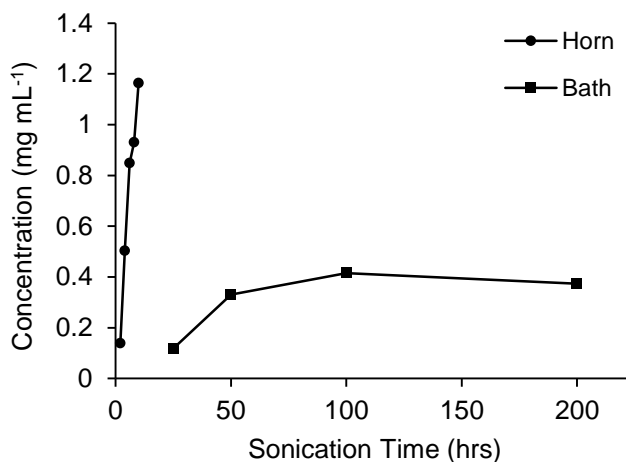


Figure 109: EGF concentration as a result of sonication time, calculated based on absorbance coefficient of 1447 mL mg⁻¹ m⁻¹.

As a means to determine whether the horn sonicator was imparting additional damage to the flakes, dynamic light scattering (DLS) was carried out on the dispersions sonicated by bath and by horn. DLS works by tracking particle motion and analyzing the results based on Brownian Motion theory. Particles with larger hydrodynamic sphere diameters are bound to move more slowly, and thus sphere size can be calculated. The intensity distribution reflects the impact of particles of various sizes on the detected results, so more weight is attributed to the larger particles since they reflect more light. Figure 110 shows the average intensity distributions for the highest concentration dispersions obtained by bath and horn sonication. Both show a bell-shaped distribution, with the bath sonicated dispersion showing additional peaks at smaller and larger diameters. Notably, the horn sonicated sample shows a larger mean intensity diameter. Rather than indicating additional damage, these results imply that horn sonication leads to larger, less broken graphite flakes.

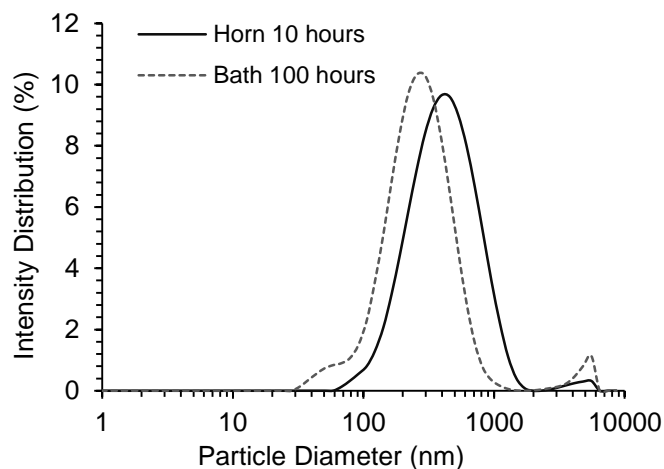


Figure 110: Particle size distribution based on intensity for EGF dispersions sonicated by bath and by horn.

Table 17 lists the intensity-average and number-average hydrodynamic sphere diameters for the various dispersions. As described above, the intensity average gives more weight to larger particles. The number average, on the other hand, counts particles as individuals and reflects an average of the most common (rather than the most influential) sphere size. The intensity average did not show a clear dependence on time or on method. The values were all in the same order of magnitude, ranging from 0.34 μm to 0.74 μm . Number average ranged from 0.11 μm to 0.28 μm . Compared to average flake size reported by other groups utilizing bath sonication, the dimensions of the flakes obtained here through horn sonication are comparable.^{144,156,242}

Table 17: Average particle diameter for EGF dispersions sonicated by horn and by bath for various dispersions, based on DLS measurements and Zetasizer software.

Sonication Method	Sonication Time (hrs)	Intensity-Average Diameter (μm)	Number-Average Diameter (μm)
Bath	50	0.58 ± 0.07	0.11 ± 0.01
	100	0.46 ± 0.03	0.17 ± 0.03
	200	0.64 ± 0.13	0.15 ± 0.02
Horn	2	0.57 ± 0.03	0.12 ± 0.02
	4	0.74 ± 0.14	0.19 ± 0.06
	6	0.68 ± 0.09	0.28 ± 0.02
	8	0.34 ± 0.04	0.13 ± 0.07
	10	0.51 ± 0.06	0.24 ± 0.06

7.3.2 Coating of 4DG Nonwovens

PET 4DG staple fiber nonwoven sheets were prepared and coated with the 100 hour bath sonicated EGF dispersion for 40 dip cycles. SEM images (Figure 111) show that the graphite flakes form a conformal coating on the fibers, neatly following the distinctive channels of the 4DG fiber. Figure 111b (inset) shows that the graphite flakes have taken on a wide range of flake dimensions.

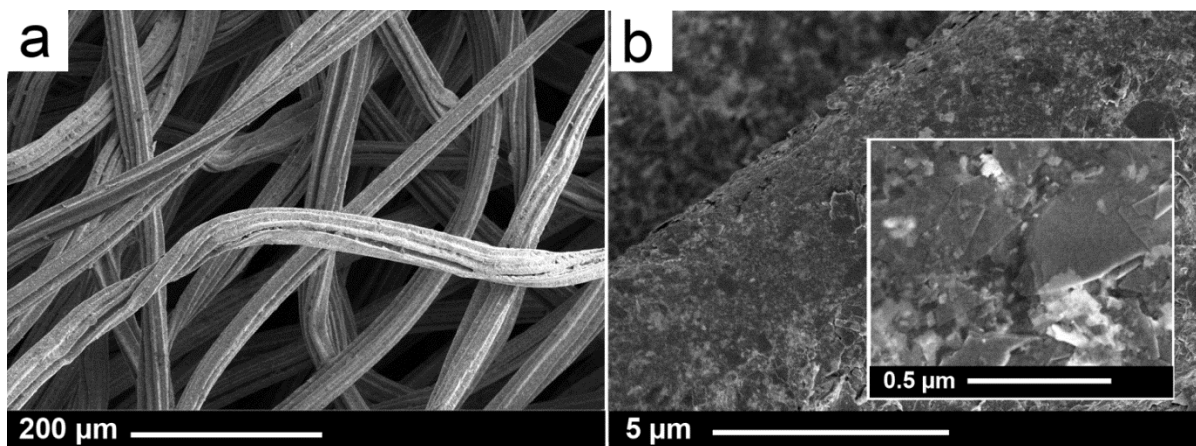


Figure 111: (a + b) PET 4DG coated with bath-sonicated EGF dispersion. Inset shows individual flakes on fiber surface.

In order to evaluate whether the method of EGF dispersion preparation affected coating performance, PET 4DG nonwovens were dip-coated with the various bath sonicated dispersions as well as the 10-hr horn sonicated dispersion. The number of dip cycles was tailored to keep the average mass gain constant at around 5.5% for all samples (Figure 111). Thanks to the higher concentration of the horn sonicated dispersion, the coating process was much more efficient. For the bath sonicated dispersions, 40 dip cycles were used; for the horn sonicated dispersion, only 10 cycles were required.

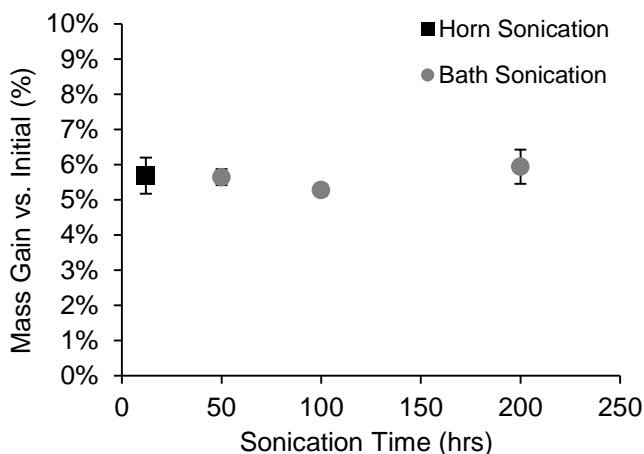


Figure 112: Mass gain of graphite PET 4DG nonwoven samples coated with EGF sonicated by horn for 10 dip cycles, and by bath for 40 dip cycles.

The horn sonicated EGF dispersion reduces both dispersion preparation time and number of dip coating cycles. However, it was unclear whether performance was negatively impacted. To answer that question, electrical properties in the x-y direction (in-plane) and the z-direction (through-plane) of the coated PET 4DG nonwovens were examined. Figure 113a shows that, in fact, the horn sonicated EGF resulted in a lower in-plane resistance (IPR) than any of the bath sonicated samples. Average IPR was under 500 Ω for the horn sonicated sample, even though the coating mass was comparable among all samples. The TPR results (Figure 113b) were similar, with the horn sonicated sample presenting the best electrical properties among the group.

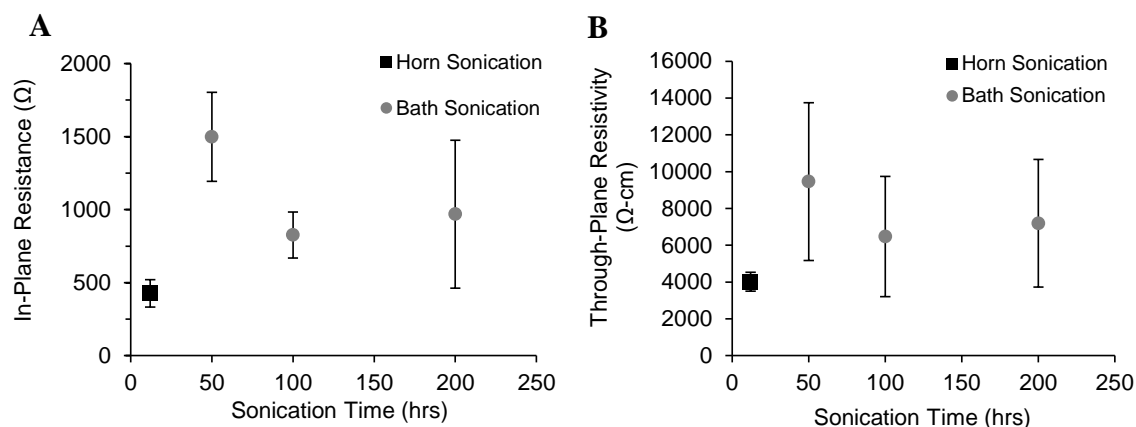


Figure 113: IPR and TPR for PET 4DG coated with around 5% graphite mass from EGF dispersions prepared by different methods.

The samples were also characterized in terms of their electric double layer capacitance (EDLC). Although the intended application is as electrodeposition substrates for pseudocapacitive material, not as EDLC-type capacitors, the double layer capacitance yields useful information. EDLC arises at the electrode-electrolyte interface in electrochemical circuits, and it can be a measure of surface area and conductivity. Thus, based on the resistance test results shown above, the EDLC of the horn-sonicated samples would be expected to show the highest EDLC. Figure 114 shows that the specific capacitance was indeed inversely related to the resistance levels of the samples, confirming that the horn sonicated samples are the most conductive and therefore most suited for use as a scaffold for electrodeposition.

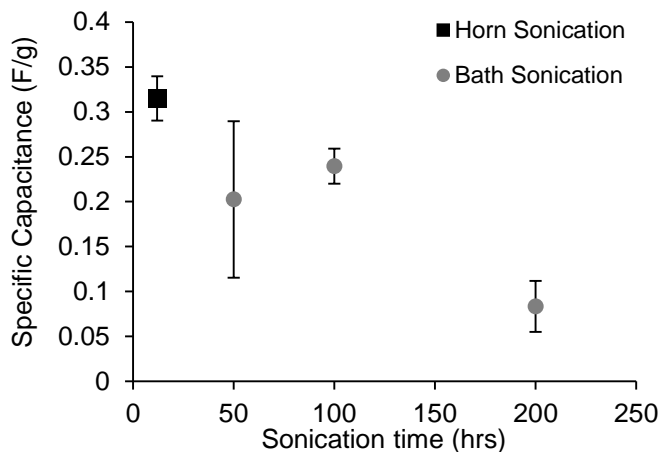


Figure 114: Specific capacitance based on galvanostatic charge-discharge tests for PET 4DG nonwovens coated with EGF prepared by different methods.

7.3.3 Impact of Web Structure on Coating Results

The limiting current of an electrochemical reaction is partially dependent on the surface area of the electrodes. Thus, one tactic to increase the energy density of supercapacitors has been to develop high surface area electrodes. According to Chappas and Pourdeyhimi, PET 4DG fibers such as those used here with a diameter of $\sim 30 \mu\text{m}$ have a specific surface area (SSA) of around $0.8 \text{ m}^2 \text{ g}^{-1}$ (Figure 115a).⁵⁷ This is typical of most textile fibers, yet some fibers are designed to have higher SSA. By incorporating a water soluble polymer in a bicomponent fiber, the sacrificial polymer can be washed away to reveal very low-diameter fibers or fibers with intricate cross-sections. One type of high SSA bicomponent fiber is the Winged Fiber (WF). In order to increase the surface area of the graphite-coated nonwovens, spunbond and hydroentangled PET WF with SSA of around $20 \text{ m}^2 \text{ g}^{-1}$ were obtained (Figure 115b).

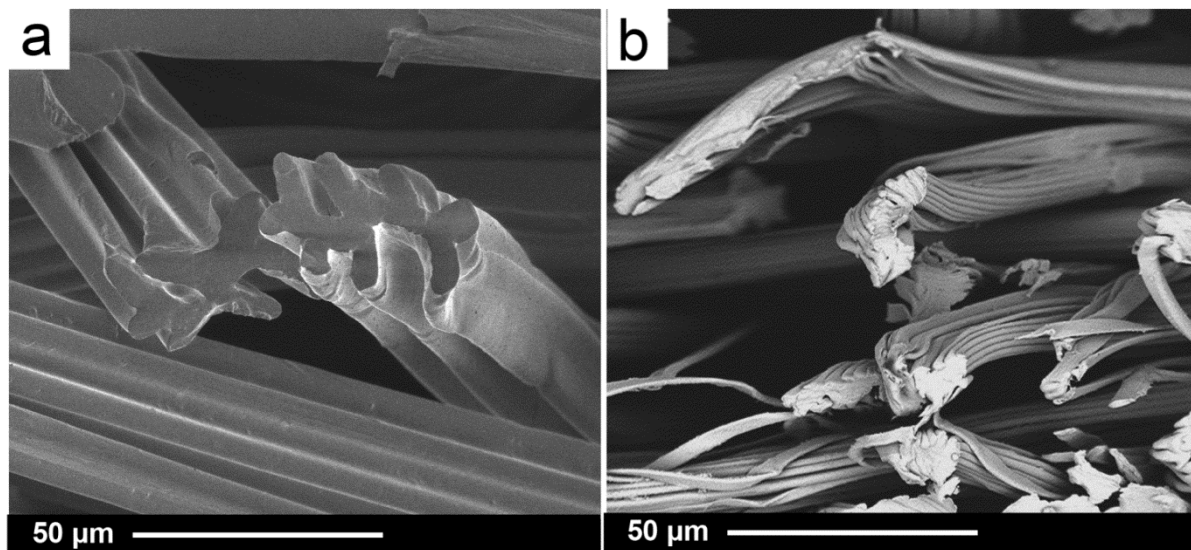


Figure 115: SEM images showing fiber shape and size of (a) 4DG and (b) WF fibers.

PET 4DG and PET WF were processed through 40 dip-coating cycles using the highly concentrated horn-sonicated EGF (10 hours sonication time). Mass gain per cycle number is shown in Figure 116. Uptake is greater for the 4DG sample, despite its lower surface area. The relatively low uptake of the WF sample is likely due to the fabric structure. Unlike the 4DG samples which was formed by carding and hydroentangling staple fibers, the WF samples were spunbonded and hydroentangled. Carding is known to produce lofty webs, whereas spunbonding is associated with compact webs. One way to quantify this difference is by measuring the solid volume fraction (SVF), which is the volume of the web occupied by fiber. Lower SVF is associated with more open, lofty webs. The two materials used here, PET 4DG and PET WF, have SVF of 0.06 and 0.16, respectively. This means that PET 4DG has a more lofty structure, while PET WF has a dense structure. In our earlier study, dense structures were seen to prevent thorough distribution of coating materials, leading to low mass loadings.²⁵² This seems to be the case here as well.

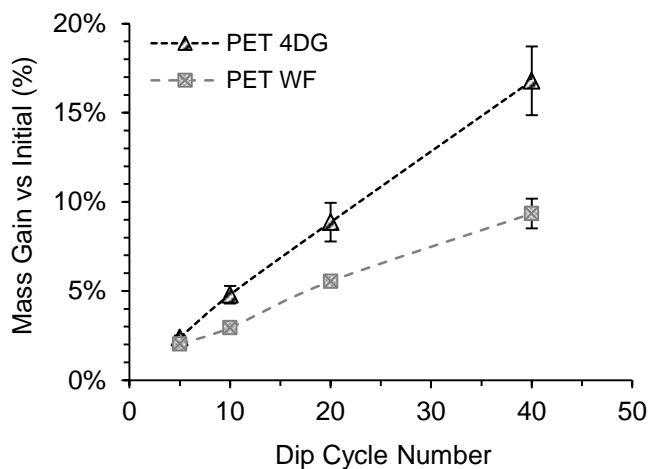


Figure 116: Mass gain of graphite compared to initial uncoated sample mass for PET 4DG and PET WF samples coated with horn-sonicated EGF dispersions.

Figure 117 shows PET WF and PET 4DG fibers coated with the horn-sonicated EGF dispersions after 5 dip cycles (Figure 117 a + c) and 40 dip cycles (Figure 117 b + d). Although all of the fibers are covered with the scale-like texture that is characteristic of EGF coatings, there are some differences worth pointing out. The cross-sectional shape of PET WF has a greater number of ridges, but they are closely spaced. It is possible that mass gain is lower for these fibers because the EGF particles are unable to fully coat the inside of these narrow channels. The channels between the ridges of PET 4DG are more widely spaced, and it can be seen that EGF particles are able to access and coat these channels.

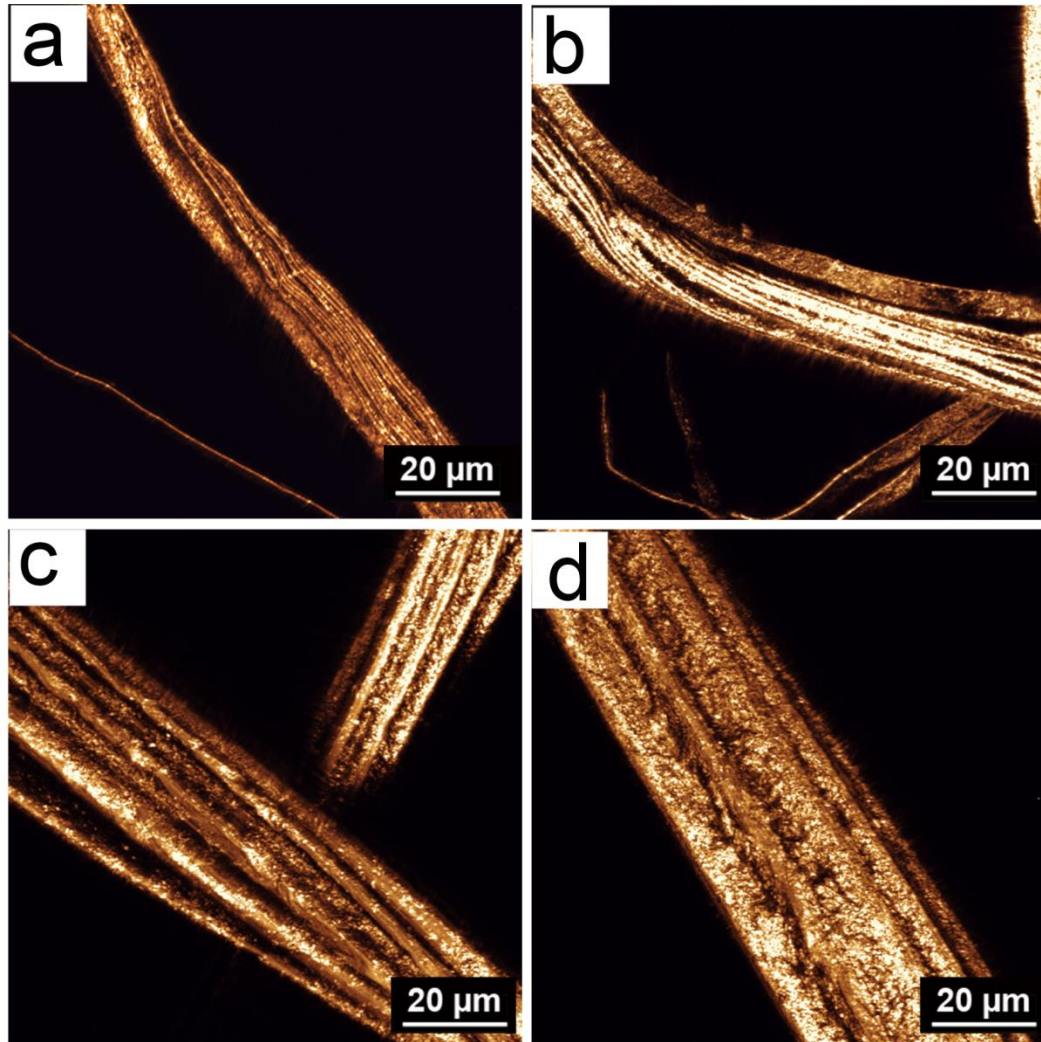


Figure 117: EGF coated PET WF with (a) 5 coats and (b) 40 coats, and PET 4DG with (c) 5 coats and (d) 40 coats.

In-plane resistance (IPR) was measured for the PET WF and PET 4DG samples (Figure 118). Resistance was lower for the PET 4DG sample at each dip number. This is to be expected based on the mass gain results above, since PET 4DG has a heavier EFG coating than PET WF at each dip number. However, when compared on the basis of resistance per mass gain (Figure 118b), the PET 4DG sample also has lower resistance values at the same level of mass gain. For example, at 10% mass loading, the PET WF had an average IPR of 394 Ω , while the PET 4DG had an average of 139 Ω . This could be attributed to differences in SSA. For a given mass loading, the coating thickness will be greater as SSA decreases since there

is less surface area for the given mass to be distributed on. Thicker coatings would likely result in higher conductivity.

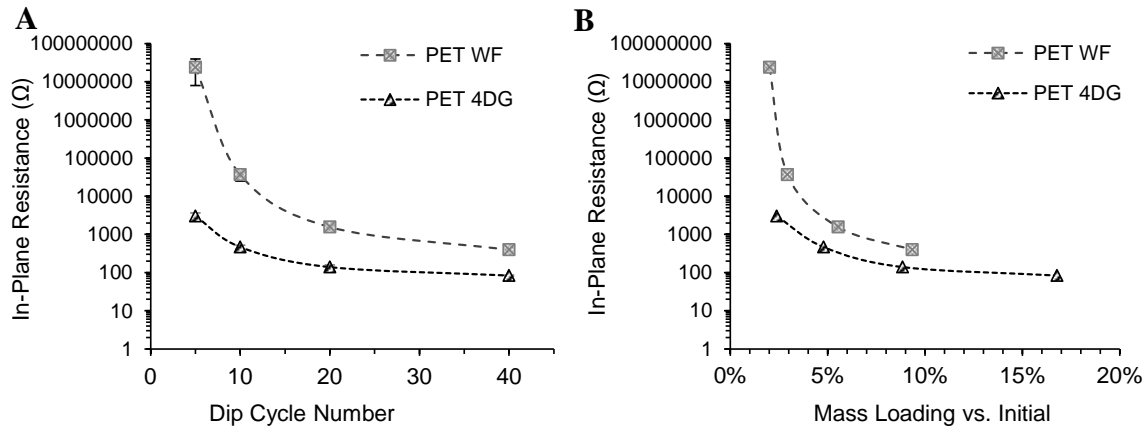


Figure 118: IPR for EGF-coated PET 4DG and PET WF nonwovens, shown as a function of (a) dip cycle number and (b) graphite mass loading.

Figure 119 shows the through-plane resistance (TPR) for the same samples. Again, we see resistance drop faster for the PET 4DG sample as a function of dip number (Figure 119a). We also see lower TPR per EGF mass gain (Figure 119b). These results support the conclusion that PET 4DG leads to better electrical performance as compared to PET WF. Having a lower SVF, the PET 4DG web allows for more uniform distribution of the EGF.

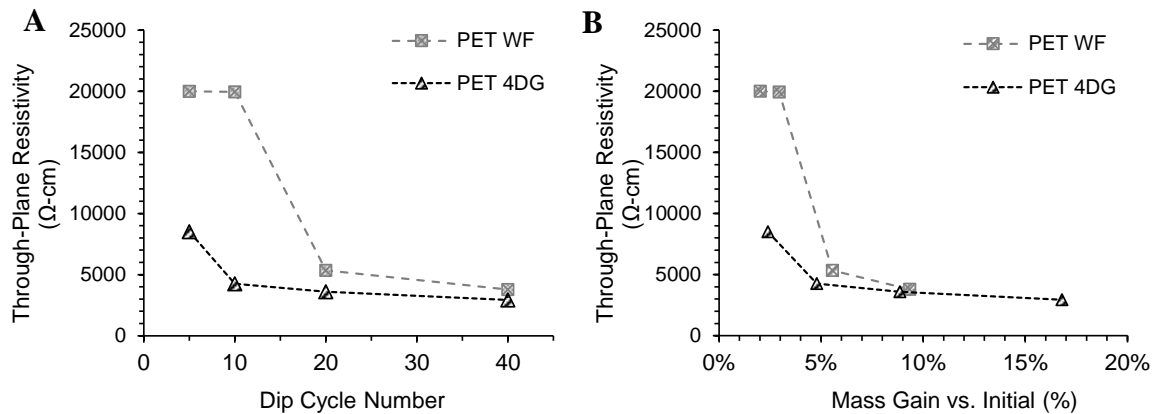


Figure 119: TPR for EGF-coated PET 4DG and PET WF nonwovens, shown as a function of (a) dip cycle number and (b) graphite mass loading.

Specific capacitance as a function of dip cycle number is shown below in Figure 120a. As with the samples presented in Figure 114 above, the specific capacitance here is completely attributed to EDLC type capacitance. EDLC forms as a result of surface area and conductivity, so values are inversely related to resistance. As would be expected, those samples with lower resistance have higher specific capacitance. Based on the total electrode mass, the PET 4DG samples with 40 dips show specific capacitance of around 0.6 F g^{-1} . However, it is more typical for results to be reported in terms of active mass only. This means that the mass of the non-conductive fiber would be disregarded, and specific capacitance would be calculated based on graphite mass only (Figure 120b). The graphite on PET 4DG seems to reach a maximum of around 4.5 F g^{-1} . On PET WF, the maximum is lower at around 3.5 F g^{-1} . This means that for each gram of graphite loaded onto the sample, the additional capacitance is greater if the substrate is PET 4DG than PET WF.

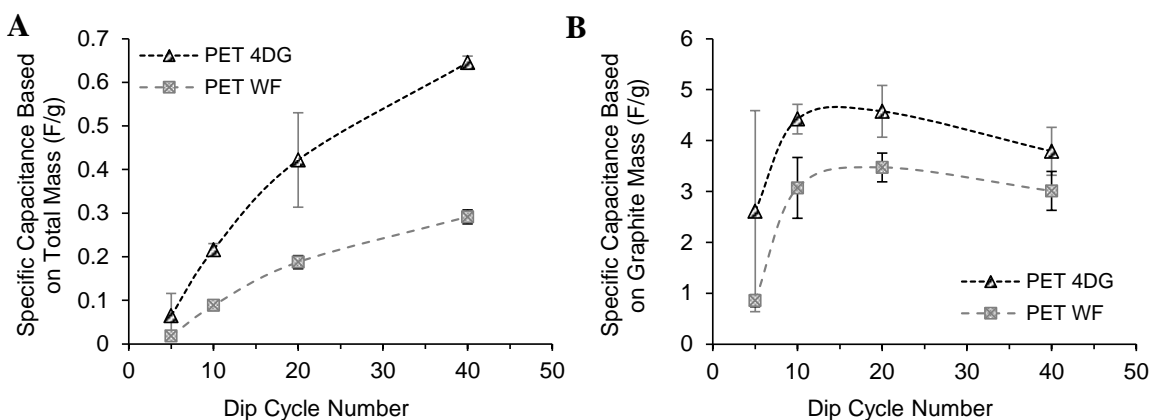


Figure 120: Specific capacitance based on galvanostatic charge-discharge tests for PET4DG and PETWF calculated based on (a) total electrode mass and (b) graphite mass only.

7.3.4 Electrodeposition of PANI onto PET Nonwovens

PANI was subsequently deposited onto the PET 4DG and PET WF fabric surfaces by electropolymerization of aniline, with the conductive nonwoven acting as the scaffold. For both types of fabric, samples with dip numbers ranging from 5 to 40 were employed. Figure 121 shows examples of the resulting PANI depositions. A shift in the PANI location can be seen from the edge of the sample for the lightest EGF coating, to the center of the sample with the heaviest EGF coating. EGF coating thickness corresponds to electrical conductivity,

as was shown above, so it can be said that the coating quality depends on how well electrons can flow on the scaffold. At low conductivities, polyaniline forms only at the edges where the deposition frame compresses the fibers and enhances conductivity, while the uncompressed central area is unable to participate in the eletropolymerization process. With each increase in conductivity, the polyaniline is concentrated more closely to the sample center, which is the ideal location. The sample with 40 EGF coatings displays the most ideal deposition result, from a visual standpoint.

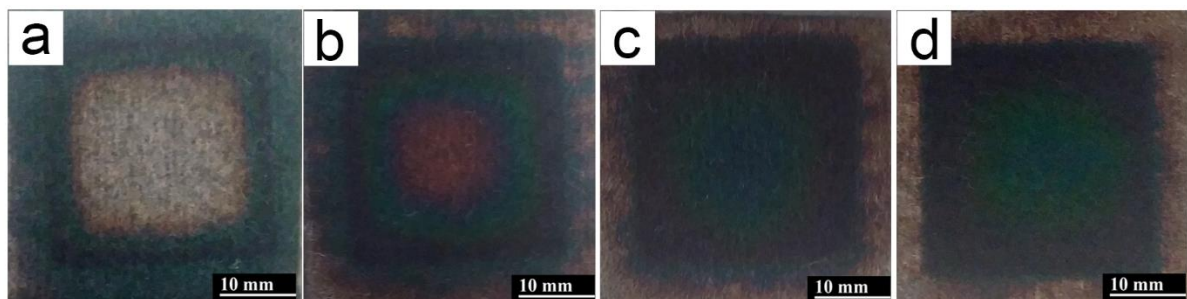


Figure 121: PET 4DG nonwovens coated with EGF and then electrodeposited with polyaniline. Number of EGF coatings is (a) 5, (b) 10, (c) 20, and (d) 40.

PET WF samples, also having between 5 and 40 coatings of EGF, were exposed to the electrodeposition process (Figure 122). Comparing the two fabric types, the PET WF samples are strikingly less supportive of PANI formation than the corresponding PET 4DG samples. This can be explained by the inferior conductivity of the PET WF samples. The electrical properties (IPR and TPR) of the PET WF sample with 40 EGF coatings are similar to those of the PET 4DG sample with 10 EGF coatings. As a result, these two samples bear visual similarities (Figure 121 b and Figure 122 d). PANI bleeds past the edge of the masked area of the PET 4DG sample because the high loft prevents the frame from making a clean cover, while the PET WF samples all show relatively clean edges. However, the unmasked areas both feature a prominent uncoated patch. Since PET WF was unable to support complete PANI formation, PET 4DG was the focus of subsequent studies.

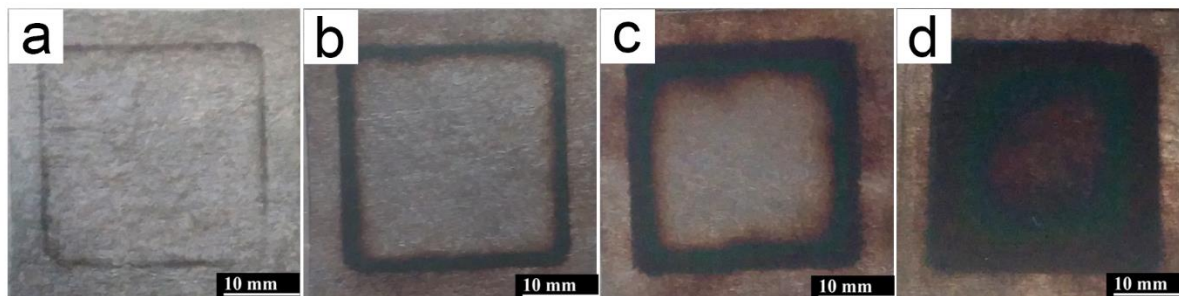


Figure 122: PET WF nonwovens coated with EGF and then electrodeposited with polyaniline. Number of EGF coatings is (a) 5, (b) 10, (c) 20, and (d) 40.

7.3.5 PANI Deposition onto PET 4DG Nonwovens Coated with Graphene or Carbon Nanotubes

Finally, to understand how the graphene EGF coating performs in comparison to the CNT coatings, PANI pseudocapacitors using both approaches were prepared. PET 4DG samples were dipped in EGF dispersion for 40 cycles as above, attaining an average mass gain of 16.7 wt%. A second set of PET 4DG samples were coated with 16.5 wt % CNT by carrying out 20 dip cycles. Based on the assumption that the CNT loading would result in better electrical properties, a third set of less conductive CNT PET 4DG samples were prepared. These were dipped in CNT dispersion for only 10 cycles, leading to a lower mass gain of 10%. IPR and TPR measurements were carried out for these three sets, and Figure 123 shows the results. Indeed, the samples coated with 16.5% CNT had the lowest electrical resistance. Higher resistance is seen for the samples coated with 10% CNT, but these still are not as resistive as the samples coated with 16.7% EGF. This confirms that CNT still has the advantage of lower electrical resistance, likely due to the CNT production process, which results in more uniform and low-scale dimensions. Additionally, the CNT dispersion does not require any surfactant, leading to a more pure coating.

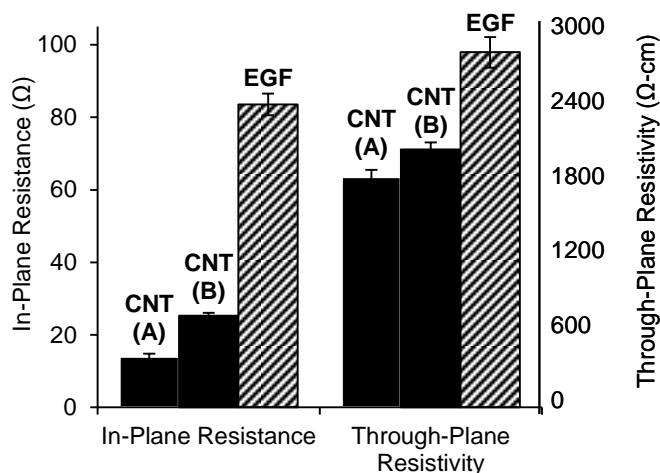


Figure 123: Electrical properties of PET 4DG coated with 16.5% CNT (A), 10.1% CNT (B) and 16.7% EGF.

Although the EGF samples are less conductive, it was shown in the previous section that they are still able to support PANI deposition. Samples of EGF and CNT coated PET 4DG were deposited with PANI under the same conditions as used previously (0.25 M aniline, 0.777 V, 20 minutes). Fibers are shown before PANI electrodeposition (Figure 124 a – c) and after PANI electrodeposition (Figure 124 d – f). Compared to the conformal scale-like texture of the EGF coatings, the CNT coatings display clusters of agglomerated particles. These clumps are masked by the thick PANI coatings, which appear rough and uneven. PANI deposited atop the EGF coated fiber also appears rough.

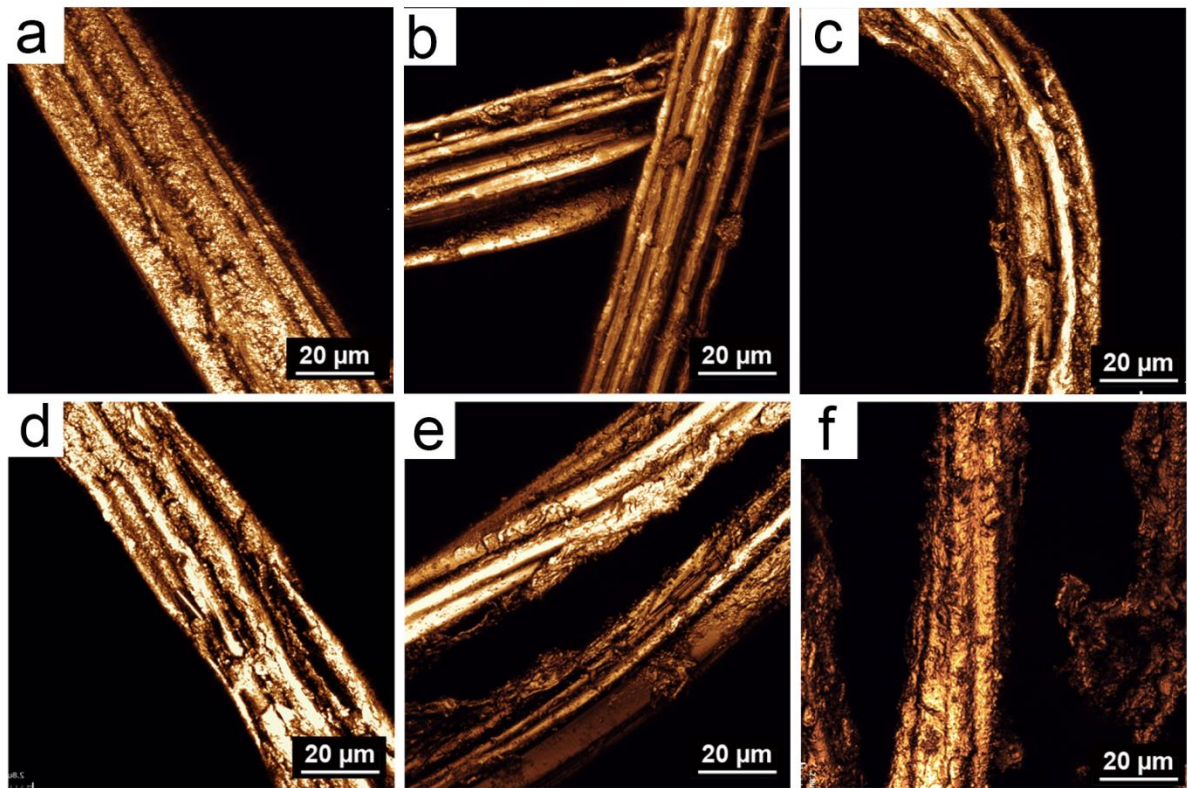


Figure 124: PET 4DG fibers coated with 16.7% graphene (a) before and (d) after PANI electrodeposition; 10.1% CNT (b) before and (e) PANI electrodeposition; and 16.5% CNT (c) before and (f) after PANI electrodeposition.

Galvanostatic charge-discharge cycling was carried out to measure the capacitance. In order to determine how much of the measured capacitance can be attributed to double-layer capacitance (EDLC) versus pseudocapacitance (PC), both were determined separately. EDLC specific capacitance was measured for samples with only EGF or CNT, and PC specific capacitance was measured for samples bearing PANI. Table 18 lists the resulting average specific capacitance values. Specific EDLC is an order of magnitude higher for the CNT coated samples as compared to the EGF coated samples. CNT contributes greater EDLC due to its lower electrical resistance. Specific surface area differences between EGF and CNT may also play a role.

PANI mass loading is also shown in Table 18. Despite the lower conductivity of the EGF samples, the PANI mass loading is almost as high as for the CNT samples. Finally, specific

PC is shown. Although it is lower for the EGF samples, the difference is less dramatic than the EDLC spread.

Table 18: Specific double layer capacitance (EDLC) for samples with three different conductive coatings. Pseudocapacitance (PC) after PANI electrodeposition is also shown. Specific PC is calculated based on full electrode mass as well as PANI mass only.

Conductive Layer	Average EDLC (F g ⁻¹)	PANI Mass Loading (%)	Average Pseudocapacitance (F g ⁻¹)	
			Normalized by full electrode mass	Normalized by PANI mass only
EGF (16.7%)	0.65	15.4%	21.63	137.85
CNT (10.1%)	4.79	17.3%	43.52	228.49
CNT (16.5%)	8.94	27.5%	49.39	154.75

In terms of the performance per coating cost, the results are interesting and indicative of the value of graphene. Raw graphite flake can be purchased for around \$0.50 per gram, and the yield of the graphite when processed into EGF in this study was just 4%, so the cost per gram of EGF is around \$12.50. Still, this is much lower than the cost per gram of CNT: \$300 - \$1000 per gram. Due to this significant price disparity, EGF is shown to provide much greater cost efficiency as compared to CNT. Figure 125 b shown capacitance normalized in terms of coating cost. For each unit cost of EGF coating, over 13 F can be expected, while CNT delivers no more than 0.7 F per unit cost.

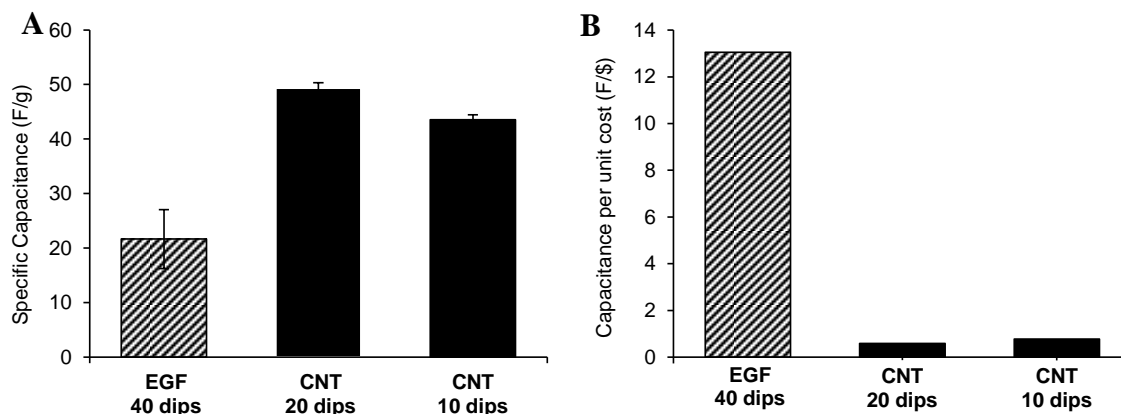


Figure 125: After pseudocapacitive PANI layer is added to electrodes, specific capacitance shown normalized by (a) total electrode mass and (b) cost of unit cost of conductive carbon coating component.

7.4 CONCLUSIONS

A route to obtaining high-concentration EGF dispersions ($> 1.0 \text{ mg mL}^{-1}$) has been shown. Despite the higher force associated with horn sonication, the quality of EGF obtained by this approach was demonstrated by DLS, TPR and IPR measurements to be slightly higher than the bath sonication approach. This surprising finding may be due to the shorter sonication time associated with horn sonication. Conformal coating of EGF on nonwoven substrates was demonstrated. The high concentration EGF dispersion was coated onto two different PET substrates – WF and 4DG. Although the PET WF substrates have a higher SSA, PET 4DG substrates gained EGF mass more efficiently as a result of the surface area being more accessible by the graphene flakes. Having higher EGF mass loading led to the PET 4DG substrates having lower IPR and TPR after fewer EGF coating cycles. EDLC for the PET 4DG samples was also higher than PET WF, even for the same EGF mass loading. Again, this indicates better circulation of active materials and electrolyte throughout the fabric structure. PANI was electrodeposited onto PET WF and PET 4DG, showing much better distribution on the PET 4DG scaffolds. Finally, EGF compared to CNT as a conductive coating material for PANI electrodeposition. The superior electrical properties of the CNT-coated scaffolds initially led to significantly higher EDLC, but the differences in capacitance were greatly reduced after PANI deposition. The cost of CNT greatly outweighs that of EGF, so when PANI pseudocapacitance is normalized by the cost of CNT or EGF, the price-based performance is much higher in the case of EGF. This demonstrates the potential use of EGF as a safer and cheaper alternative to CNT in the fabrication of flexible, conductive nonwoven pseudocapacitor scaffolds.

CHAPTER 8: Conclusions and Recommendations

8.1 OVERALL CONCLUSIONS

Flexible, high-energy density electrodes have many potential applications in electrochemical technologies, including as supercapacitor electrodes. They may be obtained by carbonizing fiber structures or coating fiber structures with carbon-containing dispersions. A preliminary review of the literature exposed the need to consider how fiber and web properties influence coating formation and performance. Several routes to obtaining flexible fiber-based supercapacitor electrodes were examined. Carbon fiber nonwovens were studied as possible precursors to activated carbon EDLC electrodes, as well as scaffolds for the formation of redox-active PC electrodes. Nonwovens of various polymer types were also coated with carbon nanoparticles (CNT and graphene) to be used as PC electrode scaffolds. During the course of this research, the following observations related to fabric structure and treatment processes were determined.

8.1.1 Conversion of carbon fiber fabrics into EDLC electrodes via activation treatment:

- It was found that most commercially available carbon fiber nonwovens are held together by a polymer resin. Since the resin is thermally unstable at high temperatures, the activation process would cause the fabric structure to disintegrate. This limits the range of possible materials to those carbon fiber nonwovens which do not rely on resin for structural integrity.
- Gas diffusion layer (GDL) materials may be used since they are formed of mechanically entangled carbon fibers. Two such samples were obtained and exposed to typical activation conditions: temperatures from 500°C to 900°C under CO₂ for 30 - 60 minutes. The post-treatment nitrogen adsorption isotherms of these samples reveal that no microporosity was imparted during treatment.
- To understand why no activation had occurred, carbon fiber nonwovens were prepared in-house under controlled conditions. PAN nonwovens were fabricated and carbonized at different temperatures (695°C, 895°C, 1095°C). XPS and XRD studies revealed that lower carbonization temperature led to smaller ordered carbon domain

size, more remnant nitrogen, and less sp^2 bonding. Consequently, lower carbonization temperature also was associated with higher electrical resistance.

- All samples were treated at 895°C under CO_2 for 60 minutes in order to impart activation. Nitrogen adsorption isotherms were of the Type III only for those which were carbonized at or below 895°C, and they showed SSA of around $200\text{ m}^2\text{ g}^{-1}$. Mode pore radius was around 0.3 nm for these samples. For those samples carbonized at 1095°C, the formation of larger ordered carbon domains hindered activation. Nitrogen adsorption isotherms exhibited Type II behavior (mixed micro- and mesoporosity).
- These observations point to high carbonization temperature as being the reason that the commercial GDL material resists activation. Since GDL materials are designed to have high conductivity, they are likely carbonized at very high temperatures which prevent the formation of micropores during subsequent activation treatments.

8.1.2 Carbon fiber nonwovens as PC electrode scaffolds:

- Although commercially available carbon fiber nonwovens are unsuitable to activation, they can be coated with a redox active species and used as pseudocapacitor electrodes. Four types were deposited with PANI. Specific capacitance was measured before and after deposition, and those which were binder-free showed a remarkable increase, from 0.02 F g^{-1} to over 14 F g^{-1} .
- PANI deposition was optimized by tuning deposition potential, aniline concentration and deposition duration. All potentials greater than 0.700 V (vs. Ag/AgCl) resulted in around the same specific capacitance, but the CV shapes became increasingly more asymmetrical as potential was increased up to 1.144 V. A potential of 0.744 V resulted in a symmetrical CV curve.
- The effect of deposition time was also studied. At an aniline concentration of 0.1 M and a potential of 0.744 V, a deposition time of 10 minutes resulted in the highest specific capacitance. However, when aniline concentration was increased to 0.5 M, the 20 minute deposition time resulted in a higher specific capacitance: 83.4 F g^{-1} .

based on total electrode mass, and 220.3 F g^{-1} in terms of PANI mass only. The 0.5 M aniline concentration was high enough to feed PANI formation throughout the 20 minute duration.

8.1.3 CNT coated nonwovens as PC electrode scaffolds:

- Unlike the commercially available carbon fiber nonwovens studied above, CNT coated nonwovens were fabricated on site. This necessitated an understanding of effects of fabric structure variables as well as the CNT coating parameters. CNT were dispersed in ethanol on one hand, and water with surfactant on the other hand. Ethanol led to a higher and more steady mass gain, due to the absence of interference from surfactants. The absence of surfactant also resulted in lower electrical resistance.
- Various types of microfiber nonwovens (all made of PA6) were coated with the ethanol-based CNT dispersion. After three dip-dry cycles, the samples showed various mass gain levels, ranging from 4% to 12%. Differences in mass gain were found to correspond to differences in web solidity (SVF). Lower SVF was associated with higher mass gain per cycle, having more of an impact than SSA.
- SEM imaging showed that caking was occurring on the surface of low SVF nonwovens, including some carded samples that were compressed to be denser. Cross-sectional images confirmed that CNT collect at the fabric surface, unable to reach past the first layers of fibers. The CNTs agglomerate into “buckypaper” sheets, trapping subsequent materials and forming a cake at the surface.
- Other researchers have reported similar processes using sponges as the coating substrate. The type of sponge used has a SVF of below 2% (meaning it is 98% void volume). However, spunbonded nonwovens of the types used here have SVF of almost 20%. Consequently, a different fabric formation method – carding – was explored. Resulting nonwovens had SVF below 5%, similar to that of the sponge. By using a carded web, low SVF is achieved. Fibers with small diameters or a multi-lobed cross section can then be used to increase surface area.

- In terms of polymer type, cellulose (in the form of cotton fibers) was able to load CNT mass more efficiently than PET and PA6. This is likely due to the proliferation of functional groups on the polymer backbone chain, as well as the higher surface area of the hollow cotton fibers. PET and PA6 gained CNT mass more slowly, but performed as well as cotton as EDLC electrodes. They also have the advantage of being melt-spinnable polymers, so fiber cross-section can be engineered.
- PET fibers with a multi-lobed cross section were carded to form a low SVF web, coated with CNT and used as MnO₂ electrodeposition scaffolds. At 5% mass loading of MnO₂, the electrodes had a specific capacitance of 13 F g⁻¹ based on total mass, and 200 F g⁻¹ based on MnO₂ mass only.

8.1.4 Graphene coated nonwovens – comparing rGO to EGF:

- PET 4DG nonwovens were coated with GO dispersion and EGF dispersion. To reach a given mass loading, the GO dispersion required only 1/5 the number of cycles required by the EGF dispersion.
- Conversion of GO to rGO was carried out by sodium dithionite, and conductivity was increased by three orders of magnitude.
- EGF coated samples had a higher conductivity than rGO coated samples, both for the same cycle number (~9,000Ω lower at 40 cycles) and mass loading (~99,000Ω lower at 5% mass loading).
- EIS revealed that rGO exhibits pseudocapacitive behavior while EGF shows the preferred EDLC behavior.
- Confocal microscopy was used to examine coating morphology, and EGF was found to produce more conformal layers on the 4DG fibers. Particle size is much lower for EGF than for GO, making it easier for the particles to trace the contours of the 4DG fibers.
- Galvanostatic charge-discharge cycling was carried out, and showed that EGF coatings result in much more stable and significant EDLC behavior. Per unit mass of graphene, EGF results in 2.12 F g⁻¹ while rGO results in only 0.03 F g⁻¹.

8.1.5 Graphene coated nonwovens – optimization for PC scaffolds

- A higher concentration of EGF was sought, in order to decrease the number of dip cycles required. Sonication time was extended to 200 hours, but UV-vis absorbance levels were not significantly higher when compared to the dispersion sonicated for 50 hours.
- By increasing initial graphite concentration and using a more powerful horn sonicator, concentration was surpassed in only 4 hours. By sonicating for 10 hours, concentration reached between 0.5 – 1.0 mg mL⁻¹. This reduced coating cycle requirement by 75%.
- Particle size intensity mean for these dispersions (0.34 μm – 0.74 μm) was similar to what was achieved with bath sonication (0.54 μm – 0.64 μm). For the same mass loading, resistance was lower for the samples coated with the horn sonicated dispersions.
- Two fabric structures were examined. PET WF has high SSA but high SVF, while PET 4DG has moderate SSA and low SVF. The PET 4DG showed faster mass gain as well as lower resistance per mass loading. Evidently, as with the CNT coatings, SVF has a bigger impact on coating performance than SSA.
- PANI was deposited on PET WF and PET 4DG as well. Due to its higher conductivity, PET WF samples showed more widespread PANI growth, although the edges of the masked area were fuzzy.
- CNT and EGF coated PET 4DG samples were compared. The CNT coated sample was much more conductive than the EGF coated sample (13 Ω compared to 80 Ω, respectively). As a result the EDLC of the CNT coated sample was much higher (50 F g⁻¹ of CNT compared to 5 F g⁻¹ for EGF).
- PANI was deposited onto the CNT and EGF coated PET 4DG samples. Due to the higher conductivity of CNT, the deposition mass loading was double that obtained on the EGF coated scaffold. Pseudocapacitance was about equal on the basis of PANI mass (around 150 F g⁻¹ of PANI). On the basis of electrode mass, specific capacitance was 49 F g⁻¹ for CNT coated scaffolds, and 21 F g⁻¹ for EGF coated scaffolds.

8.2 RECOMMENDATIONS FOR FUTURE WORK

Turning to the bigger picture of fiber-based electrochemical devices, one may wonder whether these materials can be produced at a commercially viable scale. The development of high-concentration graphene dispersions and high-surface area, high-loft fabrics has laid the groundwork for experiments in scaling up. Although progress has been shown at the lab level, unanticipated challenges will inevitably arise if these methods are carried out using a pad-drier or other high throughput coating method. For the manufacture of pseudocapacitor electrodes, additional attention needs to be focused on scaling up the subsequent electrodeposition process.

While scale-up is the single-most significant unanswered question at this point, there is a handful of remaining issues that have yet to be thoroughly explored. The largest among these is the development of activated carbon fiber nonwovens as EDLC electrodes. A possible future direction for this research could be to collaborate with the manufacturer of the commercially obtained GDL carbon fiber material. Although their material resisted activation, our study found that lower carbonization temperature could lead to a different outcome, but it's not possible to confirm that conclusion without experimenting on the manufacturing line. Working with a full-scale carbon fiber manufacturing facility (such as at a company or Oak Ridge National Lab) to examine a wider range of carbonization and activation conditions (temperature, ramp rate, gas type, gas flow rate, dwell time) could shed light on the relationship between carbonized fiber and subsequent development of microporosity. Additionally, testing the activated carbon fiber nonwovens as EDLC electrodes would lend key insights into ideal properties for this particular application area.

Another remaining question relates to the CNT coatings. These exhibited a tendency to form a cake, or skin, on the surface of high-density fabrics. However, this phenomenon was only studied while utilizing CNTs dispersed in ethanol. If an aqueous dispersion were used instead, would the presence of surfactants prevent CNTs from agglomerating and forming obstructive buckysheets between adjacent fibers?

REFERENCES

- (1) Bard, A. J. *Electrochemical methods: fundamentals and applications*, 2nd ed.; Wiley: New York, 2001.
- (2) Ehsani, M. *Modern electric, hybrid electric, and fuel cell vehicles: fundamentals, theory, and design*, 2nd ed.; Power electronics and applications series; CRC Press: Boca Raton, 2010.
- (3) Sanii, S. ANODE CATALYST LAYER ENGINEERING FOR THE DIRECT FORMIC ACID FUEL CELL, University of British Columbia, 2008.
- (4) Jüttner, K.; Galla, U.; Schmieder, H. *Electrochimica Acta* **2000**, *45* (15–16), 2575–2594.
- (5) Aricò, A. S.; Bruce, P.; Scrosati, B.; Tarascon, J.-M.; van Schalkwijk, W. *Nat. Mater.* **2005**, *4* (5), 366–377.
- (6) Anglada, A.; Urriaga, A.; Ortiz, I. *J. Chem. Technol. Biotechnol.* **2009**, *84* (12), 1747–1755.
- (7) Kinoshita, K. *Carbon: electrochemical and physicochemical properties*; Wiley: New York, 1988.
- (8) Pletcher, D.; Royal Society of Chemistry (Great Britain). *A first course in electrode processes*, 2nd ed.; Royal Society of Chemistry: Cambridge, 2009.
- (9) Wendt, H. *Electrochemical engineering: science and technology in chemical and other industries*; Springer: Berlin ; New York, 1999.
- (10) Radjenovic, J.; Bagastyo, A.; Rabaey, K.; Batstone, D.; Gernjak, W.; Mu, Y.; Rozendal, R. *Electrochemical Treatment of Problematic Water Recycle Waste Streams*; Technical Report 82; Urban Water Security Research Alliance Australia, 2012.
- (11) Okuno, K.; Katoh, M.; Harada, K.; Park, J.-J.; Iwaki, T.; Tanase, S.; Sakai, T. *SEI Tech. Rev.* **2006**, No. 62, 29–33.
- (12) Inoue, M.; Nakae, T. Porous, electrically conductive sheet and method for production thereof. EP1139471 A1, October 4, 2001.
- (13) Liu, C.-H.; Ko, T.-H.; Kuo, W.-S.; Chou, H.-K.; Chang, H.-W.; Liao, Y.-K. *J. Power Sources* **2009**, *186* (2), 450–454.

- (14) Liu, C.-H.; Ko, T.-H.; Chang, E.-C.; Lyu, H.-D.; Liao, Y.-K. *J. Power Sources* **2008**, *180* (1), 276–282.
- (15) Winter, M.; Brodd, R. J. *Chem. Rev.* **2004**, *104* (10), 4245–4270.
- (16) Rudge, A.; Davey, J.; Raistrick, I.; Gottesfeld, S.; Ferraris, J. P. *J. Power Sources* **1994**, *47* (1–2), 89–107.
- (17) Simon, P.; Gogotsi, Y. *Nat. Mater.* **2008**, *7* (11), 845–854.
- (18) Kötz, R.; Carlen, M. *Electrochimica Acta* **2000**, *45* (15–16), 2483–2498.
- (19) Becker, H. L. Low Voltage Electrolytic Capacitor. 2800616, July 13, 1957.
- (20) *EDLC Solution for Reliable Interim Power Supply in Solid State Drives*; Murata EDLC Application Note C2M1CXS-074; Murata, 2014.
- (21) Azais, P. In *Supercapacitors: Materials, Systems and Applications*; Beguin, F., Frackowiak, Eds.; Wiley-VCH: Verlag, 2013.
- (22) Chu, A.; Braatz, P. *J. Power Sources* **2002**, *112* (1), 236–246.
- (23) Fleig, P.; Lakeman, C.; Fuge, M. Capacitors with low equivalent series resistance. US7864507, January 4, 2011.
- (24) Zogbi, D. *Supercapacitors: World Markets, Technologies & Opportunities: 2013-2018*; Paumonak Publications, Inc., 2013; p 71.
- (25) Miller, J. R. In *Supercapacitors: Materials, Systems and Applications*; Beguin, F., Frackowiak, Eds.; Wiley-VCH: Verlag, 2013.
- (26) Conway, B. E. *J. Electrochem. Soc.* **1991**, *138* (6), 1539.
- (27) Conway, B. E.; Pell, W. G. *J. Solid State Electrochem.* **2003**, *7* (9), 637–644.
- (28) Murakami, K.; Mogi, Y.; Tabayashi, K.; Shimoyama, T.; Yamada, K. Carbonaceous material, its production process and electric double layer capacitor employing it. EP1049116, November 2, 2000.
- (29) Randin, J.-P.; Yeager, E. *J. Electrochem. Soc.* **1971**, *118* (5), 711.
- (30) Randin, J.-P.; Yeager, E. *J. Electroanal. Chem. Interfacial Electrochem.* **1972**, *36* (2), 257–276.
- (31) Gerischer, H. *J. Phys. Chem.* **1985**, *89* (20), 4249–4251.

- (32) Qu, D. *J. Power Sources* **2002**, *109* (2), 403–411.
- (33) González-García, J.; Bonete, P.; Expósito, E.; Montiel, V.; Aldaz, A.; Torregrosa-Maciá, R. *J. Mater. Chem.* **1999**, *9* (2), 419–426.
- (34) Frackowiak, E.; Béguin, F. *Carbon* **2001**, *39* (6), 937–950.
- (35) Biesheuvel, P. M.; Fu, Y.; Bazant, M. Z. *Phys. Rev. E* **2011**, *83* (6).
- (36) Raymundo-Piñero, E.; Kierzek, K.; Machnikowski, J.; Béguin, F. *Carbon* **2006**, *44* (12), 2498–2507.
- (37) Largeot, C.; Portet, C.; Chmiola, J.; Taberna, P.-L.; Gogotsi, Y.; Simon, P. *J. Am. Chem. Soc.* **2008**, *130* (9), 2730–2731.
- (38) Luo, D.; Zhang, G.; Liu, J.; Sun, X. *J. Phys. Chem. C* **2011**, *115* (23), 11327–11335.
- (39) Karaguzel, B. *Printing Conductive Inks on Nonwovens: Challenges and Opportunities*. PhD Dissertation, North Carolina State University: Raleigh, 2006.
- (40) Patil, A. J.; Deogaonkar, S. C. *Text. Res. J.* **2012**, *82* (15), 1517–1530.
- (41) Zhou, T.; Chen, F.; Tang, C.; Bai, H.; Zhang, Q.; Deng, H.; Fu, Q. *Compos. Sci. Technol.* **2011**, *71* (9), 1266–1270.
- (42) Motlagh, G. H.; Hrymak, A. N.; Thompson, M. R. *J. Polym. Sci. Part B Polym. Phys.* **2007**, *45* (14), 1808–1820.
- (43) *Throughplane electrical conductivity testing protocol for composite materials*; Electrical Conductivity Testing Protocol; 05-160; US Fuel Cell Council, 2004; p 5.
- (44) Landis, L.; Tucker, J. *Making Better Fuel Cells: Through-Plane Resistivity Measurement of Graphite-Filled Bipolar Plates*; 2399; Keithley Instruments Inc., 2002.
- (45) Freudenberg FCCT SE & CO.KG.
- (46) Wu, J.; Dai, W.; Li, H.; Wang, H. In *Solid State Electrochemistry II: Electrodes, Interfaces and Ceramic Membranes*; Wiley-VCH: Weinheim, Germany, 2011; Vol. 2.
- (47) Anothumakkool, B.; Torris A. T, A.; Bhange, S. N.; Badiger, M. V.; Kurungot, S. *Nanoscale* **2014**, *6* (11), 5944.
- (48) Kötz, R.; Hahn, M.; Gallay, R. *J. Power Sources* **2006**, *154* (2), 550–555.

- (49) De Levie, R. *Electrochimica Acta* **1965**, *10* (4), 395–402.
- (50) Qu, D.; Shi, H. *J. Power Sources* **1998**, *74* (1), 99–107.
- (51) Stoller, M. D.; Ruoff, R. S. *Energy Environ. Sci.* **2010**, *3* (9), 1294.
- (52) Naoi, K.; Simon, P. *J. Electrochem. Soc.* **2008**, *17* (1), 34–37.
- (53) Batra, S. K.; Pourdeyhimi, B. *Introduction to nonwovens technology*; Destech Publications: Lancaster, PA, 2012.
- (54) Honeywell June 24, 2011.
- (55) Dugan, J. S. Metal-coated fiber. US 8007904 B2, August 30, 2011.
- (56) Dresselhaus, M. S. *Graphite fibers and filaments*; Springer-Verlag: Berlin; New York, 1988.
- (57) Chappas, W.; Pourdeyhimi, B. Composite filter media with high surface area fibers. US 8410006, April 2, 2013.
- (58) Pourdeyhimi, B.; Fedorova, N.; Sharp, S. Micro and nanofiber nonwoven spunbonded fabric. US 8349232, January 8, 2013.
- (59) Shim, E. TT 504: Introduction to Nonwovens Process and Products - Spunlaid Process: Spunbond, 2013.
- (60) Shim, E. TT 504: Introduction to Nonwovens Process and Products - Staple Web Formation: Opening / Carding / Crosslapping, 2013.
- (61) Burke, A. In *Supercapacitors: Materials, Systems and Applications*; Beguin, F., Frackowiak, Eds.; Wiley-VCH: Verlag, 2013.
- (62) Tatarchuk, B. J.; Rose, M. F.; Krishnagopalan, A.; Zabasajja, J. N.; Kohler, D. A. Mixed fiber composite structures high surface area-high conductivity mixtures. US5080963 A, January 14, 1992.
- (63) Taberna, P.-L.; Simon, P.; Beguin, F. In *Supercapacitors: Materials, Systems and Applications*; Frackowiak, Ed.; Wiley-VCH: Verlag, 2013.
- (64) Maekawa, M. Process for the production of metal-plated staple fibers. US3967010 A, June 29, 1976.

- (65) Cyan-free electroless gold plating with high adhesion to various plastic films http://www.aist.go.jp/aist_e/latest_research/2008/20081105_2/20081105_2.html (accessed Feb 22, 2015).
- (66) Yuen, C. W. M.; Jiang, S. X.; Kan, C. W.; Ku, S. K. A.; Choi, P. S. R.; Tang, K. P. M.; Cheng, S. Y. *Fibers Polym.* **2013**, *14* (1), 82–88.
- (67) Kuhn, H. *Textile Chemist and Colorist*. December 1997, pp 17–20.
- (68) Hu, L.; Hecht, D. S.; Grüner, G. *Nano Lett.* **2004**, *4* (12), 2513–2517.
- (69) Liu, N.-I.; Meer, R. van der. Synergistic effect of metal flake and metal or metal coated fiber on EMI shielding effectiveness of thermoplastics. US4566990 A, January 28, 1986.
- (70) Micron-Diameter Metal Fiber Products http://www.intram micron.com/prod_metalfiber.php (accessed Feb 22, 2015).
- (71) Roberts, E. P. L.; Yu, H. *J. Appl. Electrochem.* **2002**, *32* (10), 1091–1099.
- (72) Hecht, D. S.; Hu, L.; Grüner, G. *Curr. Appl. Phys.* **2007**, *7* (1), 60–63.
- (73) Ergun, S.; Yasinsky, J. B.; Townsend, J. R. *Carbon* **1967**, *5* (4), 403–408.
- (74) Renovare International Inc.
- (75) Fraser, J. *Carbon Gas Diffusion Layers for Fuel Cell Membrane Electrode Assemblies*; for NuVant Systems; Technology Niche Analysis IED0069TN; Foresight Science & Technology, 2012.
- (76) Fuel Cell Technology Advancing in Fields Such as Non-fluorinated Electrolytes and Molded Separators: An Outline of Exhibits on Automotive Fuel Cells at the 1st International FC Expo http://www.marklines.com/en/report/rep347_200502 (accessed Jun 26, 2014).
- (77) SGL Group.
- (78) CFA213FCE. *Transport of Gases, p+and e- in PEMFC*; 2013.
- (79) Sittig, M. *Carbon and graphite fibers: Manufacture and applications*; Noyes Data Corporation: Park Ridge, 1980.
- (80) Yusof, N.; Ismail, A. F. *J. Anal. Appl. Pyrolysis* **2012**, *93*, 1–13.
- (81) Nguyen-Thai, N. U.; Hong, S. C. *Macromolecules* **2013**, *46* (15), 5882–5889.

- (82) Textile Institute (Manchester, England). *High-performance fibres*; CRC Press ; Woodhead Pub: Boca Raton : Cambridge, England, 2001.
- (83) The Right Stuff for Space Ships http://www.nasa.gov/vision/space/gettingtospace/16sep_rightstuff.html (accessed Oct 25, 2013).
- (84) Özel, M. Z. *Turk. J. Chem.* **2002**, 26 (3), 417–424.
- (85) Hanna, S. B.; Yehia, A. A.; Ismail, M. N.; Khalaf, A. I. *J. Appl. Polym. Sci.* **2012**, 123 (4), 2074–2083.
- (86) Xiao, S.; Wang, B.; Zhao, C.; Xu, L.; Chen, B. *J. Appl. Polym. Sci.* **2013**, 127 (3), 2332–2338.
- (87) Wang, B.; Xiao, S.; Cao, W.; Shi, X.; Xu, L. *J. Appl. Polym. Sci.* **2012**, 124 (4), 3413–3418.
- (88) Battistelli, E. A.; Giglia, R. D. Non-woven activated carbon fabric. US4565727 A, January 21, 1986.
- (89) Nhan, D. H.; Shuksoki, D. J.; Rekoske, M. J. Conductive Webs. US8058194 B2, November 15, 2011.
- (90) Chen, T.; Liao, J.; Liu, G.; Zhang, F.; Gong, Q. *Carbon* **2003**, 41 (5), 993–999.
- (91) Chen, T.; Wentang, Y.; Liu, G.; Baiyun, H. *Mater. Sci. Eng. A* **2009**, 505 (1–2), 48–51.
- (92) JI, A.; CUI, H.; LI, H.; CHENG, W.; JI, L. *New Carbon Mater.* **2011**, 26 (2), 109–116.
- (93) Gebedur Needle http://www.groz-beckert.com/cms/en/products_services/felting/product_range/felting_and_structuring_needles/fn_gebedur/ (accessed Oct 25, 2014).
- (94) Pierson, H. O.; Northrop, D. A. *J. Compos. Mater.* **1975**, 9 (2), 118–137.
- (95) Linck, J. S.; Kirkpatrick, C. T. Carbon-carbon parts and methods for making same. US8673188, March 18, 2014.
- (96) Schafer, W.; Jorder, K.; Rettig, H.; Salama, K.; Bock, A.; Wagener, S.; Helmbold, A. Conductive Nonwoven Fabric. U.S. Patent 7,815,887, October 19, 2010.

- (97) Matthews, A. Process for Centrifugally Spinning Pitch Carbon Fibers. US 5,066,430, November 19, 1991.
- (98) Nishimura, Y.; Watanabe, M.; Jonouchi, K. Melt blow spinning of pitch, cross lapping, stabilization, carbonization, activation and felting. US5283113 A, February 1, 1994.
- (99) Sinha-Ray, S.; Yarin, A. L.; Pourdeyhimi, B. *Carbon* **2010**, *48* (12), 3575–3578.
- (100) Chen, S.; He, G.; Carmona-Martinez, A. A.; Agarwal, S.; Greiner, A.; Hou, H.; Schröder, U. *Electrochem. Commun.* **2011**, *13* (10), 1026–1029.
- (101) Morrell, J. C. Method of Activating Carbon. US 1713347, May 14, 1929.
- (102) *The New York Times*. April 5, 1985.
- (103) Doying, E. Activation of textile forms of carbon. US3256206 A, June 14, 1966.
- (104) Yoshida, M.; Hirai, M. Oxidizing acrylonitrile polymer under tension. US 4285831 A, August 25, 1981.
- (105) Mays, T. J. In *Carbon Materials for Advanced Technologies*; Elsevier: Amsterdam, NL, 1999.
- (106) Morrell, J. C. Artificial or synthetic charcoal and process of producing the same. US 1478985, December 25, 1923.
- (107) Rodman, H. Method of Producing Activated Carbon. US 2648637, August 11, 1953.
- (108) Suzuki, M. *Carbon* **1994**, *32* (4), 577–586.
- (109) Economy, J.; Daley, M.; Mangun, C. *Am. Chem. Congr.* **1996**, *Urabana, II*.
- (110) Kynol Europa GmbH.
- (111) Nogami, T.; Nawa, M.; Mikawa, H. *J. Chem. Soc. Chem. Commun.* **1982**, No. 20, 1158.
- (112) Yoshida, A.; Tanahashi, I.; Takeuchi, Y.; Nishino, A. *IEEE Trans. Compon. Hybrids Manuf. Technol.* **1987**, *10* (1), 100–102.
- (113) Nishino, A.; Yoshida, A.; Tanahashi, I. ELECTRIC DOUBLE LAYER CAPACITOR. US 4562511, December 31, 1985.
- (114) Tanahashi, I.; Yoshida, A.; Nishino, A. *J. Electrochem. Soc.* **1990**, *137* (10), 3052–3057.

- (115) Farahmandi, C.; Dispennette, J. Aluminum-Carbon Composite Electrode. US 5777428, July 7, 1998.
- (116) Farahmandi, C.; Dispennette, J. Method of Making a High Performance Ultracapacitor. US 6059847, May 9, 2000.
- (117) Hsieh, C.-T.; Teng, H. *Carbon* **2002**, *40* (5), 667–674.
- (118) Xu, B.; Wu, F.; Chen, S.; Zhang, C.; Cao, G.; Yang, Y. *Electrochimica Acta* **2007**, *52* (13), 4595–4598.
- (119) Baughman, R. H.; Zakhidov, A. A.; Heer, W. A. de. *Science* **2002**, *297* (5582), 787–792.
- (120) Evanoff, K.; Benson, J.; Schauer, M.; Kovalenko, I.; Lashmore, D.; Ready, W. J.; Yushin, G. *ACS Nano* **2012**, *6* (11), 9837–9845.
- (121) Cai, X.; Peng, M.; Yu, X.; Fu, Y.; Zou, D. *J. Mater. Chem. C* **2014**.
- (122) Jost, K.; Stenger, D.; Perez, C. R.; McDonough, J. K.; Lian, K.; Gogotsi, Y.; Dion, G. *Energy Environ. Sci.* **2013**, *6* (9), 2698.
- (123) Lee, S. W.; Kim, J.; Chen, S.; Hammond, P. T.; Shao-Horn, Y. *ACS Nano* **2010**, *4* (7), 3889–3896.
- (124) Liu, W.; Yan, X.; Lang, J.; Peng, C.; Xue, Q. *J. Mater. Chem.* **2012**, *22* (33), 17245.
- (125) Hu, L.; Pasta, M.; Mantia, F. L.; Cui, L.; Jeong, S.; Deshazer, H. D.; Choi, J. W.; Han, S. M.; Cui, Y. *Nano Lett.* **2010**, *10* (2), 708–714.
- (126) Cloud 9 Dream Fleece, 45 in x 10 yds <http://mccallpattern.mccall.com/cloud-9-dream-fleece--45-in-x-10-yds-products-14213.php> (accessed Dec 5, 2013).
- (127) Pasta, M.; Hu, L.; La Mantia, F.; Cui, Y. *Electrochem. Commun.* **2012**, *19*, 81–84.
- (128) Chen, W.; Rakhi, R. B.; Hu, L.; Xie, X.; Cui, Y.; Alshareef, H. N. *Nano Lett.* **2011**, *11* (12), 5165–5172.
- (129) Hu, L.; Chen, W.; Xie, X.; Liu, N.; Yang, Y.; Wu, H.; Yao, Y.; Pasta, M.; Alshareef, H. N.; Cui, Y. *ACS Nano* **2011**, *5* (11), 8904–8913.
- (130) Zhang, W.; Tan, Y. Y.; Wu, C.; Silva, S. R. P. *Particuology* **2012**, *10* (4), 517–521.
- (131) Wang, K.; Zhao, P.; Zhou, X.; Wu, H.; Wei, Z. *J. Mater. Chem.* **2011**, *21* (41), 16373.

- (132) Panhuis, M. in het; Wu, J.; Ashraf, S. A.; Wallace, G. G. *Synth. Met.* **2007**, *157* (8-9), 358–362.
- (133) Gonçalves, A. G.; Jarrais, B.; Pereira, C.; Morgado, J.; Freire, C.; Pereira, M. F. R. *J. Mater. Sci.* **2012**, *47* (13), 5263–5275.
- (134) Geim, A. K.; Novoselov, K. S. *Nat. Mater.* **2007**, *6* (3), 183–191.
- (135) Ye, J.; Zhang, H.; Chen, Y.; Cheng, Z.; Hu, L.; Ran, Q. *J. Power Sources* **2012**, *212*, 105–110.
- (136) Stoller, M. D.; Park, S.; Zhu, Y.; An, J.; Ruoff, R. S. *Nano Lett.* **2008**, *8* (10), 3498–3502.
- (137) Gao, W.; Singh, N.; Song, L.; Liu, Z.; Reddy, A. L. M.; Ci, L.; Vajtai, R.; Zhang, Q.; Wei, B.; Ajayan, P. M. *Nat. Nanotechnol.* **2011**, *6* (8), 496–500.
- (138) Yu, G.; Hu, L.; Liu, N.; Wang, H.; Vosgueritchian, M.; Yang, Y.; Cui, Y.; Bao, Z. *Nano Lett.* **2011**, *11* (10), 4438–4442.
- (139) Sumboja, A.; Foo, C. Y.; Wang, X.; Lee, P. S. *Adv. Mater.* **2013**, *25* (20), 2809–2815.
- (140) Li, Z.; Mi, Y.; Liu, X.; Liu, S.; Yang, S.; Wang, J. *J. Mater. Chem.* **2011**, *21* (38), 14706.
- (141) Li, Y.; Zhao, X.; Yu, P.; Zhang, Q. *Langmuir* **2013**, *29* (1), 493–500.
- (142) Green, A. A.; Hersam, M. C. *Nano Lett.* **2009**, *9* (12), 4031–4036.
- (143) Wang, S.; Yi, M.; Shen, Z.; Zhang, X.; Ma, S. *RSC Adv.* **2014**, *4* (48), 25374.
- (144) Khan, U.; O’Neill, A.; Lotya, M.; De, S.; Coleman, J. N. *Small* **2010**, *6* (7), 864–871.
- (145) Lotya, M.; King, P. J.; Khan, U.; De, S.; Coleman, J. N. *ACS Nano* **2010**, *4* (6), 3155–3162.
- (146) Paton, K. R.; Varrla, E.; Backes, C.; Smith, R. J.; Khan, U.; O’Neill, A.; Boland, C.; Lotya, M.; Istrate, O. M.; King, P.; Higgins, T.; Barwich, S.; May, P.; Puczkarski, P.; Ahmed, I.; Moebius, M.; Pettersson, H.; Long, E.; Coelho, J.; O’Brien, S. E.; McGuire, E. K.; Sanchez, B. M.; Duesberg, G. S.; McEvoy, N.; Pennycook, T. J.; Downing, C.; Crossley, A.; Nicolosi, V.; Coleman, J. N. *Nat. Mater.* **2014**, *13* (6), 624–630.
- (147) Mao, S.; Pu, H.; Chen, J. *RSC Adv.* **2012**, *2* (7), 2643.

- (148) Chua, C. K.; Pumera, M. *Chem Soc Rev* **2014**, *43* (1), 291–312.
- (149) Stankovich, S.; Dikin, D. A.; Piner, R. D.; Kohlhaas, K. A.; Kleinhammes, A.; Jia, Y.; Wu, Y.; Nguyen, S. T.; Ruoff, R. S. *Carbon* **2007**, *45* (7), 1558–1565.
- (150) Lerf, A. *Solid State Ion.* **1997**, *101-103*, 857–862.
- (151) Erickson, K.; Erni, R.; Lee, Z.; Alem, N.; Gannett, W.; Zettl, A. *Adv. Mater.* **2010**, *22* (40), 4467–4472.
- (152) Singh, V.; Joung, D.; Zhai, L.; Das, S.; Khondaker, S. I.; Seal, S. *Prog. Mater. Sci.* **2011**, *56* (8), 1178–1271.
- (153) Dreyer, D. R.; Park, S.; Bielawski, C. W.; Ruoff, R. S. *Chem Soc Rev* **2010**, *39* (1), 228–240.
- (154) Shin, H.-J.; Kim, K. K.; Benayad, A.; Yoon, S.-M.; Park, H. K.; Jung, I.-S.; Jin, M. H.; Jeong, H.-K.; Kim, J. M.; Choi, J.-Y.; Lee, Y. H. *Adv. Funct. Mater.* **2009**, *19* (12), 1987–1992.
- (155) Pei, S.; Zhao, J.; Du, J.; Ren, W.; Cheng, H.-M. *Carbon* **2010**, *48* (15), 4466–4474.
- (156) Fugetsu, B.; Sano, E.; Yu, H.; Mori, K.; Tanaka, T. *Carbon* **2010**, *48* (12), 3340–3345.
- (157) Lynn, S. Part I: Radial Diffusion in a Turbulent Air Stream; Part II: Absorption of Light by the System Nitric Acid-Nitrogen Dioxide-Water; Part III: Kinetics of the Decomposition of Sodium Dithionite; Part IV: The Determination of Chromium by Oxidation in the Presence of Silver Nitrate. Doctor of Philosophy, California Institute of Technology: Pasadena, California, 1954.
- (158) Rinker, R. Part I: Studies in the Chemistry of Sodium Dithionite; Part II: A Preliminary Study of the Catalyzed Addition of Hydrogen Chloride to Vinyl Chloride in a Stirred Reactor. Doctor of Philosophy, California Institute of Technology: Pasadena, California, 1959.
- (159) Jhaveri, A. S.; Sharma, M. M. *Chem. Eng. Sci.* **1968**, *23*, 1–8.
- (160) Singh, D. K.; Sharma, R. N.; Srivastava, R. D. *Am. Inst. Chem. Eng. J.* **1978**, *24* (2), 232–237.
- (161) Camacho, F.; Páez, M. P.; Blázquez, G.; Jiménez, M. C.; Fernández, M. *Chem. Eng. Sci.* **1995**, *50* (7), 1181–1186.

- (162) Camacho, F.; Páez, M. P.; Jiménez, M. C.; Fernández, M. *Chem. Eng. Sci.* **1997**, *52* (8), 1387–1391.
- (163) Camacho Rubio, F.; Paez Duenas, P.; Blazquez Garcia, G.; Garrido Martin, J. M. *Chem. Eng. Sci.* **1992**, *47* (17), 4309–4314.
- (164) Mayhew, S. G. *Eur. J. Biochem.* **1978**, *85* (2), 535–547.
- (165) Redemann, C. T.; Redemann, C. E. *Org. Synth.* **1949**, *29*, 8.
- (166) Shateri-Khalilabad, M.; Yazdanshenas, M. E. *Carbohydr. Polym.* **2013**, *96* (1), 190–195.
- (167) Horng, Y.-Y.; Lu, Y.-C.; Hsu, Y.-K.; Chen, C.-C.; Chen, L.-C.; Chen, K.-H. *J. Power Sources* **2010**, *195* (13), 4418–4422.
- (168) Simon, P.; Taberna, P.-L.; Béguin, F. In *Supercapacitors*; Béguin, F., Frackowiak, E., Eds.; Wiley-VCH Verlag GmbH & Co. KGaA: Weinheim, Germany, 2013; pp 131–165.
- (169) Borland, W. Dynamite. US 443035, December 16, 1890.
- (170) Morgan, P. *Carbon fibers and their composites*; Taylor & Francis: Boca Raton, 2005.
- (171) *Activated carbon surfaces in environmental remediation*; Bandosz, T. J., Ed.; Interface science and technology; Elsevier/AP: Amsterdam, 2006.
- (172) Rodríguez-Reinoso, F.; Pastor, A. C.; Marsh, H.; Huidobro, A. *Carbon* **2000**, *38* (3), 397–406.
- (173) Shimazaki, K. *Nippon Kagaku Kaishi* **1993**, *7* (1), 54–61.
- (174) Perret, R.; Ruland, W. *J. Appl. Crystallogr.* **1970**, *3* (6), 525–532.
- (175) Tanahashi, I. *J. Appl. Electrochem.* **2005**, *35* (11), 1067–1072.
- (176) Engineered Fibers Technology, LLC 2013.
- (177) Ryu, S. K.; Jin, H.; Gondy, D.; Puset, N.; Ehrburger, P. *Carbon* **1993**, *31* (5), 841–842.
- (178) Brunauer, S.; Deming, L. S.; Deming, W. E.; Teller, E. *J. Am. Chem. Soc.* **1940**, *62* (7), 1723–1732.
- (179) Yang, M.-C.; Yu, D.-G. *J. Appl. Polym. Sci.* **1996**, *59* (11), 1725–1731.

- (180) Ko, T.-H.; chiranairadul, P.; Lu, C.-K.; Lin, C.-H. *Carbon* **1992**, *30* (4), 647–655.
- (181) Ikegami, S.; Hirai, M.; Izumi, K. Process for the Production of Fibrous Activated Carbon. US 4362646, December 7, 1982.
- (182) Lee, J. C.; Lee, B. H.; Kim, B. G.; Park, M. J.; Lee, D. Y.; Kuk, I. H.; Chung, H.; Kang, H. S.; Lee, H. S.; Ahn, D. H. *Carbon* **1997**, *35* (10-11), 1479–1484.
- (183) Wang, P. H. *J. Appl. Polym. Sci.* **2003**, *62* (10), 1771–1773.
- (184) Alcañiz-Monge, J.; Cazorla-Amorós, D.; Linares-Solano, A.; Yoshida, S.; Oya, A. *Carbon* **1994**, *32* (7), 1277–1283.
- (185) Xie, Y.; Sherwood, P. M. A. *Chem. Mater.* **1990**, *2* (3), 293–299.
- (186) Xie, Y.; Sherwood, P. M. A. *Chem. Mater.* **1989**, *1* (4), 427–432.
- (187) Hellgren, N.; Johansson, M. P.; Broitman, E.; Hultman, L.; Sundgren, J.-E. *Phys. Rev. B* **1999**, *59* (7), 5162–5169.
- (188) Emmerich, F. G.; de Sousa, J. C.; Torriani, I. L.; Luengo, C. A. *Carbon* **1987**, *25* (3), 417–424.
- (189) Geniès, E. M.; Boyle, A.; Lapkowski, M.; Tsintavis, C. *Synth. Met.* **1990**, *36* (2), 139–182.
- (190) Ito, T.; Shirakawa, H.; Ikeda, S. *J. Polym. Sci. Polym. Chem. Ed.* **1974**, *12* (1), 11–20.
- (191) Bhadra, S.; Khastgir, D.; Singha, N. K.; Lee, J. H. *Prog. Polym. Sci.* **2009**, *34* (8), 783–810.
- (192) Lota, K.; Khomenko, V.; Frackowiak, E. *J. Phys. Chem. Solids* **2004**, *65* (2-3), 295–301.
- (193) Novák, P.; Müller, K.; Santhanam, K. S. V.; Haas, O. *Chem. Rev.* **1997**, *97* (1), 207–282.
- (194) Xie, Y.; Xia, C.; Du, H.; Wang, W. *J. Power Sources* **2015**, *286*, 561–570.
- (195) Hand, R. L.; Nelson, R. F. *J. Electrochem. Soc.* **1978**, *125* (7), 1059–1069.
- (196) Carlin, C. M.; Kepley, L. J.; Bard, A. J. *J. Electrochem. Soc.* **1985**, *132* (2), 353–359.
- (197) Genies, E. M.; Tsintavis, C. *J. Electroanal. Chem. Interfacial Electrochem.* **1985**, *195* (1), 109–128.

- (198) Zotti, G.; Cattarin, S.; Comisso, N. *J. Electroanal. Chem. Interfacial Electrochem.* **1987**, *235* (1-2), 259–273.
- (199) Zotti, G.; Cattarin, S.; Comisso, N. *J. Electroanal. Chem. Interfacial Electrochem.* **1988**, *239* (1-2), 387–396.
- (200) Kanamura, K. *J. Electrochem. Soc.* **1995**, *142* (9), 2894.
- (201) Kuzmany, H.; Genies, E. M.; Syed, A. In *Electronic Properties of Polymers and Related Compounds*; Kuzmany, H., Mehring, M., Roth, S., Eds.; Cardona, M., Fulde, P., Queisser, H.-J., Series Eds.; Springer Berlin Heidelberg: Berlin, Heidelberg, 1985; Vol. 63, pp 223–226.
- (202) Fedorko, P.; Trznadel, M.; Pron, A.; Djurado, D.; Planès, J.; Travers, J. P. *Synth. Met.* **2010**, *160* (15-16), 1668–1671.
- (203) Macdiarmid, A. G.; Chiang, J. C.; Richter, A. F.; Epstein, A. J. *Synth. Met.* **1987**, *18* (1-3), 285–290.
- (204) Pron, A.; Rannou, P. *Prog. Polym. Sci.* **2002**, *27* (1), 135–190.
- (205) Elkais, A. R.; Gvozdrenović, M. M.; Jugović, B. Z.; Stevanović, J. S.; Nikolić, N. D.; Grgur, B. N. *Prog. Org. Coat.* **2011**, *71* (1), 32–35.
- (206) Gupreet, K. P. *Synthesis and Characterization of Conducting Polymer Polyaniline*, University of Thapar: Patiala, India, 2008.
- (207) Yan, X. B.; Han, Z. J.; Yang, Y.; Tay, B. K. *Sens. Actuators B Chem.* **2007**, *123* (1), 107–113.
- (208) Orth, M. *MRS Proc.* **2002**, 736.
- (209) Lu, X.; Xia, Y. *Nat. Nanotechnol.* **2006**, *1* (3), 163–164.
- (210) Ajayan, P. M.; Schadler, L. S.; Giannaris, C.; Rubio, A. *Adv. Mater.* **2000**, *12* (10), 750–753.
- (211) Safadi, B.; Andrews, R.; Grulke, E. A. *J. Appl. Polym. Sci.* **2002**, *84* (14), 2660–2669.
- (212) Xie, X.-L.; Mai, Y.-W.; Zhou, X.-P. *Mater. Sci. Eng. R Rep.* **2005**, *49* (4), 89–112.
- (213) Kharchenko, S. B.; Douglas, J. F.; Obrzut, J.; Grulke, E. A.; Migler, K. B. *Nat. Mater.* **2004**, *3* (8), 564–568.

- (214) An, K. H.; Kim, W. S.; Park, Y. S.; Moon, J.-M.; Bae, D. J.; Lim, S. C.; Lee, Y. S.; Lee, Y. H. *Adv. Funct. Mater.* **2001**, *11* (5), 387–392.
- (215) Jurewicz, K.; Delpeux, S.; Bertagna, V.; Béguin, F.; Frackowiak, E. *Chem. Phys. Lett.* **2001**, *347* (1-3), 36–40.
- (216) Pidcock, G. C.; in het Panhuis, M. *Adv. Funct. Mater.* **2012**, *22* (22), 4790–4800.
- (217) Wang, X.; Han, X.; Lim, M.; Singh, N.; Gan, C. L.; Jan, M.; Lee, P. S. *J. Phys. Chem. C* **2012**, *116* (23), 12448–12454.
- (218) Wu, Z. *Science* **2004**, *305* (5688), 1273–1276.
- (219) Zhou, C.; Kumar, S.; Doyle, C. D.; Tour, J. M. *Chem. Mater.* **2005**, *17* (8), 1997–2002.
- (220) Chou, S.-L.; Wang, J.-Z.; Chew, S.-Y.; Liu, H.-K.; Dou, S.-X. *Electrochem. Commun.* **2008**, *10* (11), 1724–1727.
- (221) Saran, N.; Parikh, K.; Suh, D.-S.; Muñoz, E.; Kolla, H.; Manohar, S. K. *J. Am. Chem. Soc.* **2004**, *126* (14), 4462–4463.
- (222) Shim, B. S.; Chen, W.; Doty, C.; Xu, C.; Kotov, N. A. *Nano Lett.* **2008**, *8* (12), 4151–4157.
- (223) Zhang, W.; Shiozawa, H.; Wu, C. W.; Hamerton, I.; Cox, D. C.; Silva, S. R. P. *J. Nanosci. Nanotechnol.* **2012**, *12* (1), 84–90.
- (224) Guo, S.; Wang, W.; Ozkan, C. S.; Ozkan, M. *J. Mater. Res.* **2013**, *28* (07), 918–926.
- (225) Alimohammadi, F.; Parvinzadeh Gashti, M.; Shamei, A. *J. Coat. Technol. Res.* **2012**, *10* (1), 123–132.
- (226) Ferrer-Anglada, N.; Pérez-Puigdemont, J.; Figueras, J.; Iqbal, M.; Roth, S. *Nanoscale Res. Lett.* **2012**, *7* (1), 571.
- (227) Fugetsu, B.; Akiba, E.; Hachiya, M.; Endo, M. *Carbon* **2009**, *47* (2), 527–530.
- (228) Favini, E.; Agnihotra, S.; Surwade, S. P.; Niezrecki, C.; Willis, D.; Chen, J.; Niemi, E.; Desabrais, K.; Charette, C.; Manohar, S. K. *J. Intell. Mater. Syst. Struct.* **2012**, *23* (17), 1969–1986.
- (229) Zhang, W.; Johnson, L.; Silva, S. R. P.; Lei, M. K. *Appl. Surf. Sci.* **2012**, *258* (20), 8209–8213.

- (230) Cao, J.; Li, X.; Wang, Y.; Walsh, F. C.; Ouyang, J.-H.; Jia, D.; Zhou, Y. *J. Power Sources* **2015**, *293*, 657–674.
- (231) Carbon Solutions, Inc. 2013.
- (232) Xie, X.; Ye, M.; Hu, L.; Liu, N.; McDonough, J. R.; Chen, W.; Alshareef, H. N.; Criddle, C. S.; Cui, Y. *Energy Environ. Sci.* **2012**, *5* (1), 5265.
- (233) Nesbitt, H. W.; Banerjee, D. *Am. Mineral.* **1998**, *83* (3-4), 305–315.
- (234) Obreja, V. V. N. *Phys. E Low-Dimens. Syst. Nanostructures* **2008**, *40* (7), 2596–2605.
- (235) Nardecchia, S.; Carriazo, D.; Ferrer, M. L.; Gutiérrez, M. C.; del Monte, F. *Chem. Soc. Rev.* **2013**, *42* (2), 794.
- (236) Xie, X.; Yu, G.; Liu, N.; Bao, Z.; Criddle, C. S.; Cui, Y. *Energy Environ. Sci.* **2012**, *5* (5), 6862.
- (237) Ferrari, A. C.; Meyer, J. C.; Scardaci, V.; Casiraghi, C.; Lazzeri, M.; Mauri, F.; Piscanec, S.; Jiang, D.; Novoselov, K. S.; Roth, S.; Geim, A. K. *Phys. Rev. Lett.* **2006**, *97* (18).
- (238) Kuila, T.; Bose, S.; Mishra, A. K.; Khanra, P.; Kim, N. H.; Lee, J. H. *Prog. Mater. Sci.* **2012**, *57* (7), 1061–1105.
- (239) Hummers, W. S.; Offeman, R. E. *J. Am. Chem. Soc.* **1958**, *80* (6), 1339–1339.
- (240) Zhou, Y.; Bao, Q.; Tang, L. A. L.; Zhong, Y.; Loh, K. P. *Chem. Mater.* **2009**, *21* (13), 2950–2956.
- (241) Amarnath, C. A.; Hong, C. E.; Kim, N. H.; Ku, B.-C.; Kuila, T.; Lee, J. H. *Carbon* **2011**, *49* (11), 3497–3502.
- (242) Ciesielski, A.; Samorì, P. *Chem Soc Rev* **2014**, *43* (1), 381–398.
- (243) Woltornist, S. J.; Oyer, A. J.; Carrillo, J.-M. Y.; Dobrynin, A. V.; Adamson, D. H. *ACS Nano* **2013**, *7* (8), 7062–7066.
- (244) Yu, G.; Hu, L.; Vosgueritchian, M.; Wang, H.; Xie, X.; McDonough, J. R.; Cui, X.; Cui, Y.; Bao, Z. *Nano Lett.* **2011**, *11* (7), 2905–2911.
- (245) Zhou, T.; Chen, F.; Liu, K.; Deng, H.; Zhang, Q.; Feng, J.; Fu, Q. *Nanotechnology* **2011**, *22* (4), 045704.

- (246) Pashley, R. M.; Rzechowicz, M.; Pashley, L. R.; Francis, M. J. *J. Phys. Chem. B* **2005**, *109* (3), 1231–1238.
- (247) Song, P.; Zhang, X.; Sun, M.; Cui, X.; Lin, Y. *RSC Adv* **2012**, *2* (3), 1168–1173.
- (248) Secor, E. B.; Prabhumirashi, P. L.; Puntambekar, K.; Geier, M. L.; Hersam, M. C. *J. Phys. Chem. Lett.* **2013**, *4* (8), 1347–1351.
- (249) Lotya, M.; Hernandez, Y.; King, P. J.; Smith, R. J.; Nicolosi, V.; Karlsson, L. S.; Blighe, F. M.; De, S.; Wang, Z.; McGovern, I. T.; Duesberg, G. S.; Coleman, J. N. *J. Am. Chem. Soc.* **2009**, *131* (10), 3611–3620.
- (250) Guardia, L.; Fernández-Merino, M. J.; Paredes, J. I.; Solís-Fernández, P.; Villar-Rodil, S.; Martínez-Alonso, A.; Tascón, J. M. D. *Carbon* **2011**, *49* (5), 1653–1662.
- (251) Leary, J. D.; Hamouda, F.; Mazé, B.; Pourdeyhimi, B. *J. Appl. Polym. Sci.* **2016**, *133* (16), n/a – n/a.
- (252) Pourdeyhimi, B.; Maze, B.; Fox, E.; Leary, J. *High-Performance Nanostructured Supercapacitor on an Engineered Nonwoven*; Final Scientific Report ADA614081; The Nonwovens Institute: Raleigh, NC, 2014.